



2015

HIGH TEMPERATURE FLOW SOLVER FOR AEROTHERMODYNAMICS PROBLEMS

Huaibao Zhang

University of Kentucky, paulhuaizhang@gmail.com

[Click here to let us know how access to this document benefits you.](#)

Recommended Citation

Zhang, Huaibao, "HIGH TEMPERATURE FLOW SOLVER FOR AEROTHERMODYNAMICS PROBLEMS" (2015). *Theses and Dissertations--Mechanical Engineering*. 64.
https://uknowledge.uky.edu/me_etds/64

This Doctoral Dissertation is brought to you for free and open access by the Mechanical Engineering at UKnowledge. It has been accepted for inclusion in Theses and Dissertations--Mechanical Engineering by an authorized administrator of UKnowledge. For more information, please contact UKnowledge@lsv.uky.edu.

STUDENT AGREEMENT:

I represent that my thesis or dissertation and abstract are my original work. Proper attribution has been given to all outside sources. I understand that I am solely responsible for obtaining any needed copyright permissions. I have obtained needed written permission statement(s) from the owner(s) of each third-party copyrighted matter to be included in my work, allowing electronic distribution (if such use is not permitted by the fair use doctrine) which will be submitted to UKnowledge as Additional File.

I hereby grant to The University of Kentucky and its agents the irrevocable, non-exclusive, and royalty-free license to archive and make accessible my work in whole or in part in all forms of media, now or hereafter known. I agree that the document mentioned above may be made available immediately for worldwide access unless an embargo applies.

I retain all other ownership rights to the copyright of my work. I also retain the right to use in future works (such as articles or books) all or part of my work. I understand that I am free to register the copyright to my work.

REVIEW, APPROVAL AND ACCEPTANCE

The document mentioned above has been reviewed and accepted by the student's advisor, on behalf of the advisory committee, and by the Director of Graduate Studies (DGS), on behalf of the program; we verify that this is the final, approved version of the student's thesis including all changes required by the advisory committee. The undersigned agree to abide by the statements above.

Huaibao Zhang, Student

Dr. Alexandre Martin, Major Professor

Dr. Haluk E. Karaca, Director of Graduate Studies

HIGH TEMPERATURE FLOW SOLVER FOR AEROTHERMODYNAMICS
PROBLEMS

DISSERTATION

A dissertation submitted in partial
fulfillment of the requirements for
the degree of Doctor of Philosophy
in the College of Engineering at the
University of Kentucky

By

Huaibao Zhang

Lexington, Kentucky

Director: Dr. Alexandre Martin, Professor of Mechanical Engineering
Lexington, Kentucky 2015

Copyright© Huaibao Zhang 2015

ABSTRACT OF DISSERTATION

HIGH TEMPERATURE FLOW SOLVER FOR AEROTHERMODYNAMICS PROBLEMS

A weakly ionized hypersonic flow solver for the simulation of reentry flow is firstly developed at the University of Kentucky. This code is the fluid dynamics module of known as Kentucky Aerothermodynamics and Thermal Response System (KATS). The solver uses a second-order finite volume approach to solve the laminar Navier–Stokes equations, species mass conservation and energy balance equations for flow in chemical and thermal non-equilibrium state, and a fully implicit first-order backward Euler method for the time integration. The hypersonic flow solver is then extended to account for very low Mach number flow using the preconditioning and switch of the convective flux scheme to AUSM family. Additionally, a multi-species preconditioner is developed.

The following part of this work involves the coupling of a free flow and a porous medium flow. A new set of equation system for both free flows and porous media flows is constructed, which includes a Darcy–Brinkmann equation for momentum, mass conservation, and energy balance equation. The volume-average technique is used to evaluate the physical properties in the governing equations. Instead of imposing interface boundary conditions, this work aims to couple the free/porous problem through flux balance, therefore, flow behaviors at the interface are satisfied implicitly.

KEYWORDS: CFD, Hypersonic, Weakly Ionized, Darcy–Brinkmann, Coupling

Author's signature: Huaibao Zhang

Date: August 19, 2015

HIGH TEMPERATURE FLOW SOLVER FOR AEROTHERMODYNAMICS
PROBLEMS

By
Huaibao Zhang

Director of Dissertation: Alexandre Martin

Director of Graduate Studies: Haluk E. Karaca

Date: August 19, 2015

Dedicated to my dear family in China and the US

ACKNOWLEDGMENTS

My deepest gratitude goes to my mentor, and supervisor, Professor Alexandre Martin. I was blessed to have the opportunity to work under his supervision and make this dissertation a reality. His patient guidance, and constant encouragement were present for the entirety of the development of this work. Furthermore, he is, to me, like a Jedi master. I am a young Padawan, who has learned from him how to follow my dream to one day be a faculty member, and have the opportunity to research, and teach, not only from books, but also, from life.

I wish to thank my co-supervisor, Professor James M. McDonough. His unique lectures such as Basic Computational Numerical Analysis and Introduction to Turbulence, are unforgettable to me. I would also like to thank the members of the committee, Professor Kaveh A. Tagavi, Professor Sean Bailey, Professor Stephen E. Rankin, Doctor Dinesh Prabhu from NASA Ames, and Professor Christopher Crawford. Their thoughtful and instructive suggestions for this work, and their incredible patience, were more than helpful to me.

I would like to give a special acknowledgment to Dr. Leonardo C. Scalabrin, Dr. Hicham Alkandry, and Prof. Paolo Francesco Barbante who engaged in many useful discussions and gave many good suggestions for my work. Thanks to Dr. Emre Sozer, Prof. M. Grae Worster, Dr. Minkwan Kim, Dr. Ioannis Nompelis, Prof. Graham V. Candler, and Dr. Michael J. Wright for helping me by patiently answering my emails.

I also wish to acknowledge Dr. Haoyue Weng, Dr. Francesco Panerai, Raghava Davuluri, David Smith, Zhiyong Li, Tingting Tang, James Polly, Olivia M Schroeder, and all the great people in our CFD group. I would not have had as much fun without their encouragement, help, and humor.

I wish to give my acknowledgement to the technicians in the High Performance Computer Center, at the University of Kentucky, Dr. Qiyou Jiang, now at Rice University, Jerry Grooms, Vikram Gazula, and Krishna Prabhala, from the Computer Maintenance Department.

I would like to give my blessings to the Sangha members of the Lexington Zen Center. I am thankful that they maintain this great community, and that they allowed me to join them in practicing meditation.

I would like to express my gratitude to Jully, Chien-Suu and Justin Kuo for being my close friends and caring so much for me.

A thanks to my parents, my brother Huaijin (Jim), and my saintly sister Min, for always having my back, whether it be with spiritual support, courage, or anything else.

Finally, a thanks to my host family, Tom and Nancy Tucker for their love and encouragement, that sustained me throughout, and my brothers and sisters, David, Ben, Yan, Weihua, and Corey, for their care, and help.

To all of my friends.

TABLE OF CONTENTS

Acknowledgments	iii
Table of Contents	v
List of Tables	vii
List of Figures	viii
Chapter 1 Introduction	1
1.1 Motivation	1
1.2 Flow Field	3
1.3 Thermal Protection System	7
1.4 The Surface	8
1.5 Coupling of the Aerothermal Free Flow and the Flow in Thermal Protection System	8
1.6 Scope of Current Work	11
Chapter 2 Governing Equations of Fluid Dynamics	14
2.1 Introduction	14
2.2 Source Terms	23
Chapter 3 Numerical Framework for Flow Dynamics	32
3.1 Introduction	32
3.2 Calculation of Flux Vector	34
3.3 Higher-order Extension of Convective Flux	37
3.4 Diffusive Flux Vector	42
3.5 Jacobian	43
3.6 Boundary Conditions	46
3.7 Linear Solver	54
Chapter 4 Hypersonic Solver: Verification and Validation	56
4.1 Mach 10 Argon Flow over a Cylinder	56
4.2 Mars Entry Spacecraft Model	57
4.3 Numerical Investigation on Stardust Capsule	66
4.4 Numerical Investigation of Low-Density Nozzle Flow of Nitrogen	73
Chapter 5 Subsonic Solver: Verification and Validation	92
5.1 Preconditioning and Low Mach Number Flow	92
5.2 Free Flow Test Case	95
5.3 Lid-driven Cavity Problem	97

Chapter 6	Coupling of A Free Flow and A Porous Medium Flow	101
6.1	Convective flux	103
6.2	Viscous flux	108
6.3	Verification of the Governing Equation System on Channel Flows . .	109
Chapter 7	Summary and Conclusions	123
7.1	Summary	123
7.2	Conclusions	127
7.3	Original Contributions	128
Appendix A.	Chemistry and Physics Data Source Table	131
	Species data	131
	Electronic energy data	131
	NASA 9 Polynomial Data	132
	Reaction data	137
	Modified Millikan and White coefficients	138
Appendix B:	Detailed Derivations: Hypersonic Solver	141
	Jacobian of the inviscid flux vector	141
	Inviscid Jacobians	146
	Viscous Jacobians	157
	Time terms in thermal non-equilibrium	162
	Time terms for thermal equilibrium	164
	Chemistry Jacobians	165
	Non-Equilibrium Jacobians	169
Bibliography	172
Vita	186
	Professional Experience	186

LIST OF TABLES

2.1	Constants	30
4.1	Free stream conditions for the flow field	56
4.2	Mars entry spacecraft model geometry	60
4.3	Free stream conditions for the flow field	61
4.4	Free stream conditions for the flow field	67
4.5	Nozzle geometry	77
4.6	Nozzle flow condition for the experimental configurations	77
6.1	Fluid properties	113
6.2	Fluid properties	119
1	Basic species chemistry data	131
2	Electronic energy modes	133
3	Electronic energy modes – continued	134
4	NASA 9 polynomial constants	135
5	NASA 9 polynomial constants – continued	136
6	Reaction Data	137
7	Coefficient φ for dissociation reaction	138
8	Modified Millikan and White Coefficients	139
9	Modified Millikan and White Coefficients – continued	140

LIST OF FIGURES

1.1	Simulation of Mach 10 Argon flow over Stardust capsule	2
3.1	Cell's neighbor cloud	38
3.2	Triangular grid	41
4.1	Computational grid for simulation of Mach 10 Argon flow over cylinder. .	57
4.2	Isocontours for the Mach 10 Argon flow over the cylinder.	58
4.3	Stagnation line results for the Mach 10 Argon flow over a cylinder. . . .	59
4.4	Surface heat flux for the Mach 10 Argon flow over a cylinder.	60
4.5	Mars entry spacecraft model geometry	61
4.6	Meshed used in this simulation	62
4.7	Solution contours	63
4.8	Properties along the stagnation line	64
4.9	Heat transfer rate on the Mars Entry Lab model forebody	65
4.10	Numerical study on the numerical error near the stagnation point	66
4.11	Stardust capsule	67
4.12	Mesh	68
4.13	Solution contour	70
4.14	Kn number	71
4.15	Mesh refinement study	72
4.16	Mass fraction for 5-species air model	73
4.17	Solution contour comparisons. The upper is 5sp model, and the lower is 11sp model	74
4.18	Temperatures along stagnations	75
4.19	Mass fraction for 11-species air model	75
4.20	Heat transfer rate comparisons	76

4.21	Nozzle geometry [1]	76
4.22	An incorrect solution unable to converge due to uniform initialization	78
4.23	Initialization configuration for pressure	78
4.24	Sketch of mesh in 2-D	80
4.25	Pressure iso-contour for the convergent-divergent nozzle flow	82
4.26	Density iso-contour for the convergent-divergent nozzle flow	82
4.27	T_{tr} iso-contour for the convergent-divergent nozzle flow	83
4.28	T_{ve} iso-contour for the convergent-divergent nozzle flow	83
4.29	Mach iso-contour for the convergent-divergent nozzle flow	84
4.30	Kn iso-contour for the convergent-divergent nozzle flow	84
4.31	U/U_o results from KATS compared to Ref. [1]	85
4.32	T/T_o results from KATS compared to Ref. [1]	87
4.33	Static pressure and Mach number results from KATs at the exit	88
4.34	Reynolds number from KATS at the exit for Mach>1	89
4.35	Normalized Pitot pressure from KATS compared to Ref. [1]	90
5.1	N_2 flow through a pipe	96
5.2	Two N_2 flow through a pipe	97
5.3	Simulation of a lid-driven cavity problem	99
5.4	Numerical solutions of KATS compared to reference numerical solutions [2]	100
6.1	Normalized streamwise velocity along the centerline of the coupling case in Section 6.3 using different reference Mach numbers for AUSM ⁺ -up scheme. The reference velocity V is the analytical free flow mean velocity in Section 6.3.	105
6.2	Effects of number of filtering times	109
6.3	Geometry configuration for a free channel flow	110
6.4	Pressure and velocity contour	111
6.5	Numerical velocity verification for the free flow	112

6.6	Geometry configuration for a Darcy problem	113
6.7	Pressure and Darcy velocity error contour for a Darcy problem	115
6.8	Streamwise properties along the centerline for a Darcy problem	116
6.9	Geometry configuration for a Darcy problem with no-slip wall boundaries	116
6.10	Pressure and darcy velocity contour for a Darcy problem with no-slip wall	117
6.11	Streamwise properties along the centerline for a Darcy problem with no- slip wall	118
6.12	Geometry configuration for free/porous domain [3]	119
6.13	Intrinsic and Darcy velocity contour	121
6.14	Static pressure and velocity along the stagnation line compared to numer- ical solutions in Ref. [4]	122

Chapter 1 Introduction

1.1 Motivation

One of the most important aspects of planetary exploration is the ability to safely enter the atmosphere of a planet, decelerate properly and land smoothly. Returning from outer space, entry vehicles travel at tremendous speed during this process. A flagship example is Stardust Sample Return Capsule (SRC), whose mission was to collect samples of interstellar dust from the tail of comet WILD-2. It entered the earth atmosphere at a velocity of 12.6 km/s [5], and is the fastest earth reentry and highest energy reentry of any artificial vehicle thus far. In such conditions, the vehicle is in the hypersonic flow regime, and a strong bow shock develops in front of it. This includes large temperature levels and gradients that can trigger chemical reactions and rapid energy transfers. The gas compression due to the shock wave, as well as surface friction of the atmospheric gas, generates vast aerodynamic heating. Although most of this heating dissipates into the surrounding atmosphere and is taken away by the flow, a fraction still reaches the vehicle through conductive heating and radiation. For instance, Fig. 1.1 shows a simulation of a Mach 10 Argon flow over a capsule, in which the temperature jumps to above 6500 K behind the shock. Since vehicles are subjected to this intense aerodynamic heating, it is critical to equip them with an appropriate Thermal Protection System (TPS) in order to protect the payload and ensure safe landing.

Early Entry, Descent and Landing (EDL) technology development and qualification mostly relied on ground testing [6]. Until recently relatively few new developments have been made since the technology was developed and qualified in the 1960s and 1970s. After the final Apollo flight in the mid-1970s, NASA's manned operation concentrated on the space shuttle program. The development of new EDL technolo-

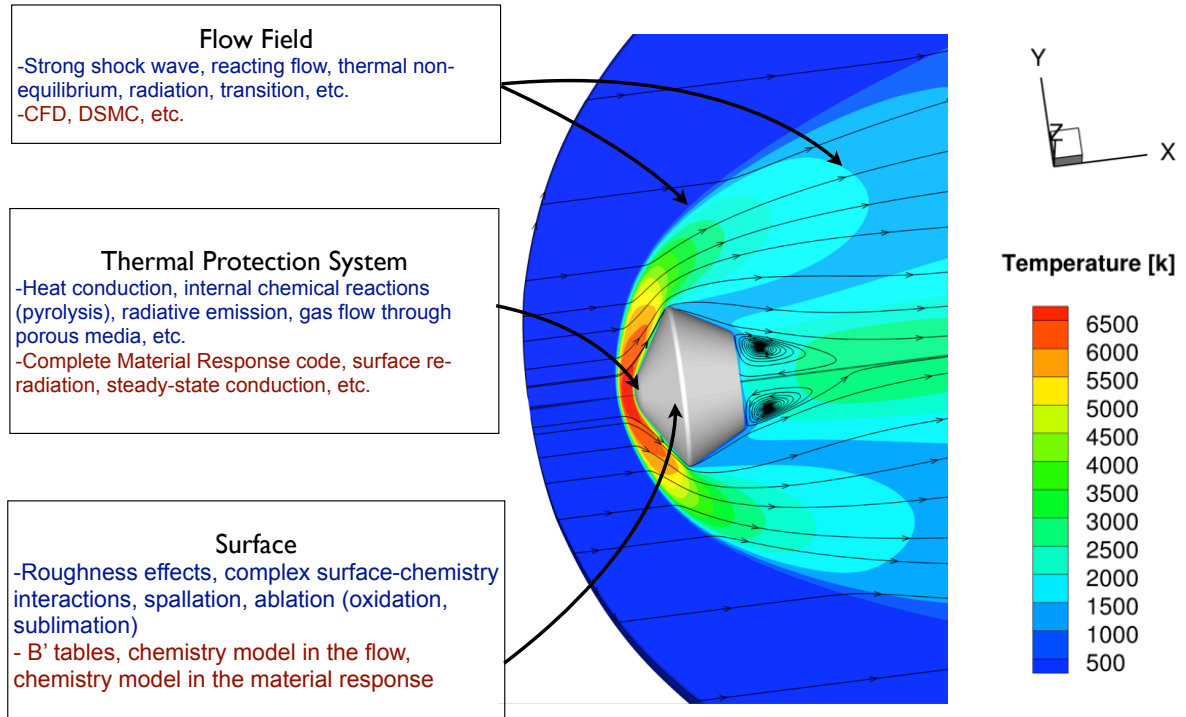


Figure 1.1: Simulation of Mach 10 Argon flow over Stardust capsule

gies has since found a new wind with the retirement of the space shuttles and the design of a new generation capsule as the space vehicle.

For ground tests, the extreme free stream conditions experienced by the re-entry vehicles are still quite difficult to reproduce, and also hard to measure in an experimental facility, even under current technology. The costs of these developmental tests are also a concern. As mankind looks toward further missions to Mars, Venus and beyond, flight tests performed on Earth are not able to assess and evaluate actual mission conditions. Numerical modeling offers an appealing solution as the cost of high-performance computation drops while the computation power increases. Different from experimental investigation, in which the fluid properties and behaviors can be determined through observation (i.e. direct measurement), the accurate modeling of phenomena in hypersonic flight regime relies on understanding every aspect of physics, and building suitable mathematical governing equations. The physical

phenomena associated to re-entry problems are shown in Fig. 1.1, and listed below:

- Flow Field: strong shock wave compression, shock layer radiation, chemical reactions, thermal non-equilibrium, transition to turbulence
- Thermal Protection System: internal chemical reactions (pyrolysis), mass momentum such as gas flow through porous media, and heat transfer such as heat conduction and radiative emission
- Surface: surface roughness effects, complex surface-chemistry interactions, ablation, spallation

Each problem can be respectively modeled by

- Flow Field: Computational Fluid Dynamics (CFD), Direct Simulation Monte Carlo (DSMC), etc.
- Thermal Protection System: complete Material Response code, surface re-radiation, steady-state ablation, etc.
- Surface: B' tables (surface thermo-chemistry data), chemistry model in the flow, chemistry model in the material response

Following the brief introduction on these three main research fields related to a typical capsule reentry, details for each of them will be discussed, with a focus on the flow field.

1.2 Flow Field

In literature, hypersonic aerothermodynamics defines flow regions in which the associated Mach number is greater than 5 [7]. As vehicles fly from subsonic (Mach<1) to supersonic regime (Mach>1), dramatic physical changes take place in the flow: a shock wave is generated by the surface of the object and physical properties are altered sharply across the shock because of intense compressibility. Different from

those of subsonic and supersonic region, in a hypersonic regime, nondimensional variables such as pressure coefficient, lift and drag coefficients, and flow field structure become Mach number independent. This is the essence of the *Mach number independence principle* [7] for hypersonic flow. To distinguish and characterize a flow from supersonic, the hypersonic regime can also be suitably defined by certain physical and chemical effects which are prominent. These effects can be mainly summarized as real gas effects, including high-temperature effects, as well as thermal and chemical non-equilibrium, as shown in the following subsections.

Mixture of Thermally Perfect Gases

It is necessary to understand the physical behavior of a gas in a hypersonic regime. A gas is a collection of particles: molecules, atoms, ions, and electrons etc, which are moving randomly. By ignoring *intermolecular forces*, the gas behaves as a *perfect gas* [7], whose equation of state can be given by

$$p = \rho RT \quad , \quad (1.1)$$

where p is the pressure, ρ is the density (inverse of the specific volume), T is the temperature, and R is the specific gas constant.

A further assumption of the invariant specific heat ratio $\gamma = Cp/Cv$ implies a *calorically perfect gas*, where Cp and Cv are constants, denoting the specific heat at constant pressure and constant volume respectively. An even further assumption, *thermally perfect gas*, is defined as the one where Cp and Cv are variables and specifically are functions of temperature only [7]. For both calorically perfect gas and thermally perfect gas, however, the perfect gas law (Eq. (1.1)) is still valid.

In this work, multi-species gases are considered. As the gas temperature increases, high-temperature effects appear. See [7, 8]:

- **γ is no longer constant.** This is due to the excitation of vibrational energy as temperature rises to a high level. The specific heats Cp and Cv act as functions

of temperature. As a result, γ depends on temperature. The vibrational energy excitation effects play important roles for air above the temperature of 800 K.

- **Chemical reactions occur.** In the entire shock layer, molecules dissociate into atoms; atoms recombine into new molecules. The gas can even be partially ionized at a much higher temperature. The gas species' composition change leads to the variation in pressure and density. Meanwhile, chemical reactions are linked to energy consumption or release, which in turn changes the temperature and gradient of the flow field. Chemical reactions can also occur in the boundary layer, changing the gas composition near the wall, shifting the onset of turbulence, and modifying the net heat flux to the surface.
- **Thermal radiation is emitted.** Besides the convective aerodynamic heating, thermal radiation emitted from the gas can become very important in a high temperature. During the Apollo reentries, radiative heating reached more than 30% of the total heat load.

By neglecting intermolecular forces, each individual species is assumed as a thermally perfect gas and obeys the perfect gas law. Therefore, the gas in total involved in this work is a mixture of thermally perfect gases.

Thermal and Chemical Non-equilibrium

For vehicles flying at hypersonic velocities during entry/re-entry, a fluid element moves through the flow field so fast that its velocity time scale may be of the same order as the thermal and chemical equilibrium relaxation time. Vibrational excitation and chemical reactions are not allowed enough time to take place, and thus the flow is considered to be in a state of thermo-chemical non-equilibrium.

Since a two-temperature model [9] is used to account for thermal non-equilibrium in this work, in which a single temperature T_{tr} is used to describe translational and rotational energy modes, and a single temperature T_{ve} is used to describe vi-

brational, electronic and electron translational energy modes, the degree of thermal non-equilibrium can be evaluated by different levels of T_{tr} and T_{ve} .

Thermal non-equilibrium can be observed in many regions of the flow field. Section 4.3 studies the re-entry of the Stardust vehicle, where the relaxation region can be seen behind the shock wave. In this region, the vibrational-electronic energy mode lags behind the translation-rotational energy mode, as is seen by the different levels of temperatures T_{tr} and T_{ve} (Fig. 4.8 (a)). Another example is shown where the flow experiences a strong expansion when it goes through a hypersonic convergent-divergent nozzle facility. In this case, the translation-rotational energy has a high degree of non-equilibrium with the vibrational-electronic energy along the radius in the nozzle outlet as implied by the two temperatures (Fig. 4.32).

As pointed out above, a gas mixture reacts chemically in a high temperature. A chemical reaction in the gas mixture occurs from collisions among the gas particles to break the molecular bond. Since the vehicle flies at high speed, the flow is allowed little time to go through the environment surrounding the vehicle. The characteristic time for traveling velocity is, therefore, comparable to the one of the chemical reactions. Thus, chemical reactions are not fully relaxed, and the flow is in chemical non-equilibrium. A finite-rate chemical kinetics model is needed to take into account this effect.

General Numerical Approach to Model the Flow Field

In the flow field, problems can be characterized by local Knudsen number Kn , which is defined as the ratio of the mean free path to some characteristic length based on geometry or gradients. The mean free path is defined as the average distance of a molecule travels before colliding with another molecule in a reference frame of the flow field. Computational Fluid Dynamics (CFD) is a powerful numerical simulation approach that has been introduced in the past three decades and can be used as a design tool for reentry flow problems. The equation system is constructed assuming

of a continuum description, which corresponds to low-Kn region. For rarefied gas or low-density flow in high-Kn region, underlying assumptions in a continuum regime tend to break down, and CFD is not valid, and other methods have to be used [10,11].

1.3 Thermal Protection System

Thermal Protection Systems are designed to withstand the high heating environment of planetary entry, and to protect the underlying vehicle structure and payload. Since the temperature level varies at different parts of the vehicle, several different materials can be chosen for the TPS, considering that each material bears specific temperature capability, durability, and weight [12,13].

There are two main categories of TPS materials: ablative materials, such as the one used on the Apollo missions, and non-ablative materials, such as the ceramic tiles of the space shuttles. The former can also be divided into two sub-categories: charring (also known as pyrolyzing) and non-charring ablators. Next generation of NASA missions calls for larger, heavier entry system. One key challenge is the development of low mass TPS for higher entry speeds. Of the many TPS options, light weight charring ablators are very promising, and are more and more used because of their effectiveness and low density. They are made of a fibrous non-pyrolyzing matrix (usually carbon or silicon carbide) and are impregnated with pyrolyzing material (often phenolic resin). These materials react to the flow through pyrolysis and the so-called “surface” ablation. Pyrolysis is the process in which the phenolic polymer gradually carbonizes at high temperatures, losing mass, generating pyrolysis gases and leaving pores within the material. These gasses are then expelled through the porous structure of the material and blown into the chemical reacting boundary layer. “Surface” ablation occurs in a thin volume near the surface TPS and takes the form of mass loss through oxidation vaporization, and other erosive processes [14].

To numerically investigate the in-depth thermo-chemical behaviors of the charring ablator problem, a Material Response (MR) code is used [15–19]. Details of the

modeling approach of charring ablators are beyond the scope of this document, but can be found in Ref. [19].

1.4 The Surface

Once the resin has pyrolyzed, the surface smoothness is altered because of the porous nature of the material. The roughness of the ablative surface must be considered: “dimples” in the surface can trigger the transition to turbulence in regions that were previously laminar, thus drastically increasing heat transfer [20].

Pyrolysis chemistry effects must also be modeled properly, which means that the pyrolysis gas flowing through the porous surface must be carefully accounted for. The flow field is affected by the chemical species that are expelled from the ablating surface and injected into the near-wall flow. The presence of this ablation gas greatly reduces the heat flux on the vehicle by (1) thickening the thermal boundary layer and reducing the temperature gradient near the wall; (2) blowing a relatively cooler gas into the flow field; and (3) changing the gas composition near the wall which triggers chemical reactions.

To account for the surface chemistry, one can use thermo-chemical tables (the so-called B' tables) that use boundary layer theory and heat transfer coefficient to extract ablation rates from equilibrium chemistry calculation. Otherwise, the surface chemistry can be assessed from the flow side or the material side, using finite-rate kinetics models.

1.5 Coupling of the Aerothermal Free Flow and the Flow in Thermal Protection System

To analyze an atmospheric entry trajectory, traditionally, the heat flux and pressure at the surface of the vehicle is calculated using a CFD solver. These surface values are then fed into an MR code which calculates surface recession rate, pyrolysis gas blowing rate, species composition and temperature evolution. In such a way, the

outer free flow and TPS can be loosely coupled. Because the entry process involves transient interactions between spacecraft and the flow field, it is of interest to develop a coupled method where both systems are solved simultaneously.

Recent research teams [21–24] have integrated a material response code within a flow solver, using a strongly coupled approach. They use trajectory data to converge the flow and compute the transient material response solution between trajectory points. Their solid-gas interface, however, are not synchronized implicitly in time. Moreover, the two solvers are not directly merged, and even though fully integrated, the two codes are still separated and independent. For some certain type of problems, a fully-coupled approach that provides time-dependent solutions for both the material and the fluid is required.

Removing those surface effects, coupling of the aerothermal flow field and the TPS can be mainly taken as the coupling of a free flow and a porous medium flow, which requires understanding of the physics at the free/porous interface. The following section reviews the general research development on coupling of a free flow and a porous medium flow to date, especially the interface condition implementations between two flow regions.

Review on Coupling of A Free Flow and A Porous Medium Flow

Fluid entering a porous medium occurs over a wide range of natural phenomena and industrial applications. It occurs, for instance, for water seeping into the ground, seawater interacting within corals reef [25], a flow going through oil filters, and a multiphase counter-current flow in a packed bed reactor [26]. The mathematical theory and numerical analysis are well established for either a free flow or a porous medium flow: the Navier–Stokes equation is considered as a full description for the free flow’s momentum in continuum, while Darcy’s law for the porous medium flow is formulated based on experiments. In spite of being a research topic and a classical problem for decades, coupling of a free flow with a porous medium flow is still unresolved. Even

the mathematical theory of the coupled problem is not completely understood [27]. It is to be noted that, strictly speaking, the Navier–Stokes and Darcy’s equations refer only to equations of momentum. A complete description of the fluid behavior also includes mass conservation and energy conservation. Thus, when referring to “coupling of a free flow with a porous medium flow”, the whole system of equation is considered, not just the momentum effects.

Coupling of a free flow and a porous medium flow can be accomplished by analyzing the whole problem in a two-domain or multi-domain method. That is, distinct equation systems that account for each side are developed respectively. Two major mathematical difficulties arise from coupling the two systems [28, 29]. First, the orders of corresponding differential operators of momentum equations (the Navier–Stokes and Darcy’s law) are different on both regions. Second, the nature of the boundary conditions at the interface between two regions is not trivial. An extension of Darcy’s law, the Brinkman model [30], can remove the first difficulty. It is formulated to account for the high porosity of the porous medium or to impose no-slip conditions on solid walls.

When it comes to an application, previous works on the topic of using the multi-domain method mainly considered incompressible, low-temperature flow regions. Mass conservation is thus simplified to a divergence-free flow. Temperature changes can be neglected most of the time, implying energy equation is not considered. Therefore, the remaining difficulty lies in defining the condition for pressure, normal velocity and tangential velocity. One classical condition states the continuity of pressure and normal velocity across the interface. This approach is robust and generally accepted as interface condition for both viscous and inviscid flows. In the case of tangential velocity, one can assume it vanishes for very low permeability or it is continuous as well for large permeability through the porous medium [31]. Beavers & Joseph [32] proved the inaccuracy of both of these choices in their experiments, and later they proposed an equation that accounts for the discontinuity of the interfacial tangential

velocity. This boundary condition was validated experimentally by Beavers & Joseph and analytically by Saffman [33]. Many other types of interfacial conditions have been proposed since then, but mainly based on the manipulation of tangential velocity and tangential shear stress [34, 35]. In addition to these, Le Bars & Worster [31] defined a viscous transition zone close to the interface on the porous medium side, which yields a solution that agrees well with the already known result.

It is noted that coupling a free flow with a porous medium flow can also be accomplished by analyzing the whole problem in a single-domain. The interface between two subdomains is now within one domain implicitly, thus avoiding a lot of mathematical difficulties. The Navier–Stokes equation or Darcy’s law is solved on either side of the interface as the momentum equation accordingly. Alternatively, a single Darcy–Brinkman equation [31] that is valid for both sides can be used. The solution for the free flow and the porous medium flow are thus fully coupled. This requires the development of a whole new universal code for both sides from the very beginning, which is a very limited constraint, or to extend the current CFD solver to become a universal code, which is more promising.

The literature related to the single-domain method concentrates on the finite-element method (FEM) [36, 37], and the control-volume finite-element method (CVFEM) [3, 4]. Recently, Schrooyen [38] extended a universal Discontinuous Galerkin Method (DGM) solver and successfully simulated a multi-species reactive flow case with the presence of a porous medium. However, traditional CFD solvers, especially the modern hypersonic fluid dynamics solvers, are constructed in terms of finite volume method (FVM).

1.6 Scope of Current Work

There is still a long way to go before having a real-time, full assessment of the whole re-entry flight integrating all of phenomena previously described. This thesis, however, aims to push the state of the art one step further by using compressible, viscous

flow, and investigating coupled effects for further use in exploring thermo-chemical non-equilibrium effects in hypersonic flows with ablation.

For this purpose, a CFD code has been developed to solve the flow field. This flow solver is part of the Kentucky Aerothermodynamics and Thermal Response System (KATS) [39] for the work. KATS also includes an MR solver, which shares the same numerical platform and framework as the CFD solver, that has been developed independently and is not part of this work [40].

This proposed work mainly consists of two topics. First, the development of a CFD solver, using FVM, capable of accurately and efficiently dealing with thermo-chemical non-equilibrium effects in weakly ionized hypersonic flows, as well as very low Mach number flows via switch of convective flux schemes and the use of a preconditioner. It has been extensively coupled with the MR solver [41] and spallation phenomenon code [42–44].

The second topic focuses on the modification or extension of the CFD solver to couple the free flow and the porous medium flow involved in the coupling of the aerothermal flow field and the TPS. A first attempt is made on the multiple-domain method [41], which is carried out to couple the existing CFD solver and MR solver through balancing the fluxes at the flow/porous interface. A series of coupling numerical tests are conducted progressively. Promising results are obtained for free flow coupled with solid material through heat and mass transfer only, both in transient and steady state. However, the boundary condition inconsistency in the full coupling flow tube problem is still a question for further investigation. Later, a single-domain method is selected. Specifically, a new Darcy–Brinkman equation for the compressible free flow and the porous medium flow is developed. The mass conservation and energy balance are also volume averaged by incorporating the porosity. The location of the free flow region and the porous medium is known *a priori*. Transitions of different regions are through controlled values of porosity and permeability. Coupling of the free flow and the porous medium flow is thus implicitly accomplished, and solutions

of the free flow field and the porous domain are solved simultaneously. Additionally, instead of imposing explicit interface boundary conditions, such as Beavers & Joseph conditions in the FEM and CVFEM, this work aims to let the flow “formulate” interface conditions implicitly. This is achieved by balancing the flux across the interface, the same as for the free flow and the porous medium flow itself.

Chapter 2 Governing Equations of Fluid Dynamics

2.1 Introduction

The governing equations necessary to model the flow field take the form of unsteady compressible Navier–Stokes equations, combined with mass conservation and energy conservation equations. They can be cast in conservation form, in three-dimensional Cartesian coordinates as

$$\frac{\partial \mathbf{Q}}{\partial t} + \nabla \cdot (\mathcal{F} - \mathcal{F}_d) = \mathbf{S} \quad . \quad (2.1)$$

By introducing the Jacobian $\mathcal{J} = \frac{\partial \mathbf{Q}}{\partial \mathbf{P}}$, the primary dependent variables in the time derivative are changed from the conservative variables \mathbf{Q} to the primitive variables \mathbf{P} while preserving the conservative formulation:

$$\mathcal{J} \frac{\partial \mathbf{P}}{\partial t} + \nabla \cdot (\mathcal{F} - \mathcal{F}_d) = \mathbf{S} \quad . \quad (2.2)$$

The reason justifying this change of dependent variables is two-fold. First, it is closely associated to the implementation of Jacobians. In this work, numerical flux Jacobians are constructed based on primitive variables rather than conservative variables. Using the primitive variables also facilitates the derivation of analytical Jacobians. Secondly, preconditioning can be accomplished by modifying only some specific terms in the matrix \mathcal{J} . Such modification is needed for very low Mach number flow. This procedure can rescale the system eigenvalues, overcome the disparity among them and successfully be able to converge a steady-state solution with satisfactory convergence rate.

In the energy equation, the flow can either be described by a single temperature T , when in equilibrium, or by two temperatures, when in non-equilibrium. The

latter assumes that the translational and rotational energy modes of the participating species are described by a single temperature T_{tr} , while the vibrational and electronic energy modes, as well as electron translational energy mode, are characterized by a single temperature T_{ve} .

Within all of the numerical context described above, the vectors of conserved variables, primitive variables and source terms respectively take the form of:

$$\mathbf{Q} = \begin{pmatrix} \rho_1 \\ \dots \\ \rho_{ns} \\ \rho u \\ \rho v \\ \rho w \\ E \\ E_{ve} \end{pmatrix}, \quad \mathbf{P} = \begin{pmatrix} \rho_1 \\ \dots \\ \rho_{ns} \\ u \\ v \\ w \\ T_{tr} \\ T_{ve} \end{pmatrix}, \quad \text{and} \quad \mathbf{S} = \begin{pmatrix} \dot{w}_1 \\ \dots \\ \dot{w}_{ns} \\ 0 \\ 0 \\ 0 \\ 0 \\ \dot{w}_v \end{pmatrix}.$$

In these expressions, ρ_i denotes density for each species, and subscript ns stands for number of species in the mixture. ρ is the total density, and u, v, w are the bulk velocity components. E , as well as E_{ve} are the total energy and vibrational-electron-electronic per unit volume characterized by temperature T_{tr} , and T_{ve} , respectively. $\dot{w}_1 \dots \dot{w}_{ns}$ are the species mass production rates introduced by chemical reactions. \dot{w}_v is the vibrational energy transfer rate between two different energy modes.

The flux matrices $\mathcal{F} = \mathbf{F} \hat{\mathbf{i}} + \mathbf{G} \hat{\mathbf{j}} + \mathbf{H} \hat{\mathbf{k}}$, and $\mathcal{F}_d = \mathbf{F}_d \hat{\mathbf{i}} + \mathbf{G}_d \hat{\mathbf{j}} + \mathbf{H}_d \hat{\mathbf{k}}$ are given by

$$\mathcal{F} = \begin{pmatrix} \rho_1 u & \rho_1 v & \rho_1 w \\ \dots & \dots & \dots \\ \rho_{ns} u & \rho_{ns} v & \rho_{ns} w \\ \rho u^2 + p & \rho v u & \rho w u \\ \rho u v & \rho v^2 + p & \rho w v \\ \rho u w & \rho v w & \rho w^2 + p \\ (E + p)u & (E + p)v & (E + p)w \\ E_{ve} u & E_{ve} v & E_{ve} w \end{pmatrix},$$

$$\mathcal{F}_d = \begin{pmatrix} -J_{x,1} & -J_{y,1} & -J_{z,1} \\ \dots & \dots & \dots \\ -J_{x,ns} & -J_{y,ns} & -J_{z,ns} \\ \tau_{xx} & \tau_{yx} & \tau_{zx} \\ \tau_{xy} & \tau_{yy} & \tau_{zy} \\ \tau_{zx} & \tau_{zy} & \tau_{zz} \\ \boldsymbol{\tau} \mathbf{u} - (\mathbf{q}_{tr} + \mathbf{q}_{ve}) - \sum_{i=1}^{ns} (\mathbf{J}_i h_i) \\ -q_{ve,x} - \sum_{i=1}^{ns} (J_{x,s} e_{ve,s}) & -q_{ve,y} - \sum_{i=1}^{ns} (J_{y,s} e_{ve,s}) & -q_{ve,z} - \sum_{i=1}^{ns} (J_{z,s} e_{ve,s}) \end{pmatrix},$$

where p is the total pressure, τ_{ij} is each component of the viscous tensor $\boldsymbol{\tau}$, $J_{i,s}$ the diffusion flux of species s in i -th direction. $q_{tr,i}$ and $q_{ve,i}$ are the directional heat fluxes. \mathbf{q}_{tr} , \mathbf{q}_{ve} , and \mathbf{J} are in vector form to maintain consistent representations.

Perfect Gas Law

As noted in Section 1.2, each species of the gas mixture can be assumed as a thermally perfect gas, and obey the perfect gas law.

$$p_s = \begin{cases} \rho_s R_s T_{tr} & \text{for molecules and atoms,} \\ \rho_e R_e T_{ve} & \text{for electrons.} \end{cases} \quad (2.3)$$

As can be observed, the partial pressure of electrons is characterized by T_{ve} rather than T_{tr} . The specific gas constant is given by

$$R_s = \frac{R_u}{M_s} \quad . \quad (2.4)$$

where R_u is the universal gas constant, given by 8.31441 J/(mol K), and M_s is the molar mass for species s , with detailed values found in Ref. [45].

Dalton's law of partial pressure states that the total pressure of a gas mixture is the summation of the partial pressures of the individual components of the gas mixture.

$$p = \sum_s^{ns} p_s \quad . \quad (2.5)$$

Similarly, the total density of a gas mixture is given by

$$\rho = \sum_s^{ns} \rho_s \quad . \quad (2.6)$$

Thermodynamic Relations: Energy, Enthalpy, and Specific Heat

The total energy per unit volume, E , and the total enthalpy per unit volume, H , are respectively given by [46]

$$E = \sum_s^{ns} \rho_s e_s + \frac{1}{2} \rho (u^2 + v^2 + w^2) \quad , \quad (2.7)$$

and

$$H = E + p \quad . \quad (2.8)$$

From Eq. (2.7), the total energy is the summation of the energy of all of the species. A molecule, for instance, has four energy modes [7]: *translational energy*, which is the translational kinetic energy of the molecule; *rotational energy*, which arises from the energy of rotating about three orthogonal axes in space; *vibrational energy*, which is due to the vibration of atoms of the molecule with respect to the equilibrium location within the molecule; *electronic energy*, which is due to the motion

of electrons about the nucleus. Each energy mode can be expressed as a reference level energy plus a zero-point energy, where the reference level energy is generally computed (or measured) easily. Then the total energy of a molecule, e_s , is thus represented as the sum of its translational, rotational, vibrational, electronic, and total zero-point energy, i.e. $e_{t,s}$, $e_{r,s}$, $e_{v,s}$, $e_{el,s}$ and h_s^o respectively.

$$e_s = e_{t,s} + e_{r,s} + e_{v,s} + e_{el,s} + h_s^o \quad , \quad (2.9)$$

where h_s^o can also be called the energy of formation.

The translational and rotational energy per unit mass of the species (except for electrons) are linear functions of temperature T_{tr} , such that

$$e_{t,s} = Cv_{t,s}T_{tr} \quad , \quad (2.10)$$

and

$$e_{r,s} = Cv_{r,s}T_{tr} \quad . \quad (2.11)$$

The vibrational and electronic energy for molecules and atoms, and electron translational energy per unit mass are taken together, given by

$$e_{ve,s} = \begin{cases} e_{v,s} + e_{el,s} & \text{for molecules and atoms,} \\ Cv_{t,e}T_{ve} & \text{for electrons.} \end{cases} \quad (2.12)$$

where it can be noticed that electrons' single energy mode, the electron translational energy mode, is characterized by T_{ve} in this work. The species vibrational energy per unit mass, $e_{v,s}$, is expressed as

$$e_{v,s} = \begin{cases} \frac{R_u}{M_s} \frac{\theta_{v,s}}{\exp(\theta_{v,s}/T_{v,e}) - 1} & \text{for molecules,} \\ 0 & \text{for atoms and electrons.} \end{cases} \quad (2.13)$$

where $\theta_{v,s}$ is the species characteristic vibrational temperature. The electronic energy per unit mass, $e_{el,s}$, shows

$$e_{el,s} = \begin{cases} \frac{R_u}{M_s} \frac{\sum_{i=1}^{\infty} g_{i,s} \theta_{el,s} \exp(-\theta_{el,i,s}/T_{v,e})}{\sum_{i=0}^{\infty} g_{i,s} \exp(-\theta_{el,i,s}/T_{v,e})} & \text{for molecules and atoms,} \\ 0 & \text{for electrons.} \end{cases} \quad (2.14)$$

where $\theta_{el,s}$, and $g_{i,s}$ are the species characteristic electronic temperature and the degeneracy of the energy level i , respectively. Note that the index of summation starts from 0 in the denominator, while from 1 in the numerator.

To sum up, the total energy, e_s , and enthalpy, h_s , per unit mass for each species is given by

$$e_s = \begin{cases} Cv_{tr,s}T_{tr} + e_{ve,s} + h_s^o & \text{for molecules and atoms,} \\ e_{ve,e} & \text{for electrons.} \end{cases} \quad (2.15)$$

and

$$h_s = \frac{p_s}{\rho_s} + e_s \quad . \quad (2.16)$$

The total energy, shown in Eq. (2.7), becomes

$$E = \sum_{s \neq e} \rho_s Cv_{tr,s}T_{tr} + \sum_s \rho_s e_{ve,s} + \sum_{s \neq e} \rho_s h_s^o + \frac{1}{2}\rho(u^2 + v^2 + w^2) \quad , \quad (2.17)$$

and the total vibrational-electron-electronic energy is give by

$$E_{ve} = \sum_s \rho_s e_{ve,s} \quad . \quad (2.18)$$

The computation of energy modes above involves the expression of associated specific heat. A generic form of the total specific heat for a species can be summarized as

$$Cv = Cv_{t,s} + Cv_{r,s} + Cv_{v,s} + Cv_{e,s} \quad , \quad (2.19)$$

where the translational specific heat $Cv_{t,s}$, as well as rotational specific heat $Cv_{r,s}$ at constant volume are constants for each species which can be added up to be

$$Cv_{tr} = Cv_{t,s} + Cv_{r,s} \quad . \quad (2.20)$$

Similarly, combining the vibrational and electronic specific heat yields a vibrational-electronic specific heat at constant volume,

$$Cv_{ve,s} = Cv_{v,s} + Cv_{e,s} \quad . \quad (2.21)$$

Each specific heat is detailed as

$$Cv_{t,s} = \frac{3 R_u}{2 M_s} \quad \text{for all species ,} \quad (2.22)$$

and

$$Cv_{r,s} = \begin{cases} \frac{R_u}{M_s} & \text{for molecules,} \\ 0 & \text{for atoms and electrons.} \end{cases} \quad (2.23)$$

The vibrational energy specific heat at constant volume, $Cv_{v,s}$, is calculated through the derivative of $e_{v,s}$ with respect to temperature T_{ve} :

$$Cv_{v,s} = \begin{cases} \frac{\partial e_{v,s}}{\partial T_{ve}} & \text{for molecules,} \\ 0 & \text{for atoms and electrons.} \end{cases} \quad (2.24)$$

where

$$\frac{\partial e_{v,s}}{\partial T_{ve}} = \frac{R_u}{M_s} \frac{(\theta_{v,s}/T_{ve})^2 \exp(\theta_{v,s}/T_{ve})}{[\exp(\theta_{v,s}/T_{ve}) - 1]^2} . \quad (2.25)$$

In a similar way, the electronic energy specific heat at constant volume, $Cv_{el,s}$, is given by

$$Cv_{el,s} = \begin{cases} \frac{\partial e_{el,s}}{\partial T_{ve}} & \text{for molecules and atoms,} \\ 0 & \text{for electrons.} \end{cases} \quad (2.26)$$

where

$$\frac{\partial e_{el,s}}{\partial T_{ve}} = \frac{R_u}{M_s} \left\{ \frac{\sum_{i=1}^{\infty} g_{i,s} (\theta_{el,i,s}/T_{ve})^2 \exp(-\theta_{el,i,s}/T_{ve})}{\sum_{i=0}^{\infty} g_{i,s} \exp(-\theta_{el,i,s}/T_{ve})} - \frac{[\sum_{i=1}^{\infty} g_{i,s} \theta_{el,i,s} \exp(-\theta_{el,i,s}/T_{ve})][\sum_{i=0}^{\infty} g_{i,s} (\theta_{el,i,s}/T_{ve})^2 \exp(-\theta_{el,i,s}/T_{ve})]}{[\sum_{i=0}^{\infty} g_{i,s} \exp(-\theta_{el,i,s}/T_{ve})]^2} \right\} . \quad (2.27)$$

Again, attention must be paid on the index of summation in this equation.

At last, the translational specific heat for electrons, $Cv_{t,e}$, has essentially already been considered in the above definitions, i.e.

$$Cv_{t,e} = \frac{3 R_u}{2 M_e} . \quad (2.28)$$

Transport Terms

Mass diffusion fluxes for each species are assumed to be modeled by Fick's first law.

$$\mathbf{I}_s = -\rho D_s \nabla Y_s \quad , \quad (2.29)$$

where D_s is the species diffusion coefficient, determined in the following subsection.

Y_s is the species mass fraction given by

$$Y_s = \frac{\rho_s}{\rho} \quad , \quad (2.30)$$

A modified version of the mass diffusion fluxes is used in this work, which ensures that the summation of mass diffusion fluxes is zero. It proves a significantly more accurate result than the original form [47].

$$\mathbf{J}_{s \neq e} = \mathbf{I}_s - Y_s \sum_{r \neq e}^{ns} \mathbf{I}_r \quad , \quad (2.31)$$

The diffusive flux of electrons is modeled differently from that of the molecules and atoms. It is constructed assuming ambipolar diffusion [48], which states the positive and negative species have the same charges in mass diffusion, thus charge neutrality of the flowfield can be maintained.

$$\mathbf{J}_e = M_e \sum_{s \neq e}^{ns} \frac{\mathbf{J}_s G_s}{M_s} \quad , \quad (2.32)$$

where G_s is the species charge.

The viscous shear stresses are modeled assuming a Newtonian fluid: they are related to the strain rate by the bulk viscosity, μ , from Stokes' hypothesis.

$$\tau_{ij} = \mu \left(\frac{\partial u_j}{\partial x_i} + \frac{\partial u_i}{\partial x_j} \right) + \lambda \frac{\partial u_k}{\partial x_k} \delta_{ij} \quad , \quad \lambda = -\frac{2}{3}\mu \quad . \quad (2.33)$$

Fourier's law is used to account for the heat fluxes:

$$\mathbf{q}_{tr} = -\kappa_{tr} \nabla T_{tr} \quad , \quad (2.34a)$$

and

$$\mathbf{q}_{ve} = -\kappa_{ve} \nabla T_{ve} \quad , \quad (2.34b)$$

where κ_{tr} and κ_{ve} is the mixture thermal conductivity for each energy mode, determined in the following section as well.

Transport Properties

The viscosity is either calculated using Sutherland viscosity model [49] or a viscosity model for reacting flow developed by Blottner [50], which calculates species viscosity using a curve fit

$$\mu_s = 0.1 \exp[(A_s \ln T + B_s) \ln T + C_s] \quad , \quad (2.35)$$

where A_s , B_s and C_s are constants determined for each species.

By relating to species viscosity, Eucken's relations [51] are used to account for species thermal conductivity,

$$k_{tr,s} = \frac{5}{2} \mu_s C v_{t,s} + \mu_s C v_{r,s} \quad \text{and} \quad k_{ve,s} = \mu_s C v_{ve,s} \quad . \quad (2.36)$$

Finally, the mixture transport properties viscosity μ and thermal conductivities κ_{tr} and κ_{ve} are approximated by using Wilke's semi-empirical mixing rule [52],

$$\mu = \sum_s^{ns} \frac{X_s \mu_s}{\phi_s} \quad \text{and} \quad \kappa = \sum_s^{ns} \frac{X_s \kappa_s}{\phi_s} \quad , \quad (2.37)$$

where X_s refers to species molar fraction, and coefficient ϕ_s is detailed as

$$\phi_s = \sum_r^{ns} X_r \frac{\left[1 + \sqrt{\frac{\mu_s}{\mu_r}} \left(\frac{M_r}{M_s} \right)^{1/4} \right]^2}{\sqrt{8 \left(1 + \frac{M_s}{M_r} \right)}} \quad . \quad (2.38)$$

The species mass diffusion coefficient D_s may not be the same for different species, however, it can be approximated by a single binary coefficient D when the typical

velocity is below 10 km/s. The value of D is calculated by assuming a constant Lewis number, Le ,

$$D = \frac{Le \kappa_{tr}}{\rho C_{ptr}} \quad , \quad (2.39)$$

C_{ptr} is the mixture translational-rotational specific heat at constant pressure.

The widely used Wilke's mixing rule, along with Blottner curve fit and Eucken's relation is simple to solve for the bulk viscosity and thermal conductivity only when the flow velocity is relatively slow and the maximum temperature is no more than 10,000 K [53,54]. For weakly ionized gas mixtures, however, Gupta's mixing rule [55] using integration method is able to provide more accurate descriptions of transport properties [53], and should be used.

2.2 Source Terms

The source terms involve two main effects: the mass production due to chemical reactions for each species, \dot{w}_s , and the vibrational energy transfer between different different energy modes, \dot{w}_v .

Chemical Kinetic Model

For a reacting flow, the classical reactions can be classified as dissociation, exchange, recombination, ionization, charge exchange and impact ionization. All these, however, can be represented in a generic way as

$$\sum_{i=1}^{ns} \nu'_{ir} A_i \rightleftharpoons \sum_{i=1}^{ns} \nu''_{ir} A_i \quad , \quad (2.40)$$

where A_i denotes any one of the species in reaction r . The species on the left-hand side are the reactants, and the ones on the right-hand side are products. In the equations, ν' and ν'' represent the stoichiometric coefficients for reactants and products respectively.

Following Eq. (2.40), the chemical production rate of species A_i in reaction r is given by

$$\dot{w}_{ir} = (\nu''_{ir} - \nu'_{ir}) \left[10^3 k_{fr} \prod_{j=1}^{ns} \left(10^{-3} \frac{\rho_j}{M_j} \right)^{\nu'_{jr}} - 10^3 k_{br} \prod_{j=1}^{ns} \left(10^{-3} \frac{\rho_j}{M_j} \right)^{\nu''_{jr}} \right] , \quad (2.41)$$

where subscript j represents the j^{th} species in this reaction. k_{fr} and k_{br} denote the forward and backward reaction rate coefficients respectively.

It should be noted that the **centimetre-gram-second** unit system (abbreviated CGS or cgs) is generally used in the calculation of chemical reactions. Therefore, the factor 10^{-3} converts the concentration from kmol/m^3 , the units of ρ_j/M_j , to mol/cm^3 in the reaction calculation, and the factor 10^3 recovers kmol/m^3 from mol/cm^3 .

The net mass rate of production of species A_i is given by

$$\dot{w}_i = M_i \sum_r \dot{w}_{ir} , \quad (2.42)$$

which has the unit of $\text{kg}/(\text{m}^3 \cdot \text{s})$. M_i denotes the molar mass of species A_i .

Coefficients k_{fr} and k_{br} take account of levels of the non-equilibrium in the flow, as they are functions of fluid temperatures. Different temperatures can influence different chemical reactions mechanism. Although there are many temperature models in the literature [56], Park's two-temperature model [57] is used in current work, which assumes that the dissociation reactions are controlled by a combination of the translational-rotational temperature T_{tr} and the vibrational-electron-electronic temperature T_{ve} . The dissociation temperature within Park's two-temperature model is given by

$$T_{P2} = T_{tr}^{a_f} T_{ve}^{b_f} . \quad (2.43)$$

The typical values for coefficients a and b are usually: $a_f = b_f = 0.5$ or $a_f = 0.7$ and $b_f = 0.3$. In this work, the first set of values is used. Park's modification to temperature expresses the fact that it is easier for the vibrationally excited molecules to dissociate.

The forward reaction rate is temperature dependent and can be calculated using an empirical formula, the Arrhenius curve fit, which is given by

$$k_{fr} = A_{fr} T_c^{\eta_r} \exp(-T_{ar}/T_c) \quad , \quad (2.44)$$

where coefficients A_{fr} , η_r and T_{ar} are all independent of temperature T_c , and can be determined from experiments [58,59]. It is noted that the characteristic activation temperature is defined by

$$T_{ar} = \frac{E_{ar}}{R_u} \quad , \quad (2.45)$$

where E_{ar} is the activation energy. T_c represents the temperature for each specific reactions scheme, for example, Park's temperature. The backward reaction rate is not directly computed. Instead, it is obtained as the ratio of the forward reaction rate over the associated equilibrium rate.

$$k_{br}(T_{bc}) = \frac{k_{fbr}(T_{bc})}{K_{cr}(T_{bc})} \quad , \quad (2.46)$$

where T_{bc} might not be the same as the T_c used for the forward reaction. Park's temperature model suggests

$$T_{bc} = T_{tr}^{a_b} T_{ve}^{b_b} \quad . \quad (2.47)$$

It can be found from Appendix A that the backward controlling temperature for dissociative recombination, impact ionization and impact dissociation is T_{ve} .

The equilibrium constant K_{cr} can be calculated by using Gibb's free energy as [7]

$$\log K_{cr} = - \sum_{i=1}^{ns} \frac{(\nu''_{ir} - \nu'_{ir}) \hat{g}_i(T_{bc})}{R_u T_{bc}} - \log (R_u T_{bc}) \sum_{i=1}^{ns} (\nu''_{ir} - \nu'_{ir}) \quad , \quad (2.48)$$

where \hat{g}_i is the Gibbs energy per unit mole of i^{th} species and it is given by

$$\hat{g}_i = \hat{h}_i - T_{bc} \hat{s}_i \quad , \quad (2.49)$$

where \hat{h}_i and \hat{s}_i are the enthalpy and entropy of species i per unit mole, respectively.

Manipulation of the Eq. (2.48) yields

$$K_{cr} = \left(\frac{p_0}{R_u T_{bc}} \right)^{\nu_r} \exp \left\{ - \sum_i \left[(\nu''_{i,r} - \nu'_{i,r}) \left(\frac{\hat{h}_i}{R_u T_{bc}} - \frac{\hat{s}_i}{R_u} \right) \right] \right\} \quad , \quad (2.50)$$

where pressure p_0 is a reference pressure set to 1 bar, while in the computation framework its value $p_0=0.1$ and $R_u = 8.31441$, which are both in CGS unit system. Also, ν_r is given by

$$\nu_r = \sum_i^{ns} (\nu''_{ir} - \nu'_{ir}) \quad . \quad (2.51)$$

The specific heat for each species, \widehat{C}_{p_i}/R_u , is a function of temperature, represented in NASA format using 7 least-squares coefficients [60]

$$\frac{\widehat{C}_{p_i}}{R_u} = \sum_{i=1}^8 a_i T_{bc}^{q_i} \quad , \quad (2.52)$$

which implies $a_8 = 0$. The normalized enthalpy and entropy are then obtained through relations to specific heat

$$\frac{\widehat{h}_i}{R_u T_{bc}} = \frac{\int \widehat{C}_{p_i} dT_{bc}}{R_u T_{bc}} \quad , \quad (2.53)$$

and

$$\frac{\widehat{S}_i}{R_u} = \int \frac{\widehat{C}_{p_i} dT_{bc}}{R_u T_{bc}} \quad . \quad (2.54)$$

Two new integration constants a_{9i} and a_{10i} will be generated in this process, in detail

$$\frac{\widehat{h}_i}{R_u T_{bc}} = -a_{1i} \frac{1}{T_{bc}^2} + a_{2i} \frac{\ln(T_{bc})}{T_{bc}} + a_{3i} + a_{4i} \frac{T_{bc}}{2} + a_{5i} \frac{T_{bc}^2}{3} + a_{6i} \frac{T_{bc}^3}{4} + a_{7i} \frac{T_{bc}^4}{5} + a_{8i} + a_{9i} \frac{1}{T_{bc}} \quad , \quad (2.55)$$

and

$$\frac{\widehat{S}_i}{R_u} = -a_{1i} \frac{1}{2T_{bc}^2} - a_{2i} \frac{1}{T_{bc}} + a_{3i} \ln(T_{bc}) + a_{4i} T_{bc} + a_{5i} \frac{T_{bc}^2}{2} + a_{6i} \frac{T_{bc}^3}{3} + a_{7i} \frac{T_{bc}^4}{4} + a_{8i} \ln(T_{bc}) + a_{10i} \quad . \quad (2.56)$$

All of the coefficients can be found in the data table in Appendix A.

Relaxation Model

Multiple energy exchange mechanisms contribute to the vibrational energy term. All of them occur in a molecular level, and there are no definitive models. Simplifications of physical and complicated energy exchange processes have to be made based on related assumption. The total vibrational energy source term is given by

$$\dot{w}_v = S_{epg} + S_{c2v} + S_{t2v} + S_{h2e} - S_{e2i} \quad . \quad (2.57)$$

Each relaxation term is described in the following subsections.

Work on Electrons

When there exists electron pressure gradient in the electric field, it does work on electrons [46,61]. The approximation to this effect is given by

$$S_{epg} = -p_e \nabla \cdot \mathbf{u} \quad . \quad (2.58)$$

It is, however, not switched on in the following simulations.

Energy Exchange due to Chemical Reactions

Two typical models can be used to account for the vibrational-electron-electronic energy, S_{c2v} , created or removed at chemical reactions rate \dot{w}_s : the preferential model and the non-preferential model. The preferential model is given by

$$S_{c2v} = \sum_{s=\text{mol.}} \dot{w}_s (D'_s + e_{el,s}) \quad , \quad (2.59)$$

which assumes the dissociation and recombination of molecules are more likely to occur in a higher vibrational states. That indicates the dissociation potential D_s is greater than the average vibrational energy $e_{v,s}$. Usually, a fraction of D_s is taken and Sharma, Huo, and Park suggest [62]

$$D'_s = \alpha D_s \quad , \quad (2.60)$$

with the typical value of α being 0.3. The dissociation potential of the molecule D_s can be found in Appendix A for the 11-species air model.

In this work, however, the non-preferential model is used, which assumes that molecules are created or consumed at the average vibrational energy – in a relative low vibrational energy level, i.e.

$$D'_s = e_{v,s} \quad . \quad (2.61)$$

Translational-Vibrational Energy Exchange

The energy exchange between the translational-rotational and vibrational-electronic energy modes for molecules, S_{t2v} , accounts for most of the total energy exchange. The model generally used was proposed by Landau-Teller [51], which assumes a single energy exchange rate given by

$$S_{t2v} = \sum_{s=\text{mol.}} \rho_s \frac{e_{vs}^* - e_{vs}}{\tau_s} \quad , \quad (2.62)$$

where the single vibrational relaxation time is

$$\tau_s = \langle \tau_s \rangle + \tau_{ps} \quad , \quad (2.63)$$

in which the molar averaged Landau-Teller relaxation time, $\langle \tau_s \rangle$, is given by

$$\langle \tau_s \rangle = \frac{\sum_r X_r}{\sum_r X_r / \tau_{sr}} \quad , \quad (2.64)$$

where X_r is the molar mass fraction of non-electronic species r , and τ_{sr} , the Landau-Teller inter-species relaxation time, can be modeled using curve fits method. Millikan and White [63] formulated a semiempirical correlation between τ_{sr} and temperature range of 300 to 8000 K,

$$\tau_{sr} = \frac{p_o}{p} \exp [A_{sr} (T^{-1/3} - B_{sr}) - 18.42] \quad . \quad (2.65)$$

The reference pressure $p_o = 101325$ Pa. And the coefficients A_{sr} and B_{sr} are given respectively by

$$A_{sr} = 1.16 \times 10^{-3} \mu_{sr}^{1/2} \theta_{vs}^{4/3} \quad , \quad (2.66)$$

$$B_{sr} = 0.015 \mu_{sr}^{1/4} \quad , \quad (2.67)$$

where μ_{sr} is the reduced molecular weight of the colliding species s and r ,

$$\mu_{sr} = \frac{M_s M_r}{M_s + M_r} \quad , \quad (2.68)$$

and θ_{vs} can be found in the Appendix A chemistry data table for each species involved in 11-species air model. Instead of computing values of A_{sr} and B_{sr} , the tabulated data for them are used in this work as shown in Appendix A. For temperature above 8000 K, Park [57] found the effective cross section given previously highly overpredicted at high temperatures, thus Millikan and White's curve fits relaxation time has to be corrected. He suggests a modification by adding an additional vibrational relaxation time τ_{ps} to $\langle \tau_s \rangle$ in Eqn. (2.64)

$$\tau_{ps} = \frac{1}{\sigma_s c_s N_s} \quad , \quad (2.69)$$

where σ_s is the limiting cross section (unit length squared) expressed by

$$\sigma_s = 10^{-21} (50,000/T)^2 \quad \text{m}^2 \quad . \quad (2.70)$$

c_s is the average molecular velocity of the species s , given by

$$c_s = \sqrt{\frac{8R_u T}{\pi M_s}} \quad , \quad (2.71)$$

and N_s is the number density of the species.

Electronic-Vibrational Energy Exchange

The energy exchange between heavy particles and electrons, S_{h2e} , is given by

$$S_{h2e} = 3R_u \rho_e (T - T_v) \sqrt{\frac{8R_u T_v}{\pi M_e}} \sum_{r \neq e} \frac{\rho_r N_a}{M_r^2} \sigma_{er} \quad . \quad (2.72)$$

For the collisions between electrons and neutrals

$$\sigma_{er} = 1 \times 10^{-19} \text{ m}^2 \quad . \quad (2.73)$$

While for the collisions between electrons and ions

$$\sigma_{er} = \frac{8\pi}{27} \left(\frac{e^2}{kT_e} \right)^2 10^{-4} \ln \left[1 + \frac{9}{4\pi} \left(\frac{kT_e}{e^2} \right)^3 \frac{1}{N_e^*} \right] \quad , \quad (2.74)$$

where

$$N_e^* = \max(1, N_e) \quad , \quad (2.75)$$

and

$$N_e = 10^{-6} N_a \frac{\rho_e}{M_e} \quad . \quad (2.76)$$

N_e and e in Eqn. (2.74) are both in **centimetre-gram-second** unit system (abbreviated CGS or cgs), while the others are in SI. T_e equals to T_{ve} in this work and it has the unit of K. The associated constants are listed in Table. 2.1.

Table 2.1: Constants

Constant	Symbol	Value	Unit
Avogadro constant	N_a	6.022045×10^{23}	mol^{-1}
Pi	π	3.14159265359	
Boltzmann constant	k	1.380662×10^{-23}	J/K
Charge of electron	e	4.8032×10^{-10}	statcoulomb

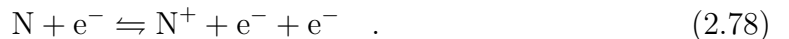
The average molecular speed of the gas species, c_i , is given by

$$c_i = \sqrt{\frac{8R_u T}{\pi M_i}} \quad , \quad (2.77)$$

where R_u is the gas constant, its value given by $R_u = 8314.41 \text{ J}/(\text{kmol}\cdot\text{K})$, T equals T_{tr} , and M_i is molar mass in kg/kmol.

Energy Exchange During Impact Ionization Reactions

In an impact ionization reaction, such as shown in Eqn. (2.78), a free electron strikes a neutral atom, and another electron is freed.



In this model, the energy used to ionize the neutral, represented by S_{e2i} , is removed from the electron translational energy, thus is a negative contributor to vibrational-electron-electronic energy, E_{ve} . For the 11-species air model, only neutral N and O are involved in impact ionization reactions. In total, the energy are accounted by

$$S_{e2i} = M_{N^+} \dot{w}_{N^+} \hat{I}_N + M_{O^+} \dot{w}_{O^+} \hat{I}_O \quad , \quad (2.79)$$

where M_{N^+} , and M_{O^+} is the molar mass, \dot{w}_{N^+} , and \dot{w}_{O^+} is the mass production rate for ionized species N^+ and O^+ , respectively. \hat{I}_N , and \hat{I}_O is the energy required to ionize the species N and O, respectively. It can be taken from the ground state, i.e. the first energy of ionization, which assumes all of ionization energy comes from the electron. This overestimates the amount of energy necessary for this reaction and probably lead to a negative E_{ve} in simulations. In this work, they are set to be 1/3 of the first energy of ionization. Compared to other source terms, the contribution from impact ionization reactions are small to the overall energy balance [46]. Associated values are listed in Appendix A.

Chapter 3 Numerical Framework for Flow Dynamics

3.1 Introduction

In this chapter, the numerical solution algorithms that have been developed and used through the years in efforts to solve the differential governing equations for hypersonic flows are derived and discussed. To begin, the set of differential equations described in the previous chapter is integrated over a computation grid (often called “weak form”), which allows discontinuous solution and non-differential solution such as the presence of shocks and expansion fans.

The conservation laws are applied to each generic cell – the control volume (or “finite volume”) – which refers to the small volume of each cell on a mesh after discretization technique is used for the fluid domain under consideration.

Starting from the governing equation derived in the previous chapter,

$$\mathcal{J} \frac{\partial \mathbf{P}}{\partial t} + \nabla \cdot (\mathcal{F} - \mathcal{F}_d) = \mathbf{S} \quad , \quad (3.1)$$

the weak form of the governing equation can be obtained by integrating over a finite volume V for an arbitrary mesh cell.

$$\iiint_V \mathcal{J} \frac{\partial \mathbf{P}}{\partial t} dV = \iiint_V \nabla \cdot (\mathcal{F}_d - \mathcal{F}) dV + \iiint_V \mathbf{S} dV \quad , \quad (3.2)$$

where $\mathcal{F} = \mathbf{F} \hat{\mathbf{i}} + \mathbf{G} \hat{\mathbf{j}} + \mathbf{H} \hat{\mathbf{k}}$ denotes the convective flux across the surface, and $\mathcal{F}_d = \mathbf{F}_d \hat{\mathbf{i}} + \mathbf{G}_d \hat{\mathbf{j}} + \mathbf{H}_d \hat{\mathbf{k}}$ is the diffusive flux at the surface, and \mathbf{S} is the chemistry and non-equilibrium source term. Applying Gauss theorem, the following is obtained:

$$\iiint_V \mathcal{J} \frac{\partial \mathbf{P}}{\partial t} dV = \iint_A (\mathcal{F}_d - \mathcal{F}) \cdot \mathbf{n} dA + \iiint_V \mathbf{S} dV \quad . \quad (3.3)$$

It is assumed that within the control volume the physical properties are uniform everywhere (although not at the faces) and can be represented by the ones at the cell center. The time derivative on the left-hand side can be taken out of the integration. The integration of the fluxes across each surface can be accounted as their summation. This gives rise to:

$$V_{cell} \mathcal{J} \frac{\partial \mathbf{P}}{\partial t} = \sum_{j \in cell} (\mathcal{F}_d - \mathcal{F}) \cdot \mathbf{n}_j A_j + V_{cell} \mathbf{S} \equiv \mathbf{R} \quad , \quad (3.4)$$

where V_{cell} is the volume enclosed by the surfaces A_j .

For hypersonic chemically reacting viscous flow, because of the wide variety of time scales involved and the exponential dependence of reaction rates on temperature, the equation system may be very stiff to solve. To maintain stability and avoid strict time step size restrictions, a backward Euler approach is used. Most current work considers a steady state solution, therefore only first order accuracy is maintained. Eq. (3.4) therefore becomes:

$$V_{cell} \mathcal{J}^n \frac{\mathbf{P}^{n+1} - \mathbf{P}^n}{\Delta t} = \mathbf{R}^{n+1} = \mathbf{R}^n + \left(\frac{\partial \mathbf{R}}{\partial \mathbf{P}} \right)^n (\mathbf{P}^{n+1} - \mathbf{P}^n), \quad (3.5)$$

where the right hand side (or residual) vector \mathbf{R} at time level $n + 1$ is linearized as a function at time level n .

Finally, the linear system is cast in the following form, allowing the direct update of the physical variables instead of the conserved quantities:

$$\left[\frac{V_{cell}}{\Delta t} \mathcal{J}^n - \left(\frac{\partial \mathbf{R}}{\partial \mathbf{P}} \right)^n \right] \Delta \mathbf{P} = \mathbf{R}^n \quad . \quad (3.6)$$

The new solution variables are given by

$$\mathbf{P}^{n+1} = \mathbf{P}^n + \Delta \mathbf{P} \quad . \quad (3.7)$$

The time dependent solution variables are therefore advanced by a physical time step size Δt . The computation starts from an initial guess, and a steady state solution will be finally achieved in this process.

The decomposition of Eq. (3.6) for a generic cell, l , leads to

$$\left[\frac{V_{cell}}{\Delta t} \mathcal{J}^n + \mathcal{A}_l^+ - \mathcal{B}_l^+ - \mathcal{C}_l - \mathcal{D}_l \right] \Delta \mathbf{P}_l + \sum_r [\mathcal{A}_r^- - \mathcal{B}_r^-] \Delta \mathbf{P}_r = \mathbf{R}_l^n \quad , \quad (3.8)$$

where the subscript r indicates its neighbors, real cell or boundary ghost cell. The Jacobian matrices are listed as

$$\mathcal{A}_l^+ = \frac{\partial \mathbf{F}_n}{\partial \mathbf{P}_l} \quad \text{and} \quad \mathcal{A}_r^- = \frac{\partial \mathbf{F}_n}{\partial \mathbf{P}_r} \quad , \quad (3.9)$$

$$\mathcal{B}_l^+ = \frac{\partial \mathbf{F}_{dn}}{\partial \mathbf{P}_l} \quad \text{and} \quad \mathcal{B}_r^- = \frac{\partial \mathbf{F}_{dn}}{\partial \mathbf{P}_r} \quad , \quad (3.10)$$

$$\mathcal{C}_l + \mathcal{D}_l = \frac{\partial \mathbf{S}_l}{\partial \mathbf{P}_l} \quad . \quad (3.11)$$

3.2 Calculation of Flux Vector

Convective Flux Vector

Multiple Riemann solvers are implemented in KATS, such as Roe flux difference scheme, AUSM⁺-up, and Steger-Warming flux splitting scheme. Among these, Steger-Warming flux works reasonably well for hypersonic flow and internal nozzle flow. Roe scheme is also adequate for hypersonic flow and supersonic flow. AUSM⁺-up is designed to be uniformly valid for flows of all speed regimes. For flow at very low Mach number, it generates more accurate results especially when combined with a low-speed preconditioning.

In the proposed work, only modified Steger-Warming flux splitting scheme, however, is discussed in detail. For more details of implementation and modification of Roe flux difference scheme and AUSM⁺-up, one can read Ref. [64] and [65].

The *homogeneity property* of the inviscid flux vector [66] at a generic face is given by

$$\mathcal{F} \cdot \mathbf{n} = \mathbf{F}_n = \mathbf{A}\mathbf{Q} \quad , \quad (3.12)$$

where the Jacobian matrix

$$\mathbf{A} = \frac{\partial \mathbf{F}_n}{\partial \mathbf{Q}} \quad . \quad (3.13)$$

A splitting of inviscid flux vector \mathbf{F}_n is then accomplished by an appropriate splitting of the Jacobian matrix \mathbf{A} , i.e.

$$\mathbf{F}_n = \mathbf{F}_n^+ + \mathbf{F}_n^- = \mathbf{A}_l^+ \mathbf{Q}_l + \mathbf{A}_r^- \mathbf{Q}_r \quad , \quad (3.14)$$

where positive flux vector \mathbf{F}_n^+ accounts for the effects of the left cell (indicated by l) and \mathbf{F}_n^- for the effects of the right cell (indicated by r) with the direction vector \mathbf{n} pointing from the left to the right. The Jacobian matrices \mathbf{A}_l^+ and \mathbf{A}_r^- are evaluated at the left cell and the right cell separately.

The time dependent conservation equations system assumes the features of *hyperbolicity* [66–68]. The Jacobian matrix \mathbf{A} is diagonalizable, namely

$$\mathbf{A} = \mathbf{L} \mathbf{\Lambda} \mathbf{R} \quad , \quad (3.15)$$

where $\mathbf{\Lambda}$ is the diagonal matrix composed of the real eigenvalues λ_i of Jacobian matrix \mathbf{A} , \mathbf{L} is the non-singular matrix whose columns are the right eigenvectors of matrix \mathbf{A} , and \mathbf{R} is the inverse of \mathbf{L} , which implies

$$\mathbf{L} \mathbf{R} = \mathbf{I} \quad . \quad (3.16)$$

Accordingly, the splitting of the Jacobian matrix \mathbf{A} is performed by decomposing the diagonal matrix $\mathbf{\Lambda} = \mathbf{\Lambda}^+ + \mathbf{\Lambda}^-$:

$$\mathbf{A}^+ = \mathbf{L} \mathbf{\Lambda}^+ \mathbf{R} \quad \text{and} \quad \mathbf{A}^- = \mathbf{L} \mathbf{\Lambda}^- \mathbf{R} \quad . \quad (3.17)$$

Steger and Warming [69] proposed an approach constructing the two diagonal matrices $\mathbf{\Lambda}^+$ and $\mathbf{\Lambda}^-$ with the eigenvalues λ_i given by

$$\lambda_i^+ = \frac{1}{2}(\lambda_i + \sqrt{\lambda_i^2 + \epsilon^2}) \quad \text{and} \quad \lambda_i^- = \frac{1}{2}(\lambda_i - \sqrt{\lambda_i^2 + \epsilon^2}) \quad . \quad (3.18)$$

The numerical dissipation added to the scheme due to the small number ϵ was originally designed to remove the sonic glitch problem [70], however, it is now used to improve the overall stability of the scheme through added numerical dissipation.

The original Steger-Warming scheme exhibits features of high dissipation compared to the others, which is expected in the region of the strong shockwave. However, the excessive numerical dissipation has to be limited in the boundary layer to avoid deterioration of the boundary layer profile [71]. A modified Steger-Warming scheme [71], is therefore used in the boundary layers:

$$\mathbf{F}_n = \mathbf{F}_n^+ + \mathbf{F}_n^- = \mathcal{A}_a^+ \mathbf{Q}_l + \mathcal{A}_a^- \mathbf{Q}_r \quad , \quad (3.19)$$

In this equation, the Jacobians \mathcal{A}_a^+ and \mathcal{A}_a^- are now evaluated using the average states \mathbf{Q}_a instead of the properties at the left and right cell. \mathbf{Q}_a is given by

$$\mathbf{Q}_a = \frac{\mathbf{Q}_l + \mathbf{Q}_r}{2} \quad . \quad (3.20)$$

To summarize, numerical dissipation is desirable close to the shock which can prevent solution oscillations. In this region, the original Steger-Warming scheme is more appropriate. For boundary layers, the amount of dissipation has to be reduced to maintain accuracy, and the modified Steger-Warming scheme is preferred.

In order to automatically switch between schemes, a pressure switch based on the evaluation of pressure difference between two adjacent cells sharing a face, is used [72].

Eq. (3.20) can, therefore, be rewritten as

$$\mathbf{Q}_a^+ = (1 - w)\mathbf{Q}_l + w\mathbf{Q}_r \quad \text{and} \quad \mathbf{Q}_a^- = w\mathbf{Q}_l + (1 - w)\mathbf{Q}_r \quad , \quad (3.21)$$

where the weight factor is

$$w = \frac{1}{2} \frac{1}{(\alpha \nabla p)^2 + 1} \quad \text{and} \quad \nabla p = \frac{|p_l - p_r|}{\min(p_l, p_r)} \quad . \quad (3.22)$$

As can be seen above, the value of ∇p determines the weight factor value, which in turn, influences the state properties, and, therefore, affects the two Jacobian matrixes

which depend on \mathbf{Q}_a^+ and \mathbf{Q}_a^- respectively. More specifically, in the vicinity of the shock region, where ∇p is large, w is close to 0, and the original Steger-Warming scheme is used. Close to the boundary the pressure difference is trivial, and the weight factor w approaches 0.5, which results in the modified Steger-Warming scheme.

In the boundary layer, the excessive artificial dissipation due to ϵ is controlled by the following approach [48]:

$$\epsilon = \begin{cases} 0.3(a + |u_n|) & \text{for } d > d_o \quad , \\ 0.3(1 - |\mathbf{n} \cdot \mathbf{w}|)(a + |u_n|) & \text{for } d \leq d_o \quad . \end{cases} \quad (3.23)$$

Note that a is the speed of sound and $|u_n|$ refers to the absolute value of normal velocity, and are both determined from the state property. d is the distance from the face to the nearest wall and d_o is a user-specified value that arbitrarily lies between the boundary layer thickness and the shock stand-off distance. \mathbf{n} is the face normal vector, and \mathbf{w} denotes the normal vector of the nearest wall boundary to the face. The term $(1 - |\mathbf{n} \cdot \mathbf{w}|)$ restricts the dissipation contribution to the faces parallel to the wall. This correction is widely used for hypersonic reentry flow case.

3.3 Higher-order Extension of Convective Flux

KATS reads all grids as if they were unstructured. Therefore, the ordering of cell index, typical of structured grids is not accounted for. Instead, for each generic cell, the surrounding neighbors are identified when loading the mesh. Since the computation of convective fluxes are carried out by looping through all of the faces, which is considerably faster than a cell-based loop routine, the grid connectivity information has to be mapped. The higher-order accurate convective flux is therefore computed using the extrapolated properties from the left and the right side of each generic face.

Quadrilateral Unstructured Grid

Fig. 3.1 shows the connected neighbors associated to cell i , highlighted by the glowing boundaries. Two cells sharing a generic face are easily found and defined to be so-called a “parent” cell (or left cell), and a “neighbor” cell (or right cell), with the face normal always being defined pointing from the left cell to the right one. Using the cell-centered properties from those neighboring cells, the convective fluxes through the sharing surface can be evaluated by a Riemann solver, recovering a first-order accuracy. Figure 3.1 shows the details of this evaluation at face $i + \frac{1}{2}$ where a local index is induced, however, just for the purpose of explanation. Associated properties are given by

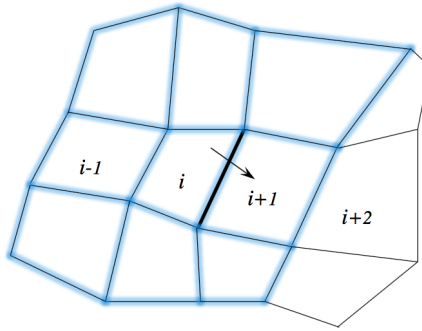


Figure 3.1: Cell's neighbor cloud

$$\begin{cases} u_l = u_i \\ u_r = u_{i+1} \end{cases} \quad (3.24)$$

Higher-order of spatial accuracy extension can be obtained from MUSCL (monotone upwind schemes for conservation laws) variable extrapolation [40], which shows effectiveness for a wide range of hypersonic flows [73], however, it requires the information of two more cells (Fig. 3.1). These additional cells can be found through searching within the mesh, and a four-cell stencil list is required for a generic face.

The extrapolation scheme is now given by

$$\begin{cases} u_l = u_i + \frac{1}{2}(u_i - u_{i-1}) \\ u_r = u_{i+1} - \frac{1}{2}(u_{i+2} - u_{i+1}) \end{cases} \quad (3.25)$$

The main issue associated with this higher-order accuracy is the appearance of oscillation. This comes from the MUSCL procedure itself, specifically the unappropriated reconstructed values at the interface $i + \frac{1}{2}$. Any overshoot or undershoot of some properties at this interface may cause it to lie outside the property interval $[u_i, u_{i+1}]$, and the oscillation is passed to the following time step. Fortunately, this can be avoided by introducing a limiter function. The idea behind limiters is that it prevents oscillations by switching to lower order scheme in the region of discontinuity while in the smooth region, it recovers second order accuracy. The price of using limiters is a loss of local accuracy. The newly constructed variable after applying the limiter function is given by

$$\begin{cases} u_l = u_i + \frac{1}{2}\text{lim}(u_{i+1} - u_i, u_i - u_{i-1}) \\ u_r = u_{i+1} - \frac{1}{2}\text{lim}(u_{i+2} - u_{i+1}, u_{i+1} - u_i) \end{cases} \quad (3.26)$$

where lim is the limiter function.

An even more detailed criteria for the definition of the limiting function is given by the Total Variation Diminishing (TVD) approach [66]. Considering the time evolution value, u_i^n , which is the numerical solution at time level n at cell i . The Total Variation is given by:

$$TV(u^n) = \sum_{i=-\infty}^{\infty} |u_{i+1}^n - u_i^n| \quad . \quad (3.27)$$

With that, a numerical scheme for the initial value problem (IVP) is said to be total variation diminishing if $TV(u^{n+1}) \leq TV(u^n)$. The fundamental properties of its solutions in TVD constraint are listed as following:

1. No new local extrema may be created in the set of solution u_i

2. The value of a local minimum is non-decreasing, and the value of a local maximum non-increasing.

The second-order, TVD limiters at least satisfy the following criteria:

$$\left\{ \begin{array}{ll} \Phi(r) = 0, & (r < 0) \\ r \leq \Phi(r) \leq 2r, & (0 \leq r < 1) \\ \Phi(r) = 1, & (r = 1) \\ 1 \leq \Phi(r) \leq \min(2, r), & (r > 1) \end{array} \right. . \quad (3.28)$$

where $r = \frac{u_{i+1}-u_i}{u_i-u_{i-1}}$ for the left side and $r = \frac{u_{i+2}-u_{i+1}}{u_{i+1}-u_i}$ for the right. These constraints can be interpreted as properties:

1. Limiter function is non-negative. $\Phi(r) \geq 0, \quad \forall r$
2. Limiter function is switched off when $r < 0$. The sign change means a local extreme is found in the solution
3. Limiter function is second order accurate in smooth regions: $\Phi(1)=1$

Differently, most of the traditional hypersonic solvers use conserved variables as the dependent variables. Each conserved variable is therefore extrapolated and slope-limited for a higher-order scheme. In the proposed work, however, MUSCL extrapolation is applied directly to primitive variables $(p_1, \dots, p_{ns}, u, v, w, T_{tr}, T_{ve})^T$. The main reason for this selection is to ensure zero pressure gradient at the stagnation region, and to gain more stability other than using primitive variables $(\rho_1, \dots, \rho_{ns}, u, v, w, T_{tr}, T_{ve})^T$. Tests on selections of some other primitive variables such as e_v and p for robustness and accuracy are needed [73]. Two typical limiter functions are cho-

sen, which are minmod and Van Albada's limiter. The widely used minmod limiter function [74] is given by

$$\left\{ \begin{array}{ll} \text{mimod}(a, b) = 0 & ab < 0 \\ \text{minmod}(a, b) = \min(a, b) & a > 0 \\ \text{minmod}(a, b) = \max(a, b) & a < 0 \end{array} \right. . \quad (3.29)$$

Van Albada's limiter function [75] is more differentiable and accurate, but less stable, given by

$$\text{VanAlbada}(a, b) = \frac{(a^2 + \epsilon)b + (b^2 + \epsilon)a}{a^2 + b^2 + 2\epsilon} , \quad (3.30)$$

where ϵ is a small number added preventing zero denominator.

Non-quadrilateral Unstructured Grid

In the case of non-quadrilateral grid, such as those composed of triangles, it is common that some cells do not have a four-cell stencil for extrapolation. A more general form combining gradient terms, however, can be used for higher-order accuracy, given by

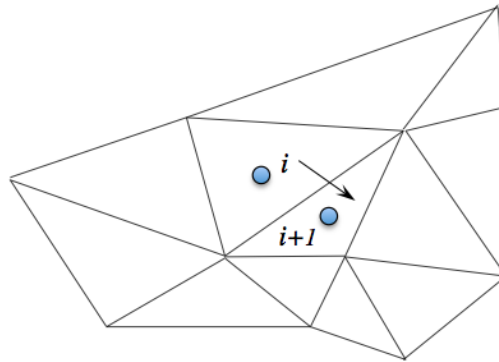


Figure 3.2: Triangular grid

$$\begin{cases} u_l = u_i + \nabla u_i \cdot d\mathbf{s}_i \\ u_r = u_{i+1} + \nabla u_{i+1} \cdot d\mathbf{s}_{i+1} \end{cases} \quad (3.31)$$

where \mathbf{s} is the location vector pointing from the cell centroid to the face centroid, and the gradient is evaluated at the cell centroid.

Similarly, a limiter function Φ can be added to limit the slope, such as

$$\begin{cases} u_l = u_i + \Phi_i \nabla u_i \cdot d\mathbf{s}_i \\ u_r = u_{i+1} + \Phi_{i+1} \nabla u_{i+1} \cdot d\mathbf{s}_{i+1} \end{cases} \quad (3.32)$$

Barth and Jespersen [76] introduced the first limiter for unstructured grids. More developed procedures were later found in Ref. [77]. To avoid the non-differentiability in some steps of the Barth-Jespersen procedure, Venkatakrishnan introduced a new smooth function [78]. It should be mentioned that for hypersonic problems, rectangular or prism cells are necessary to use [79]. The application of Venkatakrishnan limiter only shows in relatively low-speed flow where the non-regular grid can produce a valid solution. Motivated readers are also welcome to read Ref. [79], which proposes an approach valid for a wide range of problems, even with shock, and is more straightforward to implement.

3.4 Diffusive Flux Vector

Approximation of the diffusive flux terms involves the evaluation of gradient at the shared face, which is computed using the weighted least-square method [80]. This method behaves similarly to other methods, such as Green-Gauss method, for regular meshes, but is more tolerant to mesh distortions than others. However, it loses accuracy for highly stretched meshes in the presence of curvature. A deferred correction scheme using the central-differencing approach is introduced to calibrate this

gradient. Consequently, the new gradient is given by

$$\widetilde{\nabla}\phi = \nabla\phi - ((\nabla\phi) \cdot \mathbf{n})\mathbf{n} + \frac{\phi_r - \phi_l}{l}\mathbf{n} \quad . \quad (3.33)$$

In this equation, $\nabla\phi$ is the gradient for a property ϕ evaluated using weighted least-square method. Instead of using the normal of the face, a new normal, \mathbf{n} , is defined using the left and right cell centroid, with l representing the distance between them. The purpose of this correction is to calibrate the gradient contribution in the new normal direction.

Other than the gradient, the treatment of transportation properties has been discussed in Section 2.1.

3.5 Jacobian

Numerical Flux Jacobian

Implicit discretizations of the governing equation require forming Jacobian matrices, which is accomplished by using analytical or numerical derivatives of the systems of flux equations with respect to the primitive variables P_i .

Although analytical Jacobians are accurate, it requires a lot of effort to obtain one. In the context of a research code, where physical models are consistently changed and updated, this can be extremely tedious. Moreover, for a convective flux scheme like AUSM⁺-up which lacks an analytical form, an analytical Jacobian is impossible to derive. A solution to this is to use the Steger-Warming flux Jacobians while still using the Roe or the AUSM flux scheme. The underlying issue for this combination arises from the lack of consistency between the numerical flux and the flux Jacobian.

To avoid complicated derivation of the analytical Jacobian because of complexity of the discretized flux equations system, and to maintain the consistency between the numerical flux and the flux Jacobian, a more flexible numerical Jacobian can be used.

In its general form, the numerical flux Jacobian is given by

$$J_{ij} = \frac{\partial F_i}{\partial P_j} = \frac{F_i(P_j + \epsilon e_j) - F_i(P_j)}{\epsilon}, \quad (3.34)$$

for flux F_i and primitive P_j , where e_j is a unit base vector.

Eq. (3.34) is simply the forward-difference method. i.e. a first-order Taylor series expansion approximation to the analytical Jacobian. The accuracy of the numerical Jacobian is strongly affected by the perturbation ϵ : small values of ϵ can be contaminated by floating-point roundoff error. However, if too big, the derivative becomes a poor approximation: since the truncation error due to neglected terms in the Taylor expansion is $\sim \mathcal{O}(\epsilon)$. Unfortunately, the selection of optimistic perturbation ϵ is not trivial. The Complex Step Method [31] could be used to remove the uncertainty caused by ϵ , and achieve high order accuracy through the simple forward differencing.

The referred literature lists many different ways to select optimized ϵ_{opt} [81]. In this work, the selection mechanism is given by

$$\epsilon_{opt} = \begin{cases} \max(\epsilon_{small}, 0.001\Delta P_j) & \text{if } \Delta P_j > \epsilon_{small} \\ \min(-\epsilon_{small}, 0.001\Delta P_j) & \text{if } \Delta P_j < -\epsilon_{small} \\ \epsilon_{small} & \end{cases} \quad (3.35)$$

where $\epsilon_{small} = 10 \epsilon_{double}$. And ϵ_{double} is the numerical limits of double precision for a computer. The updated history of primitive variable ΔP_j is kept as reference also to scale the selection of the magnitude of ϵ .

To obtain every numerical Jacobian component for the primitive variables, each of them has to be perturbed. After the perturbation, the state properties are adjusted. For example, the perturbed density will also alter pressure and total energy, and new convective and diffusive fluxes have to be computed. This process repeats for each primitive variable. The computation expense comes from the update of the new state properties after the perturbation, the resulting new fluxes, and the final numerical differencing. Since the number of equations and primitive variables may not be trivial, this approach is more computational expensive than an analytical Jacobian.

It is to be noted that Eq. (3.34) is a first-order approximation. An extension to second-order approximation is straightforward:

$$J_{ij} = \frac{F_i(P_j + \epsilon e_j) - F_i(P - \epsilon e_j)}{2\epsilon} . \quad (3.36)$$

However, in this case, the computation time almost doubles since both $F_i(P + \epsilon e_j)$ and $F_i(P - \epsilon e_j)$ have to be computed.

Analytical Flux Jacobian

The arithmetic operation of the numerical flux Jacobian rises more than $\mathcal{O}(N^2)$, (where N is the dimensions of the system equations), which makes it prohibitively expensive to solve with increasing number of species, such as for 11-species air model. For the purpose of stability and accuracy, analytical flux Jacobian is always optimal.

Analytical Convective Flux Jacobian

Instead of using the Jacobian matrices \mathbf{A}_l^+ and \mathbf{A}_r^- for convective flux vector in the Steger-Warming scheme, a different inviscid Jacobians, the “true inviscid Jacobians” are used for the implicit operation. Details of the derivation are shown in Appendix B.

Analytical Diffusive Flux Jacobian

The computation of viscous Jacobians is different from that of inviscid Jacobians. It involves thin-layer approximation and a new set of primitive variables $\mathbf{V} = (Y_s, u, v, w, T_{tr}, T_{ve})^T$. Therefore, a map to primitive variable vector \mathbf{P} is necessary. Also, it is a lot easier to perform the derivation under face-based reference frame. The viscous flux vector can be approximated as

$$\mathbf{F}_d = \mathbf{R}^{-1} \mathbf{M}_n \mathbf{R} (\mathbf{V}_r - \mathbf{V}_l) = \mathbf{R}^{-1} \mathbf{M}_n \mathbf{R} \mathcal{N}(\mathbf{P}_r - \mathbf{P}_l) , \quad (3.37)$$

where

$$\mathcal{N} = \frac{\partial \mathbf{V}}{\partial \mathbf{P}} . \quad (3.38)$$

The viscous Jacobian is finally given by

$$\frac{\partial \mathbf{F}_d}{\partial \mathbf{P}_r} = \mathcal{R}^{-1} \mathcal{M}_n \mathcal{R} \mathcal{N} \quad \text{and} \quad \frac{\partial \mathbf{F}_d}{\partial \mathbf{P}_l} = -\mathcal{R}^{-1} \mathcal{M}_n \mathcal{R} \mathcal{N} \quad . \quad (3.39)$$

Details of the procedure are also shown in Appendix B.

Analytical Jacobian for the Source Term

The source term Jacobian takes the form of

$$J_{ij} = \frac{\partial S_i}{\partial P_j} \quad . \quad (3.40)$$

Appendix B provides more details.

3.6 Boundary Conditions

Explicit Boundary Conditions

The solution of the set of partial differential equations on a finite computational domain requires specification of dependent variables along every boundary of it. Appropriate boundary conditions must be enforced to compute the flux contribution to the solution of the system. Imposition of the explicit boundary conditions in this work uses ghost cells, which can be envisioned as an extra layer of cells added out of each boundary of the computational grid. The values in the ghost cell are updated according to the fixed boundary conditions and the state properties of its neighboring real cell. Since KATS intends to solve both subsonic and supersonic flow, different treatments are discussed in the following subsections. Note that, in the following notations, subscript r denotes the ghost cell values, and l denotes the real cell values.

Supersonic Boundary Conditions

Inlet

The inlet boundary conditions are completely specified by just using free-stream conditions. The properties in the ghost cells are given by

$$\mathbf{P}_r = \mathbf{P}_\infty \quad . \quad (3.41)$$

Outlet

Outflow boundary conditions are straightforward since this work only focuses on supersonic flows at the outlet. The properties in the ghost cell are simply extrapolated from its interior neighbor

$$\mathbf{P}_r = \mathbf{P}_l \quad . \quad (3.42)$$

Symmetry

The symmetry boundary condition zeros the normal component of the velocity, such that $\mathbf{V} \cdot \mathbf{n} = 0$, while maintains the tangent components at the boundary. In terms of implementation, the velocity vector in the ghost cell in Cartesian coordinate is given by

$$\mathbf{V}_r = \mathbf{V}_l - 2(\mathbf{V}_l \cdot \mathbf{n}) \mathbf{n} \quad . \quad (3.43)$$

Other independent variables are copied directly to the ghost cells by ensuring zero mass and energy fluxes. The momentum flux is thus given by pressure only, in detail

$$\rho_{r,s} = \rho_{l,s} \quad (3.44)$$

$$T_{tr,r} = T_{tr,l} \quad (3.45)$$

$$T_{ve,r} = T_{ve,l} \quad (3.46)$$

Wall

The inviscid no-slip wall condition enforces a zero velocity condition at the boundary. This involves simply reflecting the normal and tangential component of the velocity in the interior cell and placing them in the adjacent ghost cell. The other properties act such as those for symmetry boundary conditions. The mass flux through the wall is zero. The energy flux and the momentum flux are given by the pressure only.

$$\begin{aligned}\rho_{r,s} &= \rho_{l,s} \\ \mathbf{V}_r &= -\mathbf{V}_l \\ T_{tr,r} &= T_{tr,l} \\ T_{ve,r} &= T_{ve,l}\end{aligned} \quad . \quad (3.47)$$

Viscous Boundary Conditions

Inlet and outlet

A zero-gradient condition is assumed for these boundaries by setting

$$\mathbf{P}_{rc} = \mathbf{P}_{lc} \quad . \quad (3.48)$$

where the subscript c denotes the values stored at the centers, which accounts for the computation of gradients.

Symmetry

All of the dependent variables are set to enforce zero-gradient except the velocity vector. The symmetry boundary zeros the normal component of the velocity while maintains the tangent components, given by

$$\mathbf{V}_{rc} = \mathbf{V}_{lc} - 2(\mathbf{V}_{lc} \cdot \mathbf{n}) \mathbf{n} \quad . \quad (3.49)$$

However, other independent variables are copied directly to the ghost cells yielding zero gradient, in detail

$$\rho_{rc,s} = \rho_{lc,s} \quad (3.50)$$

$$T_{tr,rc} = T_{tr,lc} \quad (3.51)$$

$$T_{ve,rc} = T_{ve,lc} \quad (3.52)$$

Wall

The wall boundary conditions are specified by assuming no-slip velocity condition, and fixed-wall temperature, T_w . In most of the cases, Park's two temperatures use the same values at the wall boundary. The total pressure is assumed constant within the boundary layer which results in zero gradient for it. The mass fraction for each species is also continuous in the boundary layer based on the assumption of non-catalytic wall condition. In detail

$$p_{rc} = p_{lc}$$

$$Y_{rc} = Y_{lc}$$

$$\mathbf{V}_{rc} = -\mathbf{V}_{lc} \quad (3.53)$$

$$T_{tr,rc} = 2T_w - T_{tr,lc}$$

$$T_{ve,rc} = 2T_w - T_{ve,lc}$$

In the case of adiabatic wall, two temperatures are simply extrapolated

$$T_{tr,rc} = T_{tr,lc} \quad (3.54)$$

$$T_{ve,rc} = T_{ve,lc}$$

Subsonic Boundary Conditions

When dealing with subsonic flow, the dependent primitive variable set in KATS is modified to pressure-based, which tends to be more accurate [82], given by $\mathbf{P} = (p_1, \dots, p_{ns}, u, v, w, T)^T$. Additionally only the thermal equilibrium state is considered, depicted by one temperature, T .

Inlet

It has been found when a wall boundary connects to the inlet, it is not appropriate to impose velocity at the inlet [83] for a compressible flow solver. Rather the velocity is extrapolated, and the total pressure and total temperature are specified. The static pressure and static temperature are calculated from isentropic relations.

$$p_r = p_{\text{total}} \left(1 + \frac{\gamma - 1}{2} M_l^2 \right)^{\frac{\gamma}{\gamma - 1}} , \quad (3.55)$$

and

$$T_r = T_{\text{total}} \left(\frac{p_r}{p_{\text{total}}} \right)^{\frac{\gamma}{\gamma - 1}} . \quad (3.56)$$

Outlet

Static pressure is fixed at the boundary, while others are directly extrapolated from the interior cell.

Symmetry

The symmetry boundary zeros the normal component of the velocity, such that $\mathbf{V} \cdot \mathbf{n} = 0$, while maintains the tangent components at the boundary. In terms of implementation, the velocity vector in the ghost cell in Cartesian coordinate is given by

$$\mathbf{V}_r = \mathbf{V}_l - 2(\mathbf{V}_l \cdot \mathbf{n}) \mathbf{n} . \quad (3.57)$$

Other independent variables are copied directly to the ghost cells by ensuring zero mass and energy fluxes, in detail

$$p_{r,s} = p_{l,s} \quad (3.58)$$

$$T_r = T_l \quad (3.59)$$

Wall

The no-slip and adiabatic boundary yields

$$\begin{aligned} p_{r,s} &= p_{l,s} \\ \mathbf{V}_r &= -\mathbf{V}_l \\ T_r &= T_l \end{aligned} \tag{3.60}$$

and for a fixed temperature wall is defined by

$$T_r = T_w \quad . \tag{3.61}$$

Viscous Boundary Conditions

For subsonic flow problems, the ghost cell centered values are simply extrapolated using central differencing, given by

$$\mathbf{P}_{rc} = 2\mathbf{P}_w - \mathbf{P}_{lc} \quad . \tag{3.62}$$

Implicit Boundary Conditions

The main difference of implicit boundary conditions arises from the Jacobian contribution of the boundary ghost cell to the implicit operator. Recall Eqn. (3.8), after the decomposition of the equation system for a generic cell, it yields

$$\left[\frac{V_{cell}}{\Delta t} \mathcal{J}^n + \mathcal{A}_l^+ - \mathcal{B}_l^+ - \mathcal{C}_l - \mathcal{D}_l \right] \Delta \mathbf{P}_l + \sum_r [\mathcal{A}_r^- - \mathcal{B}_r^-] \Delta \mathbf{P}_r = \mathbf{R}_l^n \tag{3.63}$$

Its neighbor cells, denoted by subscript r , can be a real cell or a ghost cell. The ghost cell value update, although unknown, can be approximated by relating to cell l through the introduction of “folding” matrices. To accomplish this, the relation is given by

$$\Delta \mathbf{P}_r = \frac{\partial \mathbf{P}_r}{\partial \mathbf{P}_l} \Delta \mathbf{P}_l \quad . \tag{3.64}$$

The folding matrices $\boldsymbol{\mathcal{E}}_f = \frac{\partial \mathbf{P}_r}{\partial \mathbf{P}_l}$ can be determined from the implementation of boundaries conditions, and the inviscid and viscous folding matrices may not be identical. Since source terms are piecewise. The resulting source term Jacobians vanish for boundary ghosts.

Inviscid Folding Matrices

Looking at the boundary condition implementations for the supersonic cases in Section 3.6, the resulting folding matrices are given by

Inlet

$$\boldsymbol{\mathcal{E}}_f = \mathbf{0} \quad . \quad (3.65)$$

Outlet

$$\boldsymbol{\mathcal{E}}_f = \boldsymbol{\mathcal{I}} \quad . \quad (3.66)$$

Symmetry

Instead of imposing the symmetry boundary in the way shown in Eqn. (3.43), it is more straightforward to deal with it in face-based reference frame, such as

$$\mathbf{P}_{rn} = \boldsymbol{\Lambda} \mathbf{P}_{ln} \quad . \quad (3.67)$$

where the eigenvalues λ_i are equal to 1 except for the normal velocity component, which equals -1. In detail, $\mathbf{Dia}(\boldsymbol{\Lambda}) = (1, -1, 1, 1, 1)$. After that, the Cartesian frame based properties are mapped back. During this procedure, a rotation matrix $\boldsymbol{\mathcal{R}}$ is needed to map the properties from the Cartesian frame to the face-based reference frame, and $\boldsymbol{\mathcal{R}}^{-1}$ to do backward. The whole mapping process is given by

$$\mathbf{P}_r = \boldsymbol{\mathcal{R}}^{-1} \boldsymbol{\Lambda} (\boldsymbol{\mathcal{R}} \mathbf{P}_l) \quad . \quad (3.68)$$

In the case of folding matrix, the same form is maintained, such as

$$\Delta \mathbf{P}_r = \mathcal{R}^{-1} \mathbf{\Lambda} (\mathcal{R} \Delta \mathbf{P}_l) \quad . \quad (3.69)$$

which indicates

$$\mathcal{E}_f = \mathcal{R}^{-1} \mathbf{\Lambda} \mathcal{R} \quad . \quad (3.70)$$

Wall

For no-slip wall, it is given by

$$\mathcal{E}_f = \mathbf{\Lambda} \quad , \quad (3.71)$$

where the eigenvalues λ_i are equal to 1 except for the three velocity components, in detail, $\mathbf{Dia}(\mathbf{\Lambda}) = (1, -1, -1, -1, 1, 1)$.

Viscous Implicit Boundary Conditions

As mentioned previously, it is a lot easier to perform the calculation of viscous Jacobians under a face-based reference frame, and using a new set of primitive variables $\mathbf{V} = (Y_s, u, v, w, T_{tr}, T_{ve})^T$. The viscous flux vector is given by

$$\mathbf{F}_d = \mathcal{R}^{-1} \mathcal{M}_n \mathcal{R} (\mathbf{V}_r - \mathbf{V}_l) \quad . \quad (3.72)$$

When at the boundary, boundary conditions are imposed, which indicates $\mathbf{V}_{rn} = \mathbf{\Lambda} \mathbf{V}_{ln}$ under face-based reference frame. The flux vector now becomes

$$\mathbf{F}_d = \mathcal{R}^{-1} \mathcal{M}_n (\mathbf{\Lambda} - \mathcal{I}) \mathcal{R} \mathbf{V}_l = \mathcal{R}^{-1} \mathcal{M}_n (\mathbf{\Lambda} - \mathcal{I}) \mathcal{R} \mathcal{N} \mathbf{P}_l \quad , \quad (3.73)$$

where

$$\mathcal{N} = \frac{\partial \mathbf{V}}{\partial \mathbf{P}} \quad . \quad (3.74)$$

Note that $\mathbf{\Lambda}$ is computed using the new set of primitive variables \mathbf{V}_n . It also implies there is no need to take account of $\frac{\partial \mathbf{F}_d}{\partial \mathbf{P}_r}$ separately. Instead, the effect of the boundary ghost cell can be included its neighboring real cell without repeatble computation.

Wall

For a no-slip and fixed-temperature wall, $\mathbf{Dia}(\mathbf{\Lambda}) = (1, -1, -1, -1, -1, -1)$.

Symmetry

Only the normal velocity component is zeroed at the symmetry boundary, which indicates $\mathbf{Dia}(\mathbf{\Lambda}) = (1, -1, 1, 1, 1, 1)$.

Inlet

$$\mathbf{\Lambda} = \mathbf{I} \quad . \quad (3.75)$$

Outlet

$$\mathbf{\Lambda} = \mathbf{I} \quad . \quad (3.76)$$

3.7 Linear Solver

Time integration and space discretization of the system of equations end up with a large sparse linear system indicated by Eqn. (3.6) which is in the form of $\mathbf{Ax} = \mathbf{b}$. For such problems, iterative methods are more suitable to apply than directly solving the system through an inverse of the matrix. Considerable work has been devoted to solving the linear system with high efficiency and accuracy of the iterative solution. The LU-SGS implicit algorithm was used in Ref. [84,85], and the point or line implicit method has been successfully used in DPLR [86], LeMANS [48] and US3D [87].

In KATS, the PETSc package [88–90] which provides flexible combinations of solvers and preconditioning matrices is used. Among those solvers, the Conjugate Gradient method [91] is assumed to have the best performance by reproducing the exact solution for the linear system for N unknowns in N steps, but only if matrix \mathbf{A} is positive definite and a symmetric system [92]. The matrix of the current system, however, does not guarantee either of these conditions. A GMRES [93] method

extended for nonsymmetric systems provides more flexibility. It can be used for arbitrary, nonsingular square matrices. It starts from an initial guess solution vector such as the one from the previous step or by an explicit step and generates a sequence of orthogonal vectors. The solution vector is constructed from the sequence by adding changes at each step and the minimized linear system residuals are eventually achieved. Theoretically, this method converges at the N^{th} step, but its cost of the iterations grows as $O(N^2)$. A restarted GMRES method can prevent the iteration from being too expensive for large N by introducing a restart parameter k . This modification works in a way that the method is forced to restart after k^{th} iteration, and the k^{th} result will be taken as an initial guess for the next iteration period. Suitable restarting parameters can save the expense required to construct and store the orthogonal basis. However, a too small restart parameter diverges the iteration. $k = 30$ is considered appropriate for the proposed work.

Another aspect of the linear solution procedure is the preconditioning matrix. The general idea of a preconditioning procedure involves the selection of a matrix \mathcal{Q} , such that the new linear system is better conditioned than the original system, $\mathbf{Ax} = \mathbf{b}$ [94]. The preconditioners are by nature problem-dependent. The choice of the optimal one relies on the suitable preconditioning of the linear operator. Careful selection of a solver and its preconditioner can improve the efficiency and the stability, which is even more important, since stability has always been an issue for hypersonic reacting flow, especially when the gas mixture involves the presence of electron.

In this work, the Flexible Generalized Minimal Residual (FGMRES) method is selected as the solver, and SOR and block Jacobi preconditioning, which demonstrated the best performance in convergence rate and stability among the available preconditioners.

Chapter 4 Hypersonic Solver: Verification and Validation

4.1 Mach 10 Argon Flow over a Cylinder

As a first test-case, a 2-D Mach 10 Argon flow over a 1 meter radius cylinder is presented. Argon, a noble gas, only consists of single atom. Therefore, there is no need to take account vibrational and electronic energy, and the flow is in thermal-equilibrium state. The free stream conditions for this problem are listed in Table 4.1, and Fig. 4.1 shows the computational grid. As can be seen, grid clustering at the surface and shock alignment is used to capture important effects.

Table 4.1: Free stream conditions for the flow field

Mach Number	Velocity	Density	Temperature	Pressure
10	2624.0 m/s	1.408×10^{-4} kg/m ³	200.0 K	5.8572 Pa

The pressure distribution obtained from the fluid dynamic solver is shown in Fig. 4.2(a). A strong bow shock in front of the body forms and the isocontours are smooth, as expected. Fig. 4.2(b) depicts the corresponding temperature field for the present analysis.

The pressure and temperature obtained along the stagnation stream line are also presented in Fig. 4.3(a) and 4.3(b). A comparison with the results obtained from the CFD code LeMANS [48] indicates that the results are in very good agreement. Small deviations near the shock regions are observed, which are most likely due to a difference in the mesh refinement in this region. Finally, the heat flux profile at the cylinder surface is presented in Fig. 4.4, where peak value occurs at the stagnation point, around 3.5 W/cm².

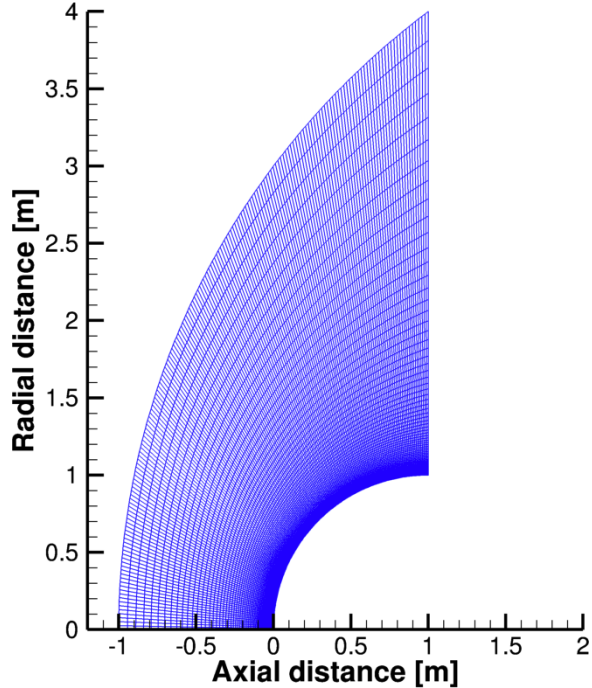


Figure 4.1: Computational grid for simulation of Mach 10 Argon flow over cylinder.

4.2 Mars Entry Spacecraft Model

This section replicates an experimental test on a Mars entry spacecraft experimental model in the HYPULSE expansion hypersonic wind tunnel [95]. In this facility, both air and carbon dioxide flow over this model have been tested, providing an aerothermodynamic database for validation of numerical codes in the development of Mars entry spacecraft. Together with the investigation of the aerothermodynamics of several related parametric configurations, the experimental study concentrates on the heat-transfer data along the model obtained at hypersonic test conditions. Compared to other conventional hypersonic wind tunnels at NASA Langley, the HYPULSE wind tunnel provides chemical and thermal non-equilibrium testing conditions to approximate those of actual planetary entry, making comparisons between experimental and numerical results more practical.

The baseline geometry model in the experimental study is a 70 degree blunted

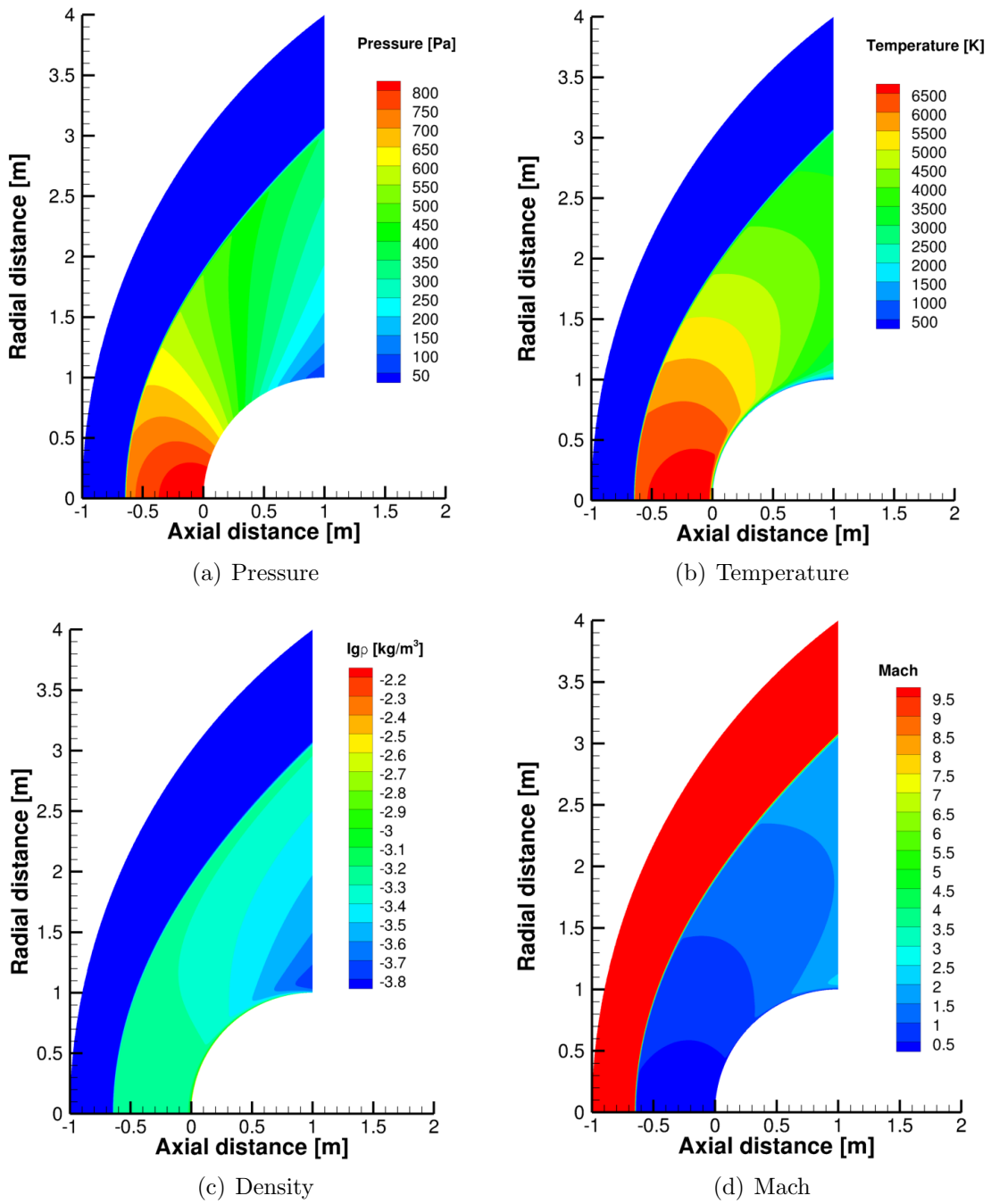
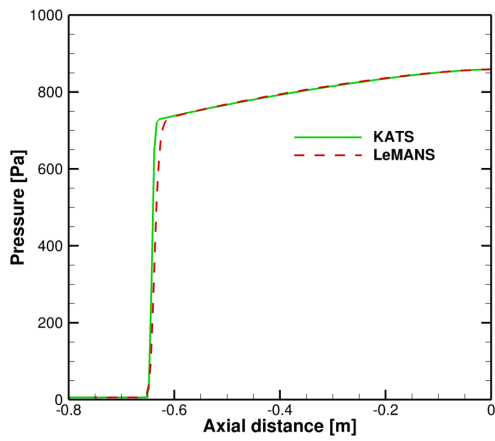
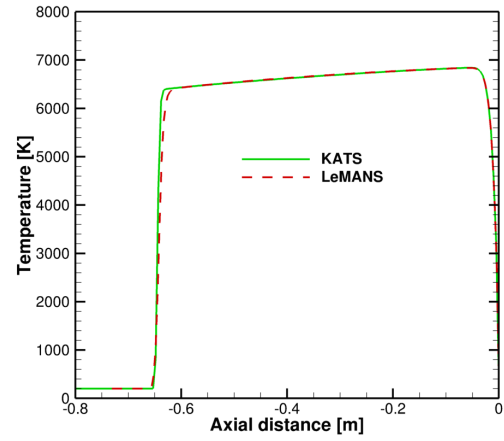


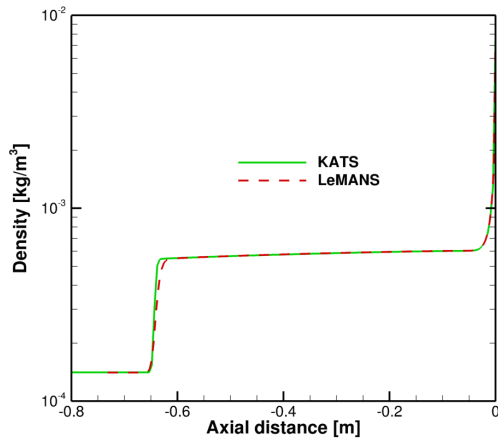
Figure 4.2: Isocontours for the Mach 10 Argon flow over the cylinder.



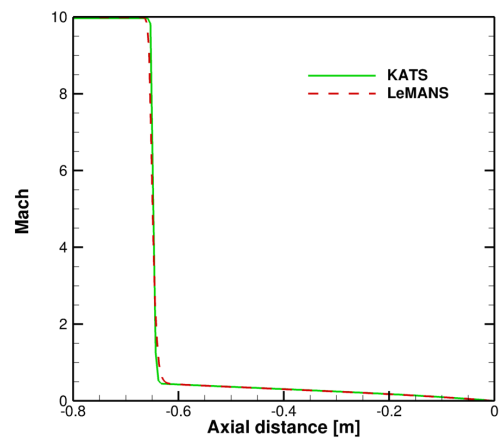
(a) Pressure



(b) Temperature



(c) Density



(d) Mach

Figure 4.3: Stagnation line results for the Mach 10 Argon flow over a cylinder.

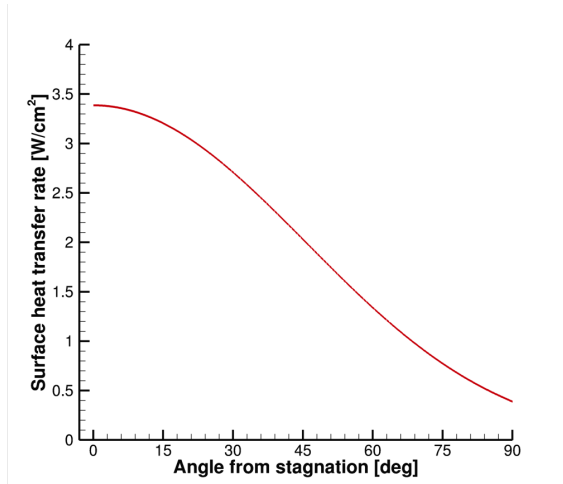


Figure 4.4: Surface heat flux for the Mach 10 Argon flow over a cylinder.

cone, the same configuration of the Mars-Pathfinder spacecraft. Figure 4.5 presents the geometry of the experimental model, and Table 4.2 lists the geometric parameters.

The main objective of this simulation is to test the capability of the developed

Table 4.2: Mars entry spacecraft model geometry

R_n	12.7 mm
R_b	25.4 mm
R_c	1.27 mm
R_f	15.24 mm
R_s	10.32 mm
α_n	70 degree
α_f	40 degree

hypersonic CFD solver in state of chemical and thermal non-equilibrium. In the current work, only air flow is considered. Specifically, a 5-species air model is used for the air mixture and chemical reaction (See Appendix A for details). To simplify the simulation, a zero angle-of-attack case is studied and compared to the experimental data. Therefore, the computation can be conducted using a 2D-axisymmetric mesh. The freestream conditions for the air flow are presented in Table 4.3, where the Knudsen number is $K_n = 2.8 \times 10^{-4}$, indicating a flow in continuum regime. The

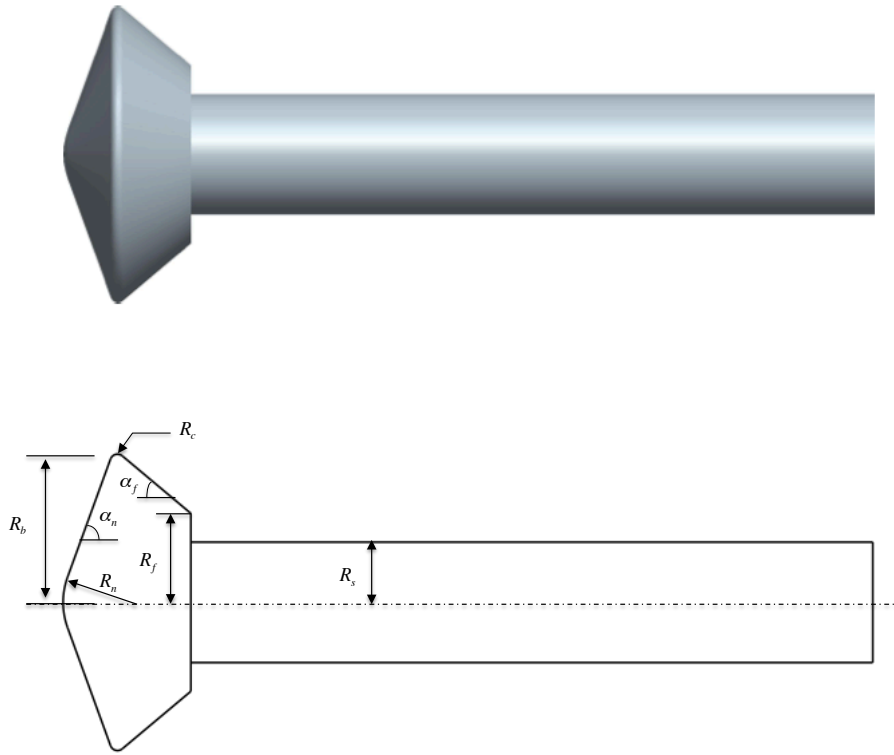


Figure 4.5: Mars entry spacecraft model geometry

mesh used in this simulation only consists of quadrilaterals as shown in Fig 4.6 and consists of 250 cells in the axial direction and 168 in the radial direction. A grid refinement study is performed close to the wall boundary with the first cell clustered at 1×10^{-7} m. The boundary layer thickness is set as 5×10^{-4} m as an input parameter for the modified Steger-Warming scheme.

Table 4.3: Free stream conditions for the flow field

ρ_∞ [kg/m ³]	u_∞ [m/s]	T_{tr} [K]	T_{ve} [K]	T_w [K]	Y_{N_2}	Y_{O_2}	Y_{NO}	Y_N	Y_O	M_∞
5.71×10^{-3}	5162.0	1113.0	1113.0	300.0	0.767	0.233	0	0	0	7.9

The flow field solution is presented in Fig. 4.7 (a). A detached shock forms in front of the model with a stand-off distance of 2 mm. The velocity magnitude decreases

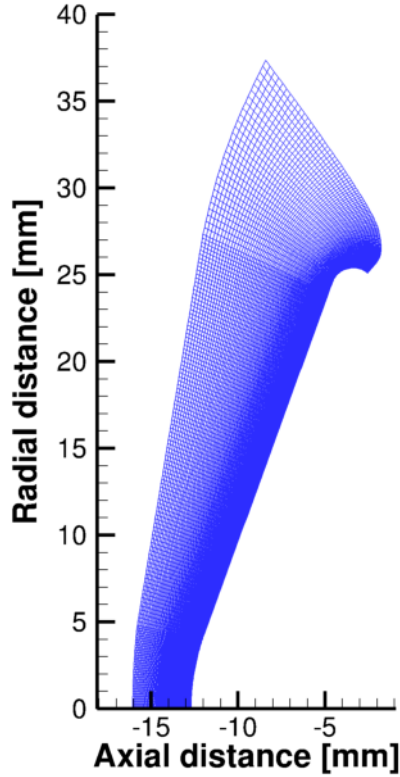


Figure 4.6: Meshed used in this simulation

from free-stream velocity to zero close to the wall. The level of nonequilibrium shown in Fig. 4.7 (b) is evaluated by computing the ratio of T_{tr} over T_{ve} . Overall, the shock layer presents a ratio above one. The peak value reaches as high as 4 in the shock wave and is decreased below 0.6 close to the shoulder, indicating strong non-equilibrium. Since vibrational temperature lags compared to the translational-rotational temperature, they do not have the time to equilibrate. The two temperatures are compared along the stagnation line in Fig. 4.8 (a), where the peak translational temperature is around 12000K. The vibrational temperature, however, does not reach as high as the translational temperature with the maximum value of around 7500 K. The two temperatures equilibrate to the same values after the shock and to the wall, indicating regions relaxed back to the equilibrium state.

The air dissociation can be observed in Fig. 4.8 (b), where the mass fractions for

each species are highlighted. Both N_2 and O_2 start to dissociate as approaching the shock layer, and O_2 is more sensitive to temperature. It starts to dissociate earlier than N_2 , and it fully dissociates after the shock. N_2 is relatively inertial compared to O_2 , and only a fraction of it is consumed. The maximum of NO mass fraction is located immediately after the shock, then then decreases. A closer look at the boundary indicates N and O rapidly decrease due to cold-wall boundary conditions, and N_2 , O_2 , and NO are formed again.

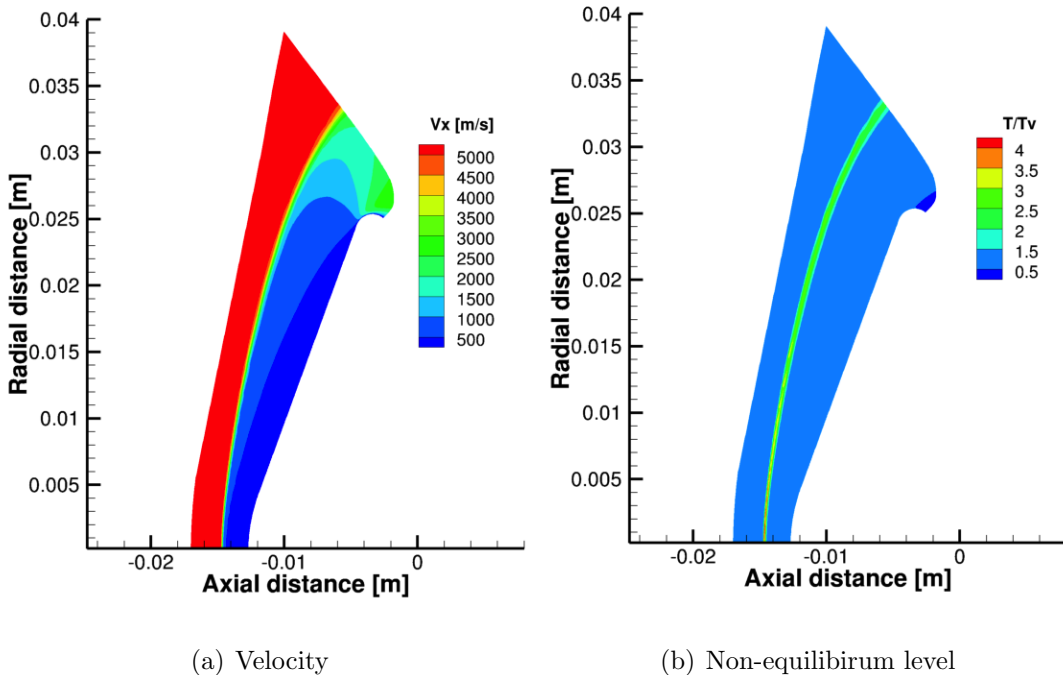


Figure 4.7: Solution contours

Heat transfer rate is an important factor considered in the reentry vehicle design. It is also the most difficult one to capture. Several numerical solutions for the forebody are compared against the experimentally measured data of Hollis [95] in Fig. 4.9.

First, a study on order of accuracy is conducted using a grid with dimensions of 251×161 . When using the second-order scheme, the overall agreement is good, and most of the numerical solutions are within the experimental uncertainty. The first-

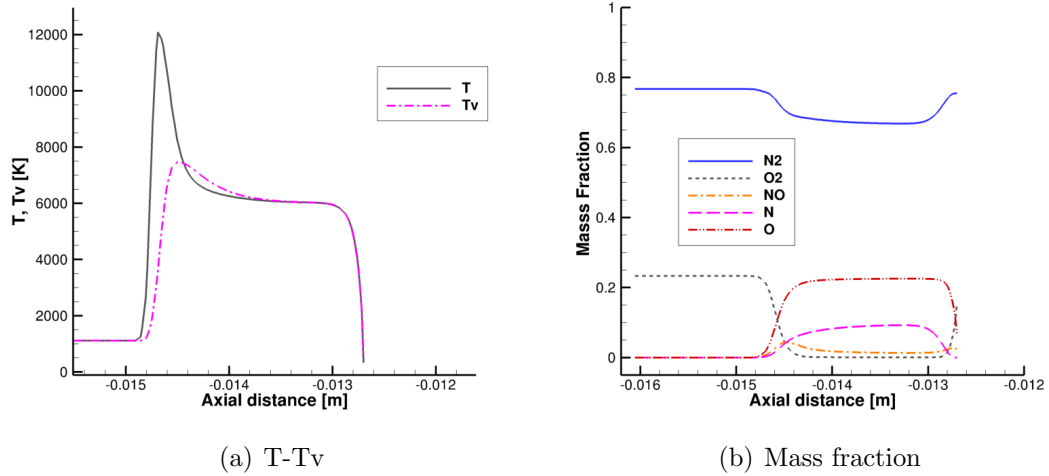


Figure 4.8: Properties along the stagnation line

order accurate scheme, however, over-predicts the experimental value at the stagnation point. Away from the stagnation point, very little discrepancy with each other can be found. Therefore, the major error comes from the stagnation region, where a more refined mesh must be used close to the wall for the first-order accurate scheme to obtain high-resolution solutions.

Second, a grid independence study is performed, where the refined mesh consists 251 cells in the direction normal to the wall. Its solution is very close to that of the 201 cell mesh, and grid independence is achieved. The stagnation region has a little dip for the result when using the first-order scheme, and for the finer mesh using the second-order scheme. The surface heat flux rate curve, however, is expected to be flat near the stagnation point. Further numerical studies are carried out on more refined mesh with careful alignment of the grid with the shock wave. However, it can be shown in Fig. 4.10 that mesh refinement and alignment do not eliminate the error.

This phenomenon is known as a “carbuncle” and it is effectively ubiquitous in the aerothermodynamics community, especially when using Steger-Warming scheme [72, 73]. The reason of this issue is mainly the misalignment of the grid with the shock wave. If the grid does not align with the shock wave perfectly (within one mesh-cell),

numerical errors are generated by the shock, which are then trapped in the stagnation region. It is also noted that these are 3D solutions computed on a pie-wedge of cells. The 3D mesh used for the simulation is made by rotating a 2D mesh with an axis by an angle of five degrees. The degenerated axis, and the degenerated face at the stagnation point make this issue even worse. Therefore, it is extremely difficult to get good heat transfer at the stagnation point. Except for the modification of Steger-Warming scheme at the stagnation region discussed in Section 3.2, careful alignment of the grid with the shock wave using an automatic feature is the only useful way to alleviate this problem. Mesh refinement, however, is not effective. The problem even worsens with grid refinement.

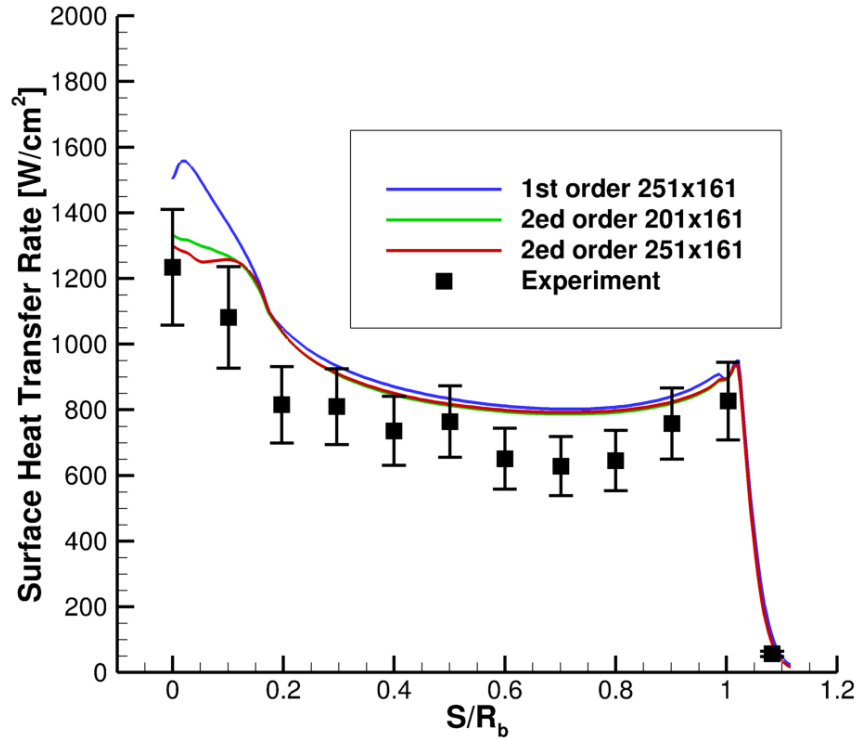


Figure 4.9: Heat transfer rate on the Mars Entry Lab model forebody

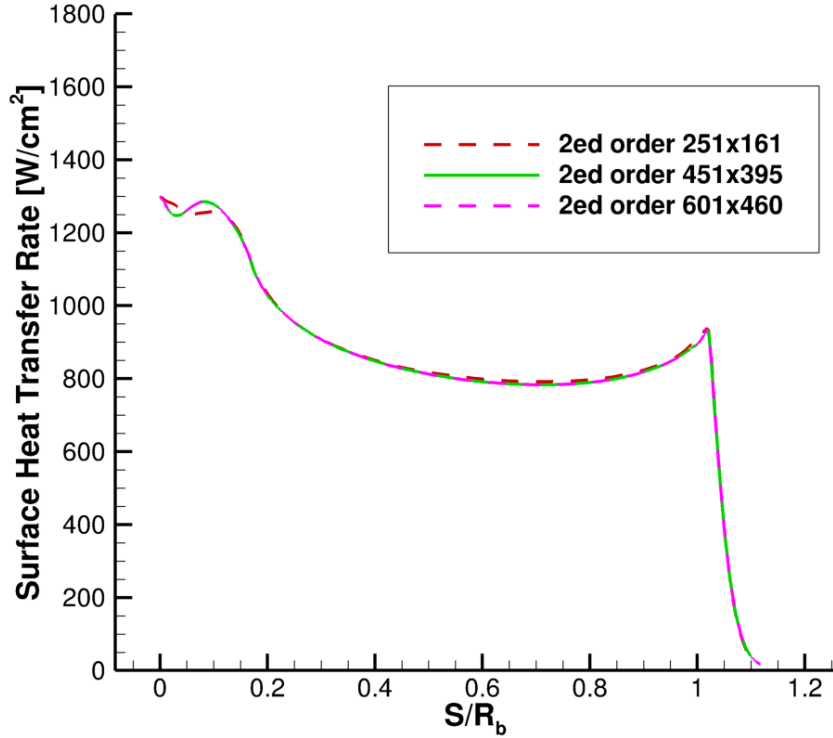


Figure 4.10: Numerical study on the numerical error near the stagnation point

4.3 Numerical Investigation on Stardust Capsule

The Stardust Sample Return capsule (Fig. 4.11) was designed by NASA to collect dust samples from the tail of comet WILD-2, and return them to Earth. Upon its return, it entered the earth atmosphere at a velocity of 12.6 km/s [5], and is the fastest earth reentry and highest energy reentry of any artificial object thus far. Modeling Stardust is challenging and is therefore an excellent test of the hypersonic thermochemical non-equilibrium models of the code. Two air models, a 5-species air model and an 11-species air model [48, 57] are used for computation and comparison. The chemical and thermal non-equilibrium modes, as well as the weak ionization effects, are evaluated.

In the present simulation, the trajectory point 36 second after Stardust's re-entry

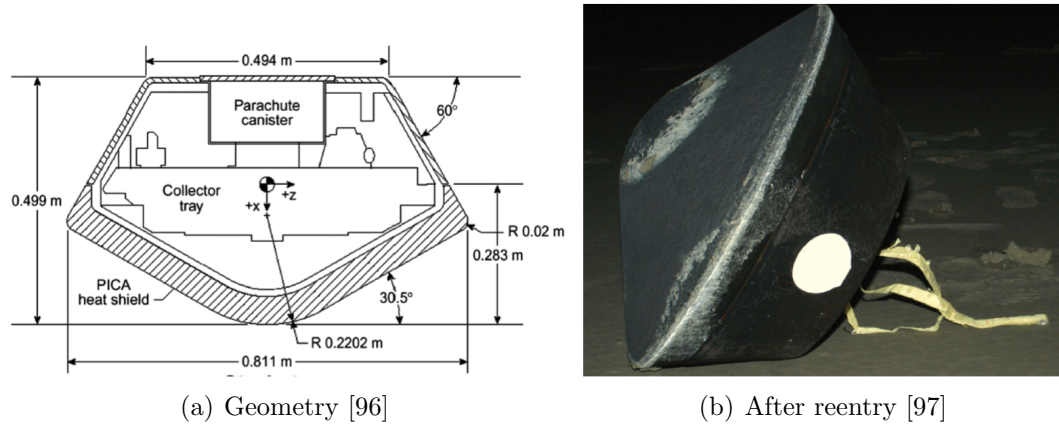


Figure 4.11: Stardust capsule

are studied. Free stream conditions are listed in Table 4.4. As the main species in the air mixture, N_2 and O_2 have initial mass fractions of 76.7%, and 23.3% respectively. All the other species, such as NO, N and O for 5-species air model, and NO, N, O, N_2^+ , O_2^+ , NO^+ , N^+ , O^+ and e for 11-species air model, have initial mass fractions of 0.

Table 4.4: Free stream conditions for the flow field

Time from entry, sec	Altitude, km	Velocity, m/sec	Density, kg/m ³	Temperature, K
36	78.46	12,336.86	1.871×10^{-5}	218.09

Full Geometry Simulation of 5-species Air over Stardust Capsule

Simulation of the whole geometry tends to be more challenged than just the forebody since the afterbody pressure can be extreme low and causes numerical difficulties for the simulations. To simplify the simulation, a 2D-axisymmetric mesh is used, shown in Fig. 4.12. It consists of 151 cells in the axial direction, and 700 cells along the capsule geometry. The mesh refinement is performed at the stagnation point and in the shoulder region.

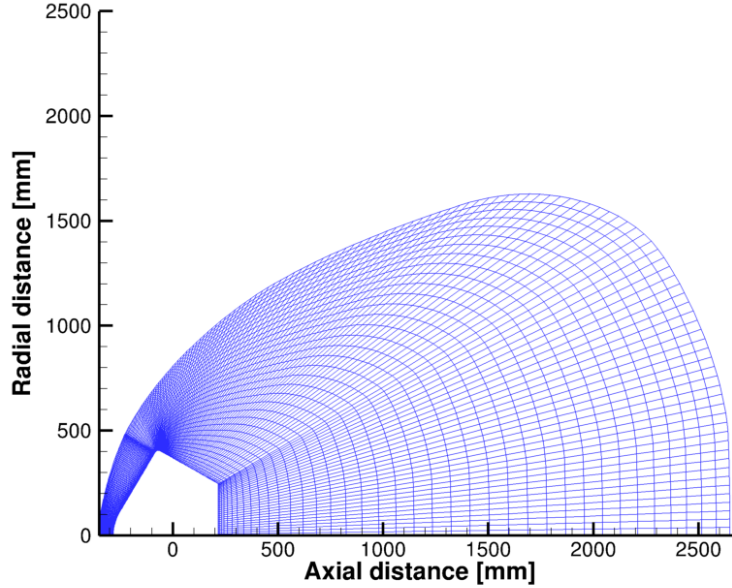


Figure 4.12: Mesh

The main features of the flow field are presented in Fig. 4.13, where a strong compression occurs in front of the capsule and forms a shock. The flow then expands around the shoulder and recirculates after the trailing edge. In the recirculation region, often referred to as the near-wake, the boundary layer separates from the surface, and forms two symmetric vortexes indicated by the streamlines. A closer look at the pressure in this region, one can find a rather low value, indicating it could possibly lie in the rarefied region. A more convincing examination, however, is done by evaluating the Knudsen number, shown in Fig. 4.14, where the mean free path is calculated as in Ref. [98]

$$\lambda = \frac{2\mu}{\rho\bar{c}} = \frac{\mu}{\rho} \sqrt{\frac{\pi}{2R_w T}} = \frac{\mu}{\rho} \sqrt{\frac{\pi\rho}{2p}} \quad . \quad (4.1)$$

and the characteristic length of the Stardust capsule uses 0.499 m (Fig. 4.11 (a)). Among those variables in Eqn. (4.1), μ is the viscosity, ρ is the total density, p is the total pressure, R_w is the mixture gas constant, T is the temperature, and \bar{c} is the mean molecular speed.

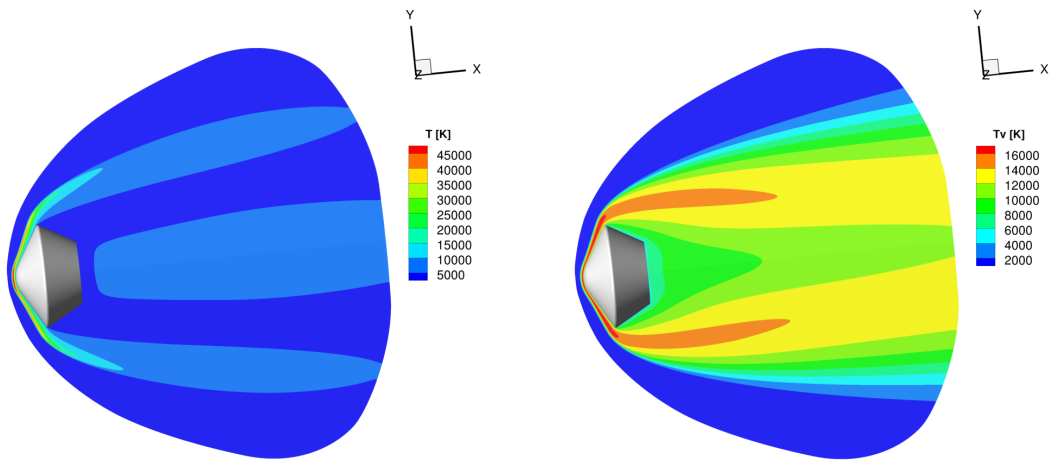
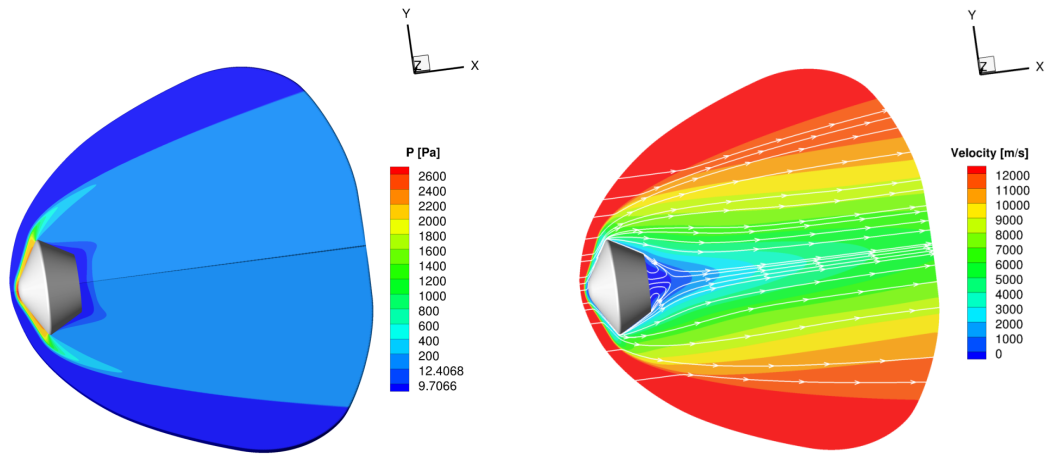
In Fig. 4.14, the free stream has a low value of Kn number, while large value of Kn number is found after the forebody, especially after the trailing edge. It is generally assumed that continuum breaks down when Kn is more than 0.05. The near-wake does lie in the rarefied region and the CFD may not be capable to solve the flow in it correctly.

Temperature contours can be found in Fig. 4.13 (c)-(d). The translational-rotational temperature, T_{tr} , and the vibrational-electron-electronic temperature, T_{ve} , have very different contours. The majority of the flow is in thermal non-equilibrium. For instance, T_{tr} after the shock can reach up to 50000 K, while T_{ve} always lags, and can only go up to 18000 K.

Simulation of 5-species Air over Stardust Capsule Forebody

To achieve higher resolution and faster run time, scaling of the problem is necessary. The following numerical study, therefore, only focuses on the forebody. A mesh independence test is first performed, in which the coarse grids consists 201 (axial) \times 331 (radial) cells while the refined mesh consists 401 (axial) \times 331 (radial) cells. The surface heat transfer rate is taken as the reference parameter and is shown in Fig. 4.15. Very few discrepancies can be found for two results and the maximum relative error close to the shoulder is 1.8%. The solution is considered to be accurate enough with the 201 \times 331 grid. Related results of this grid are presented for analysis and comparisons in the section.

The species mass fraction is illustrated in Fig. 4.16, which shows the shock layer thickness is around 40 mm, where the air mixture starts to dissociate. O_2 dissociates much faster than N_2 and becomes fully dissociated close to the wall. They are mainly converted into atomic species N and O. N has a larger mass fraction than O. NO is formed after the shock, however, it is in a relative lower level than all the other species. Close to the stagnation point, where the axial location equals zero, the non-catalytic cold-wall boundary forces recombination of O_2 . The mass fraction of NO is



(c) Translational-rotational temperature (d) Vibrational-electron-electronic temperature

Figure 4.13: Solution contour

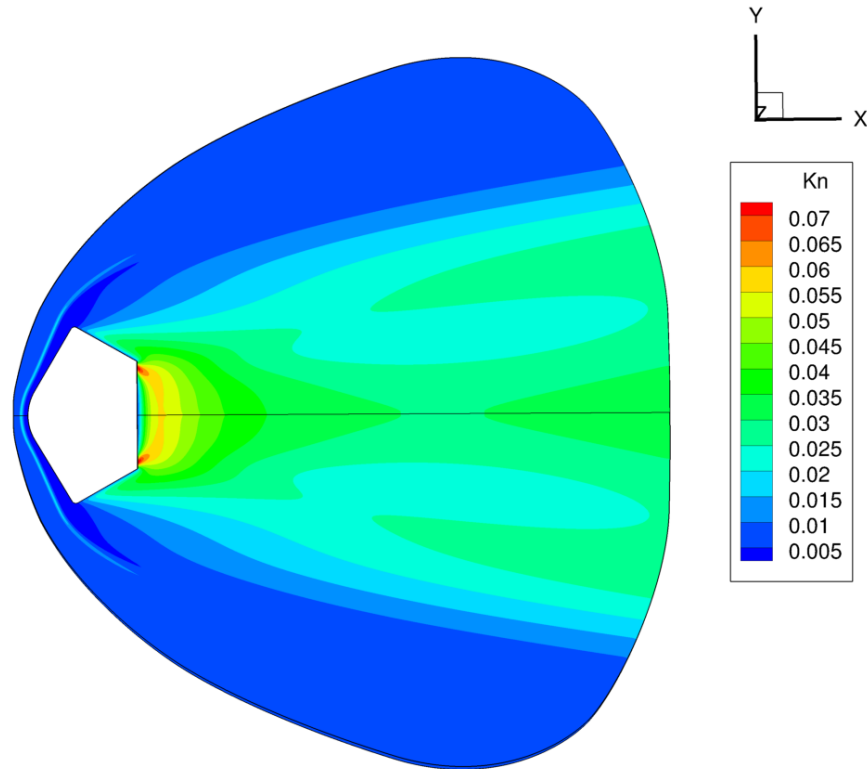


Figure 4.14: Kn number

decreased. However, not too much difference is observed for the other species.

Simulation of 11-species Air over Stardust Capsule

The 11-species air model contains ions and electron, more reactions, and more energy source modes. It is assumed more accurate in the simulation of real air for high temperatures. The simulation in this section is performed on the same 201×331 grid.

The solution contours are compared to those using 5-species air model in Fig. 4.17. The two temperatures are higher using the 5-species air model and a larger value of shock layer thickness is found.

The two temperatures along the stagnation line are extracted and compared against those from 5-species model in Fig. 4.18. It can be seen that 11-species model

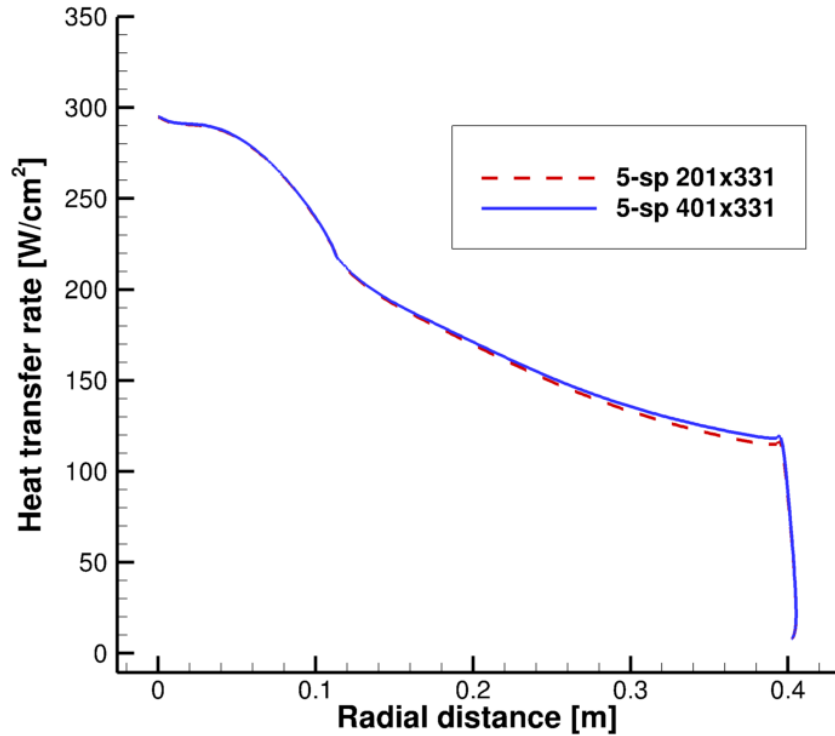


Figure 4.15: Mesh refinement study

predicts a lower values for both temperatures. This model also yields a thinner shock layer. It is mainly because ionizations are accounted and it consumes more energy, therefore, reducing the temperatures. Figure. 4.19 shows the species mass fraction along the stagnation line. Each of the O_2 , N_2 , NO , N , and O species has a similar behavior to that shown in Fig. 4.16 for the 5-species model. However, the presence of ionized species affects the flow field. N^+ and O^+ are observed with a large mass fraction after the shock and is more dominant in the boundary layer. N_2^+ , NO^+ , and O_2^+ are mainly formed after the shock. Their mass fractions are reduced in the boundary layer. Again, it is due to the cold-wall boundary.

The heat transfer rate calculated using the 11-species air model is compared to that calculated using the 5-species air model shown in Fig. 4.20. In Fig. 4.20, at the

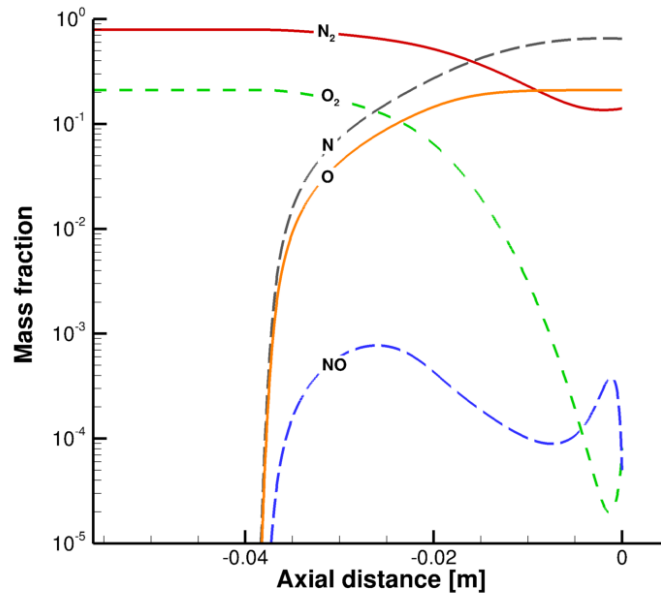
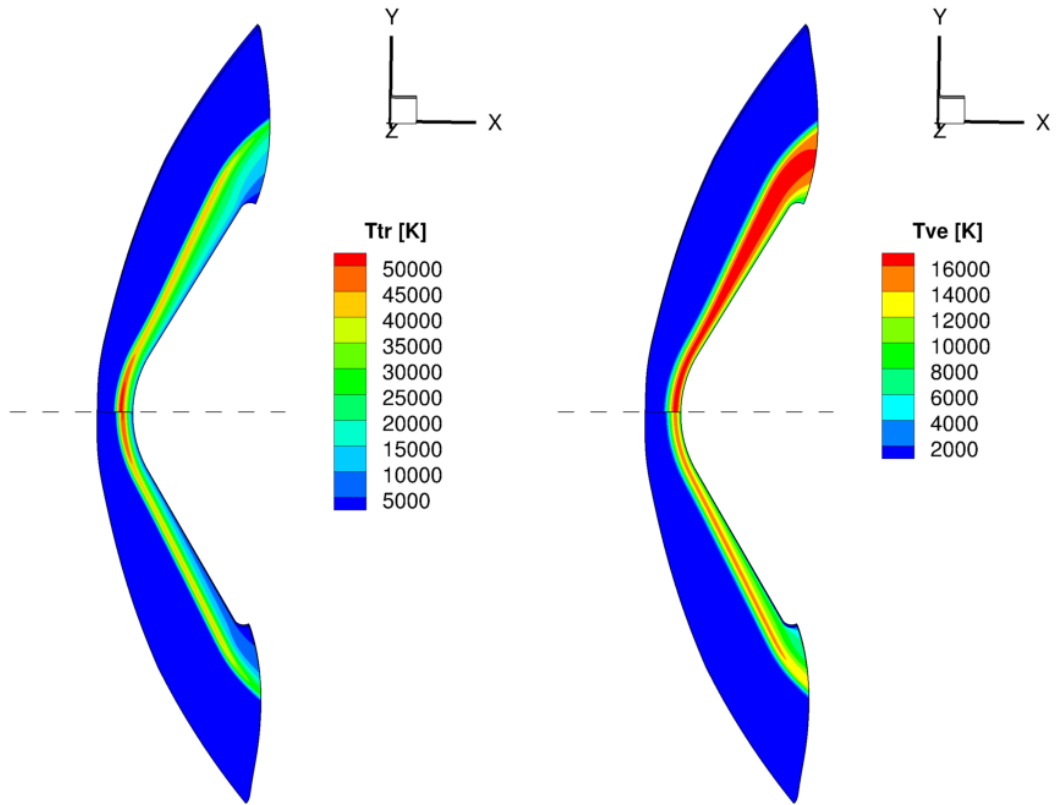


Figure 4.16: Mass fraction for 5-species air model

nose, the 11-species air model yields a lower value of heat transfer rate than using 5-species air model. Apart from the nose region, however, the 11-species air model yields a higher values of heat transfer rate. It is explained as that the high-temperature level at the nose region triggers ionizations, thus more energies are consumed. But once the gas is moving away from the nose, ionization reacts backward due to low-temperature level, thus generates energy. The resulting heat transfer to the surface increases.

4.4 Numerical Investigation of Low-Density Nozzle Flow of Nitrogen

Hypersonic flow solvers are usually developed for external flow and there is no guarantee that they could be used to solve internal flows. For instance, a convergent-divergent nozzle involves flow velocity ranging from subsonic to supersonic/hypersonic and has density near the rarefied regime. This test case investigates the capability of the KATS to do so. Using the reference problem [1], the solution is compared against



(a) Translational-rotational temperature (b) Vibrational-electron-electronic temperature

Figure 4.17: Solution contour comparisons. The upper is 5sp model, and the lower is 11sp model

other CFD result as well as DSMC and experiment results. The nozzle geometry is shown in Fig. 4.21, the configuration is listed in Table 4.5, and the free stream conditions are shown in Table 4.6.

For this type of simulation, if the initial ambient condition is taken as the same as that of inlet boundary condition, the solution may fail to converge. The same issue was found in other hypersonic codes [99]. The main difficulty comes from the initial conditions that cause insufficient pressure gradient at the throat. If the transient numerical solution is wrong, it will not converge to a solution (Fig. 4.22). A remedy for this is to initialize the whole domain into two separated zones (Fig. 4.23). Zone

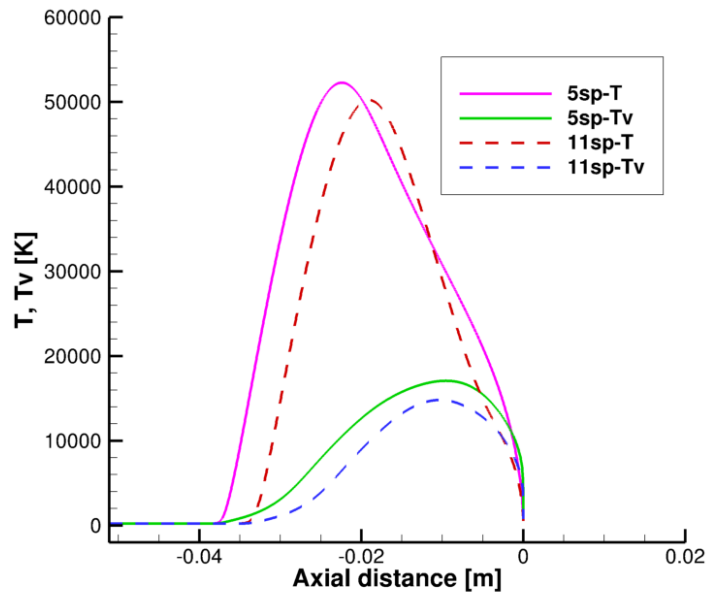


Figure 4.18: Temperatures along stagnations

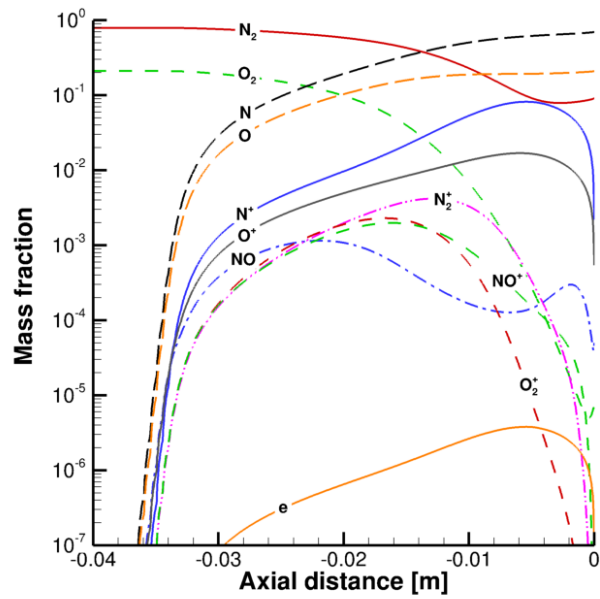


Figure 4.19: Mass fraction for 11-species air model

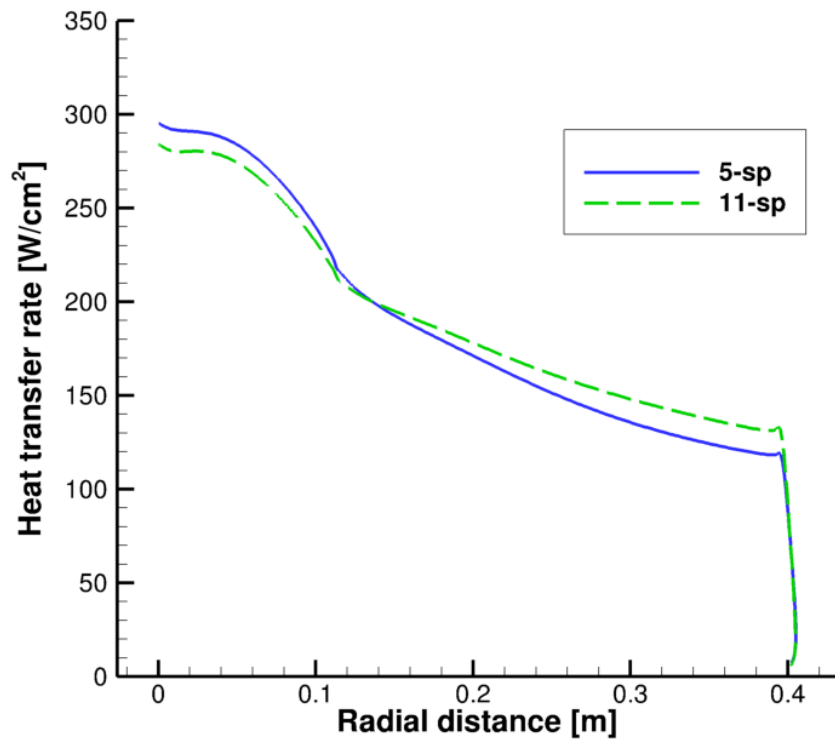


Figure 4.20: Heat transfer rate comparisons

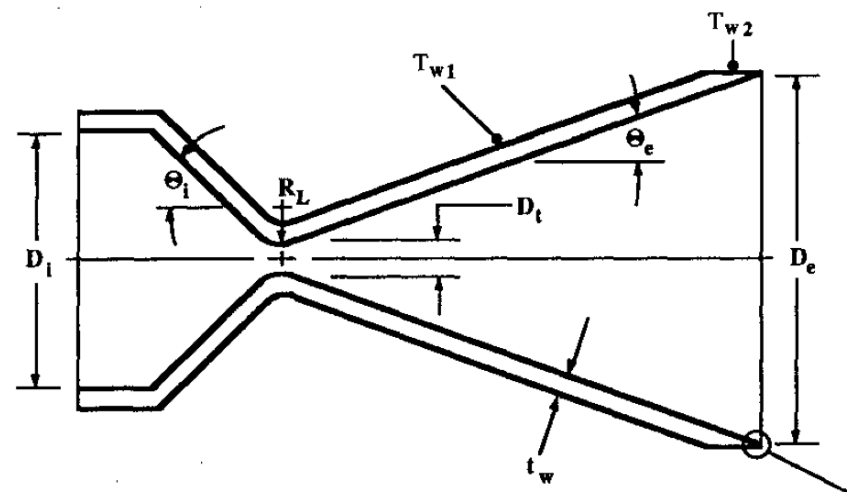


Figure 4.21: Nozzle geometry [1]

Table 4.5: Nozzle geometry

Inlet diameter D_i	22.1 mm
Throat diameter D_t	3.18 mm
Exit diameter D_e	31.8 mm
Longitudinal radius R_L	3.18 mm
Wall thickness t_w	1.65 mm
Lip thickness t_l	0.25 mm
Inlet half-angle θ_i	45 deg
Exit half-angle θ_e	20 deg
Area ration $(D_e/D_t)^2$	100

Table 4.6: Nozzle flow condition for the experimental configurations

Total pressure P_o	6400 Pa
Total temperature T_o	699 K
Mass flow rate \dot{m}	6.8×10^{-5} kg/s
Reynolds number Re^a	850
Wall temperature T_{w1}	551 K
Wall temperature T_{w2}	539 K

$Re^a = 4\dot{m}/\mu_o D_t$, where μ_o is the gas viscosity at T_o .

1 includes the region from the inlet down to the point a little downstream of the throat, and zone 2 the remaining region. Zone 1 can still be specified with the inlet boundary conditions while for zone 2, a factor 1×10^{-4} is multiplied to both pressure and density, while the temperature remains unchanged.

Numerical Investigation

The numerical simulation involves four boundaries: inlet, outlet, symmetry, and wall. Physical parameters were computed from the given testing conditions in Table 2 then used to feed inlet and wall boundary conditions. The outlet and symmetry properties are set as zero gradient, and zero normal velocity respectively.

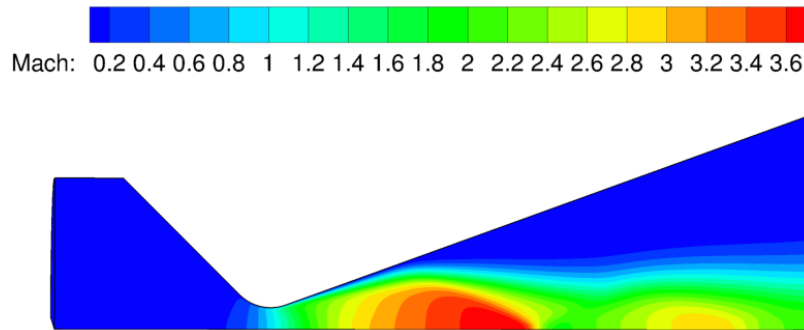


Figure 4.22: An incorrect solution unable to converge due to uniform initialization

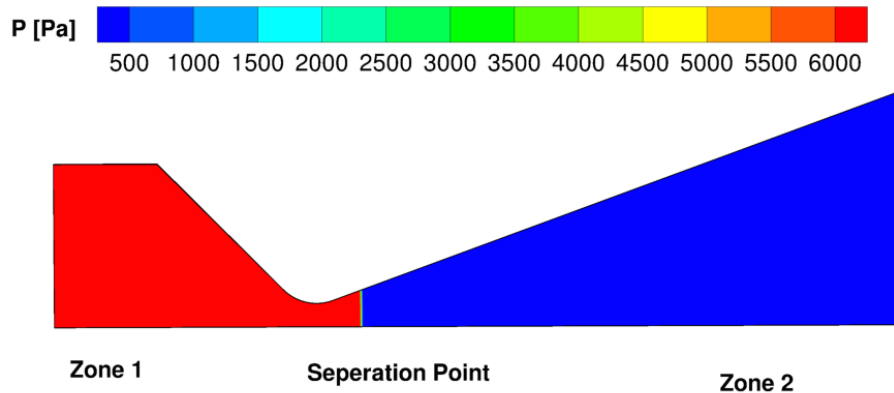


Figure 4.23: Initialization configuration for pressure

Incoming Flow Properties

Free stream properties are required to be given completely at the inlet in hypersonic simulation. Free stream velocity, static pressure and density can be computed using isentropic relations.

Isentropic flow implies reversible and adiabatic processes, which results stagnation conditions T_o , p_o and ρ_o being constant at every point across the flow field. In the current work, a real flow is involved, which is not isentropic due to viscous effect and heat transfer. To take advantage of the isentropic relations, an imaginary isentropic ex-

periment can be conducted – the flow goes through a whole new convergent-divergent nozzle isentropically. The gas expands from subsonic to supersonic speeds. Exactly at the “throat”, the sonic point occurs. Physical properties at the sonic point can be used to calculate the inlet velocity. To achieve this, the throat area has to be computed. Recall the mass flow rate is given from the reference problem, then it can be written as [100]

$$\dot{m} = \rho^* a A^* = \rho^* \sqrt{\gamma R T^*} A^* \quad , \quad (4.2)$$

where

$$\rho^* = \rho_o \left(\frac{2}{\gamma + 1} \right)^{\frac{1}{\gamma - 1}} \quad , \quad (4.3)$$

and

$$T^* = T_o \left(\frac{2}{\gamma + 1} \right) \quad . \quad (4.4)$$

In this work, associated constants γ and R for Nitrogen are assumed as 1.4 and 296.943 J/kg respectively. It can be found that A^* is not the same as the real throat area πr_t^2 in the experiments.

Substitution A^* into *area Mach number relation*,

$$\left(\frac{A}{A^*} \right)^2 = \frac{1}{M^2} \left[\frac{2}{\gamma + 1} \left(1 + \frac{\gamma - 1}{2} M^2 \right) \right]^{\frac{\gamma + 1}{\gamma - 1}} \quad (4.5)$$

will yield the inlet Mach number M , which can be solved using trial and error method or iteration method. With the Mach number, the inlet static temperature and density are determined by

$$T = T_o \left(1 + \frac{\gamma - 1}{2} M^2 \right)^{-1} \quad , \quad (4.6)$$

and

$$\rho = \rho_o \left(1 + \frac{\gamma - 1}{2} M^2 \right)^{-\frac{1}{\gamma - 1}} \quad . \quad (4.7)$$

Finally the inlet velocity is given by

$$u = Ma = M \sqrt{\gamma R T} \quad . \quad (4.8)$$

This completes the determination of all parameters required at the inlet.

Wall Properties

It is only necessary to specify the temperature at the wall. The no-slip wall boundary condition forces wall velocity to zero, and the density and pressure are extrapolated for the boundary ghost cell.

It is examined that either of the given temperatures from the reference problem (Table 4.6) is the input wall temperature. This temperature, however, is determined from Fig. 4.32 to make comparisons against the reference data. On this plot, T/T_o is 0.835 at the wall, which indicates the specified value was 583.7 K.

Mesh Configuration

Fig. 4.24 shows the details of grid line dimensions. Mesh clusters at the throat, wall and at the outlet.

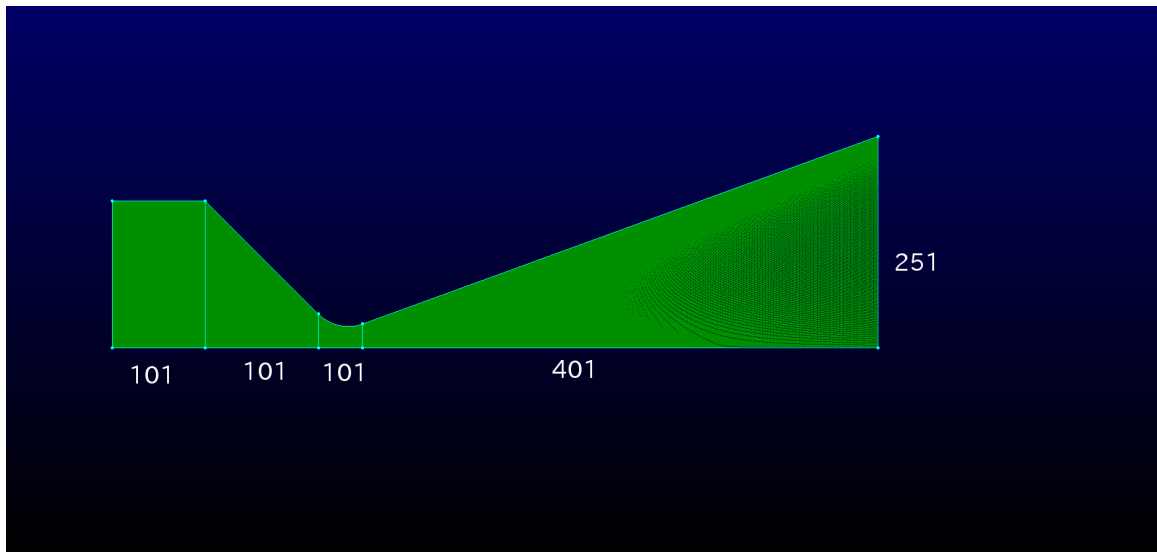


Figure 4.24: Sketch of mesh in 2-D

Results and Discussion

Iso-contours

Iso-contours of flow properties are shown in Fig. 4.25 to Fig. 4.29 . A much higher level of pressure and density can be noticed at the converging section, and both of them decrease along the streamwise direction. T_{tr} and T_{ve} have different contour patterns since the flow in this nozzle is in thermal non-equilibrium, and T_{ve} lags behind of T_{tr} . The flow accelerates out of the nozzle through the converging section which is shown from the Mach number contour. Downstream of the physical throat, but quite close to it, a Mach 1 line is shown, which indicates the actual throat location.

The nozzle flow lies in variant flow regimes, which are characterized by different Kn numbers. Mean free path is calculated according to Eqn. (4.1). The Kn number is then evaluated based on this mean free path and the nozzle outlet diameter D_e (Table 4.6) as the characteristic length. The Kn number contours are shown in Fig. 4.30, in which a large value of Kn number is found at the outlet and the maximum value occurs in the corner close to the wall boundary. The order of the magnitude of the Kn number indicates that the flow is in rarefied regime, and the possible breakdown of the continuum in the boundary layer. Therefore, CFD may fail to capture the flow behaviors in this region.

Properties Profile at Exit

The velocity in Fig. 4.31 is normalized by the thermal speed U_o in equilibrium and the radial distance R is normalized by the nozzle exit diameter D_e . U_o is defined by

$$U_o = \sqrt{2RT_o} \quad , \quad (4.9)$$

When compared to another CFD solution [1], small discrepancy is found. KATS predicts a relative lower value of velocity magnitude than the reference CFD data. The mass flow rate, however, is conserved in this work. The mass flow rates at

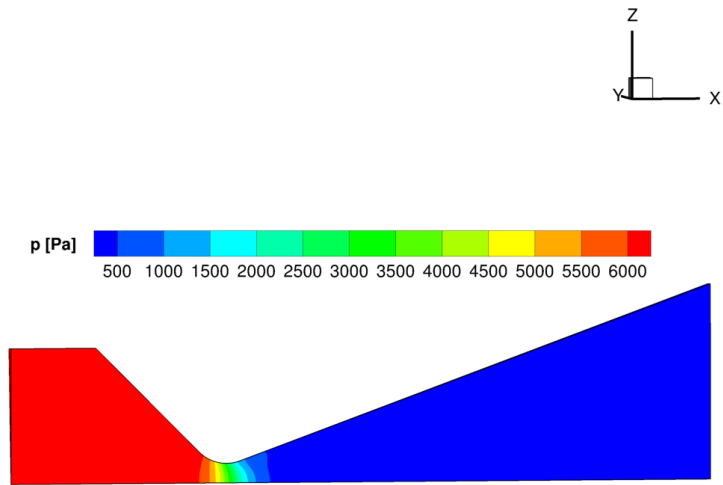


Figure 4.25: Pressure iso-contour for the convergent-divergent nozzle flow

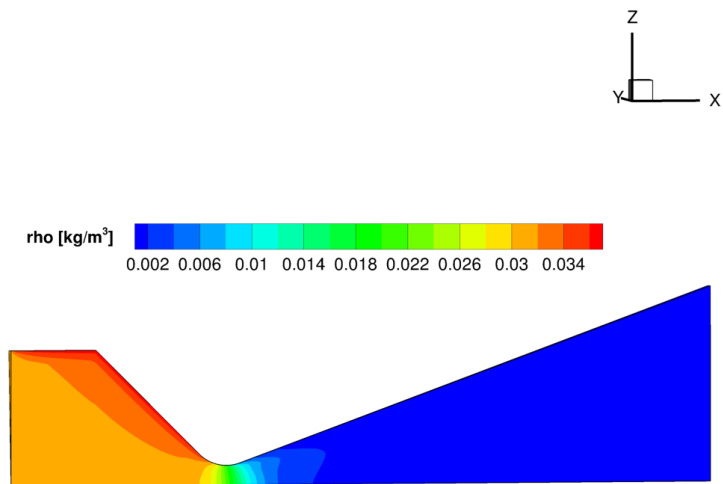


Figure 4.26: Density iso-contour for the convergent-divergent nozzle flow

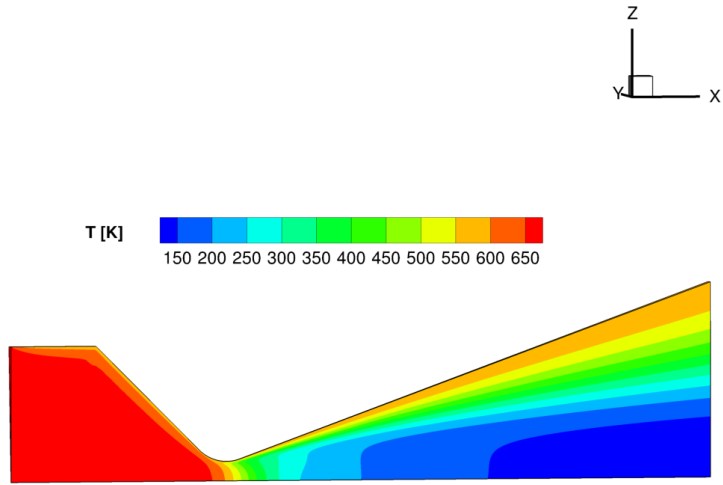


Figure 4.27: T_{tr} iso-contour for the convergent-divergent nozzle flow

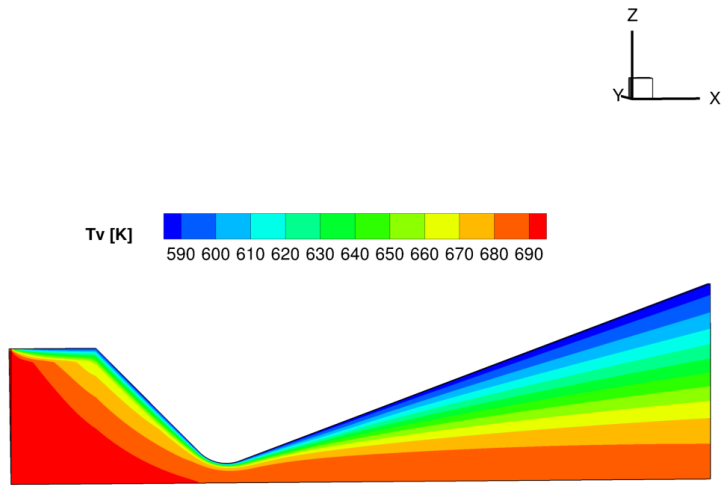


Figure 4.28: T_{ve} iso-contour for the convergent-divergent nozzle flow

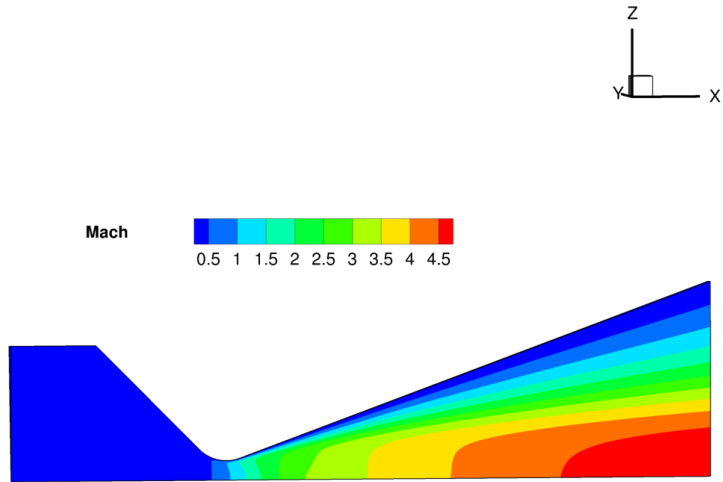


Figure 4.29: Mach iso-contour for the convergent-divergent nozzle flow

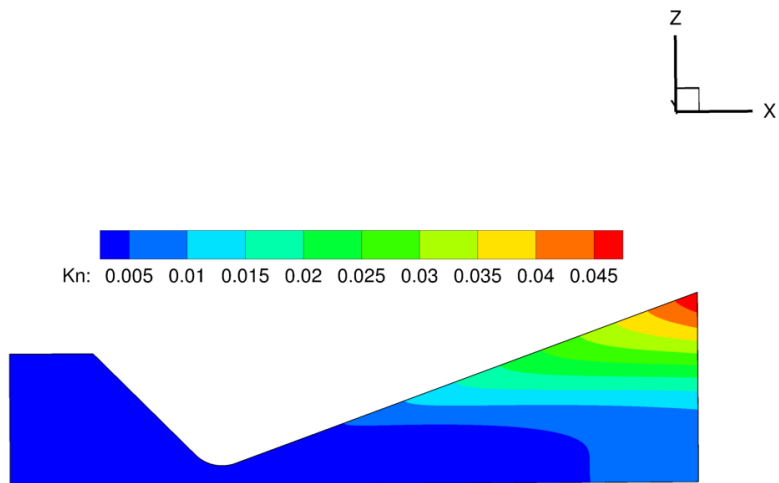


Figure 4.30: Kn iso-contour for the convergent-divergent nozzle flow

the inlet and the outlet only differ by a relative error of 0.39%. A more significant difference of velocity profile, however, occurs when compared to the DSMC result. It is to be noted that the DSMC solution is believed to be more accurate, which shows the velocity at the nozzle wall is nonzero. It also predicts a higher velocity than the CFD solution. The significant discrepancy indicates that the slip effect in rarefied flows has important effects on the boundary layer. The no-slip boundary conditions normally employed for continuum CFD code are not sufficient to capture this phenomenon. Instead, a slip wall boundary account for the rarefied effects must be used [1].

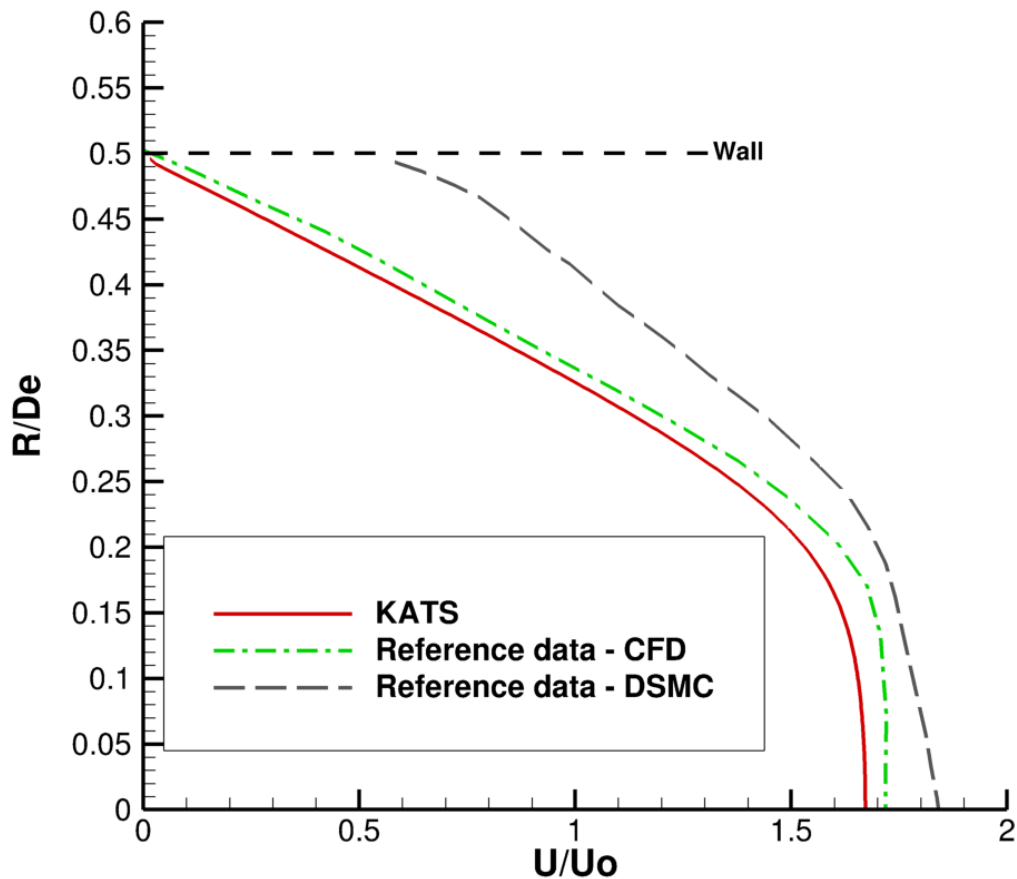


Figure 4.31: U/U_0 results from KATS compared to Ref. [1]

Fig. 4.32 shows the translational-rotational temperature T_{tr} and the vibrational-electronic-electron temperature T_{ve} from KATS normalized using the stagnation temperature T_o and compared against the reference data. It is noted that the reference CFD temperature is predicted using thermal equilibrium. However, it agrees well with T_{tr} from KATS. But these two continuum temperatures are very different than the DSMC results, over-predicting the values.

The two DSMC temperatures indicate a small degree of thermal nonequilibrium between translational and rotational energy modes. But the two CFD temperatures from KATS shows strong nonequilibrium between translational-rotational mode and the vibrational-electronic-electron mode. It has been shown that the over-prediction of temperatures is due to the inability of the continuum approach to capture thermal-nonequilibrium effects and due to the use of no-slip nozzle wall boundary for the rarefied flow [1].

The experimental pressure can be compared using reference [1]. The experiment used a Pitot tube to measure the local total pressure. The outlet axial static pressure from the numerical solution (Fig. 4.33) is not Pitot pressure and has to be converted. However, this conversion is not straightforward. Flow at the exit goes from subsonic close to the wall to supersonic and rarefied at the centerline (Fig. 4.33). A Pitot tube in a supersonic stream forms a bow shock. The measured value by the Pitot tube has to be recovered from the static pressure in the numerical simulation using normal shock relations. The Pitot pressure in the subsonic region is thus given by

$$p_o = p \left(1 + \frac{\gamma - 1}{2} M^2 \right)^{\frac{\gamma}{\gamma - 1}} , \quad (4.10)$$

while if the flow region is supersonic, the Mach number behind the normal shock wave is always subsonic,

$$M_2^2 = \frac{1 + [(\gamma - 1)/2]M_1^2}{\gamma M_1^2 - (\gamma - 1)/2} , \quad (4.11)$$

and static pressure behind the shock indicates

$$p_2 = p_1 \left[1 + \frac{2\gamma}{\gamma + 1} (M_1^2 - 1) \right] . \quad (4.12)$$

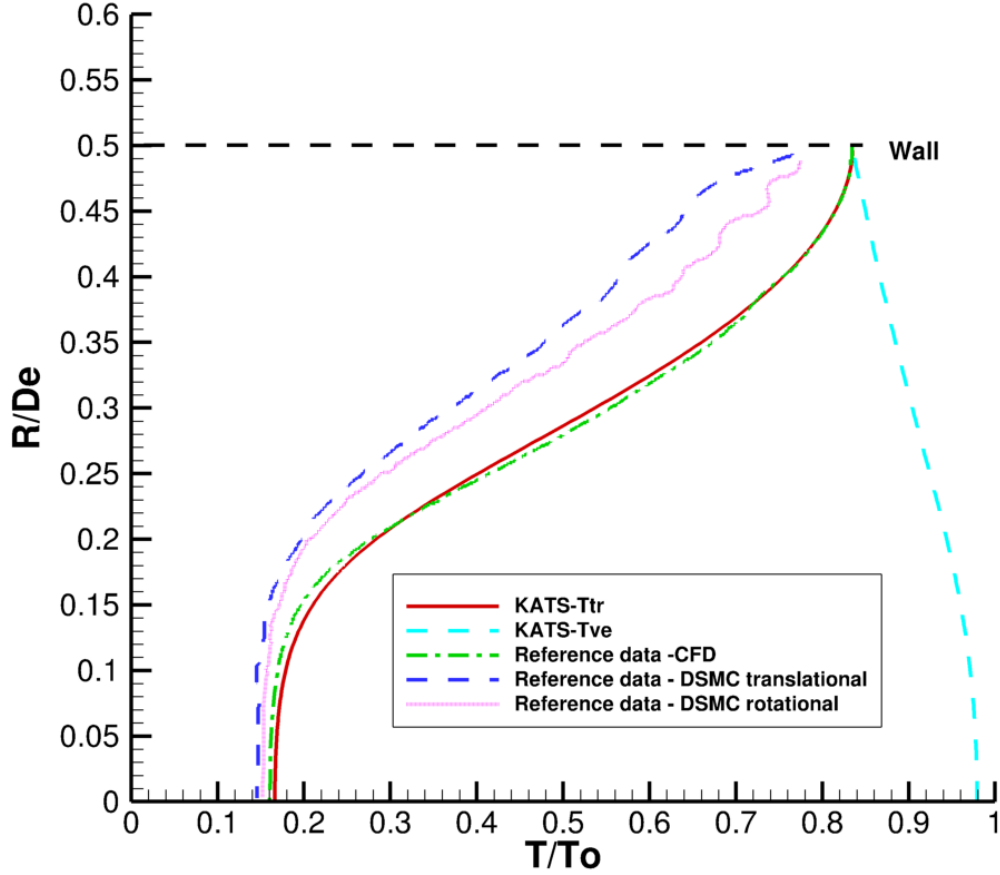


Figure 4.32: T/T_o results from KATS compared to Ref. [1]

The Pitot pressure and Mach number immediately behind the shock are related by

$$p_{o2} = p_2 \left(1 + \frac{\gamma - 1}{2} M_2^2 \right)^{\frac{\gamma}{\gamma - 1}} \quad . \quad (4.13)$$

One can also get *Rayleigh Pitot tube formula* combining the above equations.

After some manipulation, it implies

$$p_{o2} = \frac{p_{o2}}{p_2} \frac{p_2}{p_1} p_1 = p_1 \left(\frac{(\gamma + 1)^2 M_1^2}{4\gamma M_1^2 - 2(\gamma - 1)} \right)^{\frac{\gamma}{\gamma - 1}} \frac{1 - \gamma + 2\gamma M_1^2}{\gamma + 1} \quad . \quad (4.14)$$

To account for rarefaction effects, the ideal pressure p_{o2} is corrected by

$$p_{om} = \frac{10^{0.089}}{\text{Re}^{0.12}} p_{o2} \quad , \quad \text{for } \text{Re} \leq 5.6 \quad , \quad (4.15)$$

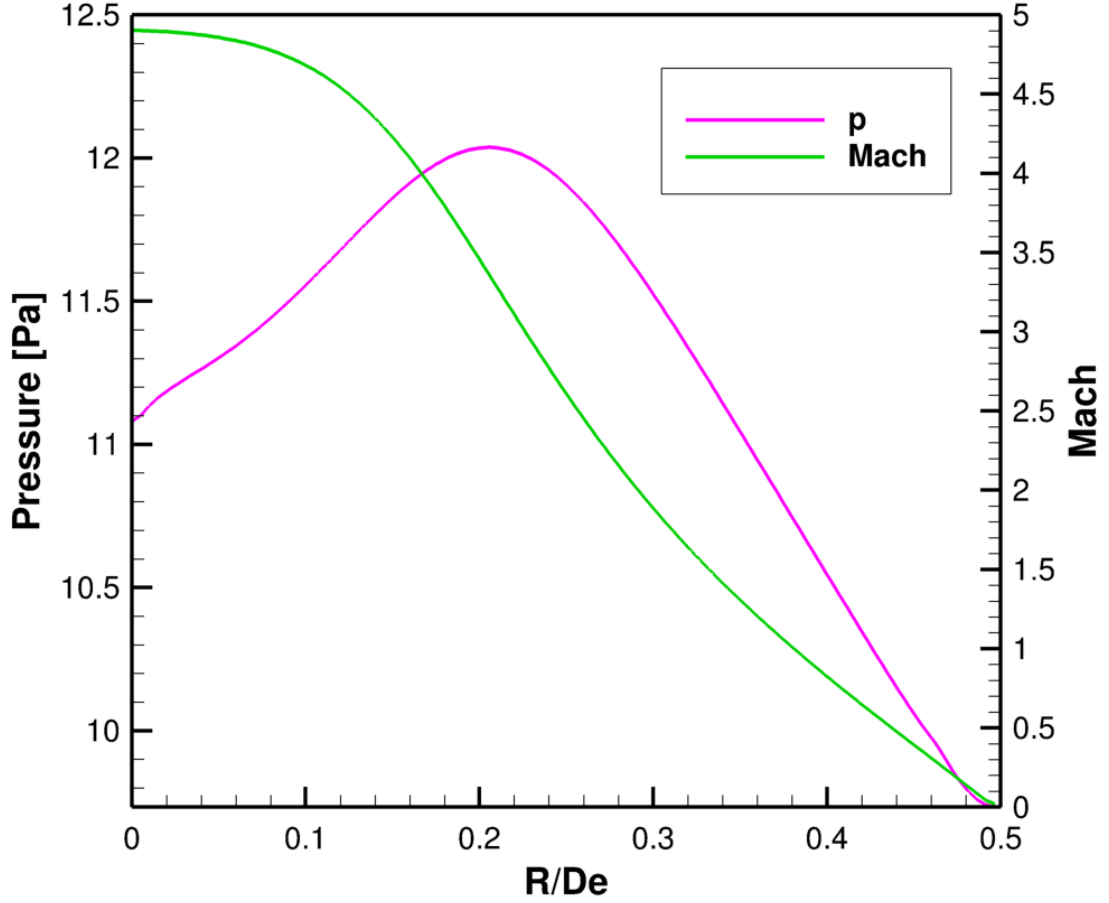


Figure 4.33: Static pressure and Mach number results from KATs at the exit

where the probe Reynolds number is defined by

$$\text{Re} = \frac{\rho_{\infty} U_{\infty} D}{\mu} \quad . \quad (4.16)$$

The diameter of the Pitot tube on the experimental apparatus is 1 mm. Since the reference values of $\rho_{\infty} U_{\infty}$ from the DSMC results are unknown, an estimated value 0.065 is used for the following computation. The resulting Re is shown in Fig. 4.34. In addition, the viscosity μ has to be calculated. The static temperature T_2 behind the shock is first computed by relating the static pressure in front of the shock.

$$T_2 = T_1 \left[1 + \frac{2\gamma}{\gamma + 1} (M_1^2 - 1) \right] \left[\frac{2 + (\gamma - 1)M_1^2}{(\gamma + 1)M_1^2} \right] \quad . \quad (4.17)$$

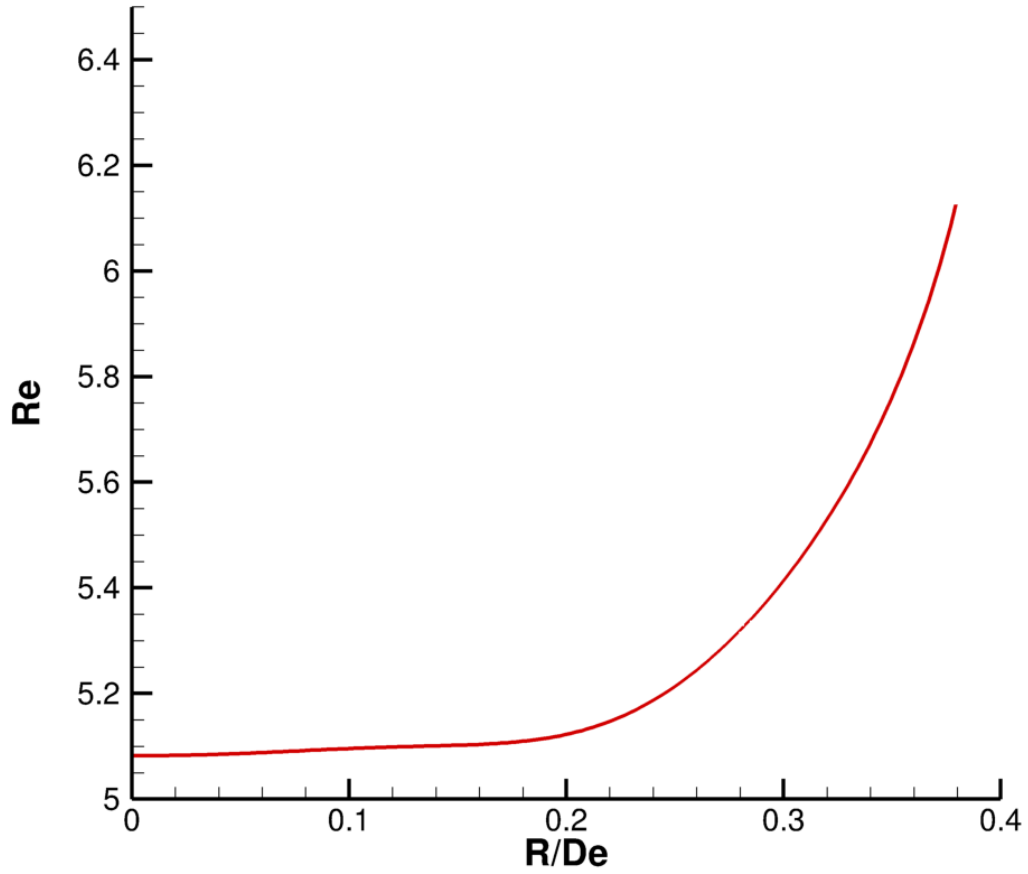


Figure 4.34: Reynolds number from KATS at the exit for Mach>1

It should be noted that in this simulation Sutherland power-law for the viscosity of gas is taken from the reference to match the condition for comparisons, which is given by

$$\mu = \mu_{ref} \left(\frac{T}{T_{ref}} \right)^\omega, \quad (4.18)$$

where μ_{ref} , the viscosity of N_2 , is taken as $2.58 \times 10^{-5} \text{ N} \cdot \text{s/m}^2$ at the reference temperature T_{ref} of 500 K, and ω is 0.75. Comparisons of the Pitot pressure are shown in Fig. 4.35. The two CFD solutions agree well with each other, but difference appears when compared to the experimental data. CFD solutions over-predict the

Pitot pressure in the center flow, and under-predict in the boundary layer.

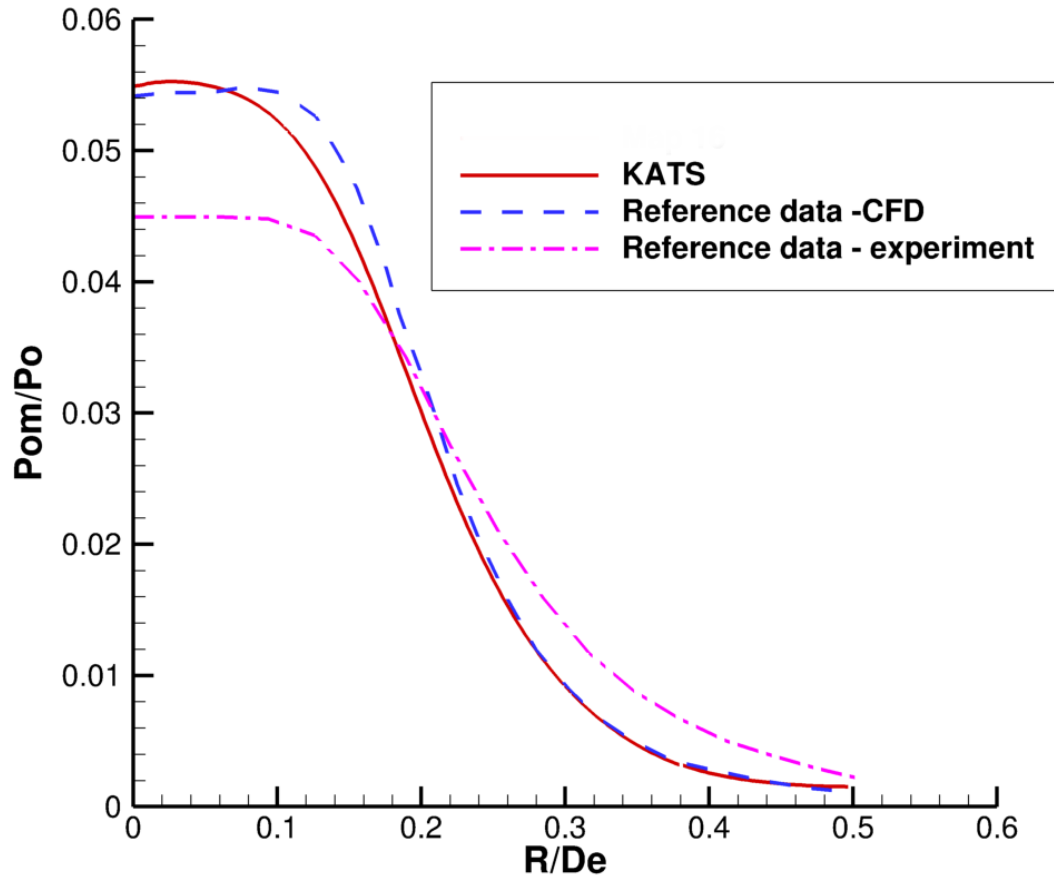


Figure 4.35: Normalized Pitot pressure from KATS compared to Ref. [1]

Conclusion

In this section, investigation of KATS flow solver on a hypersonic nozzle is performed. Associated numerical solutions are found in good agreement with other CFD results. However, comparisons against DSMC and experiments indicates some significant discrepancies, which are mainly due to the failure of the traditional continuum fluid dynamics solver when used for rarefied gas, where the DSMC technique can give a better solution. Also, the low-density, slip effects along the nozzle wall can not be

captured using the traditional no-slip wall boundary conditions in CFD and makes the comparison difficult.

Chapter 5 Subsonic Solver: Verification and Validation

5.1 Preconditioning and Low Mach Number Flow

In this section, the CFD code is extended so that it can model low-speed flow. This is mainly accomplished by switching the convective fluxes to the AUSM scheme family, and using preconditioning techniques. Specifically, a novel preconditioning method is addressed: the Weiss-Smith preconditioner is modified for greater robustness and extended to account for multi-species problems.

Computational Fluid Dynamic (CFD) schemes can be broken into two families: pressure-based and density-based methods [82]. They were originally formulated to deal with flows mainly for variant Mach numbers. Pressure-based methods were developed for incompressible and low Reynolds number flow while density-based methods have been mainly used for compressible flow in context of high Mach number condition. To avoid being limited in their traditional domains, the extension of their application into wider regimes has been a topic of great effort for decades. Traditional density-based physical time-marching algorithms have been used successfully for compressible flow simulations, and are widely used in the computation of transonic, supersonic and hypersonic flows. However, they encounter difficulty in simulating compressible flow with very low Mach number ($\text{Mach} \ll 0.3$). In the incompressible region, since density is constant, pressure cannot be updated correctly from an equation of state. The velocity and pressure in the momentum governing equations are therefore loosely coupled [101].

Mathematically, time-marching schemes are hyperbolic, therefore, they are more suitable to solve compressible flows. However, the incompressible system does not

behave hyperbolicly. Moreover, the system of equations becomes very stiff since the propagation of the acoustic wave is significantly greater than the particle convective speed. A degraded convergence rate is found and the traditional density-based time-marching method becomes insufficient.

Preconditioning techniques have been well developed to solve these issues since the 1970s [102–104]. It is able to overcome the difficulty of disparity among eigenvalues, and the equations are thus strongly coupled. Preconditioning is accomplished by altering the time-derivatives through the multiplication of a preconditioning matrix, in such a way that an artificial pressure time derivative is introduced, and the eigenvalues are modified in the same order. Preconditioning does not only rescale the eigenvalues of the system, thus eliminating the stiffness and gaining better convergence; it also improves the solution accuracy. Weiss and Smith [105] presented a time derivative preconditioning of the Navier–Stokes equations, and it has widely been accepted as a solution for the finite volume discretization and time-marching schemes. The preconditioner does not influence the accuracy of the steady-state solution, however it removes the physical time accuracy. Choi and Merkle [106] added the pseudo-time derivatives to the original physical time derivatives to be able to solve unsteady flow with physical time accuracy. This procedure carries out an inner loop and marches to a “steady state” at a given physical time level.

The objective of the present work is to develop a new preconditioning system which can expand existing time marching solvers to allow calculations for low-speed reacting flow, and effective application over a wide range of flow Mach numbers and physical time scales. The first modification of Weiss-Smith preconditioner involves the evaluation of pressure differences of the current cell and its neighboring cells. The following modification is therefore an extension of the Weiss-Smith preconditioner for multi-species.

The Jacobian of conservative variables to primitive variables is given by

$$\mathcal{J} = \begin{pmatrix} \frac{d\rho_1}{dp_1} & \frac{d\rho_1}{dp_2} & \cdots & \frac{d\rho_1}{dp_{n_s}} & \frac{d\rho_1}{du} & \frac{d\rho_1}{dv} & \frac{d\rho_1}{dw} & \frac{d\rho_1}{dT} \\ \frac{d\rho_2}{dp_1} & \frac{d\rho_2}{dp_2} & \cdots & \frac{d\rho_2}{dp_{n_s}} & \frac{d\rho_2}{du} & \frac{d\rho_2}{dv} & \frac{d\rho_2}{dw} & \frac{d\rho_2}{dT} \\ \cdots & \cdots & \cdots & \cdots & \cdots & \cdots & \cdots & \cdots \\ \frac{d\rho_{n_s}}{dp_1} & \frac{d\rho_{n_s}}{dp_2} & \cdots & \frac{d\rho_{n_s}}{dp_{n_s}} & \frac{d\rho_{n_s}}{du} & \frac{d\rho_{n_s}}{dv} & \frac{d\rho_{n_s}}{dw} & \frac{d\rho_{n_s}}{dT} \\ \frac{d\rho u}{dp_1} & \frac{d\rho u}{dp_2} & \cdots & \frac{d\rho u}{dp_{n_s}} & \frac{d\rho u}{du} & \frac{d\rho u}{dv} & \frac{d\rho u}{dw} & \frac{d\rho u}{dT} \\ \frac{d\rho v}{dp_1} & \frac{d\rho v}{dp_2} & \cdots & \frac{d\rho v}{dp_{n_s}} & \frac{d\rho v}{du} & \frac{d\rho v}{dv} & \frac{d\rho v}{dw} & \frac{d\rho v}{dT} \\ \frac{d\rho w}{dp_1} & \frac{d\rho w}{dp_2} & \cdots & \frac{d\rho w}{dp_{n_s}} & \frac{d\rho w}{du} & \frac{d\rho w}{dv} & \frac{d\rho w}{dw} & \frac{d\rho w}{dT} \\ \frac{d\rho E}{dp_1} & \frac{d\rho E}{dp_2} & \cdots & \frac{d\rho E}{dp_{n_s}} & \frac{d\rho E}{du} & \frac{d\rho E}{dv} & \frac{d\rho E}{dw} & \frac{d\rho E}{dT} \end{pmatrix}.$$

For low Mach number flow, the Jacobian matrix is preconditioned by replacing the term $\frac{d\rho_i}{dp_i}$ by Θ_i , while the other terms remain the same.

According to the Weiss-Smith preconditioner, a reference velocity for an incompressible flow is given by

$$U_r = \max(|u|, \epsilon a) \quad , \quad (5.1)$$

where a small number ϵa is used as the limit to avoid singularities in Eqn. (5.4) at the stagnation point. a is the speed of sound, and the small number ϵ is set to 1×10^{-5} .

For viscous flow, a further modification is added by introducing the dynamic viscosity μ_i and density ρ_i for each species

$$U_{r,i} = \max\left(U_r, \frac{\mu_i}{\rho_i \Delta x}\right) \quad (5.2)$$

For some cases, where the Mach number approaches zero close to a stagnation point, the preconditioning system lacks robustness. Darmofal and Siu [107] suggested modifying U_r locally by adding the evaluation of pressure difference.

$$U_{r,i} = \max\left(U_{r,i}, \epsilon \sqrt{\frac{|\Delta p_i|}{\rho_i}}\right) \quad , \quad (5.3)$$

where $|\Delta p_i|$ is the maximum of pressure difference between the current cell and all of its neighbors.

The term, Θ_i , is given by

$$\Theta_i = \left(\frac{1}{U_{r,i}^2} - \frac{d\rho_i/dT}{\rho_i c_{p,i}} \right) . \quad (5.4)$$

5.2 Free Flow Test Case

N₂ flow through a Pipe

In order to validate the preconditioned flow dynamics solver, a first test case is presented, based on the experimental setup. A pure N₂ flow going through a 22 mm diameter pipe is simulated. The free stream conditions are: $T = 898$ K, $V_{ave} = 0.379$ m/s, and $p = 12801$ Pa. The associated Mach number is 6.29×10^{-4} , and the Reynolds number is 21.31 based on the average velocity V_{ave} as the velocity scale and the pipe diameter as the length scale. The condition indicates that the flow is incompressible and laminar.

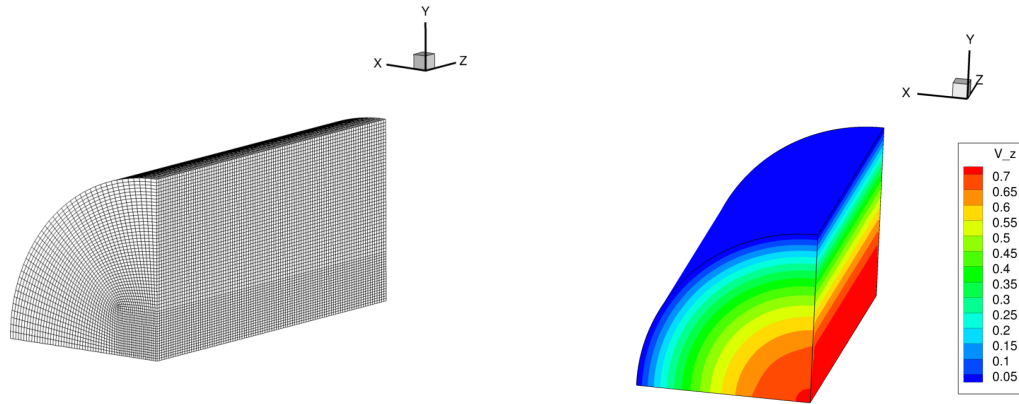
The computational grid and velocity iso-contours are shown in Fig. 5.1 (a) and (b) respectively. When the flow is fully developed, the outlet velocity shows the expected laminar pipe-flow profile. The outlet velocity solution along the radius is compared to an analytical solution in Fig. 5.1 (c). The numerical solution is found in good agreement with the analytical solution with maximum relative error 0.4%, where the analytical solution for a pipe flow is given by

$$u(r) = \frac{\Delta p}{4\mu l} (R^2 - r^2) , \quad (5.5)$$

where Δp is the difference of static pressure, μ is the viscosity, and l is the length.

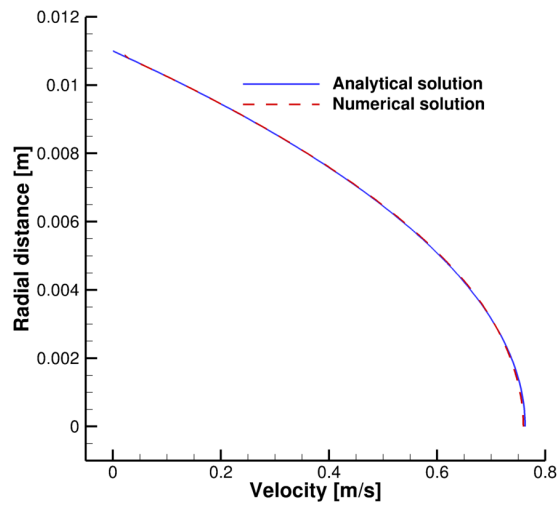
Two N₂ flow through a pipe

To investigate the ability to solve multi-species flow at low Mach number, a specific test case is designed: two N₂ flows with same free stream conditions through a pipe are simulated. The idea behind this design is that the analytical velocity solution in this case can be computed by taking the two N₂ species as one. For this simulation,



(a) Computational grid

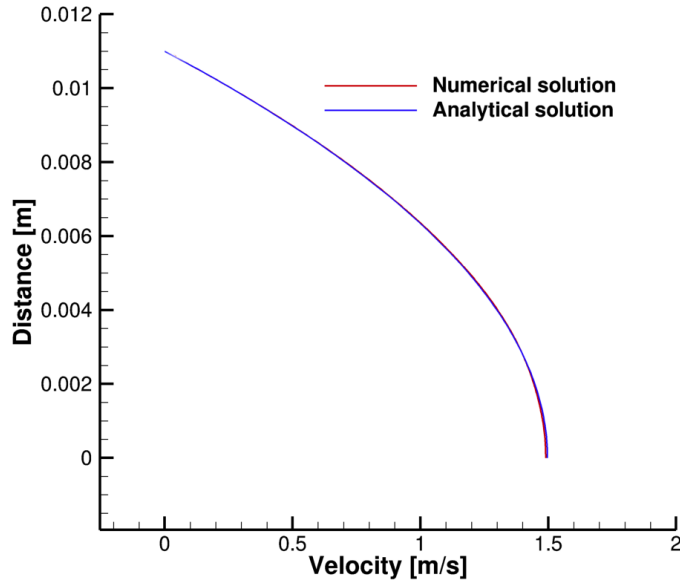
(b) Velocity iso-contour



(c) Centerline velocity

Figure 5.1: N_2 flow through a pipe

the same mesh as the previous case is used. Once converged, the fully developed flow velocity of the pipe is shown and compared to an analytical solution in Fig. 5.2, in which good agreement can be found. The maximum relative error is below 0.3%.



(a) Centerline velocity

Figure 5.2: Two N_2 flow through a pipe

In summary, a preliminary numerical investigation is performed for the development of a multi-species preconditioner. A carefully designed test case of a pipe flow is used to evaluate the performance of this preconditioner. The numerical solution of KATS is found in a good agreement with the analytical solution.

5.3 Lid-driven Cavity Problem

The research on lid-driven cavity problem can date back to the early work of Burggraf [108], and is considered a classical test problem for validation of numerical Navier–Stokes codes, both in laminar flow and turbulence. This problem was numerically investigated using incompressible approach by Ghia [2], who provided a detailed

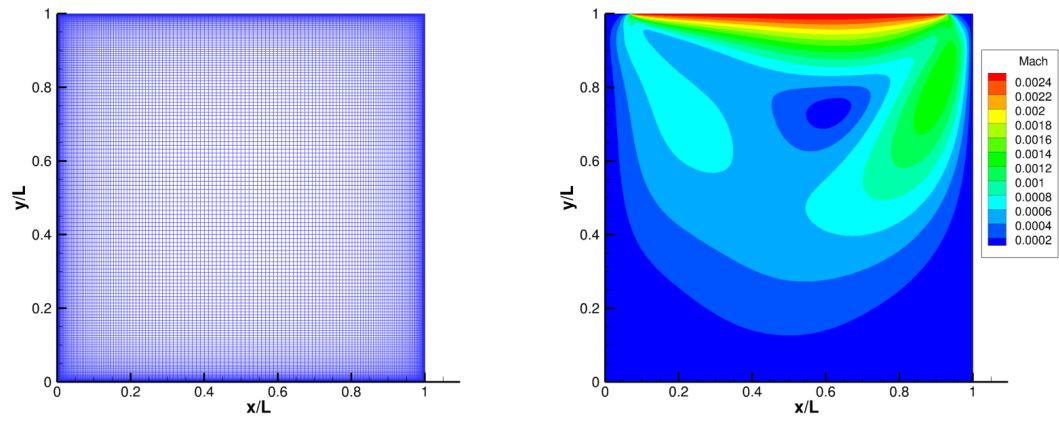
database of different Reynolds numbers. The following test involves a 2-D laminar flow in a square cavity, with the top lid driven by a uniform tangential velocity. The simulation in this work was made under a low Mach number condition. Specifically, the case of $Re = 100$ is considered, where the inlet velocity is used as the velocity scale and the cavity length as the length scale. The preconditioning technique and AUSM⁺-up convective flux scheme are used for the computation.

Numerical setup involves free stream density $\rho = 1 \text{ kg/m}^3$, lid velocity $u = 1 \text{ m/s}$, 2-D cavity length $L = 1 \times 10^{-3} \text{ m}$, viscosity $\mu = 1 \times 10^{-5} \text{ kg/(m} \cdot \text{s)}$ and $T = 300 \text{ K}$. Inlet Mach number is $\sim \mathcal{O}(10^{-3})$, indicating incompressible flow. A grid of dimensions 161×161 is used as shown in Fig. 5.3 (a), where mesh refinement was performed close to the wall boundaries.

It should be mentioned that it is not appropriate to impose a uniform velocity at the inlet considering the inconsistency of velocity boundary condition with a compressible solver. As a remedy, a boundary layer thickness is set to 5% of the length L , and the velocity is linearly scaled from the free flow velocity to zero at the boundary [109]. The Mach number for this test case is low and its contours are shown in Fig. 5.3 (b). The Mach number contours with streamlines are shown in Fig. 5.3 (c), in which the flow pattern reveals a primary vortex in the center zone and two minor ones on the left and right bottom corner.

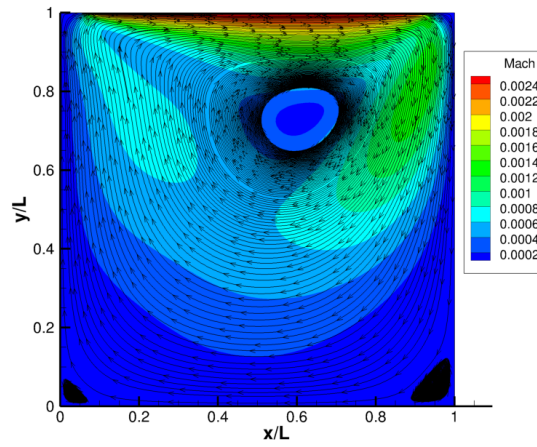
The velocity distribution through the geometric center of the cavity is compared to the reference numerical solution in Fig. 5.4 (a)-(b). The overall profiles agree well with the benchmark results. Only a small discrepancy is observed at the top and bottom peak for velocity v with a maximum relative error 0.1%. The good agreement demonstrates the feasibility and capability of the current compressible flow solver and preconditioning technique to deal with low Mach number viscous flow. More tests, however, are needed for higher Reynolds number and 3D cases.

In summary, by using an all-velocity, low dissipation, convective flux scheme, AUSM⁺-up, together with the preconditioning technique for low-speed flow, the



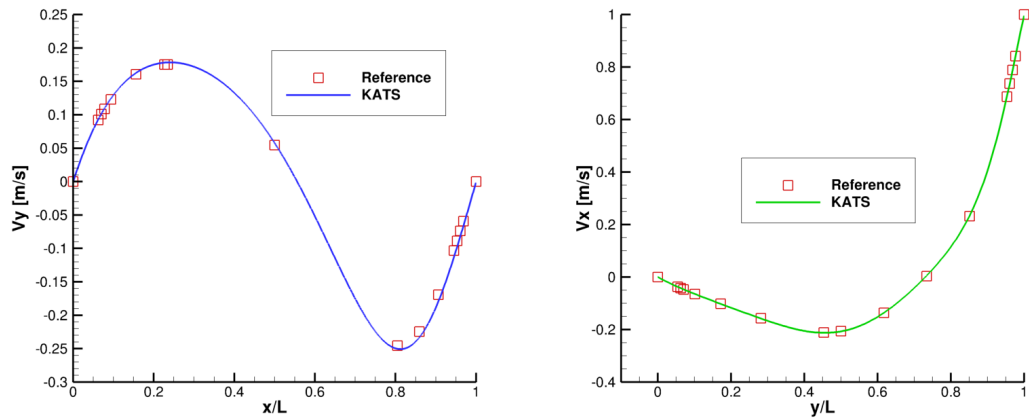
(a) Mesh

(b) Mach number



(c) Streamline

Figure 5.3: Simulation of a lid-driven cavity problem



(a) v -velocity along horizontal line through geometric center of cavity (b) u -velocity along vertical line through geometric center of cavity

Figure 5.4: Numerical solutions of KATS compared to reference numerical solutions [2]

KATS subsonic solver successfully simulates a pipe flow and a laminar lid-driven cavity problem. For the pipe flow case, excellent agreement with the analytical solution is found. A carefully designed numerical test is then conducted, which is able to verify the validity of a new multi-species preconditioner. The result is in good agreement with the analytical solution. In the study of the lid-driven cavity problem, besides the use of preconditioner and AUSM⁺-up scheme, the velocity inlet boundary condition is also modified by setting a boundary layer to make it more compatible with the compressible solver. This allows KATS to yield results in good agreement with the benchmark solution in the Ref. [2].

Chapter 6 Coupling of A Free Flow and A Porous Medium Flow

In this chapter, KATS is used to solve problems which involve both a “free flow” and a porous medium flow. Previous work on coupling combines two independent solvers: one CFD solver and one material response solver, each solving different sets of governing equations. The coupling is performed through a surface flux balance method, which results in boundary condition inconsistency. In the proposed model, a new Darcy–Brinkman equation for a compressible free flow and a porous medium flow is developed. This governing equation must be constructed to be able to solve for the individual region of free flows and porous media flows, and the conjugate free/porous interaction. The set of governing equation system combines mass conservation, the modified Darcy–Brinkman equation for momentum, and energy equation.

Mass Conservation

$$\frac{\partial(\phi\rho)}{\partial t} + \nabla \cdot (\phi\rho\mathbf{v}) = 0 \quad (6.1)$$

or in Cartesian coordinates,

$$\frac{\partial(\phi\rho)}{\partial t} + \frac{\partial(\phi\rho u)}{\partial x} + \frac{\partial(\phi\rho v)}{\partial y} + \frac{\partial(\phi\rho w)}{\partial z} = 0 \quad (6.2)$$

Momentum Balance

$$\frac{\partial(\phi\rho\mathbf{v})}{\partial t} + \nabla \cdot (\phi\rho\mathbf{v}\mathbf{v}^T) = -\nabla p - \phi\mu\frac{\mathbf{v}}{\mathbf{K}} + \nabla \cdot [\mu_e\nabla\mathbf{v} + \mu_e(\nabla\mathbf{v})^T] + \nabla(\lambda_e\nabla \cdot \mathbf{v}) \quad (6.3)$$

where $\mu_e = \mu$ and $\lambda_e = \lambda$ in the proposed model. In 3D Cartesian coordinates, the momentum equations become

$$\frac{\partial(\phi\rho u)}{\partial t} + \frac{\partial(\phi\rho uv)}{\partial x} + \frac{\partial(\phi\rho uv)}{\partial y} + \frac{\partial(\phi\rho uw)}{\partial z} = -\frac{\partial p}{\partial x} - \phi\mu\frac{u}{K_x} \quad (6.4)$$

$$+ \frac{\partial}{\partial x} \left(2\mu_e \frac{\partial u}{\partial x} + \lambda_e \nabla \cdot \mathbf{v} \right) + \frac{\partial}{\partial y} \left(\mu_e \frac{\partial u}{\partial y} + \mu_e \frac{\partial v}{\partial x} \right) + \frac{\partial}{\partial z} \left(\mu_e \frac{\partial u}{\partial z} + \mu_e \frac{\partial w}{\partial x} \right)$$

$$\frac{\partial(\phi\rho v)}{\partial t} + \frac{\partial(\phi\rho vu)}{\partial x} + \frac{\partial(\phi\rho vv)}{\partial y} + \frac{\partial(\phi\rho vw)}{\partial z} = -\frac{\partial p}{\partial y} - \phi\mu\frac{v}{K_y} \quad (6.5)$$

$$+ \frac{\partial}{\partial x} \left(\mu_e \frac{\partial v}{\partial y} + \mu_e \frac{\partial u}{\partial x} \right) + \frac{\partial}{\partial y} \left(2\mu_e \frac{\partial v}{\partial y} + \lambda_e \nabla \cdot \mathbf{v} \right) + \frac{\partial}{\partial z} \left(\mu_e \frac{\partial v}{\partial z} + \mu_e \frac{\partial w}{\partial y} \right)$$

$$\frac{\partial(\phi\rho w)}{\partial t} + \frac{\partial(\phi\rho wu)}{\partial x} + \frac{\partial(\phi\rho wv)}{\partial y} + \frac{\partial(\phi\rho ww)}{\partial z} = -\frac{\partial p}{\partial z} - \phi\mu\frac{w}{K_z} \quad (6.6)$$

$$+ \frac{\partial}{\partial x} \left(\mu_e \frac{\partial w}{\partial x} + \mu_e \frac{\partial u}{\partial z} \right) + \frac{\partial}{\partial y} \left(\mu_e \frac{\partial w}{\partial y} + \mu_e \frac{\partial v}{\partial z} \right) + \frac{\partial}{\partial z} \left(2\mu_e \frac{\partial w}{\partial z} + \lambda_e \nabla \cdot \mathbf{v} \right)$$

Energy Balance

$$\frac{\partial(\phi\rho E)}{\partial t} + \nabla \cdot (\phi(\rho E + p)\mathbf{v}) = \nabla \cdot (\phi\bar{\mathbf{T}}\mathbf{v}) - \nabla \cdot \dot{\mathbf{q}} - \phi^2\mu\frac{\mathbf{v} \cdot \mathbf{v}}{\mathbf{K}} \quad (6.7)$$

or in Cartesian coordinates,

$$\frac{\partial(\phi\rho E)}{\partial t} + \frac{\partial(\phi\rho Hu)}{\partial x} + \frac{\partial(\phi\rho Hv)}{\partial y} + \frac{\partial(\phi\rho Hw)}{\partial z} \quad (6.8)$$

$$= \frac{\partial}{\partial x} (\phi\tau_{xx}u + \phi\tau_{xy}v + \phi\tau_{xz}w) + \frac{\partial}{\partial y} (\phi\tau_{yx}u + \phi\tau_{yy}v + \phi\tau_{yz}w) + \frac{\partial}{\partial z} (\phi\tau_{zx}u + \phi\tau_{zy}v + \phi\tau_{zz}w)$$

$$- \frac{\partial\dot{q}_x}{\partial x} - \frac{\partial\dot{q}_y}{\partial y} - \frac{\partial\dot{q}_z}{\partial z} - \phi^2\mu\left(\frac{u^2}{K_x} + \frac{v^2}{K_y} + \frac{w^2}{K_z}\right)$$

One can easily find that this Darcy–Brinkman equation reverts back to the Navier–Stokes equation (See Chapter 2) by setting porosity $\phi = 1$, and permeability $K = \infty$. Therefore, it works for free flow.

It is known that Darcy’s law governs the momentum of a porous medium flow. The observations of Henry Darcy in 1856 of water supply and his experiments on steady state unidirectional flow within the porous medium composed of sand suggested Darcy’s law [110], given by

$$\frac{\partial p}{\partial x} = -\phi\frac{\mu}{K}u \quad , \quad (6.9)$$

where the *intrinsic velocity*, u , denotes the velocity averaged over the pore space. It is related to the *Darcy velocity*, V , the velocity averaged over the medium, by a porosity ϕ , given by

$$V = \phi u \quad . \quad (6.10)$$

For the Darcy–Brinkman equation in this work, the conditions of its applicability on porous media flows cannot be readily determined. However, Darcy’s law can be recovered from it using some rough assumptions. First, the time terms vanish for steady state solutions. Moreover the momentum induced by mass transfer and the viscous stress can be assumed minimal compared to the pressure gradient term for low-speed flow field. This is typical for most porous media flows, since the permeability of a porous medium is of the order of $\sim \mathcal{O}(10^{-7}) \text{ m}^2$ [111], and the gas viscosity is around $\sim \mathcal{O}(10^{-5}) \text{ kg}/(\text{m}\cdot\text{s})$. Therefore, the Darcy source term tends to be amplified by a factor of 100 of the velocity magnitude. The pressure gradient term and the Darcy term are thus balanced and dominate all other terms.

Using the governing equations and preliminary quantitative analysis above, most of the work is dedicated to formulate a method to accurately capture the fluxes across the free/porous interface, which can be decomposed into two components: the convective fluxes and viscous fluxes.

6.1 Convective flux

AUSM⁺-up scheme has been used extensively in previous work to account for low-speed viscous flow, for its consistent stability and accuracy, even sometimes without the use of a preconditioning matrix. Other schemes can not achieve this easily. Its main drawback arises from the determination of the reference Mach number. This reference Mach number essentially works as a truncation number, and becomes the only dependent variable of the scaling factor f_a , and directly scales the contribution of the diffusion term. In the development of the convective scheme, numerical tests conducted using this scheme were found to be able to solve the free channel flow, and

the Darcy problem in Section 6.3. However, for the later free/porous coupling case, it was found extremely dependent of the reference Mach number. The main reason is that big changes of pressure and velocity at the free/porous interface are sensed and treated as a shock by the AUSM⁺-up scheme, where they should not be. Although accurate results can be achieved by carefully tuning the reference Mach number, it is not convenient. Fig. 6.1 presents the solutions using different reference Mach numbers for the 2-D porous plug flow case in Section 6.3. The normalized streamwise velocities along the centerline vary noticeably for different reference Mach numbers.

Multiple attempts have been made to modify the averaged pressure and Mach number in the AUSM⁺-up scheme, especially at the interface (since the main error comes from the interface), in order to remove the hard specification of reference Mach number. None were successful.

Another scheme, an all-speed AUSM-family scheme [112], called “the simple low-dissipation AUSM”, which provides a way removing the dependence of the cutoff Mach number for low-speed flow, is referenced instead. To simplify the nomenclature, it is renamed AUSM-s in this work. This scheme demonstrates good performance in convergence rate for some cases, but it shows loss of accuracy for the low-Mach number case indicated in Fig. 6.5. Its main ability is to control the numerical dissipation contained in the pressure by introducing a non-dimensional function in the current Mach number.

The new proposed scheme in this work can be seen as a hybrid of AUSM⁺-up and AUSM-s scheme, and is named AUSM-h. In its basic implementation, the normal velocity is set by multiplying a ϕ to the intrinsic normal velocity. That is, the Darcy velocity is used. One of the variables, the averaged Mach number, is then scaled accordingly. It is constructed as

$$M_{\frac{1}{2}} = \mathcal{M}_{(4)}^+(M_L) + \mathcal{M}_{(4)}^-(M_R) \quad , \quad (6.11)$$

which is modified by removing the pressure dependence from the AUSM⁺-up scheme. This modification yields more accurate interface mass fluxes as demonstrated later.

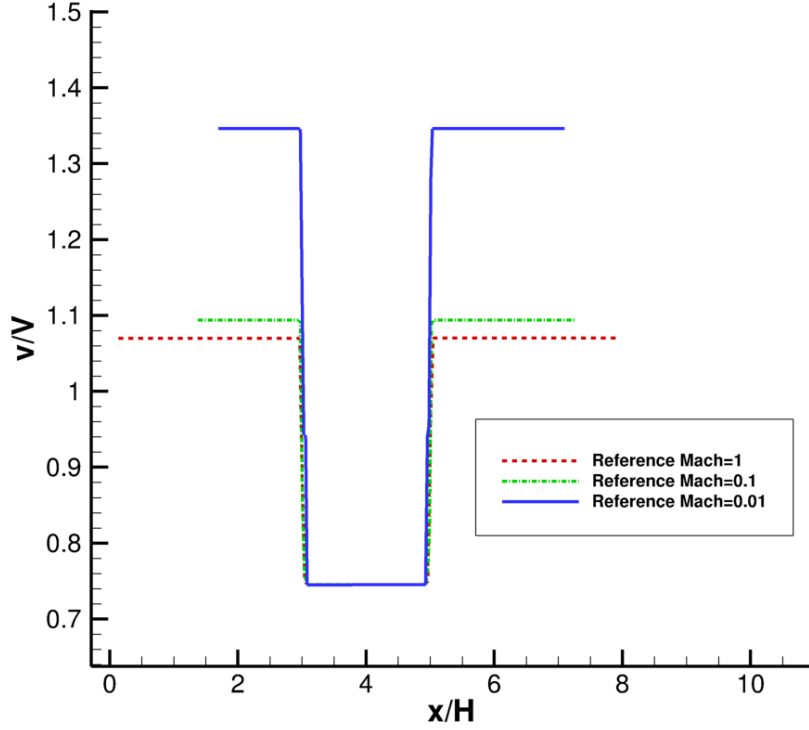


Figure 6.1: Normalized streamwise velocity along the centerline of the coupling case in Section 6.3 using different reference Mach numbers for AUSM⁺-up scheme. The reference velocity V is the analytical free flow mean velocity in Section 6.3.

The pressure in the governing equations is original and maintained without any average. The justification suggests that pressure is assumed acting on the whole control surface and is not affected by the porosity. Additionally, pressure continuity across the free/porous interface is validated in experiments, and is proved by the Beaver and Joseph boundary condition theoretically [32].

The interface pressure in the AUSM-h scheme is constructed as

$$p_{\frac{1}{2}} = \frac{p_L + p_R}{2} + \frac{\mathcal{P}_{(5)}^+(M_L) - \mathcal{P}_{(5)}^-(M_R)}{2} (p_L - p_R) + (1 - \chi) \left(\mathcal{P}_{(5)}^+(M_L) + \mathcal{P}_{(5)}^-(M_R) - 1 \right) \frac{p_L + p_R}{2}, \quad (6.12)$$

where

$$\chi = (1 - M_o)^2. \quad (6.13)$$

The reference Mach number is calculated by

$$M_o = \min(1.0, |\bar{M}|) \quad , \quad (6.14)$$

where

$$\bar{M}^2 = \frac{\phi_L^2(u_L^2 + v_L^2 + w_L^2) + \phi_R^2(u_R^2 + v_R^2 + w_R^2)}{2a_{1/2}^2} \quad . \quad (6.15)$$

It is important to note that the user specified (or free stream) Mach number has been removed from the reference Mach evaluation. Different from the original form of AUSM-s scheme, it can be found that β functions are now replaced by 5th degree polynomials $\mathcal{P}_{(5)}$ in AUSM⁺-up scheme. More details of the AUSM-h scheme can be found in the following subsection.

AUSM-h scheme

First of all, $a_{1/2}$ is evaluated as

$$a_{1/2} = \min(\hat{a}_L, \hat{a}_R) \quad , \quad (6.16)$$

where

$$\hat{a}_L = a_L^* a_L^* / \max(a_L^*, \phi_L V_{nL}) \quad , \quad \hat{a}_R = a_R^* a_R^* / \max(a_R^*, -\phi_R V_{nR}) \quad . \quad (6.17)$$

The reference Mach number is calculated by

$$M_o = \min(1.0, |\bar{M}|) \quad , \quad (6.18)$$

where

$$\bar{M}^2 = \frac{\phi_L^2(u_L^2 + v_L^2 + w_L^2) + \phi_R^2(u_R^2 + v_R^2 + w_R^2)}{2a_{1/2}^2} \quad . \quad (6.19)$$

The scaling function f_a is given by

$$f_a(M_o) = \begin{cases} 1 & \text{for } M_o \geq 1 \\ M_o(2 - M_o) & \text{otherwise} \end{cases} \quad (6.20)$$

The working Mach number is readily given by

$$M_{\frac{1}{2}} = \mathcal{M}_{(4)}^+(M_L) + \mathcal{M}_{(4)}^-(M_R) \quad , \quad (6.21)$$

where

$$M_L = \phi_L \frac{V_{nL}}{a_{1/2}} \quad , \quad M_R = \phi_R \frac{V_{nR}}{a_{1/2}} \quad . \quad (6.22)$$

The mass fluxes are defined as

$$\dot{m}_{\frac{1}{2}} = a_{1/2} M_{1/2} \begin{cases} \rho_L & \text{if } M_{1/2} > 0 \quad , \\ \rho_R & \text{otherwise} \end{cases} \quad (6.23)$$

and the pressure fluxes are given by

$$p_{\frac{1}{2}} = \frac{p_L + p_R}{2} + \frac{\mathcal{P}_{(5)}^+(M_L) - \mathcal{P}_{(5)}^-(M_R)}{2} (p_L - p_R) + (1 - \chi) \left(\mathcal{P}_{(5)}^+(M_L) + \mathcal{P}_{(5)}^-(M_R) - 1 \right) \frac{p_L + p_R}{2} \quad , \quad (6.24)$$

where

$$\chi = (1 - M_o)^2 \quad , \quad (6.25)$$

The 5th degree polynomials use the parameters

$$\alpha = \frac{3}{16} (-4 + 5f_a^2) \quad , \quad (6.26)$$

and

$$\beta = \frac{1}{8} \quad . \quad (6.27)$$

Finally, the whole convective fluxes are given by

$$\mathbf{F}_{1/2} = \dot{m}_{\frac{1}{2}} \begin{cases} \Phi_L & \text{if } M_{1/2} > 0 \\ \Phi_R & \text{otherwise} \end{cases} + \mathbf{p}_{1/2} \quad . \quad (6.28)$$

where $\Phi = (1, u, w, w, h)^T$ and $\mathbf{p}_{1/2} = p(0, n_x, n_y, n_z, 0)^T$.

6.2 Viscous flux

In the treatment of viscous fluxes, the shear stress is computed using intrinsic velocity gradient other than the gradient evaluated from Darcy velocity shown in Eqn. (6.29). The argument for this is that the gradient evaluation is better performed on the fluid since it is a local property. Also, this treatment tends to eliminate unphysical oscillations and produce smooth result especially for velocity across the free/porous interface. Velocity averaging taken over the whole control volume loses the velocity gradient information.

$$\tau_{ij} = \mu_e \left(\frac{\partial u_j}{\partial x_i} + \frac{\partial u_i}{\partial x_j} \right) + \lambda_e \frac{\partial u_k}{\partial x_k} \delta_{ij} \quad , \quad \lambda_e = -\frac{2}{3}\mu_e \quad . \quad (6.29)$$

Determination of μ_e , λ_e and their relations in porous media are not trivial. Some further investigation is required. For now, they are considered to be the same as the ones in the free flow.

The delimitation of the free flow and the porous medium domain is achieved through spatial properties such as porosity and permeability. This varies from the multi-domain coupling approach where a boundary condition is specified. The porosity, defined as volume fraction of pores over the cell space, varies from 0 to 1 in space such that a free flow has $\phi = 1$, while for porous medium domain, it lies between 0 and 1. An example, for instance, is shown in Fig. 6.2, where the porous medium in the center regions has $\phi = 0.7$, while the free flow regions on both ends have $\phi = 1$. Additionally, a filter is applied to smooth the interface region where sharp changes of porosity and permeability can occur. For a generic cell, c , the smooth function of ϕ is constructed as follows:

$$\tilde{\phi}_c = \frac{\sum_{n=1}^6 \phi_n + \beta \phi_c}{6 + \beta} \quad . \quad (6.30)$$

where $\tilde{\phi}_c$ is the smoothed porosity and subscript n denotes the adjacent neighbor cell index of cell c . The coefficient β governs the sensitivity of the smooth function, and

it is set to 6 as default in current work. The application of the filter to the porosity field can also be affected by the number of filtering times, N . One-time filtering the region does not produce too much difference, while considerable smoothings yield a smooth profile of porosity, but ends up with poor numerical solution accuracy for the coupling system. Figure 6.2 shows the effects of the number of filtering times. In this work $N = 10$ is picked for the computation. It should be noted that the same procedure is also applied to permeability.

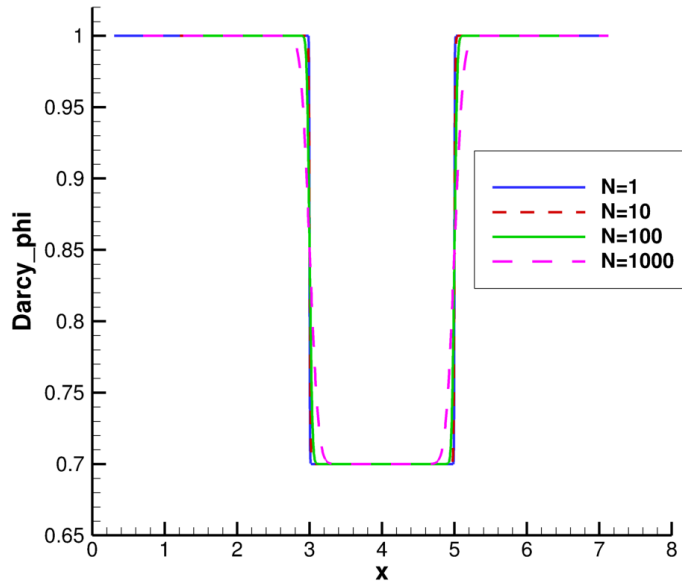


Figure 6.2: Effects of number of filtering times

6.3 Verification of the Governing Equation System on Channel Flows

The following tests were performed using an argon flow with free stream conditions $\rho = 0.2 \text{ kg/m}^3$ and viscosity $\mu = 1 \times 10^{-4} \text{ kg/(m}\cdot\text{s)}$. The inlet average velocity is carefully adjusted to be 0.1 m/s , resulting in $\text{Re}=1$, where the length scale is the channel height, $H = 5 \times 10^{-3} \text{ m}$, indicating a laminar flow. The associated Mach

number is 4.5×10^{-4} , indicative of incompressible flow. In addition, the free stream temperature is set to $T = 288.73$ K, and an adiabatic wall boundary is used.

Verification of the Coupling Equations for Free Flow

In order to verify that the code solves free flow problems, a 2-D channel flow, as a first test case, is presented. However, KATS solves it using a 3-D mesh because it is coded in this way. The geometry is shown in Fig. 6.3. The height of the channel is given by $H = 5 \times 10^{-3}$ m. The inlet boundary conditions are $p_t = 12000.144$ Pa and $T_t = 288.73$ K. Outlet boundary condition is $p = 12000$ Pa. When the flow is fully developed, pressure contours, presented in Fig. 6.4 (a), show the expected linear distribution through the channel. The velocity along the diameter of the tube also shows a nice laminar tunnel-flow profile, as depicted in Fig. 6.4 (b). Finally, in Fig. 6.5, the numerical velocity across the channel height using AUSM-h scheme is compared to the analytical solution and exhibits excellent agreement between each other. Numerical solution using AUSM-s is also presented. Its maximum relative error to the analytical solution, however, is 2.1%. The new scheme, AUMS-h, yields a higher level of accuracy than AUSM-s.

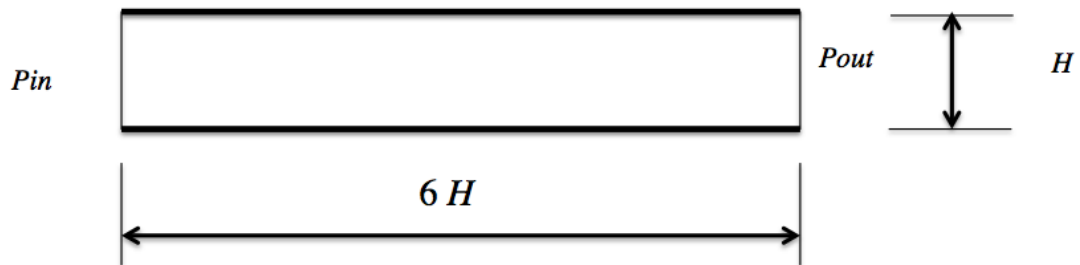
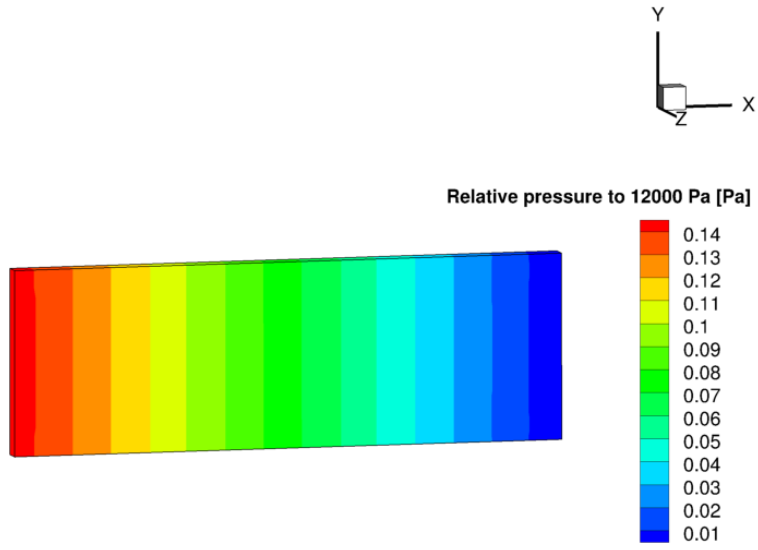
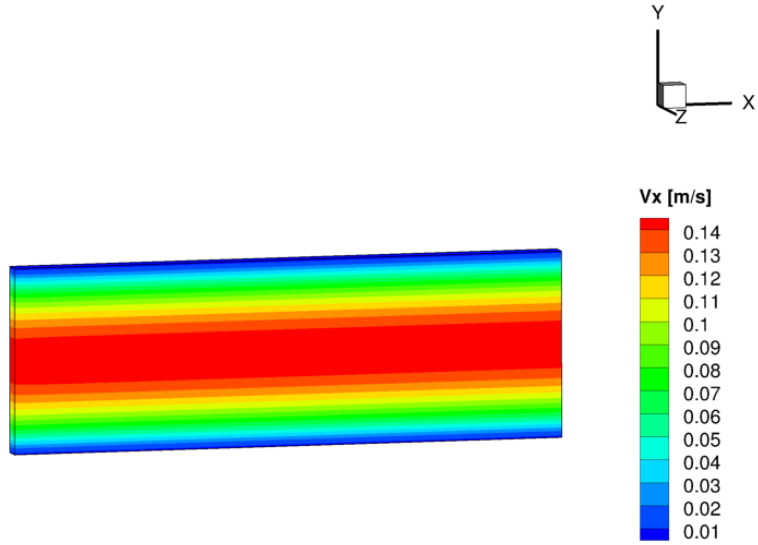


Figure 6.3: Geometry configuration for a free channel flow



(a) Relative pressure to 12000 Pa



(b) Velocity

Figure 6.4: Pressure and velocity contour

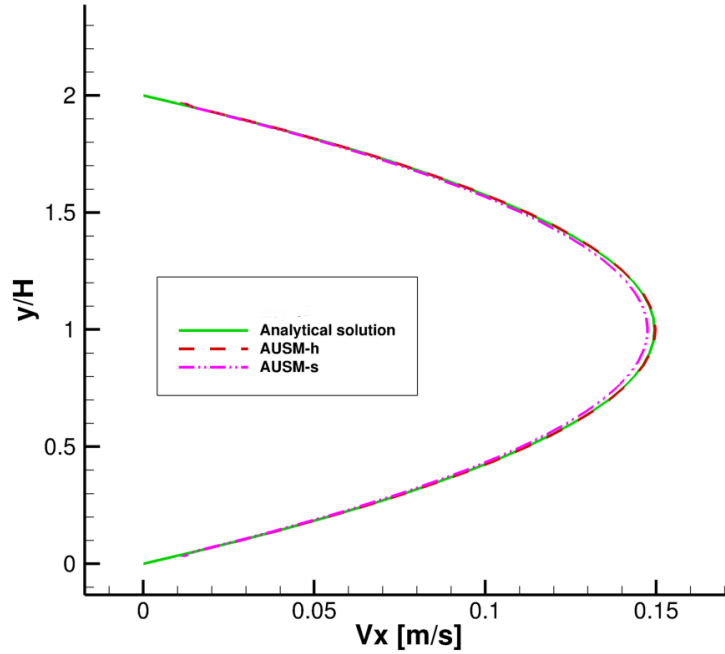


Figure 6.5: Numerical velocity verification for the free flow

Verification of the Coupling Equations for Porous Media Flows

The proposed Darcy–Brinkman model is expected to behave according to Darcy’s law (Eq. (6.9)) for porous medium. The following tests verify the ability of the scheme to do so.

A Darcy Problem

This first test replicates a Darcy’s problem. Two static pressures are specified at both the inlet and the outlet of a 2-D channel (Fig. 6.6). The resulting pressure drop forces a flow through the porous medium. The height of the channel is set to $H = 5 \times 10^{-3}$ m.

Analytical solution of the Darcy velocity V computed using Darcy’s law is given

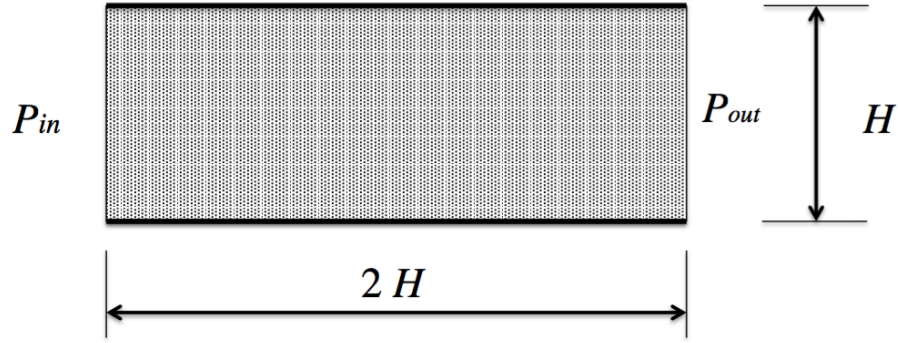


Figure 6.6: Geometry configuration for a Darcy problem

Table 6.1: Fluid properties

Variable	Value	Unit
p_{in}	12004	Pa
p_{out}	12000	Pa
ρ	0.2	kg/m ³
μ	1×10^{-4}	kg/(m·s)
K	2.5×10^{-8}	m ²
ϕ	0.7	

by

$$V = \frac{p_{in} - p_{out}}{2H} \frac{K}{\mu} = 0.1 \text{ m/s} \quad . \quad (6.31)$$

Numerical simulation of this case only specifies constant static pressure at the two ends of the channel, and symmetry conditions are used for the other boundaries. Figure 6.7 (a) shows the static pressure contour, and Figure 6.7 (b) shows the relative error percentage of the numerical Darcy velocity to the analytical solution V , where the maximum error 0.015% is found. Uniform velocity profile at every stream-wise cross plane shows no stickiness to the wall, and therefore, no boundary layer is generated. Associated streamwise properties are shown in Fig 6.8. Specifically, the pressure is almost linearly decreased in the streamwise direction. An analytical pressure for compressible flow computed according to Ref. [113] is plotted to verify the

numerical pressure solution. The Darcy velocity is predicted as expected with only slight numerical difference in the streamwise direction. Density and temperature also vary a little. However, the mass flow rates at the inlet and the outlet differ by a relative error of 4.5×10^{-6} , indicating conserved mass flow rate. Numerical differences of velocity, density and temperature can be attributed as the compressible effects when using a compressible solver.

No-slip Wall Boundary Effects

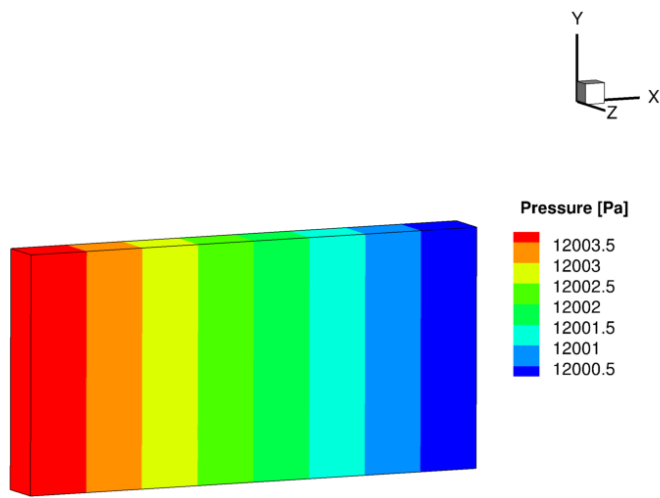
For this case, the parameters from the last case are kept, except that two no-slip walls are added to the 2-D channel sample (Fig. 6.9). Different from the last case, a boundary layer forms close to the wall because of no-slip conditions and diffusive terms. However, the boundary layer is very thin, and the velocity reaches its plateau not far from the wall relative to the height of the channel. The pressure, however, is still almost linear in the streamwise direction. Properties such as pressure, velocity, density and temperature along the centerline are shown in Fig. 6.11. Pressure can be found the same as that in the previous case, and very little difference occurs for velocity, density and pressure. It implies that effects of the boundary layer barely changes the flow properties along the centerline. Compressible effects on velocity, density and temperature can also be found in this case.

Verification of the Coupling Equations on Free/Porous Flow

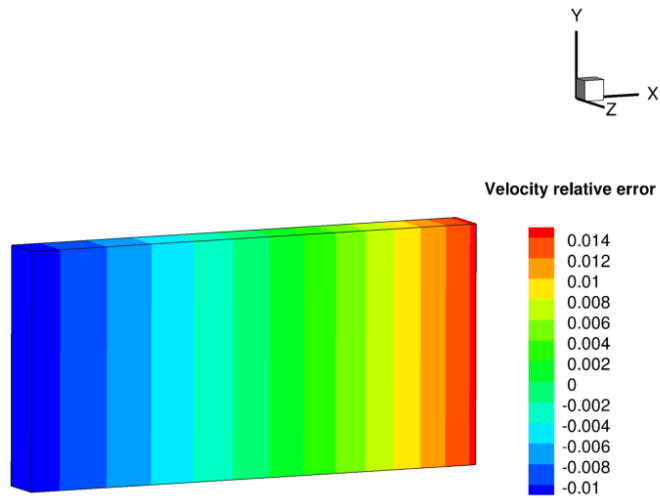
2-D porous plug flow

As a numerical verification case, a 2-D channel with a porous plug placed in the center is considered (Fig. 6.12). Free flow enters the porous region under the force of the pressure at the inlet and reverts back to free flow before exiting the channel.

Two dimensionless numbers govern the free flow and the porous medium flow in this coupling problem. The Reynolds number, given by $Re = \rho V H / \mu$, can determine the free flow. It is defined by using the free flow mean velocity, V , and the height



(a) Pressure



(b) Relative error percentage of Darcy velocity to the analytical solution

Figure 6.7: Pressure and Darcy velocity error contour for a Darcy problem

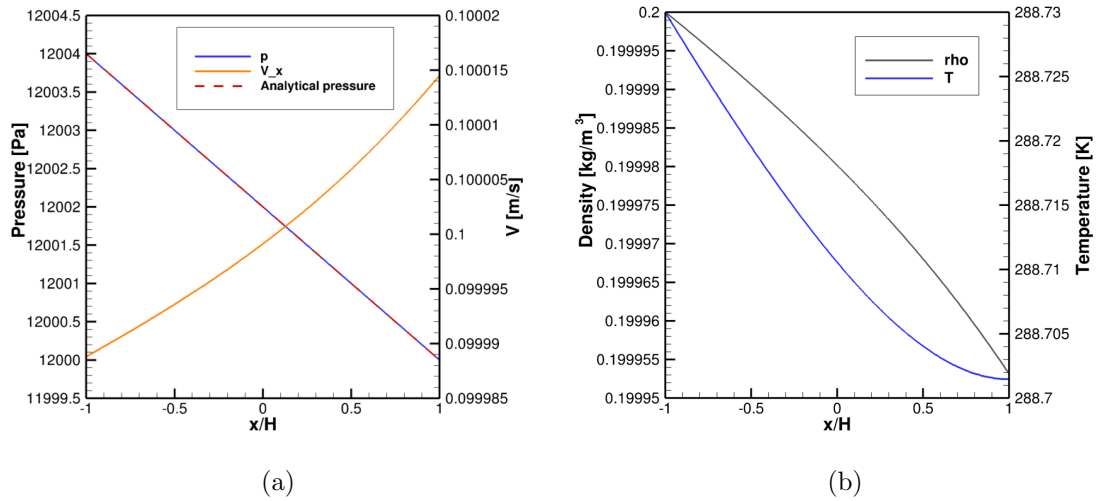


Figure 6.8: Streamwise properties along the centerline for a Darcy problem

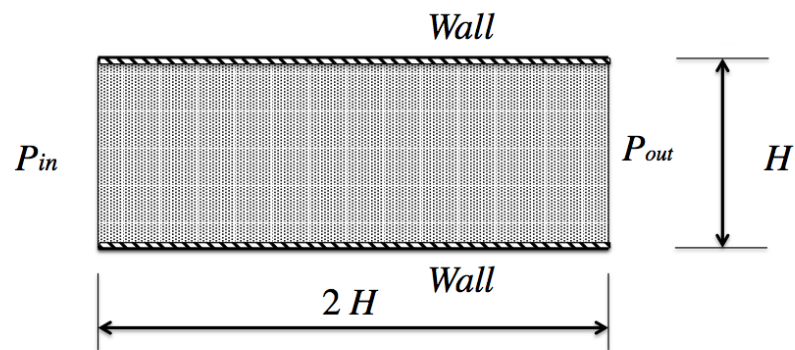
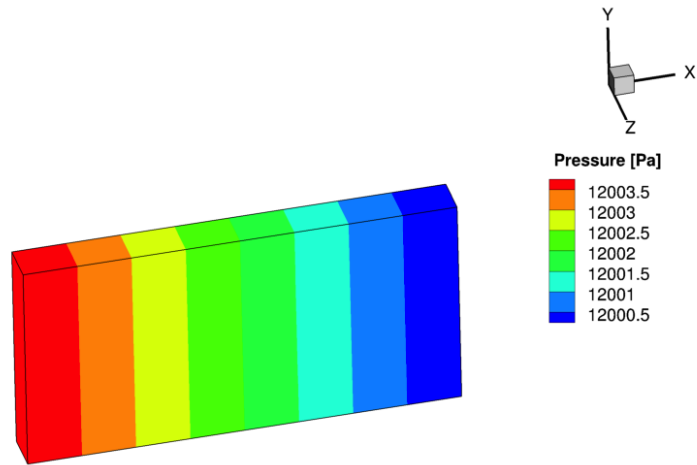
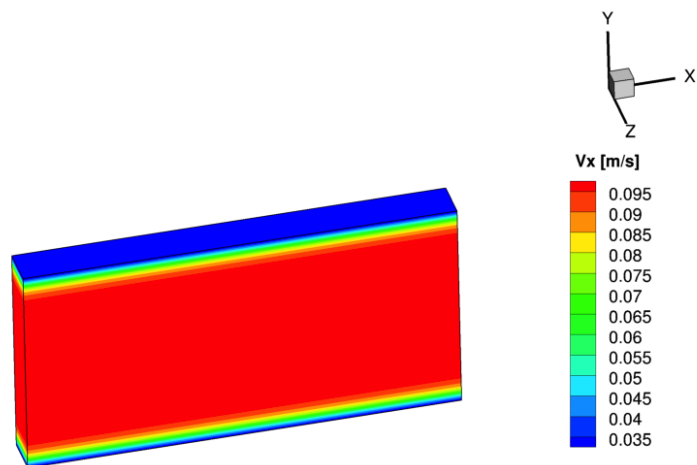


Figure 6.9: Geometry configuration for a Darcy problem with no-slip wall boundaries



(a) Pressure



(b) Darcy velocity

Figure 6.10: Pressure and darcy velocity contour for a Darcy problem with no-slip wall

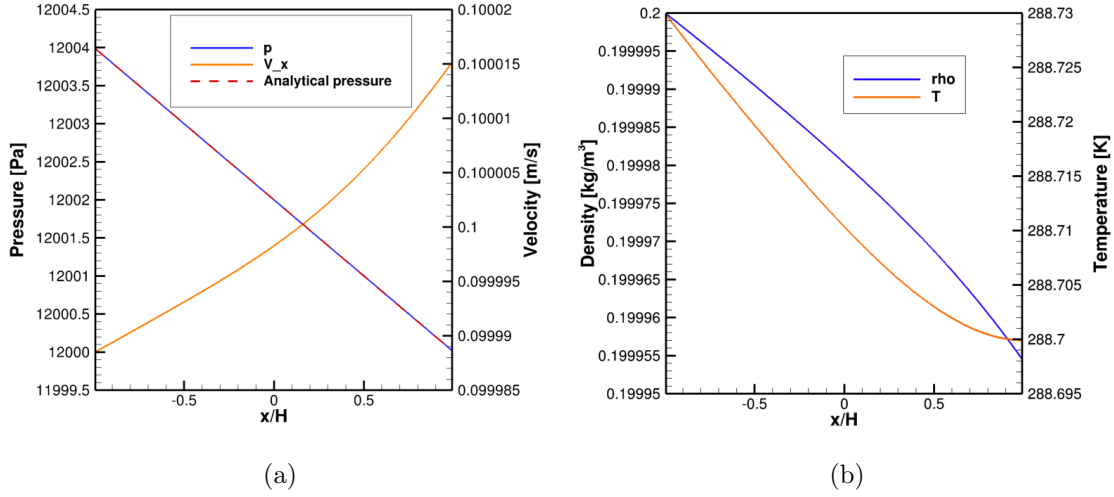


Figure 6.11: Streamwise properties along the centerline for a Darcy problem with no-slip wall

of the channel, H . The Darcy number characterizing the porous domain is given by $Da = K/H^2$, where K represents the permeability. Among others, the porosity of the material, $\phi = 0.7$, and the viscosity ratio, defined by $\alpha = \mu_B/\mu$, is set as 1 in order to generate results comparable to those of Ref. [4]. Associated variables used in the verification case are shown in Table 6.2, which yield $Re = 1$ and $Da = 10^{-3}$. To perform the numerical simulation, the velocity inlet boundary condition is not consistent with the use of a compressible flow solver for solving subsonic flow problems [83]. Instead, the total pressure and total temperature boundary conditions are applied at the inlet while at the outlet, the static pressure is used. Approximation of the pressure drop allows specification of suitable pressure conditions without spending excessive time on trial and error. By using Darcy' law, the pressure drop through the porous plug can be approximated as

$$\Delta p = \frac{\mu}{K} V(2H) = 4.0 \text{ Pa} \quad , \quad (6.32)$$

and the estimated total pressure drop of two sections free flow is

$$\Delta p = \frac{12\mu V}{H^2}(6H) = 0.144 \text{ Pa} \quad . \quad (6.33)$$

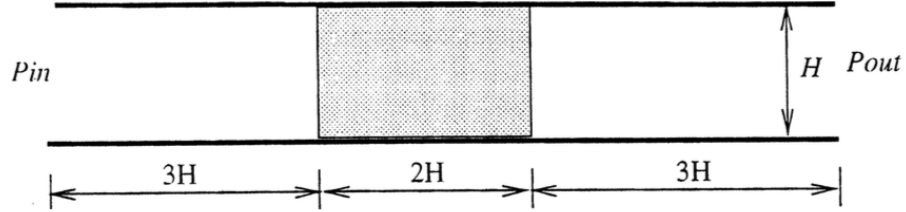


Figure 6.12: Geometry configuration for free/porous domain [3]

Table 6.2: Fluid properties

Variable	Value	Unit
ρ	0.2	kg/m ³
V	0.1	m/s
H	5×10^{-3}	m
μ	1×10^{-4}	kg/(m s)
K	2.5×10^{-8}	m ²
ϕ	0.7	

However, the pressure loss through the free/porous interface is not easy to determine and some tests are necessary to match the mean velocity to the expected values by adjusting the inlet pressure. The verification case in this work takes the following boundary conditions. The inlet boundary conditions are: $p_t = 12004.544$ Pa and $T_t = 288.73$ K. Outlet boundary condition: $p = 12000$ Pa. The wall boundary condition is no-slip and iso-thermal.

The intrinsic velocity and the Darcy velocity contours are shown in Fig. 6.13, where the intrinsic velocity u is averaged over the pore space, and the Darcy velocity, V , denotes the velocity averaged over the medium. The free flow clearly forms on either end of the channel. Once the free flow approaches the porous medium, the

velocity magnitude becomes more uniform. Non-dimensioned centerline velocity and pressure from the numerical solutions are compared to numerical solutions in Ref. [4], and shown in Fig. 6.14. It is noted that the above pressure drop does not yield the exact Darcy centerline velocity of 0.1m/s, and the actual velocity solution yields a relative error of 0.36%. Related comparisons are scaled by using this numerical velocity. A high level of agreement can be noticed for the velocity. The pressure also agrees well except at the entrance. This is due to the development region of the flow caused by the inlet boundary condition. It could be also due to the compressible effects since a compressible solver is used for this case. Different from the incompressible fluid case in Ref. [4], the change of density in this work may cause different behaviors of pressure and velocity.

In summary, a new governing equations system is constructed using volume average technique, allowing evaluation of mass, momentum and energy in 3D. To account for the convective flux, a new scheme for the compressible free flow, the porous medium flow, and the conjugate free/porous flow, named “AUSM-h”, is developed. To verify the whole model, a numerical study was performed on a 2-D channel flow. Specifically, a free flow was first simulated, and the result agrees exactly with the analytical solution. A compressible porous medium flow was then simulated, and the results were compared against to analytical solutions, showing excellent agreements. Boundary effects for the porous medium flow were also analyzed. Expected velocity drop due to no-slip wall effect was found. The study of the Darcy–Brinkman solver on coupling was also conducted. A remarkable agreement with reference data was found through the comparisons of centerline pressure and velocity, demonstrating the feasibility of flux balancing to implicitly couple the conjugate free/porous flow problem.

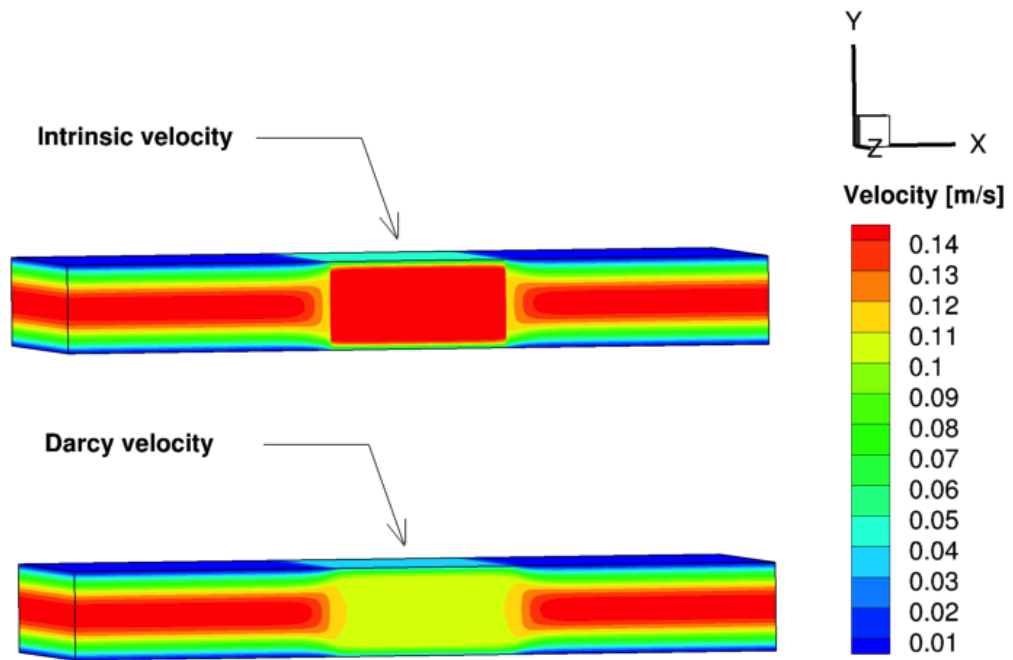
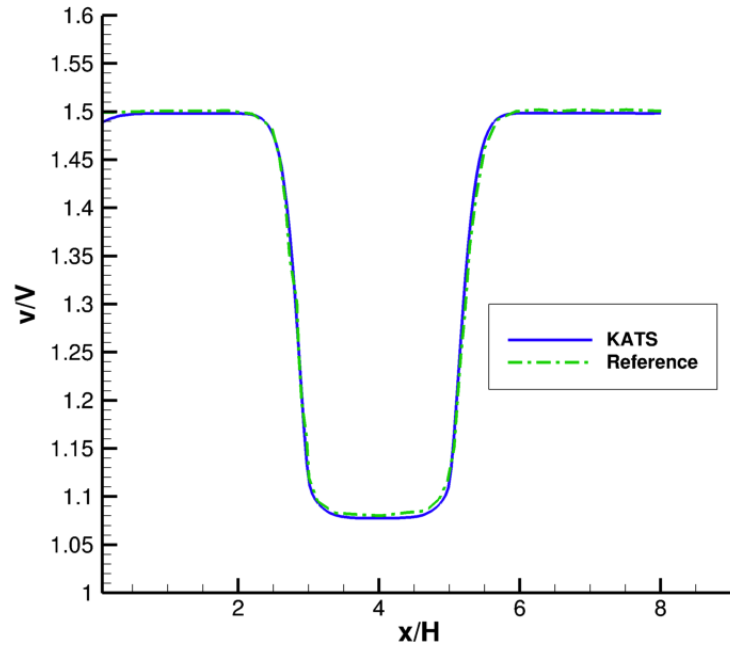
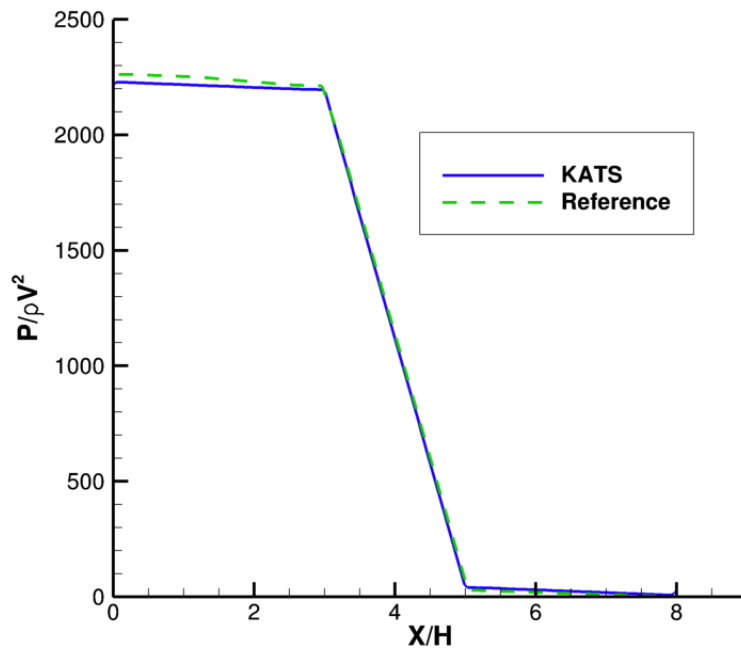


Figure 6.13: Intrinsic and Darcy velocity contour



(a) Normalized streamwise velocity along the centerline



(b) Normalized streamwise pressure along the centerline

Figure 6.14: Static pressure and velocity along the stagnation line compared to numerical solutions in Ref. [4]

Chapter 7 Summary and Conclusions

7.1 Summary

This work consists of two parts. The first part presents a three-dimensional Computational Fluid Dynamics (CFD) code to simulate weakly ionized hypersonic flow during reentry in thermal and chemical non-equilibrium states. Using the continuum hypothesis, the flow field is modeled using laminar Navier–Stokes equations, mass conservations and energy balance equations for the governing equation system. The convective flux is computed using a shock-capturing scheme. Specifically, a modified Steger-Warming Flux Vector Splitting scheme is employed. In terms of viscous fluxes, the mass diffusion for each species is modeled using Fick’s law. The viscous shear stresses are modeled in relation to strain rate by the bulk viscosity based on the assumption of a Newtonian fluid, and Stoke’s hypothesis. The heat fluxes are computed using Fourier’s law, where the mixture thermal conductivity is used. For each species, the viscosity is approximated using Blottner’s curve fit, and the thermal conductivity is related to viscosity based on Eucken’s relation. The mixture bulk viscosity and thermal conductivity are evaluated by applying Wilke’s semi-empirical mixing rule to species viscosity and thermal conductivity. A standard finite-rate chemistry model is used to account for the chemistry reactions, and thus for the chemistry source terms in the species mass conservation equation. A two temperature model is used for the thermal non-equilibrium, which assumes that the translational and rotational energy modes of the participating species are described by a single temperature T_{tr} , while the vibrational and electronic energy modes, as well as electron translational energy mode, are characterized by a single temperature T_{ve} . The energy transfer between the translational-rotational mode and the vibrational-electron-electronic mode is modeled using relaxation rate, thus an energy source term is generated.

To apply the set of governing equations to solve a flow problem, the flow field must be discretized into many small cells using structured or unstructured mesh generation technique. The set of partial differential equations is then integrated over the small volume of each cell on the domain. Finite Volume Method (FVM) is applied to convert the resulting differential equations to difference equations, which can be numerically solved by modern computers. Specifically, the time terms and source terms are evaluated at the cell center. However, the computation of fluxes are not piecewise. Gauss theorem is applied to transfer the integration of flux over the volume to the one at each cell surface. The fluxes across the face are evaluated using the properties from the cells neighboring it. For inviscid fluxes, the use of the cell-centered values can only generate first-order accuracy. The higher-order extension involves property reconstruction using more cells, and yields high-order accuracy. However, it causes numerical oscillations which deteriorate the solution in the presence of a discontinuity. A limiter function which can suppress the spurious oscillations near larger gradient, while preserve higher-order accuracy in the smooth region has to be used. Compared to inviscid fluxes, viscous fluxes are relatively straightforward to evaluate. The gradient at the face are computed using weighted least-squares approach and later calibrated by a deferred correction based on center difference scheme.

The integration over time uses first-order backward Euler method. This procedure results in the linearization of the inviscid and viscous fluxes, as well as source terms. Consequently, the Jacobian terms have to be computed for the implicit operator. The convective flux and diffusive flux Jacobian matrices, as well as source term Jacobians, are originally implemented numerically via small number perturbation to the original state property. They are later constructed to be fully analytical to maintain accuracy and stability. The set of numerical discretized equations over all the cells can be finally casted into a sparse linear system, $Ax = b$. Among the available linear solvers, the PETSc library is linked, which provides flexible linear solvers and various preconditioner approach for efficient computation.

The hypersonic flow solver is then extended to account for very low Mach number flow using preconditioning technique and switch of the convective flux scheme to AUSM⁺-up scheme. Preconditioning does not only rescale the eigenvalues of the system and thus eliminate the stiffness to gain better convergence; it also improves the solution accuracy. A modified Weiss and Smith is developed. The preconditioner is then extended for a multi-species formulation.

The second part of this work involves the coupling of a free flow and a porous medium flow. Using the volume average technique, a Darcy–Brinkmann equation for both the compressible free flow and the porous medium flow is constructed. Mass conservation and energy balance equations are also volume-averaged and constructed accordingly. When dealing with conjugate free/porous problem, this solver couples the free/porous problem through flux balance, therefore, flow behaviors at the interface are satisfied automatically and implicitly. There is no need to impose explicit interface boundary conditions. A new convective flux function of AUSM-family, AUSM-h, is developed as the Riemann solver to account for the inviscid flux over the whole domain. The viscous fluxes are computed using the original velocity gradient, while the face velocity is averaged. A filtering technique is used to smooth the porosity and permeability in the vicinity of the free/porous interface.

Using the above models, most of the cases only focus on steady state solution. A general simulation starts from an initial state. A update of the solution is obtained by solving the linear system using the current state. The time-dependent solution variables are therefore advanced by a physical time step size. Time marching proceeds and a steady state solution is finally achieved. Time accurate solution can also be obtained by controlling the physical time step size.

The numerical code package, including the hypersonic flow solver, the subsonic flow solver, and the Darcy–Brinkmann solver, is the fluid dynamic core of known as Kentucky Aerothermodynamics and Thermal Response System (KATS). It is writ-

ten in C++, object-oriented and template featured, to facilitate the development of the whole system at the University of Kentucky. KATS reads the CGNS format of the computational grid and takes advantage of parallel computing through domain decomposition (ParMETIS [114]) and OpenMPI [115]. It is configured and compiled to run parallelly on the Lipscomb High Performance Computing Cluster (DLX) at the University of Kentucky [116].

This CFD module has been proven a valuable contribution to the aerospace field. It is extensively coupled with the Material Response (MR) module [41] and the spallation phenomenon code [43] developed. For the first coupling case, each module solves its governing equation on a given mesh, i.e. the CFD solver solves the equations on the fluid mesh and the MR solver on another. The only requirement is that the meshes are aligned at their interfaces so that the area of the faces is identical on both grids. At each time step, a surface module solves the flux balance equations to obtain the primitive values at the interface. Thus, two modules are implicitly coupled through surface balance equations. For the second coupling case, a loose coupling (or one-way coupling) is achieved by running a particle-tracking code using a converged CFD solution. More than that, it is also necessary and important to take account of the impact of spallation on the flow field. The source terms from the particle-tracking code are then added to the CFD solver and solved time accurately. This is the two-way coupling. Motivated readers are welcome to read the references for more information.

In this work, KATS is employed to simulate several reentry flow over space capsule cases. It is also used to simulate a convergent-divergent nozzle flow to investigate the validity of current CFD technique to deal with low-density hypersonic nozzle flow. In terms of subsonic cases, simulations of low Mach number flows are also performed to test the precondition system. The performance of the coupling solver is investigated through a series of numerical tests, such as the pure free flow, the pure porous medium flow, and the conjugate free/porous flow problem. Related solutions

are carefully compared against the analytical solutions and the available benchmark solutions from other sources.

7.2 Conclusions

KATS successfully simulated Mach 10 Argon flow over a cylinder. Comparisons with the results obtained from the CFD code LeMANS indicates remarkable agreement between each other.

KATS successfully captured the heat transfer rate over a Mars entry spacecraft experimental model in the HYPULSE expansion hypersonic wind tunnel for airflow. Improvement of second-order scheme is shown for the heat transfer rate by comparing to the first-order scheme. First-order scheme over-predicts the value at the stagnation lines, therefore, mesh refinement is required to achieve higher resolution. Second-order scheme can obtain more accurate values, is thus more favorable to employ.

KATS successfully conducted a full simulation of the air flow over Stardust capsule, followed by a study focused on the forebody of the capsule, where mesh refinement tests are performed to guarantee a grid-independent solution. Two simulations using a 5-species air model and 11-species air model were performed to assess the difference between them. It can be noticed that stagnation temperatures are reduced for the 11-species air model, which explains as the effect of ionizations. However, away from the nose region, the heat transfer rate is increased. The explanation is that the high-temperature level at the nose region triggers ionizations, thus more energies are consumed. But once the gas is moving away from the nose, ionization reacts backward due to low temperature level, thus generates energy. The resulting heat transfer to the surface increases.

KATS successfully simulated a low-density hypersonic nozzle flow. Associated numerical solutions are found in excellent agreement with another CFD results. However, comparisons against DSMC and experiments indicates some significant discrepancies, which are mainly due to the failure of the traditional continuum fluid dynamics

solver on rarefied gas. The DSMC approach gives a better solution. More specifically, the low-density, slip effects along the nozzle wall can not be captured using the traditional no-slip wall boundary conditions in CFD, which makes the comparisons difficult. A slip-wall boundary condition must be employed to solve this difficulty.

KATS was successfully extended to deal with a low-speed flow. By using an all-velocity low dissipation convective flux scheme, AUSM⁺-up, together with the preconditioning technique for low-speed flow, KATS subsonic solver successfully simulated a pipe flow and an excellent agreement with an analytical solution is found. A carefully designed numerical test was also conducted, which is able to verify the validity of a new multi-species preconditioner. The result is, again, in good agreement with the analytical solution. In the study of lid-driven cavity problem, besides the use of preconditioner and AUSM⁺-up scheme, the velocity inlet was modified to generate a boundary layer and make the solution consistent for solving subsonic flow using a compressible flow approach. This allows KATS to yield results in excellent agreement with the benchmark solution in the reference [2].

The new Darcy–Brinkman solver successfully simulated a compressible free flow and a porous medium flow through a 2-D channel, respectively. The numerical result shows excellent agreement with analytical solutions. Boundary effects for the porous medium flow were also analyzed. Expected velocity drop due to no-slip wall effect was found. Study of the Darcy–Brinkman solver on free/porous coupling was also conducted on a 2-D coupling channel flow. A remarkable agreement with reference data was found through the comparisons of centerline pressure and velocity.

7.3 Original Contributions

1. A weakly ionized hypersonic flow solver KATS-CFD for reentry application

Although the physical models and mathematical formulations for hypersonic flow in this work are not new, the solver itself was developed independently

from other research institutes and universities. This solver is able to solve a flow in a both thermal equilibrium and non-equilibrium, as well as chemical non-equilibrium state. The main difference is that a set of density-based primitive variables is used for dependent variables, which is simple in derivation and efficient in computation, especially for the calculation of temperatures. Numerical and analytical Jacobians for convective, diffusive and source terms were both implemented.

2. **A subsonic solver for low Mach number flow**

KATS-CFD was extended to account for low Mach number flow via switch of the convective flux scheme to AUSM⁺-up scheme [65], and use of a modified Weiss and Smith preconditioner [105]. It was modified further to account for multi-species flow in low Mach regime.

3. **A Darcy–Brinkman solver for the compressible free flow and the porous medium flow**

A new set of governing equation system consisting of Darcy–Brinkman equation, mass conservation, and energy equation was developed. To account for the inviscid flux, an AUSM family scheme, AUSM-h, was developed, which removes the dependence of reference Mach number in AUSM⁺-up. It is seen as a hybrid of AUSM⁺-up the “simple low-dissipation AUSM” [112]. The viscous fluxes are evaluated using original velocity gradient, but the velocity at the face is averaged. Instead of imposing the boundary conditions at the free/porous interface, this solver couples the domains implicitly through flux balance.

4. **Study on a channel free flow, a porous medium flow using the new Darcy–Brinkman solver**

The performance of the Darcy–Brinkman solver was demonstrated on a 2-D channel flow. The numerical result shows excellent agreement with analytical

solutions. Boundary effects for the porous medium flow were also analyzed. Expected velocity drop due to no-slip wall effect was found.

5. Study on coupling channel flow using the new Darcy–Brinkman solver

Study of the Darcy–Brinkman solver on coupling was conducted on a 2-D coupling channel flow. A remarkable agreement with reference data was found through the comparisons of centerline pressure and velocity.

Appendix A. Chemistry and Physics Data Source Table

Species data

Table 1 shows the basic chemistry data for each species used in the 5-species air model and the 11-species air model, where in the 5-species air model, species N_2 , O_2 , NO , N and O are involved, and in the 11-species air model, N_2 , O_2 , NO , N , O , N_2^+ , O_2^+ , NO^+ , N^+ , O^+ , and e are involved. Specifically, M_s is the molar mass, h_s^o is the energy of formation assuming the base temperature at 0 K, A_s , B_s , and C_s are constants for the Blottner viscosity model, $\theta_{v,s}$ is the species characteristic vibrational temperature, D_s is the dissociation potential of a molecule used to account for the energy change due to chemical reactions, G_s the species charge, and finally \hat{I}_s is the first ionization energy.

Table 1: Basic species chemistry data

Species	M_s [g/mol]	h_s^o [J/kg]	A_s	B_s	C_s	$\theta_{v,s}$ [K]	D_s [J/kg]	G_s	\hat{I}_s [J/kg]
N_2	28	0	2.68142E-2	3.177838E-1	-1.13155513E1	3395	3.363E7	0	0
O_2	32	0	4.49290E-2	-8.261580E-2	-9.20194750E0	2239	1.542E7	0	0
NO	30	2.996123E6	4.36378E-2	-3.355110E-2	-9.57674300E0	2817	2.090E7	0	0
N	14	3.362161E7	1.15572E-2	6.031679E-1	-1.24327495E1	0	0	0	0
O	16	1.543119E7	2.03144E-2	4.294404E-1	-1.16031403E1	0	0	0	0
N_2^+	27.9994514	5.425897E7	2.68142E-2	3.177838E-1	-1.13155513E1	3395	3.003E7	1	0
O_2^+	31.9994514	3.658450E7	4.49290E-2	-8.261580E-2	-9.20194750E0	2239	2.009E7	1	0
NO^+	29.9994514	3.283480E7	3.02014E-1	-3.5039791	-3.73551570E0	2817	3.490E7	1	0
N^+	13.9994514	1.340460E8	1.15572E-2	6.031679E-1	-1.24327495E1	0	0	1	2.89E7
O^+	15.9994514	9.770599E7	2.03144E-2	4.294404E-1	-1.16031403E1	0	0	1	2.69E7
e	0.0005486	0	0	0	-1.20000000E1	0	0	-1	0

Electronic energy data

Species electronic modes at difference levels are shown in Table 2 and Table 3. Not just those species for the 5-species air model and the 11-species air model are listed,

but some gases once used in the development of this work, and some collaborated works, such as Ar and CO₂.

NASA 9 Polynomial Data

Table 4 and 5 present polynomial constants for the specific enthalpy and entropy, which are then used for the computation of equilibrium constant K_{cr} . The valid temperature interval for each set of coefficients is bounded by T_l and T_u . It also includes the energy of formation at the base temperature of 298.15 K.

Table 2: Electronic energy modes

Species	level i	$\theta_{el,i,s}$ [K]	$g_{i,s}$
Ar	0	0.000000000000000E+00	1
Ar	1	1.611135736988230E+05	9
Ar	2	1.625833076870950E+05	21
Ar	3	1.636126382960720E+05	7
Ar	4	1.642329518358000E+05	3
Ar	5	1.649426852542080E+05	5
Ar	6	1.653517702884570E+05	15
O	0	0.000000000000000E+00	5
O	1	2.277077570280000E+02	3
O	2	3.265688785704000E+02	1
O	3	2.283028632262240E+04	5
O	4	4.861993036434160E+04	1
O ⁺	0	0.000000000000000E+00	4
O ⁺	1	3.858334678336000E+04	10
O ⁺	2	5.822349152848000E+04	6
O ₂	0	0.000000000000000E+00	3
O ₂	1	1.139156019700800E+04	2
O ₂	2	1.898473947826400E+04	1
O ₂	3	4.755973576639200E+04	1
O ₂	4	4.991242097343200E+04	6
O ₂	5	5.092268575561600E+04	3
O ₂	6	7.189863255967200E+04	3
O ₂ ⁺	0	0.000000000000000E+00	4
O ₂ ⁺	1	4.735440815760000E+04	8
O ₂ ⁺	2	5.837398741440000E+04	4
O ₂ ⁺	3	5.841427312000000E+04	6
O ₂ ⁺	4	6.229896616000000E+04	4
O ₂ ⁺	5	6.733467936000000E+04	2
O ₂ ⁺	6	7.121937240000000E+04	4
O ₂ ⁺	7	7.654284064000000E+04	4
O ₂ ⁺	8	8.819691976000000E+04	4
O ₂ ⁺	9	8.891630736000000E+04	4
O ₂ ⁺	10	9.423977560000000E+04	8
O ₂ ⁺	11	9.495916320000000E+04	4
O ₂ ⁺	12	9.592026503360000E+04	2
O ₂ ⁺	13	9.985099888000000E+04	2
O ₂ ⁺	14	1.035918144000000E+05	4
N	0	0.000000000000000E+00	4
N	1	2.766469645581980E+04	10
N	2	4.149309313560210E+04	6
N ⁺	0	0.000000000000000E+00	1
N ⁺	1	7.006835224000000E+01	3
N ⁺	2	1.881917961600000E+02	5
N ⁺	3	2.203656871824000E+04	5
N ⁺	4	4.703183475776000E+04	1
N ⁺	5	6.731252222192000E+04	5
N ⁺	6	1.327190797527310E+05	15

Table 3: Electronic energy modes – continued

Species	level i	$\theta_{el,i,s}$ [K]	$g_{i,s}$
N ₂	0	0.000000000000000E+00	1
N ₂	1	7.223156514095200E+04	3
N ₂	2	8.577862640384000E+04	6
N ₂	3	8.605026716160000E+04	6
N ₂	4	9.535118627874400E+04	3
N ₂	5	9.805635702203200E+04	1
N ₂	6	9.968267656935200E+04	2
N ₂	7	1.048976467715200E+05	2
N ₂	8	1.116489555200000E+05	5
N ₂	9	1.225836470400000E+05	1
N ₂	10	1.248856873600000E+05	6
N ₂	11	1.282476158188320E+05	6
N ₂	12	1.338060936000000E+05	10
N ₂	13	1.404296391107200E+05	6
N ₂	14	1.504958859200000E+05	6
N ₂ ⁺	0	0.000000000000000E+00	2
N ₂ ⁺	1	1.318997164600000E+04	4
N ₂ ⁺	2	3.663323087728000E+04	2
N ₂ ⁺	3	3.668876760000000E+04	4
N ₂ ⁺	4	5.985304832000000E+04	8
N ₂ ⁺	5	6.618365920000000E+04	8
N ₂ ⁺	6	7.598991933064000E+04	4
N ₂ ⁺	7	7.625508560000000E+04	4
N ₂ ⁺	8	8.201018640000000E+04	4
N ₂ ⁺	9	8.416834920000000E+04	4
N ₂ ⁺	10	8.632651200000000E+04	8
N ₂ ⁺	11	8.920406240000000E+04	8
N ₂ ⁺	12	9.208161280000000E+04	4
N ₂ ⁺	13	9.222549032000000E+04	4
N ₂ ⁺	14	9.293768404400000E+04	2
N ₂ ⁺	15	9.639793840000000E+04	2
N ₂ ⁺	16	1.035918144000000E+05	4
NO	0	0.000000000000000E+00	4
NO	1	5.467345760000000E+04	8
NO	2	6.317139627802400E+04	2
NO	3	6.599450342445600E+04	4
NO	4	6.906120960000000E+04	4
NO	5	7.049998480000000E+04	4
NO	6	7.491055017560000E+04	4
NO	7	7.628875293968000E+04	2
NO	8	8.676188537552000E+04	4
NO	9	8.714431182368000E+04	2
NO	10	8.886077063728000E+04	4
NO	11	8.981755614528000E+04	4
NO	12	8.988445919208000E+04	2
NO	13	9.042702132000000E+04	2
NO	14	9.064283760000000E+04	2
NO	15	9.111763341600000E+04	4
NO ⁺	0	0.000000000000000E+00	1
NO ⁺	1	7.508967768800000E+04	3
NO ⁺	2	8.525462447600000E+04	6
NO ⁺	3	8.903572570160000E+04	6
NO ⁺	4	9.746982592400000E+04	3
NO ⁺	5	1.000553049584000E+05	1
NO ⁺	6	1.028033655904000E+05	2
NO ⁺	7	1.057138639424800E+05	2
CO ₂	0	0.000000000000000E+00	1
e	0	0.000000000000000E+00	1

Table 4: NASA 9 polynomial constants

species	h_s^o [J/kg]	T_l	T_u	a_1	a_2	a_3	a_4	a_5
e	0.00000000E+00	2.00000000E+02	1.00000000E+03	0.00000000E+00	0.00000000E+00	2.50000000E+00	0.00000000E+00	0.00000000E+00
e	0.00000000E+00	1.00000000E+03	6.00000000E+03	0.00000000E+00	0.00000000E+00	2.50000000E+00	0.00000000E+00	0.00000000E+00
e	0.00000000E+00	6.00000000E+03	2.00000000E+04	0.00000000E+00	0.00000000E+00	2.50000000E+00	0.00000000E+00	0.00000000E+00
N	4.72680000E+05	2.00000000E+02	1.00000000E+03	0.00000000E+00	0.00000000E+00	2.50000000E+00	0.00000000E+00	0.00000000E+00
N	4.72680000E+05	1.00000000E+03	6.00000000E+03	8.876501380E+04	-1.071231500E+02	2.362188290E+00	2.916720080E-04	-1.729515100E-07
N	4.72680000E+05	6.00000000E+03	2.00000000E+04	5.475181050E+08	-3.107574980E+05	6.916782740E+01	-6.847988130E-03	3.827572400E-07
N ⁺	1.882127624E+06	2.00000000E+02	1.00000000E+03	5.237079210E+03	2.299958320E+00	2.487488820E+00	2.737490750E-05	-3.134447580E-08
N ⁺	1.882127624E+06	1.00000000E+03	6.00000000E+03	2.904970370E+05	-8.557908610E+02	3.477389290E+00	-5.288267190E-04	1.352350310E-07
N ⁺	1.882127624E+06	6.00000000E+03	2.00000000E+04	1.646092150E+07	-1.113165220E+04	4.976986640E+00	-2.005393580E-04	1.022481360E-08
N ₂	0.00000000E+00	2.00000000E+02	1.00000000E+03	2.210371220E+04	-3.818461450E+02	6.082738150E+00	-8.530913810E-03	1.384646100E-05
N ₂	0.00000000E+00	1.00000000E+03	6.00000000E+03	5.877099080E+05	-2.239242550E+03	6.066942670E+00	-6.139652960E-04	1.491798190E-07
N ₂	0.00000000E+00	6.00000000E+03	2.00000000E+04	8.309712000E+08	-6.420481870E+05	2.020205070E+02	-3.065019610E-02	2.486855580E-06
N ₂ ⁺	1.509508424E+06	2.00000000E+02	1.00000000E+03	-3.474041040E+04	2.696215430E+02	3.164919700E+00	-2.132247600E-03	6.730486360E-06
N ₂ ⁺	1.509508424E+06	1.00000000E+03	6.00000000E+03	-2.845597470E+06	7.058889150E+03	-2.884882650E+00	3.068675270E-03	-4.361647800E-07
N ₂ ⁺	1.509508424E+06	6.00000000E+03	2.00000000E+04	-3.712830950E+08	3.139288000E+05	-9.603519860E+01	1.571193500E-02	-1.175065670E-06
NO	9.126911000E+04	2.00000000E+02	1.00000000E+03	-1.143916580E+04	1.536467740E+02	3.431468650E+00	-2.668592130E-03	8.481398770E-06
NO	9.126911000E+04	1.00000000E+03	6.00000000E+03	2.239037080E+05	-1.289656240E+03	5.433940390E+00	-3.656055460E-04	9.881017630E-08
NO	9.126911000E+04	6.00000000E+03	2.00000000E+04	-9.575307640E+08	5.912436710E+05	-1.384567330E+02	1.694339980E-02	-1.007351460E-06
NO ⁺	9.908071040E+05	2.00000000E+02	1.00000000E+03	1.398526590E+03	-1.590494940E+02	5.122917320E+00	-6.394440050E-03	1.123924890E-05
NO ⁺	9.908071040E+05	1.00000000E+03	6.00000000E+03	6.069848430E+05	-2.278388310E+03	6.080317940E+00	-6.066815840E-04	1.431994710E-07
NO ⁺	9.908071040E+05	6.00000000E+03	2.00000000E+04	2.676400910E+09	-1.832949050E+06	5.099250210E+02	-7.113820250E-02	5.317660500E-06
O	2.491750030E+05	2.00000000E+02	1.00000000E+03	-7.953611300E+03	1.607177790E+02	1.966226440E+00	1.013670310E-03	-1.110415420E-06
O	2.491750030E+05	1.00000000E+03	6.00000000E+03	2.619020260E+05	-7.298722030E+02	3.317177270E+00	-4.281334360E-04	1.036104590E-07
O	2.491750030E+05	6.00000000E+03	2.00000000E+04	1.779004260E+08	-1.082328260E+05	2.810778370E+01	-2.975232260E-03	1.854997530E-07
O ⁺	1.568787228E+06	2.00000000E+02	1.00000000E+03	0.00000000E+00	0.00000000E+00	2.50000000E+00	0.00000000E+00	0.00000000E+00
O ⁺	1.568787228E+06	1.00000000E+03	6.00000000E+03	-2.166513210E+05	6.665456150E+02	1.702064360E+00	4.714992810E-04	-1.427131820E-07
O ⁺	1.568787228E+06	6.00000000E+03	2.00000000E+04	-2.143835380E+08	1.469518520E+05	-3.680864540E+01	5.036164540E-03	-3.087873850E-07
O ₂	0.00000000E+00	2.00000000E+02	1.00000000E+03	-3.425562690E+04	4.84699860E+02	1.119011590E+00	4.293887430E-03	-6.836273130E-07
O ₂	0.00000000E+00	1.00000000E+03	6.00000000E+03	-1.037939940E+06	2.344832750E+03	1.819729490E+00	1.267848870E-03	-2.188071420E-07
O ₂	0.00000000E+00	6.00000000E+03	2.00000000E+04	4.975152610E+08	-2.866023390E+05	6.690154640E+01	-6.169718690E-03	3.016237570E-07
O ₂ ⁺	1.171828436E+06	2.00000000E+02	1.00000000E+03	-8.177460710E+04	1.004762320E+03	-3.365400540E-01	6.105378490E-03	-2.704143960E-06
O ₂ ⁺	1.171828436E+06	1.00000000E+03	6.00000000E+03	7.366130500E+04	-8.458583620E+02	4.985419980E+00	-1.613281910E-04	6.434455480E-08
O ₂ ⁺	1.171828436E+06	6.00000000E+03	2.00000000E+04	-1.562258830E+09	1.161480870E+06	-3.302670370E+02	4.711128320E-02	-3.354580850E-06

Table 5: NASA 9 polynomial constants – continued

species	h_s^o [J/kg]	T_l	T_u	a_6	a_7	a_8	a_9	a_{10}
e	0.00000000E+00	2.00000000E+02	1.00000000E+03	0.00000000E+00	0.00000000E+00	0.00000000E+00	-7.453750000E+02	-1.172081270E+01
e	0.00000000E+00	1.00000000E+03	6.00000000E+03	0.00000000E+00	0.00000000E+00	0.00000000E+00	-7.453750000E+02	-1.172081270E+01
e	0.00000000E+00	6.00000000E+03	2.00000000E+04	0.00000000E+00	0.00000000E+00	0.00000000E+00	-7.453750000E+02	-1.172081270E+01
N	4.72680000E+05	2.00000000E+02	1.00000000E+03	0.00000000E+00	0.00000000E+00	0.00000000E+00	5.610463780E+04	4.193909320E+00
N	4.72680000E+05	1.00000000E+03	6.00000000E+03	4.012657880E-11	-2.677227570E-15	0.00000000E+00	5.697351330E+04	4.865235790E+00
N	4.72680000E+05	6.00000000E+03	2.00000000E+04	-1.098367710E-11	1.277986020E-16	0.00000000E+00	2.550585620E+06	-5.848769710E+02
N ⁺	1.882127624E+06	2.00000000E+02	1.00000000E+03	1.850111330E-11	-4.447350980E-15	0.00000000E+00	2.256284740E+05	5.076835070E+00
N ⁺	1.882127624E+06	1.00000000E+03	6.00000000E+03	-1.389834120E-11	5.046166280E-16	0.00000000E+00	2.310809980E+05	-1.994142260E+00
N ⁺	1.882127624E+06	6.00000000E+03	2.00000000E+04	-2.691430860E-13	3.539931590E-18	0.00000000E+00	3.136284700E+05	-1.706645950E+01
N ₂	0.00000000E+00	2.00000000E+02	1.00000000E+03	-9.625792930E-09	2.519705600E-12	0.00000000E+00	7.108459110E+02	-1.076003200E+01
N ₂	0.00000000E+00	1.00000000E+03	6.00000000E+03	-1.923094420E-11	1.061948710E-15	0.00000000E+00	1.283206180E+04	-1.586634840E+01
N ₂	0.00000000E+00	6.00000000E+03	2.00000000E+04	-9.705792080E-11	1.437516730E-15	0.00000000E+00	4.938506630E+06	-1.672047910E+03
N ₂ ⁺	1.509508424E+06	2.00000000E+02	1.00000000E+03	-5.637311510E-09	1.621757730E-12	0.00000000E+00	1.790004460E+05	6.832959350E+00
N ₂ ⁺	1.509508424E+06	1.00000000E+03	6.00000000E+03	2.102508820E-11	5.412025190E-16	0.00000000E+00	1.340388740E+05	5.090894720E+01
N ₂ ⁺	1.509508424E+06	6.00000000E+03	2.00000000E+04	4.144441720E-11	-5.621893770E-16	0.00000000E+00	-2.217362480E+06	8.436272570E+02
NO	9.126911000E+04	2.00000000E+02	1.00000000E+03	-7.685110790E-09	2.386797580E-12	0.00000000E+00	9.097949740E+03	6.728727950E+00
NO	9.126911000E+04	1.00000000E+03	6.00000000E+03	-1.416083270E-11	9.380216420E-16	0.00000000E+00	1.750294220E+04	-8.501699080E+00
NO	9.126911000E+04	6.00000000E+03	2.00000000E+04	2.912585260E-11	-3.295110910E-16	0.00000000E+00	-4.677503290E+06	1.242081660E+03
NO ⁺	9.908071040E+05	2.00000000E+02	1.00000000E+03	-7.988624190E-09	2.107395040E-12	0.00000000E+00	1.187492240E+05	-4.398557680E+00
NO ⁺	9.908071040E+05	1.00000000E+03	6.00000000E+03	-1.747980630E-11	8.934965000E-16	0.00000000E+00	1.322706020E+05	-1.519874900E+01
NO ⁺	9.908071040E+05	6.00000000E+03	2.00000000E+04	-1.963208420E-10	2.805268500E-15	0.00000000E+00	1.443309200E+07	-4.324045180E+03
O	2.491750030E+05	2.00000000E+02	1.00000000E+03	6.517507500E-10	-1.584779250E-13	0.00000000E+00	2.840362440E+04	8.404241820E+00
O	2.491750030E+05	1.00000000E+03	6.00000000E+03	-9.438304330E-12	2.725038300E-16	0.00000000E+00	3.392428060E+04	-6.679585350E-01
O	2.491750030E+05	6.00000000E+03	2.00000000E+04	-5.796231540E-12	7.191720160E-17	0.00000000E+00	8.890942630E+05	-2.181728150E+02
O ⁺	1.568787228E+06	2.00000000E+02	1.00000000E+03	0.00000000E+00	0.00000000E+00	0.00000000E+00	1.879352840E+05	4.393376760E+00
O ⁺	1.568787228E+06	1.00000000E+03	6.00000000E+03	2.016595900E-11	-9.107157760E-16	0.00000000E+00	1.837191970E+05	1.005690380E+01
O ⁺	1.568787228E+06	6.00000000E+03	2.00000000E+04	9.186834870E-12	-1.074163270E-16	0.00000000E+00	-9.614208960E+05	3.426193080E+02
O ₂	0.00000000E+00	2.00000000E+02	1.00000000E+03	-2.023374780E-09	1.039040640E-12	0.00000000E+00	-3.391454340E+03	1.849699120E+01
O ₂	0.00000000E+00	1.00000000E+03	6.00000000E+03	2.053724110E-11	-8.193490620E-16	0.00000000E+00	-1.689012530E+04	1.738718350E+01
O ₂	0.00000000E+00	6.00000000E+03	2.00000000E+04	-7.420878880E-12	7.277440630E-17	0.00000000E+00	2.293487550E+06	-5.530449680E+02
O ₂ ⁺	1.171828436E+06	2.00000000E+02	1.00000000E+03	-3.011962020E-10	4.162722550E-13	0.00000000E+00	1.347920230E+05	2.783215910E+01
O ₂ ⁺	1.171828436E+06	1.00000000E+03	6.00000000E+03	-1.506008230E-11	1.579044210E-15	0.00000000E+00	1.446310620E+05	-5.812784070E+00
O ₂ ⁺	1.171828436E+06	6.00000000E+03	2.00000000E+04	1.168007220E-10	-1.589805270E-15	0.00000000E+00	-8.858460550E+06	2.852180690E+03

Reaction data

Table 6 and 7 present the reaction data used by DPLR, LeMANS and KATS in this work, where A , η , and T_a are for the Arrhenius curve fit equation, and a_f , b_f , a_b , and b_b are constants used in the Park's two temperature model for forward and backward reaction temperatures.

Table 6: Reaction Data

Reaction	A (cm ³ /mole)	η	T_a [K]	a_f	b_f	a_b	b_b	T_{\min} [K]
Base Dissociation								
$N_2+M \rightleftharpoons 2N+M$	7.0E21	-1.6	1.132E5	0.5	0.5	1	0	800
$O_2+M \rightleftharpoons 2O+M$	2.0E21	-1.5	5.95E4	0.5	0.5	1	0	800
$NO+M \rightleftharpoons N+O+M$	5.0E15	0	7.55E4	0.5	0.5	1	0	800
Exchange								
$N_2+O \rightleftharpoons NO+N$	6.4E17	-1	3.84E4	1	0	1	0	800
$NO+O \rightleftharpoons O_2+N$	8.4E12	0	1.945E4	1	0	1	0	800
Charge Exchange								
$N_2+O_2^+ \rightleftharpoons N_2^++O_2$	9.9E12	0	4.070E4	1	0	1	0	800
$NO^++N \rightleftharpoons O^++N_2$	3.4E13	-1.08	1.280E4	1	0	1	0	800
$NO^++O \rightleftharpoons N^++O_2$	1.0E12	0.5	7.720E4	1	0	1	0	800
$NO^++O_2 \rightleftharpoons O_2^++NO$	2.4E13	0.41	3.260E4	1	0	1	0	800
$NO^++N \rightleftharpoons N_2^++O$	7.2E13	0	3.550E4	1	0	1	0	800
$O_2^++N \rightleftharpoons N^++O_2$	8.7E13	0.14	2.860E4	1	0	1	0	800
$O^++NO \rightleftharpoons N^++O_2$	1.4E5	1.9	1.530E4	1	0	1	0	800
$NO^++O \rightleftharpoons O_2^++N$	7.2E12	0.29	4.860E4	1	0	1	0	800
$O^++N_2 \rightleftharpoons N_2^++O$	9.1E11	0.36	2.280E4	1	0	1	0	800
Dissociative Recombination								
$N+O \rightleftharpoons NO^++e$	5.3E12	0	3.190E4	1	0	0	1	800
$N+N \rightleftharpoons N_2^++e$	2.0E13	0	6.750E4	1	0	0	1	800
$O+O \rightleftharpoons O_2^++e$	1.1E13	0	8.060E4	1	0	0	1	800
Electron Impact Ionization								
$N+e \rightleftharpoons N^++e+e$	2.5E34	-3.82	1.686E5	0	1	0	1	800
$O+e \rightleftharpoons O^++e+e$	3.9E33	-3.78	1.585E5	0	1	0	1	800
Electron Impact Dissociation								
$N_2+e \rightleftharpoons 2N+e$	3.0E24	-1.6	1.132E5	0	1	0	1	800

In the three-body dissociation reaction, the collision particle M represents any of the species in the mixture. For each of them, the reaction only differs in constant A .

A coefficient φ can be multiplied to the A of the base dissociation, then recovers for each species, as shown in Table 7.

Table 7: Coefficient φ for dissociation reaction

	N ₂ , O ₂ , NO	N, O	N ₂ ⁺ , O ₂ ⁺ , NO ⁺	N ⁺ , O ⁺	e
N ₂ +M=2N+M					
φ_s	1.0	4.28571428571429	1.0	4.28571428571429	0.0
O ₂ +M=2O+M					
φ_s	1.0	5.0	1.0	5.0	0.0
NO+M=N+O+M					
φ_s	1.0	22.0	1.0	22.0	0.0

Modified Millikan and White coefficients

The tabulated values for the modified coefficients A_{sr} and B_{sr} in Millikan and White model are shown in Table 8 and 9.

Table 8: Modified Millikan and White Coefficients

Vibrator	Partner	A_{sr}	B_{sr}
N ₂	N ₂	221.53	0.029
N ₂	O ₂	228.76	0.0295
N ₂	N	180.88	0.0262
N ₂	O	72.4	0.015
N ₂	NO	225.3	0.0293
N ₂	N ₂ ⁺	221.53	0.029
N ₂	O ₂ ⁺	228.76	0.0295
N ₂	N ⁺	180.88	0.0262
N ₂	O ⁺	188.89	0.0268
N ₂	NO ⁺	225.3	0.0293
N ₂	e	1.39	0.0023
O ₂	N ₂	131.32	0.0295
O ₂	O ₂	135.91	0.03
O ₂	N	72.4	0.015
O ₂	O	47.7	0.059
O ₂	NO	133.71	0.0298
O ₂	N ₂ ⁺	131.32	0.0295
O ₂	O ₂ ⁺	135.91	0.03
O ₂	N ⁺	106.06	0.0265
O ₂	O ⁺	110.97	0.0271
O ₂	NO ⁺	133.71	0.0298
O ₂	e	0.8	0.0023
NO	N ₂	49.5	0.042
NO	O ₂	49.5	0.042
NO	N	49.5	0.042
NO	O	49.5	0.042
NO	NO	49.5	0.042
NO	N ₂ ⁺	175.67	0.0293
NO	O ₂ ⁺	181.6	0.0298
NO	N ⁺	142.62	0.0264
NO	O ⁺	149.08	0.027
NO	NO ⁺	178.76	0.0295
NO	e	1.08	0.0023

Table 9: Modified Millikan and White Coefficients – continued

Vibrator	Partner	A_{sr}	B_{sr}
N_2^+	N_2	221.53	0.029
N_2^+	O_2	228.76	0.0295
N_2^+	N	180.88	0.0262
N_2^+	O	188.89	0.0268
N_2^+	NO	225.3	0.0293
N_2^+	N_2^+	221.53	0.029
N_2^+	O_2^+	228.75	0.0295
N_2^+	N^+	180.88	0.0262
N_2^+	O^+	188.88	0.0268
N_2^+	NO^+	225.3	0.0293
N_2^+	e	1.39	0.0023
O_2^+	N_2	131.32	0.0295
O_2^+	O_2	135.91	0.03
O_2^+	N	106.06	0.0265
O_2^+	O	110.97	0.0271
O_2^+	NO	133.71	0.0298
O_2^+	N_2^+	131.32	0.0295
O_2^+	O_2^+	135.9	0.03
O_2^+	N^+	106.05	0.0265
O_2^+	O^+	110.97	0.0271
O_2^+	NO^+	133.7	0.0298
O_2^+	e	0.8	0.0023
NO^+	N_2	175.67	0.0293
NO^+	O_2	181.61	0.0298
NO^+	N	142.62	0.0264
NO^+	O	149.09	0.027
NO^+	NO	178.76	0.0295
NO^+	N_2^+	175.67	0.0293
NO^+	O_2^+	181.6	0.0298
NO^+	N^+	142.62	0.0264
NO^+	O^+	149.08	0.027
NO^+	NO^+	178.76	0.0295
NO^+	e	1.08	0.0023

Appendix B: Detailed Derivations: Hypersonic Solver

Jacobian of the inviscid flux vector

The *homogeneity property* of the inviscid flux vector [66] at a generic face yields

$$\mathcal{F} \cdot \mathbf{n} = \mathbf{F}_n = \mathcal{A}\mathbf{Q} \quad , \quad (7.1)$$

where the Jacobian matrix is given by

$$\mathcal{A} = \frac{\partial \mathbf{F}_n}{\partial \mathbf{Q}} \quad . \quad (7.2)$$

The Jacobian matrix \mathcal{A} is diagonalizable according to the assumption of *hyperbolicity* [66–68], namely

$$\mathcal{A} = \mathcal{L}\mathbf{\Lambda}\mathcal{R} \quad , \quad (7.3)$$

where $\mathbf{\Lambda}$ is the diagonal matrix composed of the real eigenvalues λ_i of Jacobian matrix \mathcal{A} , \mathcal{L} is a non-singular matrix whose columns are the right eigenvectors of matrix \mathcal{A} , and \mathcal{R} is the inverse of \mathcal{L} , which implies

$$\mathcal{L}\mathcal{R} = \mathcal{I} \quad . \quad (7.4)$$

Thermal Non-equilibrium

For flow in thermal non-equilibrium, matrix \mathcal{L} , and \mathcal{R} is respectively defined as [117]

$$\mathcal{L} = \left(\begin{array}{cccccc} \delta_{sr}/a^2 & 0 & 0 & c_s/(2a^2) & c_s/(2a^2) & 0 \\ u/a^2 & l_x & m_x & (u + an_x)/(2a^2) & (u - an_x)/(2a^2) & 0 \\ v/a^2 & l_y & m_y & (v + an_y)/(2a^2) & (v - an_y)/(2a^2) & 0 \\ w/a^2 & l_z & m_z & (w + an_z)/(2a^2) & (w - an_z)/(2a^2) & 0 \\ [\beta(u^2 + v^2 + w^2) - \tilde{\gamma}_r]/(\beta a^2) & V & W & (H + aU)/(2a^2) & (H - aU)/(2a^2) & -\phi/(\beta a^2) \\ 0 & 0 & 0 & e_{ve}/(2a^2) & e_{ve}/(2a^2) & 1/a^2 \end{array} \right)$$

and

$$\mathbf{R} = \begin{pmatrix} a^2 \delta_{sr} - c_s \tilde{\gamma}_r & \beta u c_s & \beta v c_s & \beta w c_s & -\beta c_s & -\phi c_s \\ -V & l_x & l_y & l_z & 0 & 0 \\ -W & m_x & m_y & m_z & 0 & 0 \\ \tilde{\gamma}_r - Ua & an_x - \beta u & an_y - \beta v & an_z - \beta w & \beta & \phi \\ \tilde{\gamma}_r + Ua & -an_x - \beta u & -an_y - \beta v & -an_z - \beta w & \beta & \phi \\ -e_{ve} \tilde{\gamma}_r & \beta u e_{ve} & \beta v e_{ve} & \beta w e_{ve} & -\beta e_{ve} & a^2 - \phi e_{ve} \end{pmatrix}$$

in which, n_x , n_y and n_z denotes x , y and z component of the unit normal vector to the generic face respectively. The two unit tangential vectors are denoted by (l_x, l_y, l_z) and (m_x, m_y, m_z) . The normal component of velocity through the face is given by

$$U = un_x + vn_y + wn_z \quad . \quad (7.5)$$

The tangential velocity components corresponding to \mathbf{l} and \mathbf{m} are given by

$$V = ul_x + vl_y + wl_z \quad , \quad (7.6)$$

and

$$W = um_x + vm_y + wm_z \quad . \quad (7.7)$$

The variables β , ϕ and $\tilde{\gamma}_r$ are related to the partial derivatives of total pressure with respect to \mathbf{Q} , given by

$$\beta = \frac{\partial p}{\partial E} = \frac{R_u}{\rho C v_{tr}} \sum_{s \neq e} \frac{\rho_s}{M_s} \quad (7.8)$$

$$\phi = \frac{\partial p}{\partial E_{ve}} = \frac{R_u}{\rho C v_{ve}} \frac{\rho_e}{M_e} - \beta \quad (7.9)$$

$$\tilde{\gamma}_r = \frac{\partial p}{\partial \rho_r} = \frac{R_u T_r}{M_r} + \beta \frac{u^2 + v^2 + w^2}{2} - \beta e_r - \phi e_{ve,r} \quad (7.10)$$

It is noted that $T_r = T_{tr}$ for all species except for electron, $T_r = T_{ve}$. And s denotes species s in row and r denotes species r in column when looking at the matrix \mathcal{L} and

R. The total energy, E , and total vibrational-electron-electronic energy, E_{ve} , per unit volume.

Attention should be paid here that the enthalpy, H , is defined per unit mass, given by

$$H = \frac{E + p}{\rho} \quad . \quad (7.11)$$

The frozen speed of sound a is evaluated by

$$a^2 = \sum_{s=1}^{ns} c_s \tilde{\gamma}_s + \beta[H - (u^2 + v^2 + w^2)] + \phi e_{ve} = (1 + \beta) \frac{p}{\rho} \quad . \quad (7.12)$$

Finally, the diagonal matrix of eigenvalues of \mathbf{A} is given by

$$\mathbf{\Lambda} = \begin{pmatrix} U & 0 & 0 & 0 & 0 & 0 \\ 0 & U & 0 & 0 & 0 & 0 \\ 0 & 0 & U & 0 & 0 & 0 \\ 0 & 0 & 0 & U + a & 0 & 0 \\ 0 & 0 & 0 & 0 & U - a & 0 \\ 0 & 0 & 0 & 0 & 0 & U \end{pmatrix}$$

Thermal equilibrium

KATS can solve flow in thermal equilibrium state by using just one energy equation.

In this case, matrices \mathbf{L} and \mathbf{R} are defined as

$$\mathbf{L} = \begin{pmatrix} \delta_{sr}/a^2 & 0 & 0 & c_s/(2a^2) & c_s/(2a^2) \\ u/a^2 & l_x & m_x & (u + an_x)/(2a^2) & (u - an_x)/(2a^2) \\ v/a^2 & l_y & m_y & (v + an_y)/(2a^2) & (v - an_y)/(2a^2) \\ w/a^2 & l_z & m_z & (w + an_z)/(2a^2) & (w - an_z)/(2a^2) \\ [\beta(u^2 + v^2 + w^2) - \tilde{\gamma}_r]/(\beta a^2) & V & W & (H + aU)/(2a^2) & (H - aU)/(2a^2) \end{pmatrix}$$

and

$$\mathcal{R} = \begin{pmatrix} a^2\delta_{sr} - c_s\tilde{\gamma}_{sr} & \beta uc_s & \beta vc_s & \beta wc_s & -\beta c_s \\ -V & l_x & l_y & l_z & 0 \\ -W & m_x & m_y & m_z & 0 \\ \tilde{\gamma}_r - Ua & an_x - \beta u & an_y - \beta v & an_z - \beta w & \beta \\ \tilde{\gamma}_r + Ua & -an_x - \beta u & -an_y - \beta v & -an_z - \beta w & \beta \end{pmatrix}$$

The diagonal matrix of eigenvalues of \mathcal{A} is given by

$$\mathbf{\Lambda} = \begin{pmatrix} U & 0 & 0 & 0 & 0 \\ 0 & U & 0 & 0 & 0 \\ 0 & 0 & U & 0 & 0 \\ 0 & 0 & 0 & U + a & 0 \\ 0 & 0 & 0 & 0 & U - a \end{pmatrix}$$

Derivation of Derivatives of Total Pressure with Respect to Conservative Variables for Non-equilibrium State

Details can be found in Gnoffo's technical report [46].

Derivation of Derivatives of Total Pressure with Respect to Conservative Variables for Equilibrium State

The total pressure of the mixture is written as

$$p = \sum \frac{\rho_s R_u T}{M_s} \quad . \quad (7.13)$$

Its differential expression can be written as

$$dp = R_u T \sum \frac{d\rho_s}{M_s} + \sum \frac{\rho_s R_u}{M_s} dT \quad . \quad (7.14)$$

Since

$$de = \sum dc_s e_s + \sum c_s de_s = \sum dc_s e_s + \sum c_s C_{v,s} dT \quad . \quad (7.15)$$

It yields

$$dT = \frac{de - \sum dc_s e_s}{Cv} \quad (7.16)$$

Recall

$$de = \frac{d\rho E - E d\rho - (ud\rho u + vd\rho v + wd\rho w) + (u^2 + v^2 + w^2)d\rho}{\rho} \quad (7.17)$$

$$dc_s = \frac{d\rho_s - c_s d\rho}{\rho} \quad (7.18)$$

Eqn. (7.16) can be written as

$$\begin{aligned} dT &= \frac{de - \sum dc_s e_s}{Cv} \\ &= \frac{d\rho E - E d\rho - (ud\rho u + vd\rho v + wd\rho w) + (u^2 + v^2 + w^2)d\rho - \sum (d\rho_s - c_s d\rho)e_s}{\rho Cv} \end{aligned} \quad (7.19)$$

Substitution of Eqn. (7.19) into Eqn.(7.14) ends up with

$$\begin{aligned} dp &= R_u T \sum \frac{d\rho_s}{M_s} + \sum \frac{\rho_s R_u}{M_s} dT \\ &= R_u T \sum \frac{d\rho_s}{M_s} + \sum \frac{\rho_s R_u}{M_s} \frac{d\rho E - E d\rho - (ud\rho u + vd\rho v + wd\rho w) + (u^2 + v^2 + w^2)d\rho - \sum (d\rho_s - c_s d\rho)e_s}{\rho Cv} \end{aligned} \quad (7.20)$$

Set

$$\beta = \frac{R_u}{\rho Cv} \sum \frac{\rho_s}{M_s} \quad (7.21)$$

$$\begin{aligned} dp &= R_u T \sum \frac{d\rho_s}{M_s} + \beta \left[d\rho E - E d\rho - (ud\rho u + vd\rho v + wd\rho w) + (u^2 + v^2 + w^2)d\rho - \sum (d\rho_s - c_s d\rho)e_s \right] \\ &= R_u T \sum \frac{d\rho_s}{M_s} + \beta [d\rho E - (ud\rho u + vd\rho v + wd\rho w)] + \beta \left[-E d\rho + (u^2 + v^2 + w^2)d\rho - \sum e_s d\rho_s - \sum c_s e_s d\rho \right] \\ &= R_u T \sum \frac{d\rho_s}{M_s} + \beta [d\rho E - (ud\rho u + vd\rho v + wd\rho w)] + \beta \left[\frac{1}{2}(u^2 + v^2 + w^2)d\rho - \sum e_s d\rho_s \right] \\ &= \beta [d\rho E - (ud\rho u + vd\rho v + wd\rho w)] + R_u T \sum \frac{d\rho_s}{M_s} + \beta \left[\frac{1}{2}(u^2 + v^2 + w^2)d\rho - \sum e_s d\rho_s \right] \end{aligned} \quad (7.22)$$

where

$$E = \sum c_s e_s + \frac{1}{2}(u^2 + v^2 + w^2) \quad (7.23)$$

Finally

$$\beta = \frac{\partial p}{\partial \rho E} = \frac{R_u}{\rho C v} \sum \frac{\rho_s}{M_s} \quad (7.24)$$

$$\tilde{\gamma}_s = \frac{\partial p}{\partial \rho_s} = \frac{R_u T}{M_s} + \beta \frac{u^2 + v^2 + w^2}{2} - \beta e_s \quad (7.25)$$

Inviscid Jacobians

Recall that the *homogeneity property* of the inviscid flux vector at a generic face suggests

$$\mathcal{F} \cdot \mathbf{n} = \mathbf{F}_n = \mathcal{A} \mathbf{Q} \quad , \quad (7.26)$$

and the Jacobian matrix

$$\mathcal{A} = \frac{\partial \mathbf{F}_n}{\partial \mathbf{Q}} \quad . \quad (7.27)$$

The computation of inviscid flux vector \mathbf{F}_n can be accomplished by a flux vector splitting method, for instance, Steger-Warming method, which in a generic way is given by

$$\mathbf{F}_n = \mathbf{F}_n^+ + \mathbf{F}_n^- = \mathcal{A}_l^+ \mathbf{Q}_l + \mathcal{A}_r^- \mathbf{Q}_r \quad . \quad (7.28)$$

The inviscid flux Jacobians for implicit method, however, are not the same as those used for inviscid fluxes. The reason is that the homogeneity property feature is lost for the two split fluxes. That is to say, although the split flux obtained from

$$\mathbf{F}_n^\pm = \mathcal{A}^\pm \mathbf{Q} \quad (7.29)$$

is still valid,

$$\frac{\partial \mathbf{F}_n^\pm}{\partial \mathbf{Q}} \neq \mathcal{A}^\pm \quad . \quad (7.30)$$

Therefore, it is more appropriate to use the true inviscid Jacobians $\frac{\partial \mathbf{F}_n^\pm}{\partial \mathbf{Q}}$ in the implicit operator instead of \mathcal{A}^\pm . For that purpose, the flux vector has to be found first of all, which can be formulated analytically by

$$\mathbf{F}_n^\pm = \mathcal{A}^\pm \mathbf{Q} = \mathcal{L} \Lambda^\pm \mathcal{R} \mathbf{Q} \quad (7.31)$$

Inviscid Jacobians for Non-Equilibrium State

With the details of \mathcal{L} , $\mathbf{\Lambda}$, and \mathcal{R} , and by using Eqn. (7.31), the inviscid fluxes for thermal non-equilibrium state are finally expressed as

$$\mathbf{F}_n^\pm = \begin{pmatrix} \frac{p}{\rho a^2} \frac{\partial p}{\partial \rho E} \rho_s \lambda_1^\pm + \frac{1}{2a^2} \left(a^2 - \frac{p}{\rho} \frac{\partial p}{\partial \rho E} \right) \rho_s \lambda_2^\pm + \frac{1}{2a^2} \left(a^2 - \frac{p}{\rho} \frac{\partial p}{\partial \rho E} \right) \rho_s \lambda_3^\pm \\ \frac{p}{\rho a^2} \frac{\partial p}{\partial \rho E} \rho u \lambda_1^\pm + \frac{1}{2a^2} \left(a^2 - \frac{p}{\rho} \frac{\partial p}{\partial \rho E} \right) \rho (u + an_x) \lambda_2^\pm + \frac{1}{2a^2} \left(a^2 - \frac{p}{\rho} \frac{\partial p}{\partial \rho E} \right) \rho (u - an_x) \lambda_3^\pm \\ \frac{p}{\rho a^2} \frac{\partial p}{\partial \rho E} \rho v \lambda_1^\pm + \frac{1}{2a^2} \left(a^2 - \frac{p}{\rho} \frac{\partial p}{\partial \rho E} \right) \rho (v + an_y) \lambda_2^\pm + \frac{1}{2a^2} \left(a^2 - \frac{p}{\rho} \frac{\partial p}{\partial \rho E} \right) \rho (v - an_y) \lambda_3^\pm \\ \frac{p}{\rho a^2} \frac{\partial p}{\partial \rho E} \rho w \lambda_1^\pm + \frac{1}{2a^2} \left(a^2 - \frac{p}{\rho} \frac{\partial p}{\partial \rho E} \right) \rho (w + an_z) \lambda_2^\pm + \frac{1}{2a^2} \left(a^2 - \frac{p}{\rho} \frac{\partial p}{\partial \rho E} \right) \rho (w - an_z) \lambda_3^\pm \\ \left(\rho E - \frac{H}{a^2} \left(\rho a^2 - p \frac{\partial p}{\partial \rho E} \right) \right) \lambda_1^\pm + \frac{H+aU}{2a^2} \left(\rho a^2 - p \frac{\partial p}{\partial \rho E} \right) + \frac{H-aU}{2a^2} \left(\rho a^2 - p \frac{\partial p}{\partial \rho E} \right) \lambda_3^\pm \\ \frac{p}{\rho a^2} \frac{\partial p}{\partial \rho E} \rho E_{ve} \lambda_1^\pm + \frac{1}{2a^2} \left(a^2 - \frac{p}{\rho} \frac{\partial p}{\partial \rho E} \right) \rho E_{ve} \lambda_2^\pm + \frac{1}{2a^2} \left(a^2 - \frac{p}{\rho} \frac{\partial p}{\partial \rho E} \right) \rho E_{ve} \lambda_3^\pm \end{pmatrix}.$$

It can also be simplified as

$$\mathbf{F}_n^\pm = \begin{pmatrix} \frac{\gamma-1}{\gamma} \rho_s \lambda_1^\pm + \frac{1}{2\gamma} \rho_s \lambda_2^\pm + \frac{1}{2\gamma} \rho_s \lambda_3^\pm \\ \frac{\gamma-1}{\gamma} \rho u \lambda_1^\pm + \frac{1}{2\gamma} \rho (u + an_x) \lambda_2^\pm + \frac{1}{2\gamma} \rho (u - an_x) \lambda_3^\pm \\ \frac{\gamma-1}{\gamma} \rho v \lambda_1^\pm + \frac{1}{2\gamma} \rho (v + an_y) \lambda_2^\pm + \frac{1}{2\gamma} \rho (v - an_y) \lambda_3^\pm \\ \frac{\gamma-1}{\gamma} \rho w \lambda_1^\pm + \frac{1}{2\gamma} \rho (w + an_z) \lambda_2^\pm + \frac{1}{2\gamma} \rho (w - an_z) \lambda_3^\pm \\ \frac{\gamma-1}{\gamma} \rho \epsilon_1 \lambda_1^\pm + \frac{1}{2\gamma} \rho \epsilon_2 \lambda_2^\pm + \frac{1}{2\gamma} \rho \epsilon_3 \lambda_3^\pm \\ \frac{\gamma-1}{\gamma} \rho E_{ve} \lambda_1^\pm + \frac{1}{2\gamma} \rho E_{ve} \lambda_2^\pm + \frac{1}{2\gamma} \rho E_{ve} \lambda_3^\pm \end{pmatrix}.$$

where

$$\begin{aligned} \epsilon_1 &= \frac{1}{2} (u^2 + v^2 + w^2) + e_{ve} + h^o \\ \epsilon_2 &= \frac{(3-\gamma)}{2(\gamma-1)} a^2 + \frac{1}{2} ((u + an_x)^2 + (v + an_y)^2 + (w + an_z)^2) + e_{ve} + h^o \\ \epsilon_3 &= \frac{(3-\gamma)}{2(\gamma-1)} a^2 + \frac{1}{2} ((u - an_x)^2 + (v - an_y)^2 + (w - an_z)^2) + e_{ve} + h^o \end{aligned} \quad (7.32)$$

and

$$e_{ve} = \sum \frac{\rho_s}{\rho} e_{ve,s} \quad (7.33)$$

$$h^o = \sum \frac{\rho_s}{\rho} h_s^o \quad (7.34)$$

The primary dependent variables in this work are primitive variables \mathbf{P} . The Jacobians of inviscid flux vector are thus computed with respect to them. It is a lot easier to use the chain rule to obtain the Jacobian, which is given by

$$\frac{\partial \mathbf{F}_n^\pm}{\partial \mathbf{P}} = \frac{\partial \mathbf{F}_n^\pm}{\partial \mathbf{W}} \frac{\partial \mathbf{W}}{\partial \mathbf{P}} \quad (7.35)$$

where the introduced set of variables are

$$\mathbf{W} = \begin{pmatrix} \rho_s \\ u \\ v \\ w \\ a \\ e_{ve} \end{pmatrix} .$$

The Jacobian $\frac{\partial \mathbf{F}_n^\pm}{\partial \mathbf{W}}$ is given by

$$\frac{\partial \mathbf{F}_n^\pm}{\partial \mathbf{W}} = \begin{pmatrix} \frac{\partial \mathbf{F}_{\rho s}^\pm}{\partial \rho_r} & \frac{\partial \mathbf{F}_{\rho s}^\pm}{\partial u} & \frac{\partial \mathbf{F}_{\rho s}^\pm}{\partial v} & \frac{\partial \mathbf{F}_{\rho s}^\pm}{\partial w} & \frac{\partial \mathbf{F}_{\rho s}^\pm}{\partial a} & \frac{\partial \mathbf{F}_{\rho s}^\pm}{\partial e_{ve}} \\ \frac{\partial \mathbf{F}_{\rho u}^\pm}{\partial \rho_r} & \frac{\partial \mathbf{F}_{\rho u}^\pm}{\partial u} & \frac{\partial \mathbf{F}_{\rho u}^\pm}{\partial v} & \frac{\partial \mathbf{F}_{\rho u}^\pm}{\partial w} & \frac{\partial \mathbf{F}_{\rho u}^\pm}{\partial a} & \frac{\partial \mathbf{F}_{\rho u}^\pm}{\partial e_{ve}} \\ \frac{\partial \mathbf{F}_{\rho v}^\pm}{\partial \rho_r} & \frac{\partial \mathbf{F}_{\rho v}^\pm}{\partial u} & \frac{\partial \mathbf{F}_{\rho v}^\pm}{\partial v} & \frac{\partial \mathbf{F}_{\rho v}^\pm}{\partial w} & \frac{\partial \mathbf{F}_{\rho v}^\pm}{\partial a} & \frac{\partial \mathbf{F}_{\rho v}^\pm}{\partial e_{ve}} \\ \frac{\partial \mathbf{F}_{\rho w}^\pm}{\partial \rho_r} & \frac{\partial \mathbf{F}_{\rho w}^\pm}{\partial u} & \frac{\partial \mathbf{F}_{\rho w}^\pm}{\partial v} & \frac{\partial \mathbf{F}_{\rho w}^\pm}{\partial w} & \frac{\partial \mathbf{F}_{\rho w}^\pm}{\partial a} & \frac{\partial \mathbf{F}_{\rho w}^\pm}{\partial e_{ve}} \\ \frac{\partial \mathbf{F}_{\rho E}^\pm}{\partial \rho_r} & \frac{\partial \mathbf{F}_{\rho E}^\pm}{\partial u} & \frac{\partial \mathbf{F}_{\rho E}^\pm}{\partial v} & \frac{\partial \mathbf{F}_{\rho E}^\pm}{\partial w} & \frac{\partial \mathbf{F}_{\rho E}^\pm}{\partial a} & \frac{\partial \mathbf{F}_{\rho E}^\pm}{\partial e_{ve}} \\ \frac{\partial \mathbf{F}_{\rho E v e}^\pm}{\partial \rho_r} & \frac{\partial \mathbf{F}_{\rho E v e}^\pm}{\partial u} & \frac{\partial \mathbf{F}_{\rho E v e}^\pm}{\partial v} & \frac{\partial \mathbf{F}_{\rho E v e}^\pm}{\partial w} & \frac{\partial \mathbf{F}_{\rho E v e}^\pm}{\partial a} & \frac{\partial \mathbf{F}_{\rho E v e}^\pm}{\partial e_{ve}} \end{pmatrix}$$

Details for each term are listed as

$$\begin{aligned}
\frac{\partial \mathbf{F}_{\rho_s}^\pm}{\partial \rho_r} &= \frac{\gamma-1}{\gamma} \lambda_1^\pm + \frac{1}{2\gamma} \lambda_2^\pm + \frac{1}{2\gamma} \lambda_3^\pm \\
\frac{\partial \mathbf{F}_{\rho_s}^\pm}{\partial u} &= \rho_s \left(\frac{\gamma-1}{\gamma} \frac{\partial \lambda_1^\pm}{\partial u} + \frac{1}{2\gamma} \frac{\partial \lambda_2^\pm}{\partial u} + \frac{1}{2\gamma} \frac{\partial \lambda_3^\pm}{\partial u} \right) \\
\frac{\partial \mathbf{F}_{\rho_s}^\pm}{\partial v} &= \rho_s \left(\frac{\gamma-1}{\gamma} \frac{\partial \lambda_1^\pm}{\partial v} + \frac{1}{2\gamma} \frac{\partial \lambda_2^\pm}{\partial v} + \frac{1}{2\gamma} \frac{\partial \lambda_3^\pm}{\partial v} \right) \\
\frac{\partial \mathbf{F}_{\rho_s}^\pm}{\partial w} &= \rho_s \left(\frac{\gamma-1}{\gamma} \frac{\partial \lambda_1^\pm}{\partial w} + \frac{1}{2\gamma} \frac{\partial \lambda_2^\pm}{\partial w} + \frac{1}{2\gamma} \frac{\partial \lambda_3^\pm}{\partial w} \right) \\
\frac{\partial \mathbf{F}_{\rho_s}^\pm}{\partial a} &= \rho_s \left(\frac{\gamma-1}{\gamma} \frac{\partial \lambda_1^\pm}{\partial a} + \frac{1}{2\gamma} \frac{\partial \lambda_2^\pm}{\partial a} + \frac{1}{2\gamma} \frac{\partial \lambda_3^\pm}{\partial a} \right) \\
\frac{\partial \mathbf{F}_{\rho_s}^\pm}{\partial e_{ve}} &= \rho_s \left(\frac{\gamma-1}{\gamma} \frac{\partial \lambda_1^\pm}{\partial e_{ve}} + \frac{1}{2\gamma} \frac{\partial \lambda_2^\pm}{\partial e_{ve}} + \frac{1}{2\gamma} \frac{\partial \lambda_3^\pm}{\partial e_{ve}} \right)
\end{aligned} \tag{7.36}$$

$$\begin{aligned}
\frac{\partial \mathbf{F}_{\rho u}^\pm}{\partial \rho_r} &= \frac{\gamma-1}{\gamma} u \lambda_1^\pm + \frac{1}{2\gamma} (u + an_x) \lambda_2^\pm + \frac{1}{2\gamma} (u - an_x) \lambda_3^\pm \\
\frac{\partial \mathbf{F}_{\rho u}^\pm}{\partial u} &= \rho \left(\frac{\gamma-1}{\gamma} \lambda_1^\pm + \frac{1}{2\gamma} \lambda_2^\pm + \frac{1}{2\gamma} \lambda_3^\pm \right) + \frac{\gamma-1}{\gamma} \rho u \frac{\partial \lambda_1^\pm}{\partial u} + \frac{1}{2\gamma} \rho (u + an_x) \frac{\partial \lambda_2^\pm}{\partial u} + \frac{1}{2\gamma} \rho (u - an_x) \frac{\partial \lambda_3^\pm}{\partial u} \\
\frac{\partial \mathbf{F}_{\rho u}^\pm}{\partial v} &= \frac{\gamma-1}{\gamma} \rho u \frac{\partial \lambda_1^\pm}{\partial v} + \frac{1}{2\gamma} \rho (u + an_x) \frac{\partial \lambda_2^\pm}{\partial v} + \frac{1}{2\gamma} \rho (u - an_x) \frac{\partial \lambda_3^\pm}{\partial v} \\
\frac{\partial \mathbf{F}_{\rho u}^\pm}{\partial w} &= \frac{\gamma-1}{\gamma} \rho u \frac{\partial \lambda_1^\pm}{\partial w} + \frac{1}{2\gamma} \rho (u + an_x) \frac{\partial \lambda_2^\pm}{\partial w} + \frac{1}{2\gamma} \rho (u - an_x) \frac{\partial \lambda_3^\pm}{\partial w} \\
\frac{\partial \mathbf{F}_{\rho u}^\pm}{\partial a} &= \frac{\rho}{2\gamma} n_x \lambda_2^\pm - \frac{\rho}{2\gamma} n_x \lambda_3^\pm + \frac{\gamma-1}{\gamma} \rho u \frac{\partial \lambda_1^\pm}{\partial a} + \frac{1}{2\gamma} \rho (u + an_x) \frac{\partial \lambda_2^\pm}{\partial a} + \frac{1}{2\gamma} \rho (u - an_x) \frac{\partial \lambda_3^\pm}{\partial a} \\
\frac{\partial \mathbf{F}_{\rho u}^\pm}{\partial e_{ve}} &= \frac{\gamma-1}{\gamma} \rho u \frac{\partial \lambda_1^\pm}{\partial e_{ve}} + \frac{1}{2\gamma} \rho (u + an_x) \frac{\partial \lambda_2^\pm}{\partial e_{ve}} + \frac{1}{2\gamma} \rho (u - an_x) \frac{\partial \lambda_3^\pm}{\partial e_{ve}}
\end{aligned} \tag{7.37}$$

$$\begin{aligned}
\frac{\partial \mathbf{F}_{\rho v}^{\pm}}{\partial \rho_r} &= \frac{\gamma-1}{\gamma} v \lambda_1^{\pm} + \frac{1}{2\gamma} (v + an_y) \lambda_2^{\pm} + \frac{1}{2\gamma} (v - an_y) \lambda_3^{\pm} \\
\frac{\partial \mathbf{F}_{\rho v}^{\pm}}{\partial u} &= \frac{\gamma-1}{\gamma} \rho v \frac{\partial \lambda_1^{\pm}}{\partial u} + \frac{1}{2\gamma} \rho (v + an_y) \frac{\partial \lambda_2^{\pm}}{\partial u} + \frac{1}{2\gamma} \rho (v - an_y) \frac{\partial \lambda_3^{\pm}}{\partial u} \\
\frac{\partial \mathbf{F}_{\rho v}^{\pm}}{\partial v} &= \rho \left(\frac{\gamma-1}{\gamma} \lambda_1^{\pm} + \frac{1}{2\gamma} \lambda_2^{\pm} + \frac{1}{2\gamma} \lambda_3^{\pm} \right) + \frac{\gamma-1}{\gamma} \rho v \frac{\partial \lambda_1^{\pm}}{\partial v} + \frac{1}{2\gamma} \rho (v + an_y) \frac{\partial \lambda_2^{\pm}}{\partial v} + \frac{1}{2\gamma} \rho (v - an_y) \frac{\partial \lambda_3^{\pm}}{\partial v} \\
\frac{\partial \mathbf{F}_{\rho v}^{\pm}}{\partial w} &= \frac{\gamma-1}{\gamma} \rho v \frac{\partial \lambda_1^{\pm}}{\partial w} + \frac{1}{2\gamma} \rho (v + an_y) \frac{\partial \lambda_2^{\pm}}{\partial w} + \frac{1}{2\gamma} \rho (v - an_y) \frac{\partial \lambda_3^{\pm}}{\partial w} \\
\frac{\partial \mathbf{F}_{\rho v}^{\pm}}{\partial a} &= \frac{\rho}{2\gamma} n_y \lambda_2^{\pm} - \frac{\rho}{2\gamma} n_y \lambda_3^{\pm} + \frac{\gamma-1}{\gamma} \rho v \frac{\partial \lambda_1^{\pm}}{\partial a} + \frac{1}{2\gamma} \rho (v + an_y) \frac{\partial \lambda_2^{\pm}}{\partial a} + \frac{1}{2\gamma} \rho (v - an_y) \frac{\partial \lambda_3^{\pm}}{\partial a} \\
\frac{\partial \mathbf{F}_{\rho v}^{\pm}}{\partial e_{ve}} &= \frac{\gamma-1}{\gamma} \rho v \frac{\partial \lambda_1^{\pm}}{\partial e_{ve}} + \frac{1}{2\gamma} \rho (v + an_y) \frac{\partial \lambda_2^{\pm}}{\partial e_{ve}} + \frac{1}{2\gamma} \rho (v - an_y) \frac{\partial \lambda_3^{\pm}}{\partial e_{ve}}
\end{aligned} \tag{7.38}$$

$$\begin{aligned}
\frac{\partial \mathbf{F}_{\rho w}^{\pm}}{\partial \rho_r} &= \frac{\gamma-1}{\gamma} w \lambda_1^{\pm} + \frac{1}{2\gamma} (w + an_z) \lambda_2^{\pm} + \frac{1}{2\gamma} (w - an_z) \lambda_3^{\pm} \\
\frac{\partial \mathbf{F}_{\rho w}^{\pm}}{\partial u} &= \frac{\gamma-1}{\gamma} \rho w \frac{\partial \lambda_1^{\pm}}{\partial u} + \frac{1}{2\gamma} \rho (w + an_z) \frac{\partial \lambda_2^{\pm}}{\partial u} + \frac{1}{2\gamma} \rho (w - an_z) \frac{\partial \lambda_3^{\pm}}{\partial u} \\
\frac{\partial \mathbf{F}_{\rho w}^{\pm}}{\partial v} &= \frac{\gamma-1}{\gamma} \rho w \frac{\partial \lambda_1^{\pm}}{\partial v} + \frac{1}{2\gamma} \rho (w + an_z) \frac{\partial \lambda_2^{\pm}}{\partial v} + \frac{1}{2\gamma} \rho (w - an_z) \frac{\partial \lambda_3^{\pm}}{\partial v} \\
\frac{\partial \mathbf{F}_{\rho w}^{\pm}}{\partial w} &= \rho \left(\frac{\gamma-1}{\gamma} \lambda_1^{\pm} + \frac{1}{2\gamma} \lambda_2^{\pm} + \frac{1}{2\gamma} \lambda_3^{\pm} \right) + \frac{\gamma-1}{\gamma} \rho w \frac{\partial \lambda_1^{\pm}}{\partial w} + \frac{1}{2\gamma} \rho (w + an_z) \frac{\partial \lambda_2^{\pm}}{\partial w} + \frac{1}{2\gamma} \rho (w - an_z) \frac{\partial \lambda_3^{\pm}}{\partial w} \\
\frac{\partial \mathbf{F}_{\rho w}^{\pm}}{\partial a} &= \frac{\rho}{2\gamma} n_z \lambda_2^{\pm} - \frac{\rho}{2\gamma} n_z \lambda_3^{\pm} + \frac{\gamma-1}{\gamma} \rho w \frac{\partial \lambda_1^{\pm}}{\partial a} + \frac{1}{2\gamma} \rho (w + an_z) \frac{\partial \lambda_2^{\pm}}{\partial a} + \frac{1}{2\gamma} \rho (w - an_z) \frac{\partial \lambda_3^{\pm}}{\partial a} \\
\frac{\partial \mathbf{F}_{\rho w}^{\pm}}{\partial e_{ve}} &= \frac{\gamma-1}{\gamma} \rho w \frac{\partial \lambda_1^{\pm}}{\partial e_{ve}} + \frac{1}{2\gamma} \rho (w + an_z) \frac{\partial \lambda_2^{\pm}}{\partial e_{ve}} + \frac{1}{2\gamma} \rho (w - an_z) \frac{\partial \lambda_3^{\pm}}{\partial e_{ve}}
\end{aligned} \tag{7.39}$$

$$\begin{aligned}\frac{\partial \rho \epsilon_1}{\partial v} &= \rho v \\ \frac{\partial \rho \epsilon_2}{\partial v} &= \rho(v + an_y)\end{aligned}\tag{7.43}$$

$$\begin{aligned}\frac{\partial \rho \epsilon_3}{\partial v} &= \rho(v - an_y) \\ \frac{\partial \rho \epsilon_1}{\partial w} &= \rho w \\ \frac{\partial \rho \epsilon_2}{\partial w} &= \rho(w + an_z)\end{aligned}\tag{7.44}$$

$$\frac{\partial \rho \epsilon_3}{\partial w} = \rho(w - an_z)$$

$$\begin{aligned}\frac{\partial \rho \epsilon_1}{\partial a} &= 0 \\ \frac{\partial \rho \epsilon_2}{\partial a} &= \rho \left[\frac{3 - \gamma}{\gamma - 1} a + (u + an_x)n_x + (v + n_y)n_y + (w + n_z)n_z \right] \\ \frac{\partial \rho \epsilon_3}{\partial a} &= \rho \left[\frac{3 - \gamma}{\gamma - 1} a - (u - an_x)n_x - (v - n_y)n_y - (w - n_z)n_z \right]\end{aligned}\tag{7.45}$$

Since

$$\mathbf{W} = \begin{pmatrix} \rho_1 \\ \vdots \\ \rho_{ns} \\ u \\ v \\ w \\ a \\ e_{ve} \end{pmatrix}, \quad \text{and} \quad \mathbf{P} = \begin{pmatrix} \rho_1 \\ \vdots \\ \rho_{ns} \\ u \\ v \\ w \\ T \\ T_{ve} \end{pmatrix}.$$

The Jacobian $\frac{\partial \mathbf{W}}{\partial \mathbf{P}}$ is given by

$$\frac{\partial \mathbf{W}}{\partial \mathbf{P}} = \begin{pmatrix} 1 & \cdots & 0 & 0 & 0 & 0 & 0 & 0 \\ \vdots & \ddots & \vdots & \vdots & \vdots & \vdots & \vdots & \vdots \\ 0 & \cdots & 1 & 0 & 0 & 0 & 0 & 0 \\ 0 & \cdots & 0 & 1 & 0 & 0 & 0 & 0 \\ 0 & \cdots & 0 & 0 & 1 & 0 & 0 & 0 \\ 0 & \cdots & 0 & 0 & 0 & 1 & 0 & 0 \\ 0 & \cdots & 0 & 0 & 0 & 0 & \frac{\partial a}{\partial T} & 0 \\ \frac{\partial e_{ve}}{\partial \rho_1} & \cdots & \frac{\partial e_{ve}}{\partial \rho_{ns}} & 0 & 0 & 0 & 0 & \frac{\partial e_{ve}}{\partial T_{ve}} \end{pmatrix}$$

where

$$\frac{\partial a}{\partial T} = \frac{1 + \beta}{2a} R_w \quad (7.46)$$

Since

$$e_{ve} = \sum \frac{\rho_s}{\rho} e_{ve,s} = \frac{1}{\rho} \sum \rho_s e_{ve,s} \quad (7.47)$$

its derivatives with respect to p_r , T and T_{ve} are given by

$$\frac{\partial e_{ve}}{\partial \rho_r} = \frac{\frac{\partial(\sum \rho_s e_{ve,s})}{\partial \rho_r} \rho - (\sum \rho_s e_{ve,s}) \frac{\partial \rho}{\partial \rho_r}}{\rho^2} = \frac{e_{ve,r} \rho - \sum \rho_s e_{ve,s}}{\rho^2} \quad (7.48)$$

$$\frac{\partial e_{ve}}{\partial T} = 0 \quad (7.49)$$

$$\frac{\partial e_{ve}}{\partial T_{ve}} = \frac{(\sum \rho_s C v_{ve,s}) \rho}{\rho^2} = \frac{(\sum \rho_s C v_{ve,s})}{\rho} \quad (7.50)$$

The True Inviscid Jacobians for Equilibrium State

The inviscid fluxes for thermal equilibrium state is given by

$$\mathbf{F}_n^\pm = \begin{pmatrix} \frac{p}{\rho a^2} \frac{\partial p}{\partial \rho E} \rho_s \lambda_1^\pm + \frac{1}{2a^2} \left(a^2 - \frac{p}{\rho} \frac{\partial p}{\partial \rho E} \right) \rho_s \lambda_2^\pm + \frac{1}{2a^2} \left(a^2 - \frac{p}{\rho} \frac{\partial p}{\partial \rho E} \right) \rho_s \lambda_3^\pm \\ \frac{p}{\rho a^2} \frac{\partial p}{\partial \rho E} \rho u \lambda_1^\pm + \frac{1}{2a^2} \left(a^2 - \frac{p}{\rho} \frac{\partial p}{\partial \rho E} \right) \rho (u + an_x) \lambda_2^\pm + \frac{1}{2a^2} \left(a^2 - \frac{p}{\rho} \frac{\partial p}{\partial \rho E} \right) \rho (u - an_x) \lambda_3^\pm \\ \frac{p}{\rho a^2} \frac{\partial p}{\partial \rho E} \rho v \lambda_1^\pm + \frac{1}{2a^2} \left(a^2 - \frac{p}{\rho} \frac{\partial p}{\partial \rho E} \right) \rho (v + an_y) \lambda_2^\pm + \frac{1}{2a^2} \left(a^2 - \frac{p}{\rho} \frac{\partial p}{\partial \rho E} \right) \rho (v - an_y) \lambda_3^\pm \\ \frac{p}{\rho a^2} \frac{\partial p}{\partial \rho E} \rho w \lambda_1^\pm + \frac{1}{2a^2} \left(a^2 - \frac{p}{\rho} \frac{\partial p}{\partial \rho E} \right) \rho (w + an_z) \lambda_2^\pm + \frac{1}{2a^2} \left(a^2 - \frac{p}{\rho} \frac{\partial p}{\partial \rho E} \right) \rho (w - an_z) \lambda_3^\pm \\ \left(\rho E - \frac{H}{a^2} \left(\rho a^2 - p \frac{\partial p}{\partial \rho E} \right) \right) \lambda_1^\pm + \frac{H+aU}{2a^2} \left(\rho a^2 - p \frac{\partial p}{\partial \rho E} \right) + \frac{H-aU}{2a^2} \left(\rho a^2 - p \frac{\partial p}{\partial \rho E} \right) \lambda_3^\pm \end{pmatrix}.$$

It can also be simplified as

$$\mathbf{F}_n^\pm = \begin{pmatrix} \frac{\gamma-1}{\gamma} \rho_s \lambda_1^\pm + \frac{1}{2\gamma} \rho_s \lambda_2^\pm + \frac{1}{2\gamma} \rho_s \lambda_3^\pm \\ \frac{\gamma-1}{\gamma} \rho u \lambda_1^\pm + \frac{1}{2\gamma} \rho (u + an_x) \lambda_2^\pm + \frac{1}{2\gamma} \rho (u - an_x) \lambda_3^\pm \\ \frac{\gamma-1}{\gamma} \rho v \lambda_1^\pm + \frac{1}{2\gamma} \rho (v + an_y) \lambda_2^\pm + \frac{1}{2\gamma} \rho (v - an_y) \lambda_3^\pm \\ \frac{\gamma-1}{\gamma} \rho w \lambda_1^\pm + \frac{1}{2\gamma} \rho (w + an_z) \lambda_2^\pm + \frac{1}{2\gamma} \rho (w - an_z) \lambda_3^\pm \\ \frac{\gamma-1}{\gamma} \rho \epsilon_1 \lambda_1^\pm + \frac{1}{2\gamma} \rho \epsilon_2 \lambda_2^\pm + \frac{1}{2\gamma} \rho \epsilon_3 \lambda_3^\pm \end{pmatrix}.$$

where

$$\begin{aligned} \epsilon_1 &= \frac{1}{2} (u^2 + v^2 + w^2) + e_{ve} + h^o \\ \epsilon_2 &= \frac{(3-\gamma)}{2(\gamma-1)} a^2 + \frac{1}{2} ((u + an_x)^2 + (v + an_y)^2 + (w + an_z)^2) + e_{ve} + h^o \\ \epsilon_3 &= \frac{(3-\gamma)}{2(\gamma-1)} a^2 + \frac{1}{2} ((u - an_x)^2 + (v - an_y)^2 + (w - an_z)^2) + e_{ve} + h^o \end{aligned} \quad (7.51)$$

and

$$e_{ve} = \sum \frac{\rho_s}{\rho} e_{ve,s} \quad (7.52)$$

$$h^o = \sum \frac{\rho_s}{\rho} h_s^o \quad (7.53)$$

The Jacobians of inviscid flux vector with respect to \mathbf{P} can be directly computed where the introduced set of variables are now

$$\mathbf{P} = \begin{pmatrix} \rho_s \\ u \\ v \\ w \\ T \end{pmatrix}.$$

The Jacobian $\frac{\partial \mathbf{F}_n^\pm}{\partial \mathbf{P}}$ is given by

$$\frac{\partial \mathbf{F}_n^\pm}{\partial \mathbf{W}} = \begin{pmatrix} \frac{\partial \mathbf{F}_{\rho_s}^\pm}{\partial \rho_r} & \frac{\partial \mathbf{F}_{\rho_s}^\pm}{\partial u} & \frac{\partial \mathbf{F}_{\rho_s}^\pm}{\partial v} & \frac{\partial \mathbf{F}_{\rho_s}^\pm}{\partial w} & \frac{\partial \mathbf{F}_{\rho_s}^\pm}{\partial T} \\ \frac{\partial \mathbf{F}_{\rho_u}^\pm}{\partial \rho_r} & \frac{\partial \mathbf{F}_{\rho_u}^\pm}{\partial u} & \frac{\partial \mathbf{F}_{\rho_u}^\pm}{\partial v} & \frac{\partial \mathbf{F}_{\rho_u}^\pm}{\partial w} & \frac{\partial \mathbf{F}_{\rho_u}^\pm}{\partial T} \\ \frac{\partial \mathbf{F}_{\rho_v}^\pm}{\partial \rho_r} & \frac{\partial \mathbf{F}_{\rho_v}^\pm}{\partial u} & \frac{\partial \mathbf{F}_{\rho_v}^\pm}{\partial v} & \frac{\partial \mathbf{F}_{\rho_v}^\pm}{\partial w} & \frac{\partial \mathbf{F}_{\rho_v}^\pm}{\partial T} \\ \frac{\partial \mathbf{F}_{\rho_w}^\pm}{\partial \rho_r} & \frac{\partial \mathbf{F}_{\rho_w}^\pm}{\partial u} & \frac{\partial \mathbf{F}_{\rho_w}^\pm}{\partial v} & \frac{\partial \mathbf{F}_{\rho_w}^\pm}{\partial w} & \frac{\partial \mathbf{F}_{\rho_w}^\pm}{\partial T} \\ \frac{\partial \mathbf{F}_{\rho E}^\pm}{\partial \rho_r} & \frac{\partial \mathbf{F}_{\rho E}^\pm}{\partial u} & \frac{\partial \mathbf{F}_{\rho E}^\pm}{\partial v} & \frac{\partial \mathbf{F}_{\rho E}^\pm}{\partial w} & \frac{\partial \mathbf{F}_{\rho E}^\pm}{\partial T} \end{pmatrix}$$

$$\begin{aligned} \frac{\partial \mathbf{F}_{\rho_s}^\pm}{\partial \rho_r} &= \frac{\gamma-1}{\gamma} \lambda_1^\pm + \frac{1}{2\gamma} \lambda_2^\pm + \frac{1}{2\gamma} \lambda_3^\pm \\ \frac{\partial \mathbf{F}_{\rho_s}^\pm}{\partial u} &= \rho_s \left(\frac{\gamma-1}{\gamma} \frac{\partial \lambda_1^\pm}{\partial u} + \frac{1}{2\gamma} \frac{\partial \lambda_2^\pm}{\partial u} + \frac{1}{2\gamma} \frac{\partial \lambda_3^\pm}{\partial u} \right) \\ \frac{\partial \mathbf{F}_{\rho_s}^\pm}{\partial v} &= \rho_s \left(\frac{\gamma-1}{\gamma} \frac{\partial \lambda_1^\pm}{\partial v} + \frac{1}{2\gamma} \frac{\partial \lambda_2^\pm}{\partial v} + \frac{1}{2\gamma} \frac{\partial \lambda_3^\pm}{\partial v} \right) \\ \frac{\partial \mathbf{F}_{\rho_s}^\pm}{\partial w} &= \rho_s \left(\frac{\gamma-1}{\gamma} \frac{\partial \lambda_1^\pm}{\partial w} + \frac{1}{2\gamma} \frac{\partial \lambda_2^\pm}{\partial w} + \frac{1}{2\gamma} \frac{\partial \lambda_3^\pm}{\partial w} \right) \\ \frac{\partial \mathbf{F}_{\rho_s}^\pm}{\partial T} &= \rho_s \left(\frac{\gamma-1}{\gamma} \frac{\partial \lambda_1^\pm}{\partial a} + \frac{1}{2\gamma} \frac{\partial \lambda_2^\pm}{\partial a} + \frac{1}{2\gamma} \frac{\partial \lambda_3^\pm}{\partial a} \right) \frac{\partial a}{\partial T} \end{aligned} \tag{7.54}$$

$$\begin{aligned} \frac{\partial \mathbf{F}_{\rho_u}^\pm}{\partial \rho_r} &= \frac{\gamma-1}{\gamma} u \lambda_1^\pm + \frac{1}{2\gamma} (u + an_x) \lambda_2^\pm + \frac{1}{2\gamma} (u - an_x) \lambda_3^\pm \\ \frac{\partial \mathbf{F}_{\rho_u}^\pm}{\partial u} &= \rho \left(\frac{\gamma-1}{\gamma} \lambda_1^\pm + \frac{1}{2\gamma} \lambda_2^\pm + \frac{1}{2\gamma} \lambda_3^\pm \right) + \frac{\gamma-1}{\gamma} \rho u \frac{\partial \lambda_1^\pm}{\partial u} + \frac{1}{2\gamma} \rho (u + an_x) \frac{\partial \lambda_2^\pm}{\partial u} + \frac{1}{2\gamma} \rho (u - an_x) \frac{\partial \lambda_3^\pm}{\partial u} \\ \frac{\partial \mathbf{F}_{\rho_u}^\pm}{\partial v} &= \frac{\gamma-1}{\gamma} \rho u \frac{\partial \lambda_1^\pm}{\partial v} + \frac{1}{2\gamma} \rho (u + an_x) \frac{\partial \lambda_2^\pm}{\partial v} + \frac{1}{2\gamma} \rho (u - an_x) \frac{\partial \lambda_3^\pm}{\partial v} \\ \frac{\partial \mathbf{F}_{\rho_u}^\pm}{\partial w} &= \frac{\gamma-1}{\gamma} \rho u \frac{\partial \lambda_1^\pm}{\partial w} + \frac{1}{2\gamma} \rho (u + an_x) \frac{\partial \lambda_2^\pm}{\partial w} + \frac{1}{2\gamma} \rho (u - an_x) \frac{\partial \lambda_3^\pm}{\partial w} \\ \frac{\partial \mathbf{F}_{\rho_u}^\pm}{\partial T} &= \left[\frac{\rho}{2\gamma} n_x \lambda_2^\pm - \frac{\rho}{2\gamma} n_x \lambda_3^\pm + \frac{\gamma-1}{\gamma} \rho u \frac{\partial \lambda_1^\pm}{\partial a} + \frac{1}{2\gamma} \rho (u + an_x) \frac{\partial \lambda_2^\pm}{\partial a} + \frac{1}{2\gamma} \rho (u - an_x) \frac{\partial \lambda_3^\pm}{\partial a} \right] \frac{\partial a}{\partial T} \end{aligned} \tag{7.55}$$

where

$$\begin{aligned}\frac{\partial \rho \epsilon_1}{\partial \rho_r} &= \frac{1}{2} (u^2 + v^2 + w^2) + e_{ve,r} + h_r^o \\ \frac{\partial \rho \epsilon_2}{\partial \rho_r} &= \frac{(3 - \gamma)}{2(\gamma - 1)} a^2 + \frac{1}{2} ((u + an_x)^2 + (v + an_y)^2 + (w + an_z)^2) + e_{ve,r} + h_r^o \\ \frac{\partial \rho \epsilon_3}{\partial \rho_r} &= \frac{(3 - \gamma)}{2(\gamma - 1)} a^2 + \frac{1}{2} ((u - an_x)^2 + (v - an_y)^2 + (w - an_z)^2) + e_{ve,r} + h_r^o\end{aligned}\quad (7.59)$$

$$\begin{aligned}\frac{\partial \rho \epsilon_1}{\partial u} &= \rho u \\ \frac{\partial \rho \epsilon_2}{\partial u} &= \rho(u + an_x) \\ \frac{\partial \rho \epsilon_3}{\partial u} &= \rho(u - an_x)\end{aligned}\quad (7.60)$$

$$\begin{aligned}\frac{\partial \rho \epsilon_1}{\partial v} &= \rho v \\ \frac{\partial \rho \epsilon_2}{\partial v} &= \rho(v + an_y) \\ \frac{\partial \rho \epsilon_3}{\partial v} &= \rho(v - an_y)\end{aligned}\quad (7.61)$$

$$\begin{aligned}\frac{\partial \rho \epsilon_1}{\partial w} &= \rho w \\ \frac{\partial \rho \epsilon_2}{\partial w} &= \rho(w + an_z) \\ \frac{\partial \rho \epsilon_3}{\partial w} &= \rho(w - an_z)\end{aligned}\quad (7.62)$$

$$\begin{aligned}\frac{\partial \rho \epsilon_1}{\partial T} &= \sum \rho_s C v_{ve,s} \\ \frac{\partial \rho \epsilon_2}{\partial T} &= \rho \left[\frac{3 - \gamma}{\gamma - 1} a + (u + an_x)n_x + (v + an_y)n_y + (w + an_z)n_z \right] \frac{\partial a}{\partial T} + \sum \rho_s C v_{ve,s} \\ \frac{\partial \rho \epsilon_3}{\partial T} &= \rho \left[\frac{3 - \gamma}{\gamma - 1} a - (u - an_x)n_x - (v - an_y)n_y - (w - an_z)n_z \right] \frac{\partial a}{\partial T} + \sum \rho_s C v_{ve,s}\end{aligned}\quad (7.63)$$

Viscous Jacobians

It is more convenient to deal with viscous Jacobians using face-based reference frame rather than the usual Cartesian frame. Take a generic face for analysis, and let \mathbf{n} , \mathbf{l} and \mathbf{m} denote the unit normal vector, and two unit tangential vectors to it respectively.

Only the fluxes normal to the face are under consideration since they are the only one effectively going across the face. The fluxes in two tangential directions are no need to taken into account. The normal viscous fluxes across a generic face in Cartesian frame is given by

$$\mathbf{F}_{dn} = \mathcal{F}_d \cdot \mathbf{n} \quad (7.64)$$

are given by

$$\mathbf{F}_{dn} = \begin{pmatrix} -J_{n,1} \\ \vdots \\ -J_{n,ns} \\ \tau_{nn} \\ \tau_{nl} \\ \tau_{nm} \\ \tau_{nm}u + \tau_{nl}v + \tau_{nm}w - q_{tr,n} - q_{ve,n} - \sum(J_{n,s} h_s) \\ -q_{ve,n} - \sum(J_{n,s} e_{ve,s}) \end{pmatrix} .$$

A rotation matrix \mathcal{R} is needed to map the fluxes from the Cartesian frame to the face based reference frame, and \mathcal{R}^{-1} to do backwards. They are given receptively by

$$\mathcal{R} = \begin{pmatrix} 1 & 0 & 0 & 0 & 0 & 0 \\ 0 & n_x & n_y & n_z & 0 & 0 \\ 0 & l_x & l_y & l_z & 0 & 0 \\ 0 & m_x & m_y & m_z & 0 & 0 \\ 0 & 0 & 0 & 0 & 1 & 0 \\ 0 & 0 & 0 & 0 & 0 & 1 \end{pmatrix} \quad \text{and} \quad \mathcal{R}^{-1} = \begin{pmatrix} 1 & 0 & 0 & 0 & 0 & 0 \\ 0 & n_x & l_x & m_x & 0 & 0 \\ 0 & n_y & l_y & m_y & 0 & 0 \\ 0 & n_z & l_z & m_z & 0 & 0 \\ 0 & 0 & 0 & 0 & 1 & 0 \\ 0 & 0 & 0 & 0 & 0 & 1 \end{pmatrix} .$$

And the mapping procedure is given by

$$\mathbf{F}_{dn} = \mathcal{R}\mathbf{F}_d \quad \text{and} \quad \mathbf{F}_d = \mathcal{R}^{-1}\mathbf{F}_{dn} \quad (7.65)$$

Thin-layer approximation assumes the derivatives $\partial/\partial l$ and $\partial/\partial m$ can be neglected leaving only derivative in normal directions. This simplifies the formulation of shear stresses. The viscous fluxes \mathbf{F}_{dn} can be expressed as

$$\mathbf{F}_{dn} = \begin{pmatrix} \rho D_1 \frac{\partial Y_1}{\partial n} \\ \vdots \\ \rho D_{ns} \frac{\partial Y_{ns}}{\partial n} \\ (2\mu + \lambda) \frac{\partial u_n}{\partial n} \\ \mu \frac{\partial u_l}{\partial n} \\ \mu \frac{\partial u_m}{\partial n} \\ (2\mu + \lambda) \frac{\partial u_n}{\partial n} u_n + \mu \frac{\partial u_l}{\partial l} u_l + \mu \frac{\partial u_m}{\partial m} u_m + \\ k_{tr,n} \frac{\partial T_{tr,n}}{\partial n} + k_{ve,n} \frac{\partial T_{ve,n}}{\partial n} + \sum \rho \frac{\partial Y_s}{\partial n} h_s \\ k_{ve,n} \frac{\partial T_{ve,n}}{\partial n} + \sum \rho \frac{\partial Y_s}{\partial n} e_{ve,s} \end{pmatrix} .$$

Further assumption states that viscous fluxes can be linearized by introducing a matrix \mathcal{M} and a property vector \mathbf{V}_n , i.e.

$$\mathbf{F}_{dn} = \mathcal{M} \frac{\partial \mathbf{V}_n}{\partial n} , \quad (7.66)$$

All of the identities in \mathcal{M} are constants in terms of transport properties, and they do not involve any derivatives. The derivatives, however, are completely taken into account by $\frac{\partial \mathbf{V}_n}{\partial n}$, which are approximated by

$$\frac{\partial \mathbf{V}_n}{\partial n} \approx \frac{\mathbf{V}_{nR} - \mathbf{V}_{nL}}{\Delta n} , \quad (7.67)$$

where \mathbf{V}_{nR} and \mathbf{V}_{nL} are the property vectors on either side of the generic face. If define $\mathcal{M}_n = \mathcal{M}/\Delta n$, the viscous flux vectors are written as

$$\mathbf{F}_{dn} = \mathcal{M}_n (\mathbf{V}_{nR} - \mathbf{V}_{nL}) , \quad (7.68)$$

After substituting those rotation matrices, the viscous flux vectors, \mathbf{F}_v and the property vectors, \mathbf{V} , both in Cartesian coordinate frame can be related by

$$\mathbf{F}_d = \mathcal{R}^{-1} \mathcal{M}_n \mathcal{R} (\mathbf{V}_R - \mathbf{V}_L) = \mathcal{R}^{-1} \mathcal{M}_n \mathcal{R} \mathcal{N} (\mathbf{P}_R - \mathbf{P}_L) \quad , \quad (7.69)$$

where

$$\mathcal{N} = \frac{\partial \mathbf{V}}{\partial \mathbf{P}} \quad (7.70)$$

The viscous Jacobian is finally given by

$$\frac{\partial \mathbf{F}_d}{\partial \mathbf{P}_R} = \mathcal{R}^{-1} \mathcal{M}_n \mathcal{R} \mathbf{N} \quad \text{and} \quad \frac{\partial \mathbf{F}_d}{\partial \mathbf{P}_L} = -\mathcal{R}^{-1} \mathcal{M}_n \mathcal{R} \mathbf{N} \quad . \quad (7.71)$$

Details of these vectors and matrices mentioned above are listed as

$$\mathbf{V}_n = \begin{pmatrix} Y_1 \\ \vdots \\ Y_{ns} \\ u_n \\ u_l \\ u_m \\ T \\ T_{ve} \end{pmatrix} , \quad \mathbf{V} = \begin{pmatrix} Y_1 \\ \vdots \\ Y_{ns} \\ u \\ v \\ w \\ T \\ T_{ve} \end{pmatrix} , \quad \text{and} \quad \mathbf{P} = \begin{pmatrix} \rho_1 \\ \vdots \\ \rho_{ns} \\ u \\ v \\ w \\ T \\ T_{ve} \end{pmatrix}$$

$$\mathcal{M}_n = \begin{pmatrix} M_{(1,1)} & \cdots & M_{(1,ns)} & 0 & 0 & 0 & 0 & 0 \\ \vdots & \ddots & \vdots & \vdots & \vdots & \vdots & \vdots & \vdots \\ M_{(ns,1)} & \cdots & M_{(ns,ns)} & 0 & 0 & 0 & 0 & 0 \\ 0 & \cdots & 0 & \frac{2\mu+\lambda}{\Delta n} & 0 & 0 & 0 & 0 \\ 0 & \cdots & 0 & 0 & \frac{\mu}{\Delta n} & 0 & 0 & 0 \\ 0 & \cdots & 0 & 0 & 0 & \frac{\mu}{\Delta n} & 0 & 0 \\ M_{(n-1,1)} & \cdots & M_{(n-1,ns)} & \frac{(2\mu+\lambda)u_n}{\Delta n} & \frac{\mu u_t}{\Delta n} & \frac{\mu u_r}{\Delta n} & \frac{k_{tr}}{\Delta n} & \frac{k_{ve}}{\Delta n} \\ M_{(n,1)} & \cdots & M_{(n,ns)} & 0 & 0 & 0 & 0 & \frac{k_{ve}}{\Delta n} \end{pmatrix}$$

For $k \leq ns$, and for electron

$$M_{s,r} = \begin{cases} \frac{\rho D_r}{\Delta n} \left(1 + \frac{C_r}{M_r} M_e\right) & \text{for } s \neq r \\ 0 & \text{otherwise} \end{cases} \quad (7.72)$$

For normal species, only diagonal term exists, which is given by

$$M_{s,s} = \frac{\rho D_s}{\Delta n} \quad (7.73)$$

And for the rest terms

$$M_{(n-1,r)} = \begin{cases} 0 & \text{for electron,} \\ \frac{\rho D_r}{\Delta n} (h_r + \frac{C_r}{M_r} M_e h_e) & \text{otherwise} \end{cases} \quad (7.74)$$

$$M_{(n,r)} = \begin{cases} 0 & \text{for electron,} \\ \frac{\rho D_r}{\Delta n} (e_{ve,r} + \frac{C_r}{M_r} M_e e_{ve,e}) & \text{otherwise} \end{cases} \quad (7.75)$$

$$\mathcal{N} = \frac{\partial \mathbf{V}}{\partial \mathbf{P}} = \begin{pmatrix} \frac{\partial Y_1}{\partial \rho_1} & \dots & \frac{\partial Y_1}{\partial \rho_{ns}} & 0 & 0 & 0 & 0 & 0 \\ \vdots & \ddots & \vdots & \vdots & \vdots & \vdots & \vdots & \vdots \\ \frac{\partial Y_{ns}}{\partial \rho_1} & \dots & \frac{\partial Y_{ns}}{\partial \rho_{ns}} & 0 & 0 & 0 & 0 & 0 \\ 0 & 0 & 0 & 1 & 0 & 0 & 0 & 0 \\ 0 & 0 & 0 & 0 & 1 & 0 & 0 & 0 \\ 0 & 0 & 0 & 0 & 0 & 1 & 0 & 0 \\ 0 & 0 & 0 & 0 & 0 & 0 & 1 & 0 \\ 0 & 0 & 0 & 0 & 0 & 0 & 0 & 1 \end{pmatrix}$$

$$Y_s = \frac{\rho_s}{\rho} \quad (7.76)$$

$$\frac{\partial Y_s}{\partial \rho_r} = \frac{\delta_{sr}\rho - \rho_s}{\rho^2} \quad (7.77)$$

Time terms in thermal non-equilibrium

The vectors of conserved variables and primitive variables take the form of

$$\mathbf{Q} = \begin{pmatrix} \rho_1 \\ \vdots \\ \rho_{ns} \\ \rho u \\ \rho v \\ \rho w \\ E \\ E_{ve} \end{pmatrix}, \quad \text{and} \quad \mathbf{P} = \begin{pmatrix} \rho_1 \\ \vdots \\ \rho_{ns} \\ u \\ v \\ w \\ T \\ T_{ve} \end{pmatrix}$$

The Jacobian of conservative variables \mathbf{Q} with respect to primitive variables \mathbf{P} , is given by

$$\mathcal{J} = \frac{\partial \mathbf{Q}}{\partial \mathbf{P}} = \begin{pmatrix} \frac{\partial \rho_1}{\partial \rho_1} & \cdots & \frac{\partial \rho_1}{\partial \rho_{ns}} & \frac{\partial \rho_1}{\partial u} & \frac{\partial \rho_1}{\partial v} & \frac{\partial \rho_1}{\partial w} & \frac{\partial \rho_1}{\partial T} & \frac{\partial \rho_1}{\partial T_{ve}} \\ \vdots & \ddots & \vdots & \vdots & \vdots & \vdots & \vdots & \vdots \\ \frac{\partial \rho_{ns}}{\partial \rho_1} & \cdots & \frac{\partial \rho_{ns}}{\partial \rho_{ns}} & \frac{\partial \rho_{ns}}{\partial u} & \frac{\partial \rho_{ns}}{\partial v} & \frac{\partial \rho_{ns}}{\partial w} & \frac{\partial \rho_{ns}}{\partial T} & \frac{\partial \rho_{ns}}{\partial T_{ve}} \\ \frac{\partial \rho u}{\partial \rho_1} & \cdots & \frac{\partial \rho u}{\partial \rho_{ns}} & \frac{\partial \rho u}{\partial u} & \frac{\partial \rho u}{\partial v} & \frac{\partial \rho u}{\partial w} & \frac{\partial \rho u}{\partial T} & \frac{\partial \rho u}{\partial T_{ve}} \\ \frac{\partial \rho v}{\partial \rho_1} & \cdots & \frac{\partial \rho v}{\partial \rho_{ns}} & \frac{\partial \rho v}{\partial u} & \frac{\partial \rho v}{\partial v} & \frac{\partial \rho v}{\partial w} & \frac{\partial \rho v}{\partial T} & \frac{\partial \rho v}{\partial T_{ve}} \\ \frac{\partial \rho w}{\partial \rho_1} & \cdots & \frac{\partial \rho w}{\partial \rho_{ns}} & \frac{\partial \rho w}{\partial u} & \frac{\partial \rho w}{\partial v} & \frac{\partial \rho w}{\partial w} & \frac{\partial \rho w}{\partial T} & \frac{\partial \rho w}{\partial T_{ve}} \\ \frac{\partial E}{\partial \rho_1} & \cdots & \frac{\partial E}{\partial \rho_{ns}} & \frac{\partial E}{\partial u} & \frac{\partial E}{\partial v} & \frac{\partial E}{\partial w} & \frac{\partial E}{\partial T} & \frac{\partial E}{\partial T_{ve}} \\ \frac{\partial E_{ve}}{\partial \rho_1} & \cdots & \frac{\partial E_{ve}}{\partial \rho_{ns}} & \frac{\partial E_{ve}}{\partial u} & \frac{\partial E_{ve}}{\partial v} & \frac{\partial E_{ve}}{\partial w} & \frac{\partial E_{ve}}{\partial T} & \frac{\partial E_{ve}}{\partial T_{ve}} \end{pmatrix}$$

A few of the identities are obviously zero, therefore

$$\mathcal{J} = \begin{pmatrix} 1 & \cdots & 0 & 0 & 0 & 0 & 0 & 0 \\ \vdots & \ddots & \vdots & \vdots & \vdots & \vdots & \vdots & \vdots \\ 0 & \cdots & 1 & 0 & 0 & 0 & 0 & 0 \\ u & \cdots & u & \rho & 0 & 0 & 0 & 0 \\ v & \cdots & v & 0 & \rho & 0 & 0 & 0 \\ w & \cdots & w & 0 & 0 & \rho & 0 & 0 \\ \frac{\partial E}{\partial \rho_1} & \cdots & \frac{\partial E}{\partial \rho_{ns}} & \rho u & \rho v & \rho w & \frac{\partial E}{\partial T} & \frac{\partial E}{\partial T_{ve}} \\ \frac{\partial E_{ve}}{\partial \rho_1} & \cdots & \frac{\partial E_{ve}}{\partial \rho_{ns}} & 0 & 0 & 0 & 0 & \frac{\partial E_{ve}}{\partial T_{ve}} \end{pmatrix}$$

The total energy per unit volume, E , is given by

$$\begin{aligned} E &= \sum_s \rho_s e_s + \frac{1}{2} \rho (u^2 + v^2 + w^2) \\ &= \sum_{s \neq e} \rho_s C v_{tr,s} T + \sum_s \rho_s e_{ve,s} + \sum_{s \neq e} \rho_s h_s^o + \frac{1}{2} \rho (u^2 + v^2 + w^2) \quad , \end{aligned} \tag{7.78}$$

Its derivatives are calculated as

$$\begin{aligned}\frac{\partial E}{\partial \rho_s} &= e_s + \frac{1}{2}(u^2 + v^2 + w^2) \\ \frac{\partial E}{\partial T} &= \sum_{s \neq e} \rho_s C v_{tr,s} \\ \frac{\partial E}{\partial T_{ve}} &= \sum_s \rho_s C v_{ve,s}\end{aligned}\tag{7.79}$$

The mixture vibrational-electron-electronic energy per unit volume, E_{ve} , is given by

$$E_{ve} = \sum_s \rho_s e_{ve,s}\tag{7.80}$$

Its derivatives are given by

$$\begin{aligned}\frac{\partial E_{ve}}{\partial \rho_s} &= e_{ve,s} \\ \frac{\partial E_{ve}}{\partial T_{ve}} &= \sum_s \rho_s C v_{ve,s}\end{aligned}\tag{7.81}$$

Time terms for thermal equilibrium

The vectors of conserved variables and primitive variables now take the form of

$$\mathbf{Q} = \begin{pmatrix} \rho_1 \\ \vdots \\ \rho_{ns} \\ \rho u \\ \rho v \\ \rho w \\ E \end{pmatrix}, \quad \text{and} \quad \mathbf{P} = \begin{pmatrix} \rho_1 \\ \vdots \\ \rho_{ns} \\ u \\ v \\ w \\ T \end{pmatrix}$$

Then the Jacobian of conservative variables \mathbf{Q} with respect to primitive variables \mathbf{P} , is given by

$$\mathcal{J} = \frac{\partial \mathbf{Q}}{\partial \mathbf{P}} = \begin{pmatrix} 1 & \cdots & 0 & 0 & 0 & 0 & 0 \\ \vdots & \ddots & \vdots & \vdots & \vdots & \vdots & \vdots \\ 0 & \cdots & 1 & 0 & 0 & 0 & 0 \\ u & \cdots & u & \rho & 0 & 0 & 0 \\ v & \cdots & v & 0 & \rho & 0 & 0 \\ w & \cdots & w & 0 & 0 & \rho & 0 \\ \frac{\partial E}{\partial \rho_1} & \cdots & \frac{\partial E}{\partial \rho_{ns}} & \rho u & \rho v & \rho w & \frac{\partial E}{\partial T} \end{pmatrix}$$

The total energy per unit volume, E , is given by

$$\begin{aligned} E &= \sum_s \rho_s e_s + \frac{1}{2} \rho (u^2 + v^2 + w^2) \\ &= \sum_s \rho_s C v_{tr,s} T + \sum_s \rho_s e_{ve,s} + \sum_s \rho_s h_s^o + \frac{1}{2} \rho (u^2 + v^2 + w^2) \quad . \end{aligned} \quad (7.82)$$

It yields

$$\begin{aligned} \frac{\partial E}{\partial \rho_s} &= e_s + \frac{1}{2} (u^2 + v^2 + w^2) \\ \frac{\partial E}{\partial T} &= \sum_s \rho_s (C v_{tr,s} + C v_{ve,s}) \end{aligned} \quad (7.83)$$

Chemistry Jacobians

The chemistry Jacobians take the form of

$$\frac{\partial \mathbf{S}}{\partial \mathbf{P}} = \begin{pmatrix} \frac{\partial \dot{w}_i}{\partial \rho_s} & \frac{\partial \dot{w}_i}{\partial u} & \frac{\partial \dot{w}_i}{\partial v} & \frac{\partial \dot{w}_i}{\partial w} & \frac{\partial \dot{w}_i}{\partial T_{tr}} & \frac{\partial \dot{w}_i}{\partial T_{ve}} \\ 0 & 0 & 0 & 0 & 0 & 0 \\ 0 & 0 & 0 & 0 & 0 & 0 \\ 0 & 0 & 0 & 0 & 0 & 0 \\ 0 & 0 & 0 & 0 & 0 & 0 \\ 0 & 0 & 0 & 0 & 0 & 0 \end{pmatrix}$$

Recall the chemical production rate of species A_i in reaction r is given by

$$\dot{w}_{ir} = (\nu''_{ir} - \nu'_{ir}) \left[10^3 k_{fr} \prod_{j=1}^{ns} \left(10^{-3} \frac{\rho_j}{M_j} \right)^{\nu'_{jr}} - 10^3 k_{br} \prod_{j=1}^{ns} \left(10^{-3} \frac{\rho_j}{M_j} \right)^{\nu''_{jr}} \right] . \quad (7.84)$$

And the net mass production of species A_i is given by

$$\dot{w}_i = M_i \sum_{r=1}^{nr} (\nu''_{ir} - \nu'_{ir}) \left[k_{fr} \frac{R_f}{k_{fr}} - k_{br} \frac{R_b}{k_{br}} \right] . \quad (7.85)$$

where nr is the number of reaction, and

$$\frac{R_{fr}}{k_{fr}} = 10^3 \prod_{j=1}^{ns} \left(10^{-3} \frac{\rho_j}{M_j} \right)^{\nu'_{jr}} \quad (7.86)$$

$$\frac{R_{br}}{k_{br}} = 10^3 \prod_{j=1}^{ns} \left(10^{-3} \frac{\rho_j}{M_j} \right)^{\nu''_{jr}} \quad (7.87)$$

The Jacobians of \dot{w}_i with respect to primitive variables are given by

$$\frac{\partial \dot{w}_i}{\partial \mathbf{P}} = M_i \sum_{r=1}^{nr} (\nu''_{ir} - \nu'_{ir}) \left[\frac{\partial k_{fr}}{\partial \mathbf{P}} \frac{R_{fr}}{k_{fr}} + k_{fr} \frac{\partial}{\partial \mathbf{P}} \left(\frac{R_{fr}}{k_{fr}} \right) - \frac{\partial k_{br}}{\partial \mathbf{P}} \frac{R_{br}}{k_{br}} - k_{br} \frac{\partial}{\partial \mathbf{P}} \left(\frac{R_{br}}{k_{br}} \right) \right] \quad (7.88)$$

The forward reaction rate coefficient is given by

$$k_{fr} = A_{fr} T_c^{\eta_r} \exp(-T_{ar}/T_c) \quad (7.89)$$

Its derivatives, $\frac{\partial k_{fr}}{\partial \mathbf{P}}$, are given by

$$\frac{\partial k_{fr}}{\partial \mathbf{P}} = k_{fr} \left(\frac{\eta_r}{T'_c} + \frac{T_{ar}}{T_c^2} \right) \frac{dT'_c}{dT_c} \left(a_r \frac{T_c}{T_{tr}} \frac{\partial T_{tr}}{\partial \mathbf{P}} + b_r \frac{T_c}{T_{ve}} \frac{\partial T_{ve}}{\partial \mathbf{P}} \right) \quad (7.90)$$

$$T'_c = \frac{1}{2} \left[(T_c + T_{min}) + \sqrt{(T_c - T_{min})^2 + \epsilon^2} \right], \quad (7.91)$$

$$\frac{dT'_c}{dT_c} = \frac{1}{2} + \frac{1}{2} \frac{T_c - T_{min}}{\sqrt{(T_c - T_{min})^2 + \epsilon^2}} \quad (7.92)$$

The backward reaction rate coefficient is given by

$$k_{br}(T_{bc}) = \frac{k_{fbr}(T_{bc})}{K_{cr}(T_{bc})} \quad (7.93)$$

Its derivatives, $\frac{\partial k_{br}}{\partial \mathbf{P}}$, are given by

$$\frac{\partial k_{br}}{\partial \mathbf{P}} = -k_{br} \frac{1}{K_{cr}} \frac{dK_{cr}}{dT'_{bc}} \left(a_r \frac{T_{bc}}{T_{tr}} \frac{\partial T_{tr}}{\partial \mathbf{P}} + b_r \frac{T_{bc}}{T_{ve}} \frac{\partial T_{ve}}{\partial \mathbf{P}} \right) + \frac{1}{K_{cr}} \frac{\partial k_{fbr}}{\partial \mathbf{P}} \quad (7.94)$$

$$\frac{1}{K_{cr}} \frac{\partial k_{fbr}}{\partial \mathbf{P}} = k_{br} \left(\frac{\eta_r}{T'_{bc}} + \frac{E_r}{T'^2_{bc}} \right) \frac{dT'_b}{dT'_{bc}} \left(a_r \frac{T_{bc}}{T_{tr}} \frac{\partial T_{tr}}{\partial \mathbf{P}} + b_r \frac{T_{bc}}{T_{ve}} \frac{\partial T_{ve}}{\partial \mathbf{P}} \right) \quad (7.95)$$

and

$$\frac{1}{K_{cr}} \frac{dK_{cr}}{dT'_{bc}} = \sum_{i=1}^{ns} (\nu'_{ir} - \nu'_{ir}) \frac{1}{T'_{bc}} \left(\frac{\hat{h}_i}{RT'_{bc}} - 1 \right) \quad (7.96)$$

The derivatives of the forward reaction rate divided by the forward reaction rate coefficient, $\frac{\partial}{\partial \mathbf{P}} \left(\frac{R_{fr}}{k_{fr}} \right)$, are given by

$$\begin{aligned} \frac{\partial}{\partial \rho_s} \left(\frac{R_{fr}}{k_{fr}} \right) &= \frac{\nu'_{sr}}{\rho_s} \left(10^3 \prod_{j=1}^{ns} \left(10^{-3} \frac{\rho_j}{M_j} \right)^{\nu'_{jr}} \right) \\ \frac{\partial}{\partial u} \left(\frac{R_{fr}}{k_{fr}} \right) &= 0 \\ \frac{\partial}{\partial v} \left(\frac{R_{fr}}{k_{fr}} \right) &= 0 \\ \frac{\partial}{\partial w} \left(\frac{R_{fr}}{k_{fr}} \right) &= 0 \\ \frac{\partial}{\partial T_{tr}} \left(\frac{R_{fr}}{k_{fr}} \right) &= 0 \\ \frac{\partial}{\partial T_{ve}} \left(\frac{R_{fr}}{k_{fr}} \right) &= 0 \end{aligned} \quad (7.97)$$

In detail

$$\begin{aligned} \frac{\partial}{\partial \rho_s} \left(\frac{R_{fr}}{k_{fr}} \right) &= \frac{\partial}{\partial \rho_s} \left(10^3 \prod_{j=1}^{ns} \left(10^{-3} \frac{\rho_j}{M_j} \right)^{\nu'_{jr}} \right) \\ &= 10^3 \left[10^{-3} \frac{\nu'_{sr} \rho_s}{M_s \rho_s} \left(10^{-3} \frac{\rho_s}{M_s} \right)^{\max(0, \nu'_{sr} - 1)} \prod_{j \neq s} \left(10^{-3} \frac{\rho_j}{M_j} \right)^{\nu'_{jr}} \right] \\ &= 10^3 \left[\frac{\nu'_{sr}}{\rho_s} \left(10^{-3} \frac{\rho_s}{M_s} \right)^{\nu'_{sr}} \prod_{j \neq s} \left(10^{-3} \frac{\rho_j}{M_j} \right)^{\nu'_{jr}} \right] \\ &= \frac{\nu'_{sr}}{\rho_s} \left(10^3 \prod_{j=1}^{ns} \left(10^{-3} \frac{\rho_j}{M_j} \right)^{\nu'_{jr}} \right) \end{aligned} \quad (7.98)$$

The derivatives of the translational-rotational temperature, T_{tr} , are given by

$$\begin{aligned}
 \frac{\partial T_{tr}}{\partial \rho_s} &= 0 \\
 \frac{\partial T_{tr}}{\partial u} &= 0 \\
 \frac{\partial T_{tr}}{\partial v} &= 0 \\
 \frac{\partial T_{tr}}{\partial w} &= 0 \\
 \frac{\partial T_{tr}}{\partial T_{tr}} &= 1 \\
 \frac{\partial T_{tr}}{\partial T_{ve}} &= 0
 \end{aligned} \tag{7.99}$$

The derivatives of the vibrational-electron-electronic temperature, T_{ve} , are given by

$$\begin{aligned}
 \frac{\partial T_{ve}}{\partial p_s} &= 0 \\
 \frac{\partial T_{ve}}{\partial u} &= 0 \\
 \frac{\partial T_{ve}}{\partial v} &= 0 \\
 \frac{\partial T_{ve}}{\partial w} &= 0 \\
 \frac{\partial T_{ve}}{\partial T_{tr}} &= 0 \\
 \frac{\partial T_{ve}}{\partial T_{ve}} &= 1
 \end{aligned} \tag{7.100}$$

The backward reaction rate divided by the backward reaction rate coefficient, $\frac{R_{br}}{k_{br}}$, is given by

$$\frac{R_{br}}{k_{br}} = 10^3 \prod_{j=1} (10^{-3} \frac{\rho_j}{M_j})^{\nu''_{j'r}} \tag{7.101}$$

Its derivatives are similar to those of forward.

Non-Equilibrium Jacobians

The non-equilibrium Jacobians take the form of

$$\frac{\partial \mathbf{S}_v}{\partial \mathbf{P}} = \begin{pmatrix} 0 & \cdots & 0 & 0 & 0 & 0 & 0 & 0 \\ \vdots & \ddots & \vdots & \vdots & \vdots & \vdots & \vdots & \vdots \\ 0 & \cdots & 0 & 0 & 0 & 0 & 0 & 0 \\ 0 & \cdots & 0 & 0 & 0 & 0 & 0 & 0 \\ 0 & \cdots & 0 & 0 & 0 & 0 & 0 & 0 \\ 0 & \cdots & 0 & 0 & 0 & 0 & 0 & 0 \\ \frac{\partial \dot{w}_v}{\partial \rho_1} & \cdots & \frac{\partial \dot{w}_v}{\partial \rho_{ns}} & \frac{\partial \dot{w}_v}{\partial u} & \frac{\partial \dot{w}_v}{\partial v} & \frac{\partial \dot{w}_v}{\partial w} & \frac{\partial \dot{w}_v}{\partial T} & \frac{\partial \dot{w}_v}{\partial T_{ve}} \end{pmatrix}$$

The total vibrational energy is composed of

$$\dot{w}_v = S_{c2v} + S_{t2v} + S_{h2e} - S_{e2i} \quad . \quad (7.102)$$

Its Jacobians are given by

$$\frac{\partial \dot{w}_v}{\partial \mathbf{P}} = \frac{\partial S_{c2v}}{\partial \mathbf{P}} + \frac{\partial S_{t2v}}{\partial \mathbf{P}} + \frac{\partial S_{h2e}}{\partial \mathbf{P}} - \frac{\partial S_{e2i}}{\partial \mathbf{P}} \quad . \quad (7.103)$$

The derivatives of chemistry terms are given by

$$\frac{\partial S_{c2v}}{\partial \mathbf{P}} = \sum_{s=\text{mol.}} \left[\frac{\partial \dot{w}_s}{\partial \mathbf{P}} (D'_s + e_{el,s}) + \dot{w}_s \left(\frac{\partial D'_s}{\partial \mathbf{P}} + \frac{\partial e_{el,s}}{\partial \mathbf{P}} \right) \right] \quad (7.104)$$

where

$$\frac{\partial D'_s}{\partial \mathbf{P}} = \begin{cases} 0 & \text{for the preferential model} \\ \frac{\partial e_{v,s}}{\partial \mathbf{P}} & \text{for the non-preferential model} \end{cases} \quad , \quad (7.105)$$

The derivatives of translational-vibrational energy relaxation term are given by

$$\frac{\partial S_{t2v}}{\partial \mathbf{P}} = \sum_{s=\text{mol.}} \left[\frac{\partial \rho_s}{\partial \mathbf{P}} \frac{e_{vs}^* - e_{vs}}{\tau_s} + \rho_s \frac{\partial e_{vs}^*/\partial \mathbf{P} - \partial e_{vs}/\partial \mathbf{P}}{\tau_s} \right] \quad , \quad (7.106)$$

where the relaxation time, τ_s , is assumed to be constant.

The derivatives of electron-vibrational energy relaxation terms, $\frac{\partial S_{h2e}}{\partial \mathbf{P}}$ are quite straightforward, whose derivation is neglected here.

Finally, the derivatives of electron impact ionization energy relaxation term are given by

$$\frac{\partial S_{e2i}}{\partial \mathbf{P}} = M_N^+ \hat{I}_N \frac{\partial \dot{w}_{N^+,eii}}{\partial \mathbf{P}} + M_O^+ \hat{I}_O \frac{\partial \dot{w}_{O^+,eii}}{\partial \mathbf{P}} \quad (7.107)$$

where the subscript, *eii*, denotes the electron impact ionization reaction.

Three-body dissociation reaction

A speedup approach can be used for a dissociation reaction where one reactant denoted by *AB*, is going to be dissociated into atoms *A* and *B*. The collision partner involved can be any of the species (*AB*, *A* or *B*) in the gas mixture. It is denoted by *M* in the following reaction.



Dealing with reaction in terms of each collision partner *M* separately would be time consuming. An efficient way which can take account of them all together proposed by Alexandre Martin is used in this work. The associated computations are then immensely speeded up.

In the dissociation of *AB* coming about by collision with a particle *M*, there is no production change for *M* in this reaction, leaving only *AB*, *A* and *B* to be considered. The chemical production rate of *AB* can be given by

$$\begin{aligned} \dot{w}_{AB} &= (\nu''_{AB} - \nu'_{AB}) \left[10^3 k_f \prod_j (10^{-3} \frac{\rho_j}{M_j})^{\nu'_{jk}} - 10^3 k_b \prod_j (10^{-3} \frac{\rho_j}{M_j})^{\nu''_{jk}} \right] \\ &= (0 - 1) \left[10^3 k_f (10^{-3} \frac{\rho_{AB}}{M_{AB}}) (10^{-3} \frac{\rho_M}{M_M}) - 10^3 k_b (10^{-3} \frac{\rho_A}{M_A}) (10^{-3} \frac{\rho_B}{M_B}) (10^{-3} \frac{\rho_M}{M_M}) \right] \\ &= (0 - 1) (10^{-3} \frac{\rho_M}{M_M}) \left[10^3 k_f (10^{-3} \frac{\rho_{AB}}{M_{AB}}) - 10^3 k_b (10^{-3} \frac{\rho_A}{M_A}) (10^{-3} \frac{\rho_B}{M_B}) \right] \end{aligned}$$

Forward and backward reaction rate coefficients, k_f and k_b may not be the same for variant collision particles. However, by setting reference reaction rate coefficients, denoted by k_f^* and k_b^* , and introducing a ratio coefficient φ which can account for the variation of them, it ends up with a form of more consistency.

$$\dot{w}_{AB} = (0 - 1) \sum_{i=1}^{nbs} \left(10^{-3} \frac{\rho_{M_i}}{M_{M_i}} \varphi_i\right) \left[10^3 k_f^* \left(10^{-3} \frac{\rho_{AB}}{M_{AB}}\right) - 10^3 k_b^* \left(10^{-3} \frac{\rho_A}{M_A}\right) \left(10^{-3} \frac{\rho_B}{M_B}\right)\right] \quad (7.109)$$

Similarly, the production rate of species A is calculated by

$$\dot{w}_A = (1 - 0) \sum_{i=1}^{nbs} \left(10^{-3} \frac{\rho_{M_i}}{M_{M_i}} \varphi_i\right) \left[10^3 k_f^* \left(10^{-3} \frac{\rho_{AB}}{M_{AB}}\right) - 10^3 k_b^* \left(10^{-3} \frac{\rho_A}{M_A}\right) \left(10^{-3} \frac{\rho_B}{M_B}\right)\right] \quad (7.110)$$

Note that the variation of k_f or k_b for each collision particle M only comes from the coefficient of A_{fr} in Arrhenius curve fit equation. By using this trick, the chemical production rate of the species due to all dissociation reactions can be taken account of together without doing repeatable work. This can greatly save computation time.

Bibliography

- [1] I. D. Boyd, P. F. Penko, D. L. Meissner, and K. J. Dewitt, “Experimental and numerical investigations of low-density nozzle and plume flows of nitrogen,” *AIAA Journal*, vol. 30, no. 10, pp. 2453–2461, 1992.
- [2] U. Ghia, K. N. Ghia, and C. Shin, “High-resolutions for incompressible flow using the navier-stokes equations and a multigrid method,” *Journal of computational physics*, vol. 48, no. 3, pp. 387–411, 1982.
- [3] V. Costa, L. Oliveira, B. Baliga, and A. Sousa, “Simulation of coupled flows in adjacent porous and open domains using a control-volume finite-element method,” *Numerical Heat Transfer, Part A: Applications*, vol. 45, no. 7, pp. 675–697, 2004.
- [4] L. Betchen, A. G. Straatman, and B. E. Thompson, “A nonequilibrium finite-volume model for conjugate fluid/porous/solid domains,” *Numerical Heat Transfer, Part A: Applications*, vol. 49, no. 6, pp. 543–565, 2006.
- [5] K. A. Trumble, I. Cozmuta, S. Sepka, P. Jenniskens, and M. Winter, “Post-flight aerothermal analysis of the stardust sample return capsule,” *Journal of Spacecraft and Rockets*, vol. 47, no. 5, pp. 765–774, 2010.
- [6] M. Adler, M. Wright, C. Campbell, I. Clark, W. Engelund, and T. Rivellini, “Entry, descent, and landing roadmap,” *NASA TA09, April*, 2012.
- [7] J. D. Anderson, *Hypersonic and High Temperature Gas Dynamics*. McGraw-Hill, 1989.
- [8] P. F. Barbante, *Accurate and efficient modelling of high temperature nonequilibrium air flows*. PhD thesis, Von Karman Institute for Fluid Dynamics, 2001.

- [9] C. Park, "Assessment of a two-temperature kinetic model for dissociating and weakly ionizing nitrogen," *Journal of Thermophysics and Heat Transfer*, vol. 2, pp. 8–16, Jan 1 1988.
- [10] T. E. Schwartzentruber, *A modular particle-continuum numerical algorithm for hypersonic non-equilibrium flows*. PhD thesis, The University of Michigan, Ann Arbor, MI, 2007.
- [11] E. D. Farbar, A. Martin, and I. D. Boyd, "Modeling ablation with the DSMC method," poster, 4th AFOSR/SNL/NASA Ablation Workshop, Albuquerque, NM, March 2011.
- [12] P. K. Ackerman, A. L. Baker, and C. W. Newquist, "Thermal protection system," 1994.
- [13] E. Venkatapathy, C. E. Szalai, B. Laub, H. H. Hwang, J. L. Conley, J. Arnold, and N. ARC, "Thermal protection system technologies for enabling future sample return missions," *White paper submitted to the Planetary Science Decadal Survey, National Research Council, Washington, DC*, 2009.
- [14] A. J. Amar, "Modeling of one-dimensional ablation with porous flow using finite control volume procedure," Master's thesis, North Carolina State University, Raleigh, NC, 2006.
- [15] C. B. Moyer and R. A. Rindal, "An analysis of the coupled chemically reacting boundary layer and charring ablator. part 2 - finite difference solution for the in-depth response of charring materials considering surface chemical and energy balances," Contractor Report CR-1061, NASA, 1968.
- [16] B. F. Blackwell and R. E. Hogan, "One-dimensional ablation using landau transformation and finite control volume procedure," *Journal of Thermophysics and Heat Transfer*, vol. 8, pp. 282–287, April-June 1994.

- [17] R. E. Hogan, B. F. Blackwell, and R. J. Cochran, “Numerical solution of two-dimensional ablation problems using the finite control volume method with unstructured grids,” in *6th AIANASME Joint Thermophysics and Heat Transfer Conference*, no. AIAA 94-2085, June 20-23 1994.
- [18] A. Martin and I. D. Boyd, “Simulation of pyrolysis gas within a thermal protection system,” in *40th AIAA Thermophysics Conference*, no. AIAA-2008-3805, (Seattle, WA), June 23-26 2008.
- [19] A. J. Amar, N. D. Calvert, and B. S. Kirk, “Development and verification of the charring ablating thermal protection implicit system solver,” in *49th AIAA Aerospace Sciences Meeting*, no. AIAA-2011-144, (Orlando, FL), Jan. 4-7 2011.
- [20] M. Miller, H. Zhang, S. Bailey, and A. Martin, “Investigation of turbulent structure modification by momentum injection into turbulent flow over a rough surface,” in *51st AIAA Aerospace Sciences Meeting including the New Horizons Forum and Aerospace Exposition*, no. AIAA 2013-534, May 2013.
- [21] A. Martin and I. D. Boyd, “Implicit implementation of material response and moving meshes for hypersonic re-entry ablation,” in *47th AIAA Aerospace Sciences Meeting and Exhibit*, no. AIAA-2009-0670, (Orlando, FL), Jan. 5-8 2009.
- [22] A. Martin and I. D. Boyd, “Mesh tailoring for strongly coupled computation of ablative material in nonequilibrium hypersonic flow,” in *10th AIAA/ASME Joint Thermophysics and Heat Transfer Conference*, no. AIAA-2010-5062, (Chicago, IL), June 28th to July 1st 2010.
- [23] Y.-K. Chen and T. Gökçen, “Implicit coupling approach for simulation of charring carbon ablators,” *Journal of Spacecraft and Rockets*, pp. 1–10, April 2014.
- [24] A. Turchi, *A gas-surface interaction model for the numerical study of rocket nozzle flows over pyrolyzing ablative materials*. PhD thesis, Von Karman Institute for Fluid Dynamics, 2013.

- [25] R. H. Ong, A. J. C. King, B. J. Mullins, T. F. Cooper, and M. J. Caley, “Development and validation of computational fluid dynamics models for prediction of heat transfer and thermal microenvironments of corals,” *PLoS ONE*, vol. 7, p. e37842, June 2012.
- [26] L. Yang, *CFD Modeling of Multiphase Counter-Current Flow in Packed Bed Reactor for Carbon Capture*. PhD thesis, The University of Kentucky, Lexington, KY, 2015.
- [27] W. J. Layton, F. Schieweck, and I. Yotov, “Coupling fluid flow with porous media flow,” *SIAM Journal on Numerical Analysis*, vol. 40, no. 6, pp. 2195–2218, 2002.
- [28] W. Jäger, A. Mikelić, *et al.*, “On the boundary conditions at the contact interface between a porous medium and a free fluid,” in *Pisa, Classe Fisiche e Matematiche-Serie IV*, Citeseer, 1996.
- [29] A. Mikelić, “Boundary conditions between free fluid flow and a porous medium,” in *Workshop on Filtration Problems in Porous Media and Paper Manufacturing*, (Eindhoven University of Technology), May 9 2003.
- [30] H. Brinkman, “A calculation of the viscous force exerted by a flowing fluid on a dense swarm of particles,” *Applied Scientific Research*, vol. 1, no. 1, pp. 27–34, 1949.
- [31] M. L. Bars and M. G. Worster, “Interfacial conditions between a pure fluid and a porous medium: implications for binary alloy solidification,” *J. Fluid Mech*, vol. 550, pp. 149–173, March 2006.
- [32] G. S. Beavers and D. D. Joseph, “Boundary conditions at a naturally permeable wall,” *Journal of fluid mechanics*, vol. 30, no. 01, pp. 197–207, 1967.

- [33] P. G. Saffman, “Boundary condition at surface of a porous medium,” *Studies in Applied Mathematics*, vol. 50, no. 2, pp. 93–101, 1971.
- [34] J. A. Ochoa-Tapia and S. Whitaker, “Momentum transfer at the boundary between a porous medium and a homogeneous fluid—I. theoretical development,” *International Journal of Heat and Mass Transfer*, vol. 38, pp. 2635–2646, September 1995.
- [35] M. Cieszko and J. Kubik, “Derivation of matching conditions at the contact surface between fluid-saturated porous solid and bulk fluid,” *Transport in Porous Media*, vol. 34, no. 1-3, pp. 319–336, 1999.
- [36] A. G. Salinger, R. Aris, and J. J. Derby, “Finite element formulations for largescale, coupled flows in adjacent porous and open fluid domains,” *International Journal for Numerical Methods in Fluids*, vol. 18, no. 12, pp. 1185–1209, 1994.
- [37] D. Gartling, C. Hickox, and R. Givler, “Simulation of coupled viscous and porous flow problems,” *International Journal of Computational Fluid Dynamics*, vol. 7, no. 1-2, pp. 23–48, 1996.
- [38] P. Schrooyen, K. Hillewaert, T. E. Magin, and P. Chatelain, “Fully implicit integrated approach for the numerical simulation of aerothermal flows through and around ablative thermal protection systems,” in *8th European Symposium on Aerothermodynamics for Space Vehicles*, 2015.
- [39] H. Zhang, A. Martin, and J. M. McDonough, “Parallel efficiency of the freecd code for hypersonic flows with chemistry,” in *24th International Conference on Parallel Computational Fluid Dynamics*, (Atlanta, GA), May 21-25 2012.
- [40] H. Weng, *Multidimensional Modeling of Pyrolysis Gas Transport Inside Orthotropic Charring Ablators*. Mechanical Engineering, University of Kentucky, Lexington, Kentucky, December 2014.

- [41] H. Zhang, H. Weng, and A. Martin, "Simulation of flow-tube oxidation on the carbon preform of PICA," in *52nd Aerospace Sciences Meeting*, no. AIAA 2014-1209, (National Harbor, MD), January 2014.
- [42] R. Davuluri and A. Martin, "Numerical study of spallation phenomenon in an arc-jet environment," in *11th AIAA/ASME Joint Thermophysics and Heat Transfer Conference*, American Institute of Aeronautics and Astronautics, 2014.
- [43] R. S. C. Davuluri, H. Zhang, and A. Martin, "Numerical study of spallation phenomenon in an arc-jet environment," *Journal of Thermophysics and Heat Transfer*, vol. 29, pp. 1–10, July 2015.
- [44] A. Martin, Bailey, S. C. C., F. Panerai, R. S. C. Davuluri, A. R. Vazsonyi, H. Zhang, Z. S. Lippay, N. N. Mansour, J. A. Inman, B. F. Bathel, S. C. Splinter, and P. M. Danehy, "Preliminary numerical and experimental analysis of the spallation phenomenon," in *8th European Symposium on Aerothermodynamics for Space Vehicles*, (Lisbon, Portugal), March 2015.
- [45] M. W. Chase, "NIST-JANAF thermochemical tables, fourth edition," *Journal of Physical and Chemical Reference Data*, no. 9, 1994.
- [46] P. A. Gnoffo, R. N. Gupta, and J. L. Shinn, "Conservation equations and physical models for hypersonic air flows in thermal and chemical nonequilibrium," Technical Report NASA-TP-2867, NASA Langley Research Center, Feb 1 1989.
- [47] K. Sutton and P. A. Gnoffo, "Multi-component diffusion with application to computational aerothermodynamics," in *7th AIAA/ASME Joint Thermophysics and Heat Transfer Conference*, no. AIAA 1998-2575, (Albuquerque, NM), June 15-18 1998.
- [48] L. C. Scalabrin, *Numerical Simulation of Weakly Ionized Hypersonic Flow Over Reentry Capsules*. PhD thesis, The University of Michigan, Ann Arbor, MI, 2007.

- [49] F. M. White, *Viscous Fluid Flow*. New York, NY: McGraw-Hill, 2nd ed., 1991.
- [50] F. G. Blottner, M. Johnson, and M. Ellis, “Chemically reacting viscous flow program for multi-component gas mixtures,” Technical Report SC-RR-70-754, Sandia Laboratories, January 1971.
- [51] W. G. Vincenti and C. H. Kruger, *Introduction to physical gas dynamics*. New York: Wiley, 1965.
- [52] C. Wilke, “A viscosity equation for gas mixtures,” *J. Chem. Phys.*, vol. 18, no. 4, pp. 517–519, 1950.
- [53] G. E. Palmer and M. J. Wright, “A comparison of methods to compute high-temperature gas viscosity,” in *8th AIAA/ASME Joint Thermophysics and Heat Transfer Conference*, no. AIAA 2002-3342, 2002.
- [54] H. Alkandry, I. D. Boyd, and A. Martin, “Comparison of models for mixture transport properties for numerical simulations of ablative heat-shields,” in *51st AIAA Aerospace Sciences Meeting*, no. AIAA 2013-0303, (Grapevine, TX), January 7–10 2013.
- [55] R. N. Gupta, J. M. Yos, R. A. Thompson, and K.-P. Lee, “A review of reaction rates and thermodynamic and transport properties for an 11-species air model for chemical and thermal nonequilibrium calculations to 30000 K,” Tech. Rep. NASA-RP-1232, NASA Langley Research Center, 1989.
- [56] J. J. Bertin, *Hypersonic Aerothermodynamics*. AIAA Education Series, 1994.
- [57] C. Park, *Nonequilibrium Hypersonic Aerothermodynamics*. Wiley-Interscience, February 1990.
- [58] F. Liu, T. Li, Y. Zhang, J. K. Neathery, K. Liu, and K. Saito, “Characterization and kinetics study of ilmenite for chemical looping combustion,” in *Spring*

Technical Meeting of the Central States Section of the Combustion Institute,
April 22–24 2012.

- [59] F. Liu, Y. Zhang, L. Chen, D. Qian, J. K. Neathery, K. Saito, and K. Liu, “Investigation of a canadian ilmenite as an oxygen carrier for chemical looping combustion,” *Energy & Fuels*, vol. 27, no. 10, pp. 5987–5995, 2013.
- [60] S. Gordon and B. J. McBride, “Computer program for calculation of complex chemical equilibrium compositions and applications I. analysis,” Tech. Rep. NASA RP-1311, NASA Lewis Research Center, 1994.
- [61] G. V. Candler and R. W. MacCormack, *Computation of weakly ionized hypersonic flows in thermochemical nonequilibrium*. PhD thesis, 1991.
- [62] S. P. Sharma, W. M. Huo, and C. Park, “Rate parameters for coupled vibration-dissociation in a generalized ssh approximation,” *Journal of Thermophysics and Heat Transfer*, vol. 6, pp. 9–21, January 1992.
- [63] R. C. Millikan and D. R. White, “Systematics of Vibrational Relaxation,” *Journal of Chemical Physics*, vol. 39, pp. 3209–3213, 1963.
- [64] P. L. Roe, “Approximate Riemann solvers, parameter vectors and difference schemes,” *Journal of Computational Physics*, vol. 43, pp. 357–372, 1981.
- [65] M.-S. Liou, “A sequel to AUSM, part II: AUSM+-up for all speeds,” *J. Comput. Phys.*, vol. 214, no. 1, pp. 137–170, 2006.
- [66] E. F. Toro, *Riemann Solvers and Numerical Methods for Fluid Dynamics: A Practical Introduction*. 3rd ed. Springer, 2009.
- [67] J. M. McDonough, “ME 690 Lectures on Computational Numerical Analysis of Partial Differential Equations,” lecture notes, University of Kentucky, 2015.
- [68] J. M. McDonough, “ME 692 Lectures on CFD II - Compressible Flows,” lecture notes, University of Kentucky, 2015.

- [69] J. L. Steger and R. Warming, “Flux vector splitting for the inviscid gasdynamic equations with applications to finite difference methods,” *Journal of Computational Physics*, vol. 40, pp. 263–293, 1981.
- [70] P. G. Buning and J. L. Steger, “Solution of the two-dimensional euler equations with generalized coordinate transformation using flux vector splitting,” in *3rd Joint Thermophysics, Fluids, Plasma and Heat Transfer Conference*, no. AIAA-1982-971, June 1982.
- [71] R. W. MacCormack and G. V. Candler, “The solution of the navier-stokes equations using gauss-seidel line relaxation,” *Computers & fluids*, vol. 17, no. 1, pp. 135–150, 1989.
- [72] M.-C. Druguet, G. V. Candler, and I. Nompelis, “Effects of numerics on navier-stokes computations of hypersonic double-cone flows,” *AIAA Journal*, vol. 43, pp. 616–623, April 2005.
- [73] G. V. Candler and I. Nompelis, “Computational fluid dynamics for atmospheric entry,” tech. rep., 2009.
- [74] S. Chakravarthy and S. Osher, “High resolution applications of the Osher upwind scheme for the Euler equations,” in *6th Computational Fluid Dynamics Conference Danvers*, AIAA Paper 1983-1943, June 1983.
- [75] G. Van Albada, B. Van Leer, and W. Roberts Jr, “A comparative study of computational methods in cosmic gas dynamics,” *Astronomy and Astrophysics*, vol. 108, pp. 76–84, 1982.
- [76] T. J. Barth and D. C. Jespersen, “The design and application of upwind schemes on unstructured meshes,” in *27th AIAA Aerospace Sciences Meeting and Exhibits*, no. AIAA-1989-0366, 1989.

- [77] K. Michalak and C. Ollivier-Gooch, “Limiters for unstructured higher-order accurate solutions of the euler equations,” *Journal of Computational Physics*, vol. 228 (23), pp. 8693–8711, 2009.
- [78] V. Venkatakrishnan, “On the accuracy of limiters and convergence to steady-state solutions,” in *31st Aerospace Sciences Meeting & Exhibit*, no. AIAA 93-0880, January 11-14 1993.
- [79] G. V. Candler, M. Barnhardt, T. W. Drayna, I. Nompelis, D. M. Peterson, and P. Subbareddy, “Unstructured grid approaches for accurate aeroheating simulations,” in *18th AIAA Computational Fluid Dynamics Conference*, no. AIAA 2007-3959, (Miami, FL), June 25-28 2007.
- [80] E. Sozer, C. Brehm, and C. C. Kiris, “Gradient calculation methods on arbitrary polyhedral unstructured meshes for cell-centered cfd solvers,” in *52nd Aerospace Sciences Meeting*, no. AIAA 2014-1440, (National Harbor, MD), January 2014.
- [81] D. A. Knoll and D. E. Keyes, “Jacobian-free newton–krylov methods: a survey of approaches and applications,” *Journal of Computational Physics*, vol. 193, no. 2, pp. 357–397, 2004.
- [82] C. Merkle, S. Venkateswaran, and P. Buelow, “The relationship between pressure-based and density-based algorithms,” in *30th Aerospace Sciences Meeting and Exhibit*, no. AIAA-1992-425, January 1992.
- [83] J.-R. Carlson, “Inflow/outflow boundary conditions with application to FUN3D,” Tech. Rep. NASA/TM-2011-217181, L-20011, NF1676L-12459, NASA Langley Research Center, October 2011.
- [84] S. Yoon and A. Jameson, “Lower-upper symmetric-gauss-seidel method for the euler and navier-stokes equations,” *AIAA Journal*, vol. 26, no. 9, pp. 1025–1026, 1988.

- [85] L. T. Tam, “LU-SGS implicit scheme for entry vehicle flow computation and comparison with aerodynamic data,” in *10th Applied Aerodynamics Conference*, no. AIAA-92-2671-CP, June 1992.
- [86] M. J. Wright, *A Family of Data-Parallel Relaxation Methods for the Navier-Stokes equations*. PhD thesis, University of Minnesota, Minneapolis, MN, June 1997.
- [87] I. Nompelis, T. W. Drayna, and G. V. Candler, “A parallel unstructured implicit solver for hypersonic reacting flow simulation,” in *17th AIAA Computational Fluid Dynamics Conference*, no. AIAA 2005-4867, (Toronto, ON), 2005.
- [88] S. Balay, W. D. Gropp, L. C. McInnes, and B. F. Smith, “Efficient management of parallelism in object oriented numerical software libraries,” *Modern Software Tools for Scientific Computing*, pp. 163–202, 1997.
- [89] S. Balay, S. Abhyankar, M. F. Adams, J. Brown, P. Brune, K. Buschelman, L. Dalcin, V. Eijkhout, W. D. Gropp, D. Kaushik, M. G. Knepley, L. C. McInnes, K. Rupp, B. F. Smith, S. Zampini, and H. Zhang, “PETSc Users Manual,” Tech. Rep. ANL-95/11 - Revision 3.5, Argonne National Laboratory, 2014.
- [90] S. Balay, J. Brown, K. Buschelman, W. D. Gropp, D. Kaushik, M. G. Knepley, L. C. McInnes, B. F. Smith, and H. Zhang, “PETSc Web page.” <http://www.mcs.anl.gov/petsc>, May 2014.
- [91] J. R. Shewchuk, “An introduction to the conjugate gradient method without the agonizing pain,” 1994.
- [92] I. Nompelis, J. Bender, and G. Candler, “Implementation and comparisons of parallel implicit solvers for hypersonic flow computations on unstructured meshes,” in *20th AIAA Computational Fluid Dynamics Conference*, no. AIAA 2011-3547, June 27 - 30 2011.

- [93] Y. Saad and M. H. Schultz, “GMRES: A generalized minimal residual algorithm for solving nonsymmetric linear systems,” *SIAM Journal on scientific and statistical computing*, vol. 7, no. 3, pp. 856–869, 1986.
- [94] M. Benzi, “Preconditioning techniques for large linear systems: a survey,” *Journal of Computational Physics*, vol. 182, no. 2, pp. 418–477, 2002.
- [95] B. R. Hollis, “Experimental and computational aerothermodynamics of a mars entry vehicle,” Tech. Rep. 201633, 1996.
- [96] I. D. Boyd, K. A. Trumble, and M. J. Wright, “Modeling of stardust entry at high altitude, part 1: Flowfield analysis,” *Journal of Spacecraft and Rockets*, vol. 47, pp. 708–717, September 2010.
- [97] <http://stardust.jpl.nasa.gov/photo/er.html>.
- [98] T. Gökçen and R. W. MacCormack., “Nonequilibrium effects for hypersonic transitional flows using continuum approach,” in *27th Aerospace Sciences Meeting*, no. AIAA-89-0416, Jan. 7-10 1989.
- [99] M. McKeown, “Validation of LeMANS CFD code for nozzle flows,” AE590 report, The University of Michigan, 2008.
- [100] J. D. Anderson, *Modern compressible flow: with historical perspective*. McGraw-Hill, 3rd ed., 2002.
- [101] D. Vigneron, J.-M. Vaassen, and J.-A. Essers, “An implicit finite volume method for the solution of 3d low mach number viscous flows using a local preconditioning technique,” *Journal of Computational and Applied Mathematics*, vol. 215, no. 2, pp. 610 – 617, 2008.
- [102] A. J. Chorin, “A numerical method for solving incompressible viscous flow problems,” *Journal of computational physics*, vol. 2, no. 1, pp. 12–26, 1967.

- [103] E. Turkel, “Preconditioning techniques in computational fluid dynamics,” *Annual Review of Fluid Mechanics*, vol. 31, no. 1, pp. 385–416, 1999.
- [104] E. Turkel, “Preconditioned methods for solving the incompressible and low speed compressible equations,” *Journal of Computational Physics*, vol. 72, no. 277-298, 1987.
- [105] W. A. Weiss, Jonathan M.; Smith, “Preconditioning applied to variable and constant density flows,” in *AIAA Journal*, vol. 33, pp. 2050–2057, 1995.
- [106] D. Choi and C. L. Merkle, “Application of time-iterative schemes to incompressible flow,” *AIAA Journal*, vol. 23, pp. 1518–1524, October 1985.
- [107] D. Darmofal and K. Siu, “A robust multigrid algorithm for the euler equations with local preconditioning and semi-coarsening,” *Journal of Computational Physics*, vol. 151, no. 2, pp. 728–756, 1999.
- [108] O. R. Burggraf, “Analytical and numerical studies of the structure of steady separated flows,” *Journal of Fluid Mechanics*, vol. 24, pp. 113–151, 1 1966.
- [109] P. Shah, B. Rovagnati, F. Mashayek, and G. B. Jacobs, “Subsonic compressible flow in two-sided lid-driven cavity. part i: Equal walls temperatures,” *International Journal of Heat and Mass Transfer*, vol. 50, pp. 4206–4218, 10 2007.
- [110] H. Darcy, *Les fontaines publiques de la ville de Dijon*. 1856.
- [111] D. A. Nield and A. Bejan, *Convection in porous media*. springer, 2006.
- [112] E. Shima and K. Kitamura, “Parameter-free simple low-dissipation AUSM-family scheme for all speeds,” *AIAA Journal*, vol. 49, no. 8, pp. 1693–1709, 2011.
- [113] Y.-S. Wu, K. Pruess, and P. Persoff, “Gas flow in porous media with klinkenberg effects,” vol. 32, no. 1, pp. 117–137, 1998.

- [114] G. Karypis and V. Kumar, *METIS: A Software Package for Partitioning Unstructured Graphs, Partitioning Meshes, and Computing Fill-Reducing Orderings of Sparse Matrices*. Univeristy of Minnesota, Minneapolis, MN, 1998.
- [115] E. Gabriel, G. E. Fagg, G. Bosilca, T. Angskun, J. J. Dongarra, J. M. Squyres, V. Sahay, P. Kambadur, B. Barrett, A. Lumsdaine, R. H. Castain, D. J. Daniel, R. L. Graham, and T. S. Woodall, “Open MPI: Goals, Concept, and Design of a Next Generation MPI Implementation,” in *Proceedings, 11th European PVM/MPI Users’ Group Meeting*, (Budapest, Hungary), pp. 97–104, September 2004.
- [116] University of Kentucky, “High performance computing.” <http://hpc.uky.edu>, August 2015.
- [117] M. Kim, A. Gülhan, and I. D. Boyd, “Modeling of electron energy phenomena in hypersonic flows,” *Journal of thermophysics and heat transfer*, vol. 26, no. 2, pp. 244–257, 2012.

Vita

Huaibao (Paul) Zhang

Professional Preparation

Ph.D. Student, Thermal-Fluid Science, University of Kentucky, Lexington, KY, USA
Oct. 2010-pres.

Master of Engineering Program, Engineering Thermophysics, Southeast University,
Nanjing, Jiangsu, China Oct. 2009-Jun. 2010

Bachelor of Engineering, Engineering Thermophysics, Intensive Training Class of
Mechanical & Power Engineering, Southeast University, Nanjing, Jiangsu, China Oct.
2005-Jun. 2009

Professional Experience

Graduate Research Assistant, University of Kentucky, Lexington, Kentucky, USA
2015–Present

- Joined Kentucky Re-entry Universal Payload System (KRUPS) program, which allows real-time data gathering using universal modular data system at low cost during reentry
- Performed related hypersonic aerodynamics computations for reentry process of KRUPS
- Provided the information of heat flow rate, pressure and their distributions on the surface for the coating of thermal protection materials

Graduate Research Assistant, University of Kentucky, Lexington, Kentucky, USA
2010–Present

Thesis Project 2: Coupling of Free Flow and Compressible Porous Flow

- Constructed a new Darcy-Brinkman equation for 3D compressible free flow and porous media flow
- Coupled free flow into porous media through a NASA flow tube problem

Thesis Project 1: Development of a Hypersonic Flow Solver

- Developed a 3D, structured/unstructured grid, finite-volume Navier-Stokes code for weakly ionized hypersonic flows in thermo-chemical non-equilibrium state
- Used MPI for inter-processors communications, linked PETSc FGMRES as linear solver
- Enhanced solver to work with Low mach number viscous flow
- Analyzed impact of spallation on thermal protection system (TPS) by coupling a particle tracking solver
- Investigated interactions between flow field and TPS through coupling a thermal response solver
- Implemented $k-w$ model

Experimental Investigation of Turbulence

- Collaborated on study of duct flow over a rough-walled, momentum injected boundary conditions

Graduate Teaching Assistant, University of Kentucky, Lexington, Kentucky, USA
2010–Present

- Gave lectures for 80 students on undergraduate class ME 330 Fundamentals of Fluid Mechanics, graded assignments and reports, and tutored on course work

- Mentored 6 undergraduates to use ANSYS Fluent/CFX on independent study and research projects

Undergraduate Research Group Leader, Southeast University, Nanjing, Jiangsu, China
2008–2009

Research Project: Coal-fired CO₂ Reduction Unit Design Based on Novel Inner Circulating Fluidized Bed

- Designed new inner circulating structure, involved in novel structure design, assembly and optimization
- Participated in cold-state experiments to measure the circulating particles volume and gas diffusion features
- Wrote planning documents and reports, planned final competition thesis defense

Awards and Certifications

2011 Graduate Certificate in Computational Fluid Dynamics, University of Kentucky, USA

2010 Academic Scholarship, University of Kentucky, USA

2008 Second Prize at the First National College Student Competition for Energy Saving and Emission Reduction Technologies, China

2008 Excellent Monitor, Southeast University, China

2007 He Yaoguang Scholarship, Southeast University, China 2006 Jiangsu Provincial Scholarship, Southeast University, China

Professional association

AIAA Student Member

Interests

Hiking, Swimming, Zen Meditation